Processing
of
Space Surveillance Observations

Inauguraldissertation
der Philosophisch-naturwissenschaftlichen Fakultät
der Universität Bern

vorgelegt von

Benedikt Reihs

aus Deutschland

Leiter der Arbeit:
Prof. Dr. T. Schildknecht
Astronomisches Institut der Universität Bern

Ko-Leiter der Arbeit:
Dr. A. Vananti
Astronomisches Institut der Universität Bern

Processing
of
Space Surveillance Observations

Inauguraldissertation
der Philosophisch-naturwissenschaftlichen Fakultät
der Universität Bern

vorgelegt von

Benedikt Reihs

aus Deutschland

Leiter der Arbeit:
Prof. Dr. T. Schildknecht
Astronomisches Institut der Universität Bern

Ko-Leiter der Arbeit:
Dr. A. Vananti
Astronomisches Institut der Universität Bern

Von der Philosophisch-naturwissenschaftlichen Fakultät angenommen.

Bern, 21.06.2021

Der Dekan:
Prof. Dr. Zoltan Balogh

Abstract

This thesis covers the processing of different types of space surveillance measurements. The emphasis is on the initial build-up of a catalogue. Most experiments focus on the identification of objects from pairs of observations by testing whether these two observations could originate from the same object. The advantage of this approach is that an orbit from two passes is usually more precise than that from a single pass and thus the chance of associating subsequent measurements with this newly derived orbit is higher.

The main contribution is the introduction of a method for perturbed initial orbit determination and observation correlation from two radar tracklets. The perturbed initial orbit determination provides the solutions for all possible numbers of revolutions from two positions under consideration of the secular J_2-perturbations, which causes for example the rotation of the orbital plane. The perturbations are considered analytically in an iterative process. From the different numbers of revolutions, the most probable solution can either be selected via the minimum Mahalanobis distance, using the range-rate as a remaining observable, or after an additional post-processing. The robustness and applicability of the method is shown using real radar measurements, which includes a large percentage of successful initial orbit determinations for tracklets which are more than 20 days apart. This method is also extended to the combination of optical and radar measurements for objects in Highly Elliptical Orbits.

Concerning the simulation of a cold-start of a catalogue, two different processing strategies are introduced. One is adding a least squares orbit determination using a pair of possibly correlated tracklets, while the other approach collects data over a longer time span and generates a graph network from which clusters of tracklets are derived as new candidate objects.

Further analysis focuses on aspects of operational processing of space surveillance measurements. This includes the automated decision making process for the monitoring of the quality of existing catalogue objects and the design of an autonomous processing pipeline for optical measurements at the Zimmerwald observatory. A potential space mission to observe the Geostationary Orbit is also analysed with regard to its performance during the catalogue build-up.

Acknowledgements

Contents

List of Figures

List of Tables

List of Abbreviations

AoP	Argument of Perigee
AOS	Attributable Optimised Coordinate System
AS	Anti-solar
AT	Along track
CCD	Charge-coupled device
ESA	European Space Agency
FN	False Negative
FoR	Field of Regard
FP	False Positive
GEO	Geostationary Orbit
GMM	Gaussian Mixture Model
GSO	Geosynchronous Orbit
GTO	Geostationary Transfer Orbit
HEO	Highly Elliptical Orbit
HPBW	Half-power beamwidth
IADC	Inter-Agency Space Debris Coordination Committee
IOD	Initial Orbit Determination
KSR	Kiwi Space Radar
LEO	Low Earth Orbit
LSQ-OD	Least Squares Orbit Determination
MHT	Multi Hypothesis Tracking
MSR	Midland Space Radar
PFISR	Poker Flat Incoherent Scatter Radar
PRT	Pulse Repetition Time
RAAN	Right Ascension of the Ascending Node
RCS	Radar Cross Section
RFS	Random Finite Sets
RMS	Root Mean Square
RPP	Residuals Post Processing
RTN	Radial, tangential/along-track, normal
SSO	Sunsynchronous Orbit
TCA	Time of closest approach
TCC	Tracklet-Catalogue Correlation
TLE	Two-Line Elements
TP	True Positive
TPWO	True Positive with Wrong Orbit
UCT	Uncorrelated Tracklet

UHF	Ultra High Frequency
ZSM	ZimSMART
ZTW	ZimTWIN

Nomenclature

A	Area
$\mathcal{A}$	Attributable vector
a	Semi-major axis
az	Azimuth
c	Speed of light
d	Distance
E	Expectation value
e	Eccentricity
el	Elevation
f	Frequency
G	Antenna gain
H	Entropy
h_a	Altitude over ground
I	Information content (surprisal)
i	Inclination
J	Jacobian matrix
J_2	Perturbation coefficient (oblateness)
L	Line of Sight
M	Mean anomaly
M_{d}	Mahalanobis distance
N	Orbit normal (vector)
N	Quantity
$\mathcal{N}$	Normal distribution
n	Mean motion
$\mathcal{O}$	Observables
P	Power
$\mathcal{P}$	Probability
p	Semi-latus rectum
p	Probability density function
p_t	T-test probability
R_{E}	Earth radius
r	Position
S	Score
t	Epoch
v	Velocity
x	State
z	Measurement (general), z-Score

α	Right ascension
δ	Declination
θ	Observation angle (AOS, general)
λ	Wavelength
μ_{E}	Gravitational parameter (Earth)
μ	Mean
ν	Degrees of freedom
ρ	Range
σ	Standard deviation
σ_{RCS}	Radar Cross Section
Σ	Covariance matrix
τ	Pulse Length
ϕ	Phase (electromagnetic wave)
φ	True anomaly
Ω	Right ascension of the ascending node
ω	Argument of perigee

Mathematical Notation

Δ	Difference operator
$\dot{x}$	Time derivative $\partial x / \partial t$
$\vec{x}$	Vector
$\lvert \vec{x} \rvert$	L_2-norm of vector
X^T	Transposed matrix/vector
$\overline{x}$	Average
X^{-1}	Inverse matrix
$\langle \vec{x}, \vec{y} \rangle$	Inner (scalar) product

INTRODUCTION

1.1 Space Debris Environment

Since the launch of the first object into an orbit around Earth in 1957 by the Soviet Union, activities in space have increased continuously, e.g. the number of launches, the applications based on satellites and the participating nations. Because not all objects in space are functional satellites, the term *space debris* is used to refer to human-made objects "including fragments and elements thereof, in Earth orbit or re-entering the atmosphere, that are non functional" (IADC, 2007) as defined by the Inter-Agency Space Debris Coordination Committee (IADC). Especially the generation of space debris has lead to a steady increase in the number of artificial objects in space around Earth over the past 60 years, see Figure 1.1 (ESA, 2019). The numbers in this figure can be obtained from DISCOS (McLean et al., 2017), the database of the European Space Agency (ESA) containing information on the objects from the public space object catalogues by the US military and the Russian Vimpel corporation, see Section 2.1.

There are two prominent step increases visible in the plot as part of the payload fragmentation debris. One is due to the Chinese anti-satellite missile test in 2007, during which a weather satellite in approximately 800 km altitude was destroyed which caused a large cloud of fragments. The second major increase is caused by the fragmentation clouds from the collision between two communication satellites, one French Iridium and one Russian Cosmos satellite, in 2009. Recently, there are also increases due to other fragment-generating events such as the explosion of rocket bodies which were left in orbit after delivering the payload. There can be various reasons for these explosions, see (Braun et al., 2017) for an in-depth discussion. Further details on the current space object environment can be found in ESA's Space Environment Report (ESA, 2019).
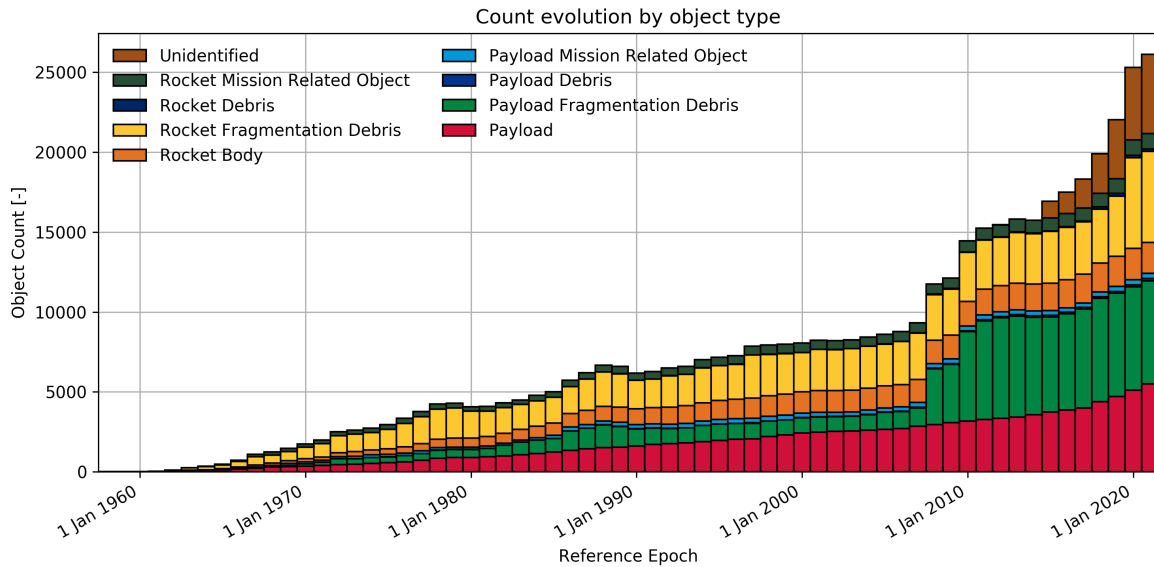
Figure 1.1: Evolution of the space debris environment for different object types (Source: `https://sdup.esoc.esa.int/discosweb/statistics/`).

The orbiting objects are not distributed uniformly around Earth, but there are certain orbital regimes of interest where large numbers of objects have accumulated. Two of those are the Low Earth Orbit (LEO) and the Geosynchronous Orbit (GSO). LEO is a common choice for example for remote sensing or communication constellations. This orbital regime is a compromise between being high enough to reduce the atmospheric drag force and staying low enough to reduce the required transmission power towards the Earth surface. The definition by the IADC considers LEO to be all orbits with an altitude of less than 2 000 km (IADC, 2007). The current distribution of LEO objects over their semi-major axis is shown in Figure 1.2a based on a snapshot of the US American TLE catalogue, see Section 2.1. The peak at semi-major axes of 7 100 km - 7 300 km , which is roughly equivalent to 800 km - 1 000 km altitude, is due to objects in so-called Sunsynchronous Orbits (SSO). The orbital plane of an SSO rotates around the Earth with the same rate as the Earth's rotation around the Sun and thus the relative position of the Sun towards such an orbital plane is always the same. Considering Earth observation, this leads to the effect that the illumination conditions on ground are always the same when the satellite passes over the same location. An SSO also requires a matching retrograde inclination around 97° - 99°, which leads to the visible peak in the inclinations' distribution in Figure 1.2b.

The second regime of interest, the GSO, is of interest because it allows at an altitude of approximately 36 000 km that satellites are orbiting at the same angular rate as the Earth rotation. The orbit which is exactly at the correct altitude and has an inclination and an eccentricity of zero is referred to as the Geostationary Orbit (GEO), because an object in such an orbit always stays above the same point on the equator. Thus, this orbit is a popular choice for communication or television satellites which are servicing a specific region of the Earth. In practical applications, it is not possible or desired to reach this orbit exactly due to the constraints of satellite operation, but all objects which are kept under control close to these orbital parameters are referred to as a GEO object throughout this thesis. The term GSO is used in this thesis to refer to objects in the vicinity of GEO, it is defined more

(a) Semi-major Axis (b) Inclination
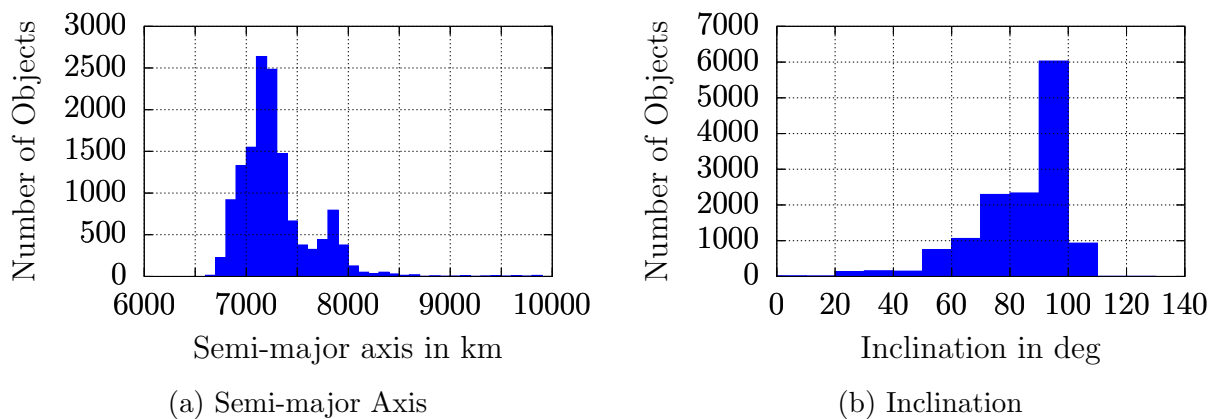
Figure 1.2: Distribution of the TLE objects' semi-major axis and inclination for LEO objects.

strictly in Section 6.3. The peak due to GEO objects is visible in Figure 1.3 for both the semi-major axis and the inclination. The maximum inclination of 15° is due to the natural perturbations of the Earth gravitational field and the third body perturbations by the Moon and the Sun (Schildknecht, 2007). This distribution is discussed further in Section 1.2.2.

(a) Semi-major Axis (b) Inclination
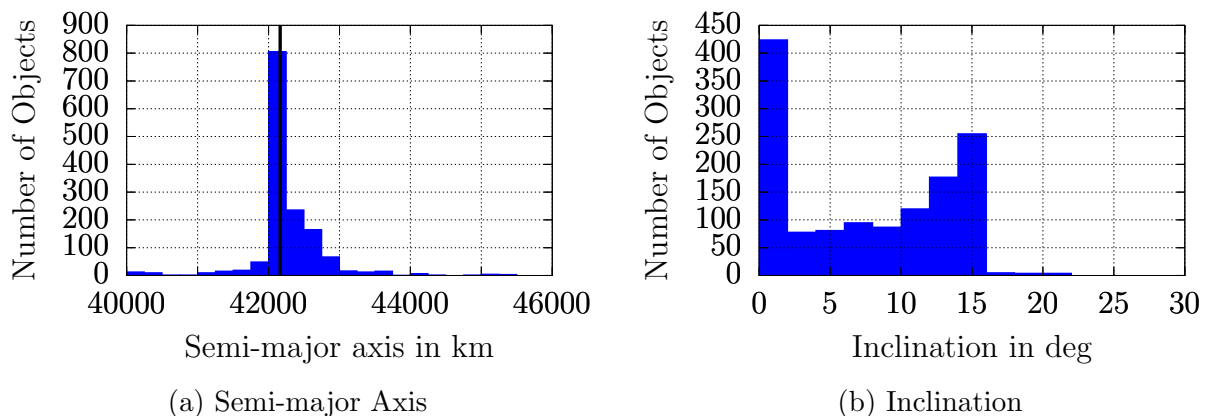
Figure 1.3: Distribution of the TLE objects' semi-major axis and inclination for GSO objects (GEO altitude indicated by vertical black line).

Future trends in the commercial use of space may lead to an immense increase in the number of objects in space. Several plans exist to create so-called *megaconstellations* of thousands of satellites, which would have a significant impact on the long-term sustainability of orbits around Earth (Lewis et al., 2017). At the same time, concepts for post-mission disposal of satellites and rocket bodies after the completion of their mission are studied and implemented to reduce the growth of the space debris environment. Even missions for the active removal of defunct objects from space are in development.

The clustering of objects in similar regions and the resulting collision risk leads to a potential chain reaction of consecutive collisions due to the increasing number of objects from previous collisions (Kessler and Cour-Palais, 1978). This effect, commonly called Kessler syndrome, could render parts of the orbits around Earth effectively useless for space flight due to the large densities of uncontrolled objects. Even if this worst-case scenario does not occur, the steady increase of objects around Earth requires it to extend and improve

methods of observations as well as the processing thereof. This is collected under the term *space surveillance* or *space debris monitoring*. Common techniques to acquire observations of space objects are discussed in the next section. Further information on multiple aspects of the space debris problem can be found in the literature, e.g. (Klinkrad, 2006).

1.2 Observation Techniques

In order to enable safe operations of satellites in the space environment, regular observations of space objects are necessary to estimate their orbits and potentially derive further information. The two most common observation techniques in space surveillance, radar and telescope, are introduced in the following concerning their functionality and application to space object observations. The emphasis is on radar systems as these are the main source of data for this work, but also the general principles of the telescope are introduced.

Concerning the nomenclature related to measurements, the following is valid throughout the entire thesis. The terms *detection*, *measurement* and *observation* are used synonymously for a single set of observables at a given epoch. The term *pass* refers to the entire arc of a satellite when it is above the horizon for a given station and thus it is, at least theoretically, visible for a period of time. If this term is used relating to measurements, it refers to the entire subset of observations during this pass. To refer to a sequence of measurements during one pass, the term *tracklet* is used. This expression originates from sequences of optical observations which are too short to calculate an orbit, but here it will be used in general for series of measurements during the same pass by the same station. Within the domain of radar measurements, also the term *track* refers to a sequence of detections. It is often used in the context of identifying all detections from the same object during a single pass. To avoid confusion, this expression is not used in this thesis and its meaning is covered by *tracklet*.

For both sensors, radar and telescopes, there are different sensor-specific methods to extract tracklets from a series of detections. This includes rejecting false detections and separating multiple tracklets which are measured within the same data set. These tracklet-building algorithms and also the extraction of detections from the raw sensor output are not considered within this thesis. After the introduction of the sensor technology in the following section, it is assumed within the remaining chapters that the output of the sensor is a tracklet with measurements belonging to a single object.

1.2.1 Radar

The term *radar* was originally introduced as an abbreviation for *radio detection and ranging*. This technique is based on the active emission of electromagnetic waves from a transmitting antenna. If these waves intercept an object, commonly called target in radar engineering, they can be reflected depending on the physical properties of the object. If the reflected waves are detected by a receiving antenna, which may or may not be the same as the transmitting antenna, the object has been observed. A *monostatic radar* has a single antenna for transmission and reception, whereas a radar with separate antennas is called *bistatic*. The sequence of interactions can be used to derive the radar range equation as a simplified

estimation of the received power P_r in case of a monostatic radar (Skolnik, 2001):

$$P_r = \underbrace{P_t \cdot G}_{\substack{\text{Effectively} \\ \text{emitted power}}} \cdot \underbrace{\frac{1}{4\pi\rho^2}}_{\substack{\text{Density} \\ \text{at target}}} \cdot \underbrace{\sigma_{\text{RCS}}}_{\substack{\text{Effective} \\ \text{reflection area}}} \cdot \underbrace{\frac{1}{4\pi\rho^2}}_{\substack{\text{Density} \\ \text{at antenna}}} \cdot \underbrace{A_e}_{\substack{\text{Effective} \\ \text{reception area}}} ,$$

$$P_r = \frac{P_t \cdot G \cdot A_e \cdot \sigma_{\text{RCS}}}{(4\pi)^2 \cdot \rho^4} , \qquad (1.1)$$

containing the transmit power P_t, the antenna gain G, the effective antenna area A_e, the radar cross section (RCS) σ_{RCS} of the detected object and the one-way range ρ, i.e. the distance between antenna and target. If P_r is larger than the minimum detectable signal $S_{\min}$ of the sensor, the object can be detected. From Equation 1.1 it is visible that due to the ρ^{-4}-proportionality, it is difficult to detect objects at large distances as this requires either a large transmission power or a large antenna. This is the reason why radar measurements in space surveillance are mainly used for LEO objects.

The antenna gain G is a correcting factor to account for the directivity of the antenna which refers to the concentration of the propagating wave in a specific direction compared to the simple, isotropically radiating antenna. For example, the gain of a dish antenna depends on the radar's wavelength λ:

$$G = \frac{4\pi \cdot A_e}{\lambda^2} . \qquad (1.2)$$
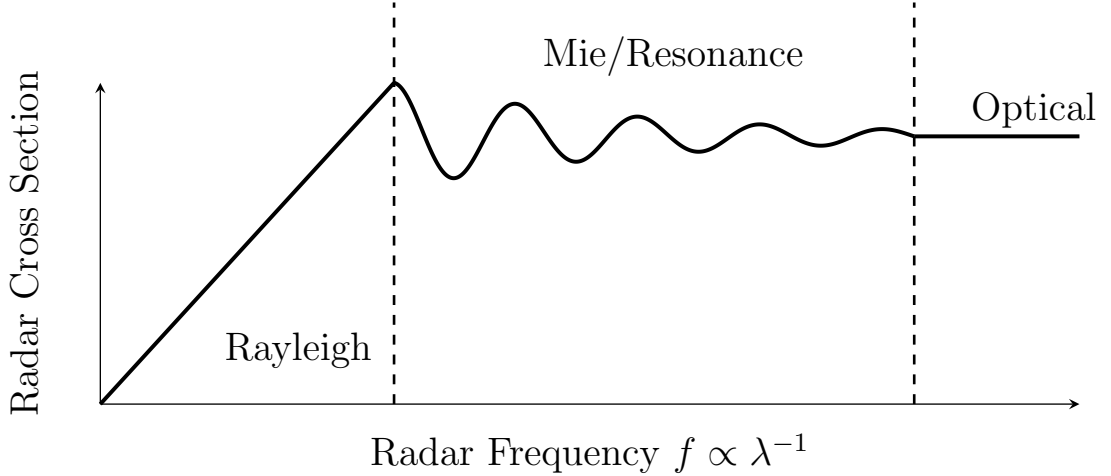
Figure 1.4: Different scattering regions of radar waves.

Another parameter of special interest is the RCS. It has the unit m^2 and can be interpreted as the effective scattering area of the object. This should not be confused with the physical cross section A_p of the object, because the RCS also includes effects due to the material, i.e. relation of absorption and reflection, and the interaction between the radar wave and the object. Figure 1.4 shows the idealised dependency between the frequency of the radar and the RCS. The frequency is related to the wavelength via the speed of light c:

$$f = \frac{c}{\lambda} . \qquad (1.3)$$

There are three different scattering regions depending on the relation between the physical size of the object and the wavelength. If the wavelength is much smaller than the object, the RCS is constant in the optical scattering region. Depending on the reflectivity of the object, the RCS can be proportional to the illuminated physical area in that region. As the name indicates, this is the typical case for the reflection of visible light. If the wavelength is much larger than the object, a continuous increase of the RCS with an increase in frequency is visible, which is the so-called Rayleigh region. In between the optical and Rayleigh scattering regions, the Mie or resonance region is characterised by oscillations in the RCS due to more complex interactions between the object and the waves. Due to these scattering properties, also the size of the objects which shall be detected by a radar has to be considered when planning a radar and selecting its frequency. More information on scattering properties can be found in the literature, e.g. (Skolnik, 2001). As an example for wavelengths used in space surveillance, the LeoLabs, Inc. radars, see Section 5.2, operate in UHF (Ultra High Frequency) at $\lambda \approx 70$ cm (Nicolls et al., 2017). The Spanish S3T radar operates in S-Band, which translates to a wavelength of $\lambda \approx 20$ cm (Gomez et al., 2019).

Considering the implementation of a radar into a physical structure, there are two main technologies. One is the already mentioned dish antenna, which consists of a, for example hyperbolical, dish to reflect the electromagnetic wave and the feeder from where the wave is emitted onto the dish. The pointing of the antenna is done by mechanically steering the entire antenna towards the desired direction. This requires various additional parts, e.g. motors and bearings, which becomes more complex with a growing size of the antenna.

In contrast to the dish, the phased array has no mechanical steering but is based on a planar structure of small emitting antennas. Each antenna is a single emitter and due to the interaction of these small elements, a consistent wave pattern can form at a certain distance from the array in the so-called far-field. A simplified example of a linear phased array is shown in Figure 1.5 to visualise the interaction and beam steering. The array consists of N_e elements which have a constant spatial separation of d_e. The broadside angle Θ_B is defined as the angle from the local zenith to define the direction relative to the array including the current steering angle Θ_S. The electrical steering is achieved by introducing an offset between the phases ϕ_e of the emitted waves from the different elements. This has the same effect as a time delay between the emitters, which also occurs naturally when a wave is refracted at the boundary between two media with a different wave propagation velocity. The distance between the elements also has an effect on the beam width and the radiation pattern.

The phase shift $\Delta\phi$ between two adjacent elements, which is required to steer an array with the distance d_e between the elements and a wavelength of λ by an angle of Θ_S, is:

$$\Delta\phi = \frac{360° \cdot d_e \cdot \sin(\Theta_S)}{\lambda} \ . \tag{1.4}$$

The interaction of the single elements leads to a consistent radiation pattern in the far-field at distances $\rho \gg \frac{2 \cdot (N_e \cdot d_e)^2}{\lambda}$. Figure 1.6 shows an example of such a radiation pattern of a linear phased array as the one shown in Figure 1.5. The plot depicts the power levels over one half of the possible broadside angles relative to the maximum in the current steering direction Θ_S. For $\Theta_S = 0°$, the pattern is line symmetric about $\Theta_B = 0°$. The -3dB-line is added to the plot to indicate where the radiation power has dropped to half of the maximum value, which is a common performance figure of a radar as the half-power beamwidth (HPBW).
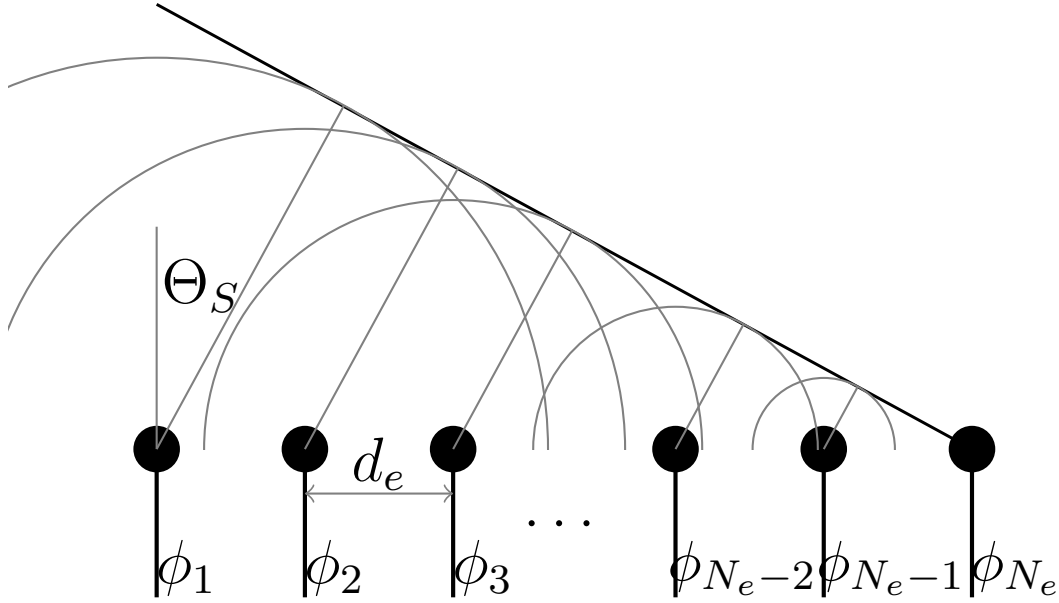
Figure 1.5: Simplified example of a one-dimensional phased array and its beam steering via phase-shifting.

For a linear phased array, this HPBW of the main lobe can be approximated by the formula:

$$\Theta_{HPBW} \approx \frac{0.886}{N_e \cdot \cos(\Theta_S)} \cdot \frac{\lambda}{d_e} \text{ radians} . \tag{1.5}$$

From this formula it is also visible, that steering away from the local zenith leads to an increase of the beamwidth. For the example of $\Theta_S = 45°$ in Figure 1.6, this gives a HPBW of approximately 10° compared to roughly 7° at zenith. As the plot shows, there are also multiple sidelobes. While the number of these sidelobes depends on the number of elements, the relative power of the first sidelobe is always at -13dB for the linear phased array if all elements are fed with the same power. In order to reduce the sidelobes, it is possible to emit less power via the elements at the side of the array. This is called *tapering*. More information on phased arrays can be found in (Mailloux, 2017). The electrical steering of a phased array allows it to rapidly switch between targets and directions, which makes it a favourable choice for modern space surveillance radars.

In addition to the different implementations of a radar, there are also different operation modes regarding the emission of radio waves. In the following, the pulsed monostatic radar is discussed as a common form of radar. Such a radar emits single pulses of radiation at a constant rate and is available to detect the echoes between the emission of two pulses. The emission cycle of such a radar is shown in Figure 1.7. As it can be seen in the figure, the radar emits a pulse of the length τ in regular intervals according to the pulse repetition time (PRT) T_p. These characteristic times are also influencing the radar's maximum theoretical performance. A pulsed radar measures the distance to the object via the total time t_s between emission and reception of the reflected signal:

$$\rho = \frac{c \cdot t_s}{2} . \tag{1.6}$$
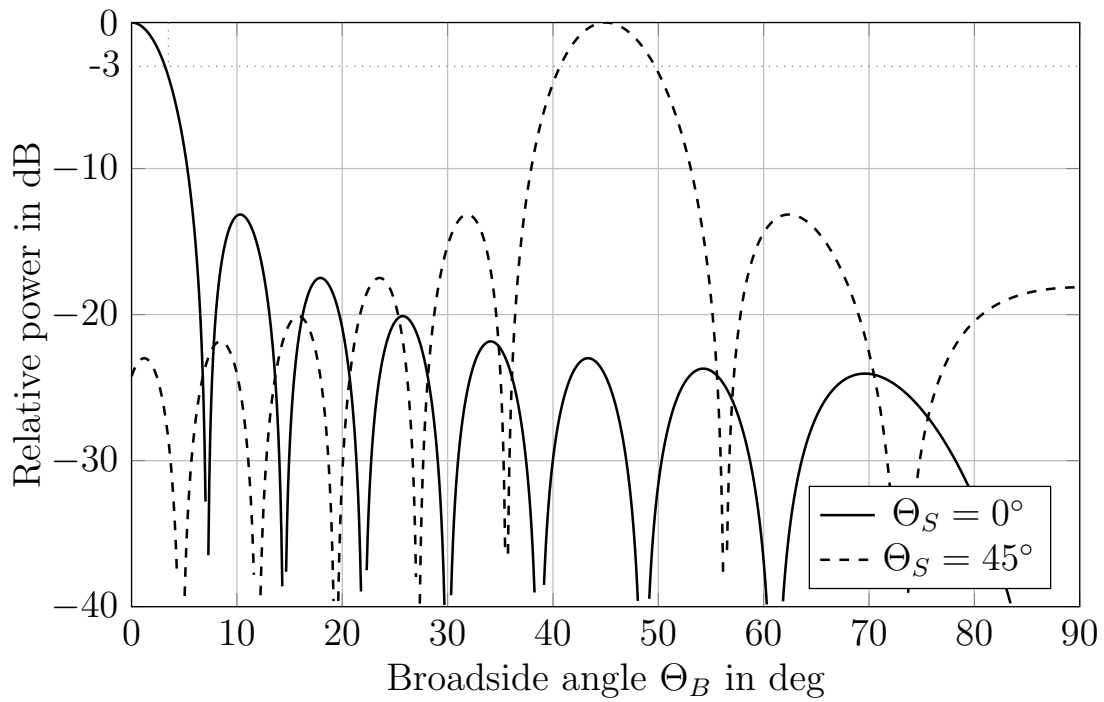
Figure 1.6: Simplified example of a one-dimensional phased array radiation pattern for two different steering directions ($\frac{\lambda}{d_e} = 0.5$, $N_e = 16$).
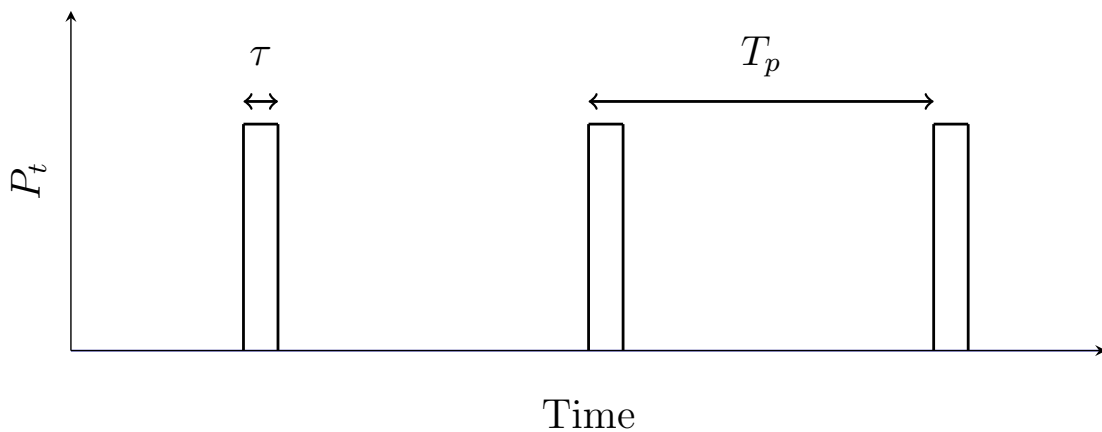
Figure 1.7: Simplified duty cycle of a pulsed radar.

The factor 1/2 is added because the radar pulse travels the distance ρ twice during t_s. Due to the non-infinitesimal pulse length τ, two targets need a minimum distance $\Delta\rho$ in order to be separable by the radar:

$$\Delta\rho = \frac{c \cdot \tau}{2} \ , \tag{1.7}$$

otherwise the two reflected echoes are overlapping and cannot be distinguished. Additionally, there is a maximum unambiguous range ρ_{max}, which indicates the maximum distance to ensure that the reflected pulse is received before the next pulse is emitted. Thus this value is related to the PRT:

$$\rho_{\mathrm{max}} = \frac{c \cdot (T_p - \tau)}{2} \ . \tag{1.8}$$

In addition to the range, the doppler shift f_d of the transmit frequency can be detected which is due to the velocity of the target along the radial direction. This velocity is equivalent to the derivative of the range, also called range-rate $\dot{\rho}$. The frequency shift also depends on the transmit frequency f_{Tx}:

$$f_d = \frac{2 \cdot \dot{\rho} \cdot f_{Tx}}{c} \ . \tag{1.9}$$

The electronic signal processing which is necessary to create and detect the signal of the electromagnetic waves or techniques to improve a radar's performance are not discussed here. Further explanations can be found in the literature, see e.g. (Skolnik, 2001; Mailloux, 2017).

Resulting from this short discussion, the two main observables of the radar are the range and the range-rate, which can be measured with a relatively high precision. In contrast to this, the angular resolution of the radar is limited by the pointing accuracy and the beamwidth, which is comparatively coarse as seen earlier. The pointing of a radar is usually given via the two direction angles azimuth az and elevation el, which are defined in the local topocentric coordinate system. The azimuth gives the direction projected onto the local horizontal plane with North being defined as 0° and increasing values going towards East. The elevation is the angle above the local horizontal plane. This leads to the complete set of radar observables:

$$\mathcal{O}_{\mathrm{radar}} = \{\rho, \dot{\rho}, az, el\} \ . \tag{1.10}$$

The application of radar measurements to space surveillance has three main forms. The first one is the dedicated tracking of objects as follow-up measurements based on previously known orbits to improve them. The second one is the scanning of a predefined Field of Regard (FoR) to detect all objects which are passing through this field without a dedicated tracking strategy. Objects are still detected multiple times within the FoR to obtain a tracklet. For example, this is the mode of operation of the S3T radar (Gomez et al., 2019). Combining regular scanning with follow-up measurements is particularly well achievable with the phased array radar, because the beam can switch rapidly between tracking different objects and scanning the FoR. This is the most common operation in space surveillance and can be found in many radar systems, e.g. GESTRA (Wilden et al., 2017), LeoLabs, Inc. (Nicolls et al., 2017) and the new US fence radar (Fonder et al., 2017). Finally, a common experiment is the so-called beam-park. In this set-up, the radar beam is constantly pointing in the same direction for a specific period of time, e.g. 24 hours. This is similar to the surveillance scan but without any active motion, see e.g. (Vierinen et al., 2019). The results of this

experiment are not intended to derive orbits of the objects and catalogue them, but to get information on the statistical distribution of objects. A special case is also the EISCAT_3D radar which usually probes the ionosphere, but it can also be used as a space surveillance sensor (McCrea et al., 2015).

1.2.2 Telescope

Telescopes are used to observe objects in high-altitudes at large ranges, because they detect electromagnetic radiation passively. Passive means, compared to the active radar, that the telescope does not provide its own source of radiation but uses reflections from other sources. For space surveillance, this is the reflected sunlight. Thus the distance to the object is less critical because no power has to be provided for the emission of the wave and the intensity at the telescope reduces according to ρ^{-2}. Concerning the wavelength, space surveillance applications which acquire positions of the objects are using visible light as a source, but also other wavelengths can be used, for example infrared to obtain characteristic physical properties of the scattering surface. Due to the passive nature and the use of sunlight, there is no time or frequency reference for the received radiation and thus no range or range-rate can be estimated, with the exception that characteristic frequencies in the spectrum of the Sun may be used to estimate doppler frequencies (Pantalone and Kudenov, 2018). However, this is not used in regular space surveillance.

The light is collected by an optical aperture and directed onto a detector. Commonly this is a charge-coupled device (CCD), which creates electric charges proportional to the amount of incoming light within a regular grid of pixels. Depending on the brightness of the observed object, the radiation is collected over a pre-set period of time called *exposure time*. Then the electrical charges in the single pixels are read out and can be translated again to a picture with varying brightness. The resulting picture contains also the stars in the background. Because the directions in the geocentric frame towards these stars are well-known and catalogued, they can be used as references to calculate the direction angles to the satellite in the image. This gives the relatively precise direction angles right ascension α and declination δ in the inertial geocentric system, which are used as the main observables of the telescope:

$$\mathcal{O}_{\text{Optical}} = \{\alpha, \delta\} \ . \tag{1.11}$$

The declination is the elevation over the equatorial plane of the Earth and the right ascension is the direction projected onto this plane measured from the vernal equinox. Additionally, the brightness of the satellite, called *magnitude*, can be considered as another observable. If a satellite is tracked over several minutes, variations in the magnitude can be used to infer its attitude motion (Rachman et al., 2018).

Due to the Earth rotation and the motion of the satellites, there are two different approaches to point the telescope during the exposure time. The telescope can compensate the motion of the Earth and thus always point in the same inertial direction. In this case, the stars in the background are points and a satellite would appear as a streak on the image. Conversely, it is also possible to move the telescope at a rate which coincides with that of the expected motion of the satellite. If a satellite with the expected motion is in the field of view, it appears as a point while the stars are now streaks.

(a) $\Omega - i$

(b) $\alpha - \delta$
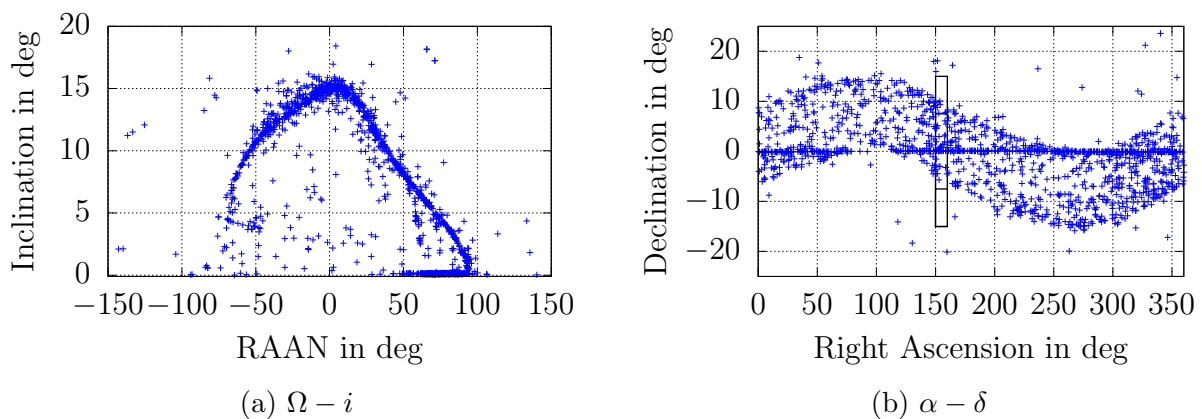
Figure 1.8: Distribution of the TLE objects in GSO.

When planning observations of objects in GSO, the characteristic distribution of these objects has to be considered. Due to the non-spherical Earth gravitational field and the luni-solar third body perturbations, the orbital plane of a GSO object precesses around the so-called Laplace plane with a period of approximately 53 years (Allan and Cook, 1964). Due to the Laplace plane's inclination of roughly 7.5°, an object which is released at a low inclination will build up an inclination of approximately 15° within half of that period, before reducing it again. The orientation of the Laplace vector is such that the right ascension of the ascending node (RAAN) of the perturbed orbit will move from 90° to 270°, reaching the maximum inclination at $\Omega = 0°$. The resulting distribution of objects can be seen in Figure 1.8a. If this distribution is projected into the right ascension-declination system for an observer at the Earth centre, it forms a sine-like wave around GEO, see Figure 1.8b. Based on this distribution, it is possible to identify areas with a high probability of passing objects without considering a specific population. Objects which are not following these dominant patterns, have either been located in their orbit by means of propulsion or they are high area-to-mass ratio objects, for which the solar radiation pressure becomes a significant source of acceleration (Schildknecht, 2007).

When scanning the observable region as in Figure 1.8b, different scanning strategies are possible to maximise the number of detected objects. The observations can either be made along the constant declination of the GEO to avoid missing objects (Schildknecht, 2007) or multiple fields with different declinations along a constant right ascension can be observed (Herzog et al., 2010). In the second case, it is necessary to thoroughly plan the series of right ascensions to minimise the number of objects passing without being detected. Further information on optical surveys of high-altitude orbits, which also includes the Highly Eccentric Orbits (HEO), can be found in (Schildknecht, 2007).

1.3 Scope of this Work

This thesis introduces a method for the association of radar measurements based on a perturbed initial orbit determination (IOD). This also includes the selection of the number of revolutions between the two measurements. This method is applied to different measurement scenarios also in combination with algorithms to build-up a space object database. Various analysis are made towards supporting the implementation of an operational processing algorithm of space surveillance measurements.

These aspects are discussed in the different chapters as follows. In Chapter 2, the basic motivation and steps towards building and maintaining a space object catalogue are introduced. A new coordinate system to improve the processing of tracklets is also presented. In Chapter 3, an overview of the association of measurements is given and a clustering algorithm based on a graph network is described. The developed association method is discussed in detail in Chapter 4. Its performance is validated with simulated and real measurement data for different observation scenarios in Chapter 5. Extensions of the method towards other data sources including tests of operational implementations of the tracklet association is shown in Chapter 6. The closing remarks and a discussion of possible future work items is found in Chapter 7.

OBSERVATION PROCESSING

2.1 Space Object Orbit Database

2.1.1 Overview

The overall goal of regular observations of space objects is to maintain a database with space objects and their characteristics, e.g. orbit, size or attitude behaviour. For this thesis, the focus is on the orbital information of the objects for a space object orbit database, which is commonly called catalogue. Such a database can be used for various important tasks regarding the space debris environment and space safety. Some examples are given in the following. One of the most important aspects is the collision avoidance for active satellites. Based on a catalogue of space object orbits, it is possible to scan all these objects for potentially dangerous close encounters, called conjunction events. Satellite operators perform this constantly to monitor the threat level for their satellites and plan avoidance manoeuvres if necessary and possible (Merz et al., 2017). A space object catalogue can also be used to validate models of the space debris environment, especially with regard to long-term evolutions and fragmentations. In case of fragmentations, the distribution of the newly created objects' orbits can be used to improve the models of fragmentation events (Braun et al., 2019). Also for future mission planning, the current distribution of objects in space has to be considered. This is especially critical if the possible impact of fragmentation events is considered which may be dramatic for certain orbital regimes (Letizia et al., 2020). Already with these examples, it is clear that a space object orbit database is an important tool to maintain the sustainability of orbits around Earth.

Concerning the availability of these catalogues, the most popular publicly available space object catalogue is the Two-Line Element (TLE) catalogue[1] by the USSPACECOM. It currently includes more than 20,000 objects in orbit across all orbital regimes. The catalogue is based on a wide network of both optical and radar sensors. The objects in this catalogue are the so-called unclassified objects, which have a known, non US-military, source. These TLE are designed to be propagated with the SGP4/SDP4 model, which is an analytical propagation based on simplified dynamics. A complementary database is the Russian Vimpel catalogue[2]. It is based on a large network of optical telescopes and focuses on objects in high-altitude orbits, mainly GEO and HEO. Additionally there are private companies with a variety of different sensor networks, which also create object orbit databases with a commercial motivation. One example is the US American company LeoLabs, Inc.[3], which operates three radars and is the data source for the experiments in Section 5.2.

2.1.2 Data Processing

Maintaining a space object orbit database from regular observations can be split into two main tasks. Firstly, the orbits in the database have to be updated regularly with new observations. To achieve this, it is necessary to perform an association between the measurements and the orbits in the database, here referred to as: Tracklet-Catalogue Correlation (TCC). If such an association is found, the update of the orbit has to be performed. The method depends on the chosen orbit determination approach of the catalogue operator. One option is the batch orbit determination with a least squares estimation. This approach needs a definition of the considered time interval of observations, i.e. how many old observations from the past are still considered. Alternatively, a type of Kalman filter (Kalman, 1960) can be used to update the state, which does not require the definition of an update interval. The Kalman filter is a sequential approach, which always integrates the most recent measurement into the state. For both approaches, the orbit state and the uncertainty, i.e. covariance, are updated and usually also moved to a new epoch.

The second aspect is to populate the database with new objects from measurements which could not be associated to a known object. This requires it to estimate an initial orbit from a small number of measurements, maybe only a single pass. In general, the more data from different passes is available, the more precise and reliable is the orbit. This also motivates the work in this thesis. To improve the initialisation of new objects, the pairwise association of two tracklets and also further processing steps are investigated for radar measurements.

A graphical overview of the possible components of the catalogue maintenance and its relations is shown in Figure 2.1. It also serves as an overview of the work in this thesis. It is not intended to represent the flow graph of the implementation of a catalogue maintenance software, but rather gives the logical connections between the different tasks. The origin is the input of new observations, which are mainly from radars in this work. From this point, there is the previously discussed separation between the TCC and the pairwise correlation to create new objects. The TCC is discussed in the context of automated database maintenance in Section 6.1. The processing of observations which could not be associated to a database object has several steps. In this thesis, the correlation uses attributables as an input. The

---

[1]`https://www.space-track.org`
[2]`www.spacedata.vimpel.ru`
[3]`https://www.leolabs.space`
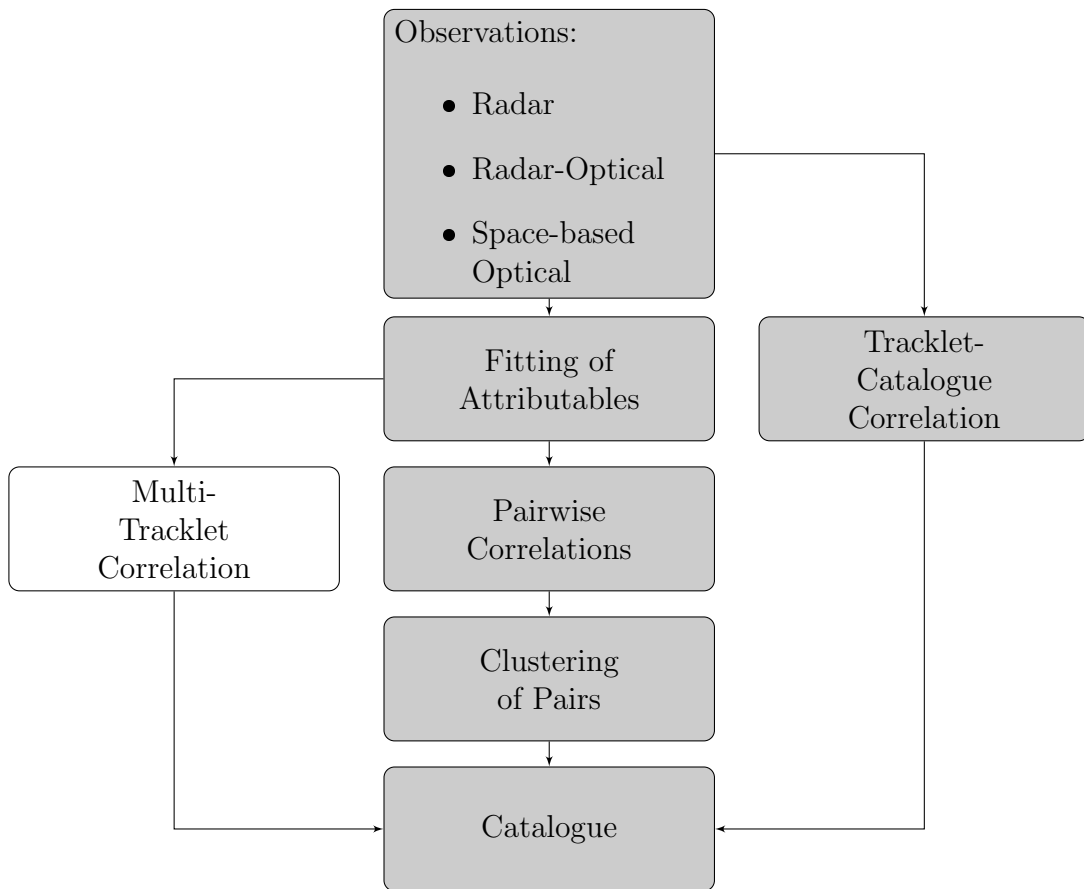
Figure 2.1: Flow diagram of catalogue operations. Grey boxes are topics which are covered in this thesis.

background and the fitting process of them is discussed in Section 2.2. As a next step, the processing can be separated for pairwise correlations and the correlation of more than two tracklets. Using three or more tracklets for the correlation may give better results, but it it also greatly increases the number of different combinations of tracklets which all need to be checked. This may be approached via a heuristic search to approximate the ideal solution (Zittersteijn et al., 2016), which is not considered in this work. Here, the focus is on the more classical pairwise correlations, see Section 3.2. To increase the robustness of the correlation, an approach for the clustering of tracklets based on a graph is discussed in Section 3.3. As an example of an operational application of a catalogue, Section 6.4 introduces an experimental automated processing pipeline for the telescopes of the Zimmerwald observatory.

2.2 Attributable Optimised Coordinate System

The figures and text in the following section have been taken from (Reihs et al., 2021) and have been adjusted for the use in this thesis.

2.2.1 Attributable Fitting

The measurements are processed to form attributables at a reference epoch t (Milani et al., 2004). The idea of the attributable is to average out noise and obtain a single, virtual measurement, which contains the condensed information of the entire tracklet. The attributable is obtained by fitting the raw measurements of each observable independently to a function over time and by picking the function values at a common epoch as the virtual measurements.

As explained in Section 1.2, it is assumed that the radar provides four observables, namely the range ρ, the range-rate $\dot{\rho}$, the azimuth az and the elevation el. Together with the reference epoch t the radar attributable in this work is defined as:

$$\mathcal{A}_{\mathrm{AE}} = \{t, \rho, \dot{\rho}, az, el\} \ , \tag{2.1}$$

which practically could also be extended to include additional information, e.g. the location of the observing station, but this is left out here for simplicity.

The fit to a specific observable's measurement vector $\vec{m}$ containing M successive detections from a single pass is calculated with a linear least squares approach for a polynomial of degree n which contains $k = n + 1$ parameters based on a Taylor series:

$$m(t) = p_0 + p_1 \cdot \Delta t + \cdots + \frac{p_n}{n!} \cdot \Delta t^n \ , \tag{2.2}$$

with the parameter vector $\vec{p} = [p_0, p_1, \ldots, p_n]$. For the fitting process, all measurement epochs are used as the relative offset from the reference epoch which is set at the centre of the measurement interval with $\Delta t = 0$ s. The virtual measurements for the attributable are also set at the reference epoch, which has the advantage that the fitted parameter vector is equivalent to the values in the attributable vector without further processing, including the uncertainties and derivatives with the n-th derivative at $\Delta t = 0$ being equal to p_n. For example, if the radar does not provide the range-rate as a separate measurement, it can be obtained from the first derivative of the range fit.

The solution of the fit is obtained via the classical least squares algorithm:

$$\vec{p} = \left(A^T \cdot \Sigma_M^{-1} \cdot A\right)^{-1} \cdot \left(A^T \cdot \Sigma_M^{-1} \cdot \vec{m}\right) \ , \tag{2.3}$$

$$A = \begin{bmatrix} 1 & \Delta t_1 & \cdots & \frac{\Delta t_1^n}{n!} \\ \vdots & \vdots & \ddots & \vdots \\ 1 & \Delta t_M & \cdots & \frac{\Delta t_M^n}{n!} \end{bmatrix} ., \tag{2.4}$$

with the measurement covariance matrix Σ_M. If the measurement errors are uncorrelated, i.e. Σ_M has only elements on the main diagonal, Equation 2.3 is equivalent to the weighted least squares. The covariance of the parameters $\vec{p}$ is taken directly from the covariance matrix $\left(A^T \cdot \Sigma_M^{-1} \cdot A\right)^{-1}$. This approach has two main possible sources of error. The first one is that it requires a realistic input uncertainty of the measurements, otherwise the fit and the parameters' covariance will not be realistic. Additionally if different observables with correlated errors are fitted together, the correlations between the errors can become overly dominant and lead to unreasonable results especially for tracklets with a small number of data points.

Throughout this work, it is assumed that the measurement errors are unknown and thus the unweighted least squares is used:

$$\vec{p} = \left(A^T \cdot A\right)^{-1} \cdot \left(A^T \cdot \vec{m}\right) \ . \tag{2.5}$$

In this case, the uncertainty of the estimated parameters has to be estimated from the fit. The uncertainty σ_{p_s} of the desired parameter $p_s, s \in [0, n]$ is derived from the covariance matrix $C = \left(A^T \cdot A\right)^{-1}$ (Johnson and Bhattacharyya, 2010):

$$\sigma_{p_s}^2 = \sigma_m^2 \cdot C_{s,s} \ , \tag{2.6}$$

with σ_m as the standard deviation of the measurements and $C_{s,s}$ the s-th value on the main diagonal of the covariance matrix. The residuals $\vec{r}$ of the fit can be used to obtain an unbiased estimate of the measurement noise (Johnson and Bhattacharyya, 2010):

$$\sigma_m^2 = \frac{\vec{r} \cdot \vec{r}}{(M - k)} \tag{2.7}$$

In contrast to radar measurements, optical observations of objects in high-altitudes show less variations in their observables over the duration of measurement. For this reason, usually first or second order polynomials are sufficient. Deriving the angular rates from the fit is the main motivation of the optical attributable, because this quantity cannot be measured directly. The resulting optical attributable is defined for this work as:

$$\mathcal{A}_{\text{Opt}} = \left\{ t, \alpha, \delta, \dot{\alpha}, \dot{\delta} \right\} \ , \tag{2.8}$$

The following analysis focuses on radar observables for LEO objects because their variability is much larger.

2.2.2 Coordinate Systems

When attempting to fit a function to the measurements, the typical graph of the observables' function over the duration of a single pass has to be considered. Firstly, the four directly measurable radar observables as presented in Section 1.2 are considered. Figure 2.2 depicts an example of the observables' development for a LEO object (semi-major axis $a \approx 7163$ km, eccentricity $e \approx 0.008$, inclination $i \approx 99°$) over a nearly 10 minutes long radar pass. These graphs result from the orbital motion being projected into the observer's topocentric coordinate system. Although the specific numbers of the maximum and minimum values are depending on the geometry of each pass, the general shape is similar for all passes. The vertical line in the plots marks the time of closest approach (TCA).

(a) Range

(b) Range-Rate

(c) Azimuth

(d) Elevation
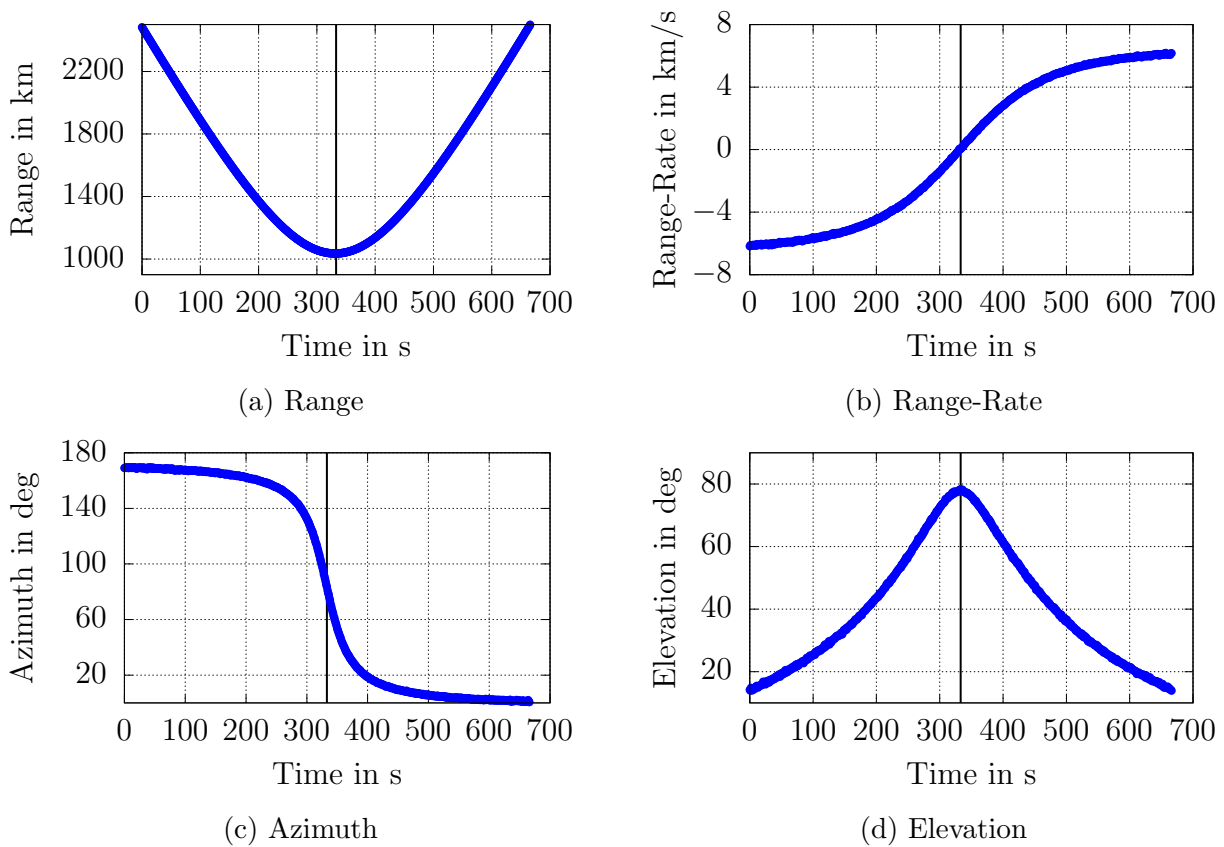
Figure 2.2: Example graphs of radar observables over a full pass of an object in LEO. The vertical line indicates the time of closest approach.

The graph of the range has a parabola-like minimum at TCA, which is encompassed by two monotonic arcs towards larger values. Range-rate and azimuth are both close to the shape of the inverse tangent. For the range-rate the absolute values for minimum and maximum are nearly the same and it always switches from negative (approaching) to positive (departing). The extreme values of the azimuth are up to 180° apart depending on the maximum elevation of the pass, which also influences the slope at TCA. The higher this elevation, the more pronounced is the slope. For example if the object passes right above the observer, the azimuth would jump instantaneously by 180°. The shape of the elevation is comparable

to two exponential branches connected by a small parabola. From these plots, it can be concluded that it is presumably very difficult to fit even a higher order polynomial over longer time spans. Especially close to TCA and for high elevations, fitting the attributables may become problematic.

To overcome this issue, three options for deriving new observables from the given range-azimuth-elevation are introduced in the following with the goal to increase the robustness of the fitting process. All examples in the following show the same pass as in Figure 2.2. The range-rate cannot be replaced and has to be used for all of the following systems.

(a) X-Coordinate

(b) Y-Coordinate

(c) Z-Coordinate
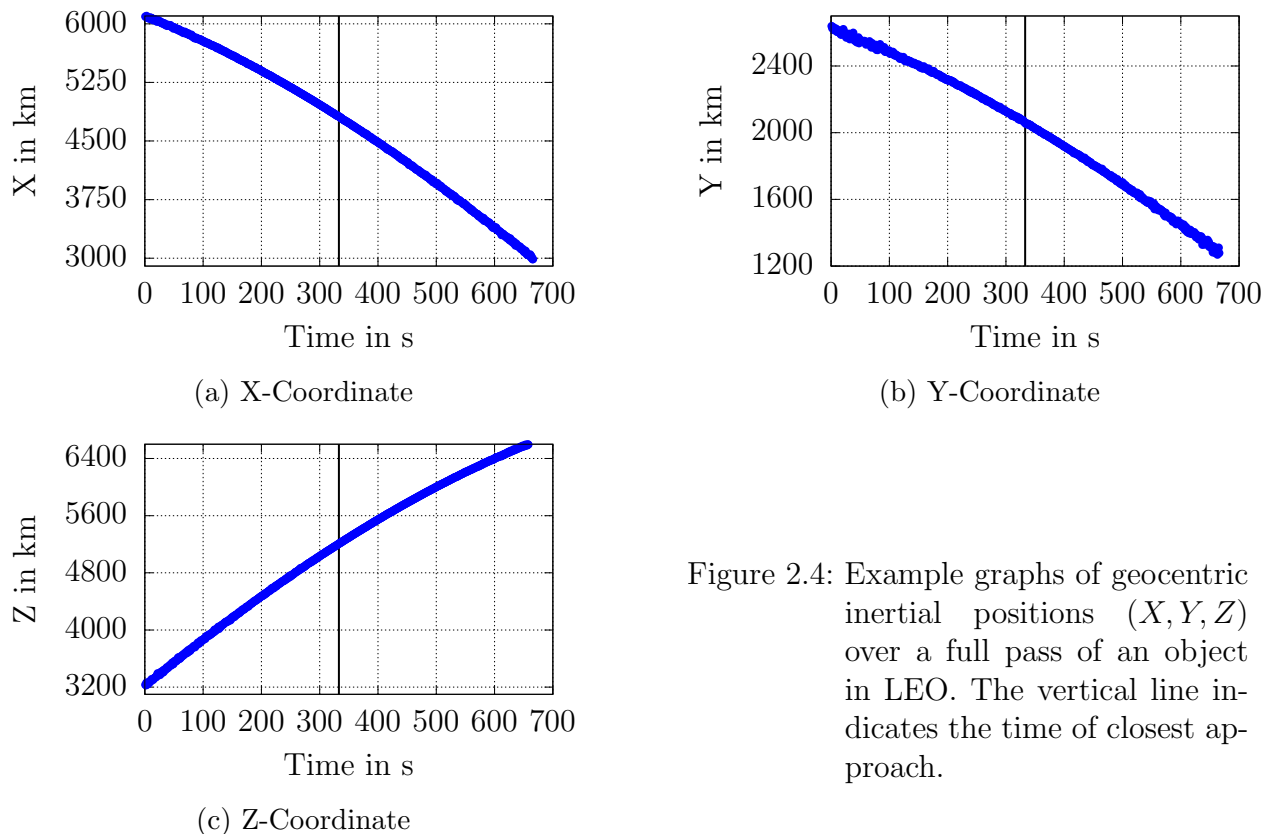
Figure 2.4: Example graphs of geocentric inertial positions (X, Y, Z) over a full pass of an object in LEO. The vertical line indicates the time of closest approach.

The first option is to transform each individual measurement to a position in a geocentric, inertial frame. This is possible by combining the ranges and angles of the radar measurement with the known location of the measurement station. The fit is then performed using the inertial positions. This leads to the definition of an alternative attributable:

$$\mathcal{A}_{\mathrm{XYZ}} = \{t, \dot{\rho}, X, Y, Z\} \ , \tag{2.9}$$

where (X, Y, Z) are the inertial, geocentric coordinates. The two versions of the attributable are equivalent and can be interchanged by an appropriate non-linear transformation, but performing the fit might be easier in one of the systems especially with regard to estimating the uncertainties. The example plot using the geocentric inertial positions is shown in Figure 2.4. In general, it can be seen that the three coordinates have a slightly curved but simple shape. The disadvantage of this system is that the behaviour of the individual components is heavily correlated with the orbit of the observed object and the location at which it is observed on the orbit. For example, observing a mid-inclination object at its

most northern or southern point would lead to a parabola-like shape of the Z-coordinate, whereas the Z-coordinate would be a nearly straight line for a polar orbit. This reduces the consistency of observables over a population of many different objects. The uncertainties for each coordinate can be directly extracted from the fit neglecting the correlation of the errors after the transformation to the inertial coordinate system which will be discussed further at the end of this section.

(a) In-Plane Angle   (b) Off-Plane Angle
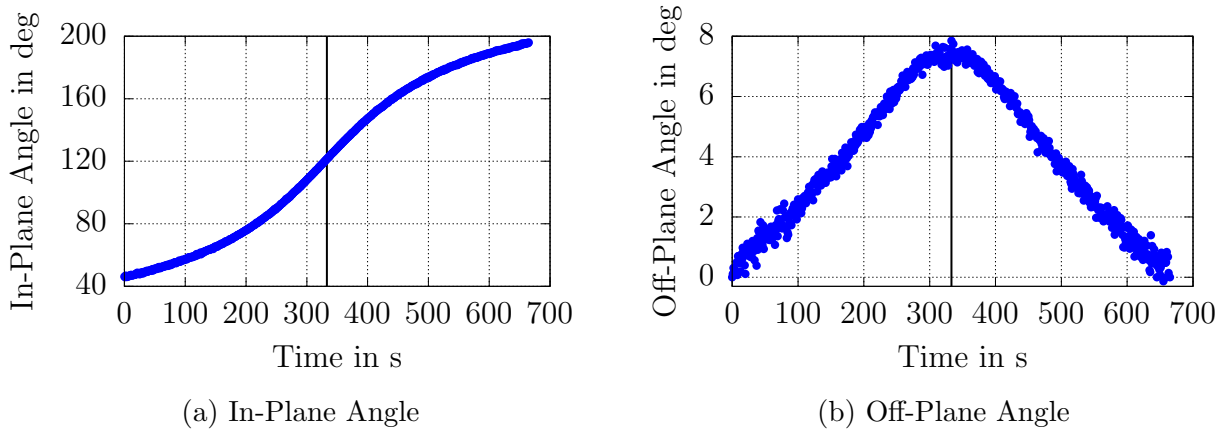
Figure 2.5: Example graphs of topocentric AOS angles over a full pass of an object in LEO. The vertical line indicates the time of closest approach.

The second alternative coordinate system is referred to in the following as topocentric Attributable Optimised Coordinate System (AOS). This system uses the same topocentric origin at the observer location and thus also the same range measurement as before. The only change is the definition of the angular observables. The new coordinate system is defined with the motivation to reduce the dependency of the angles on the pass geometry. It is defined by a reference plane through three points in the inertial space: the observer's location (neglecting its own motion), the first detection of the pass and the last detection of the pass. The angular position of each detection can thus be expressed as the in-plane angle θ_1, which gives the direction angle from the station to the object within the reference plane comparable to the azimuth, and the off-plane angle θ_2, which gives the elevation over the reference plane, also with the station as the reference. The direction $\theta_1 = 0°$ can be defined arbitrarily within the plane, but here it is chosen to be consistent with the inertial direction of the vernal equinox projected onto the plane. The behaviour of these two angles can be seen in Figure 2.5 and they have a far lower variability among different passes compared to azimuth-elevation. These coordinates also do not have the singularity at $el = 90°$. The main influence is the length of the pass. For a short pass, the off-plane angle would be close to zero all the time and only long passes as in the example shown here lead to a distinct peak. To increase the comparability with the original topocentric frame and to use the measurements as an input for the correlation, the fitted AOS angles are transformed back to azimuth-elevation. The uncertainties which are estimated from the AOS fits have to be transformed as well and it has to be considered that this leads to a correlation of azimuth-elevation uncertainties which requires the use of a 2x2 covariance matrix with non-

zero off-diagonal elements. The resulting attributable is the same as $\mathcal{A}_{\mathrm{AE}}$. It should be noted that this coordinate system could also be used for optical observations by adding two arbitrary range values to the first and last observation or using unit vectors, because the ranges do not affect the definition of the plane.

(a) Geocentric Range

(b) Off-Plane Angle

(c) In-Plane Angle
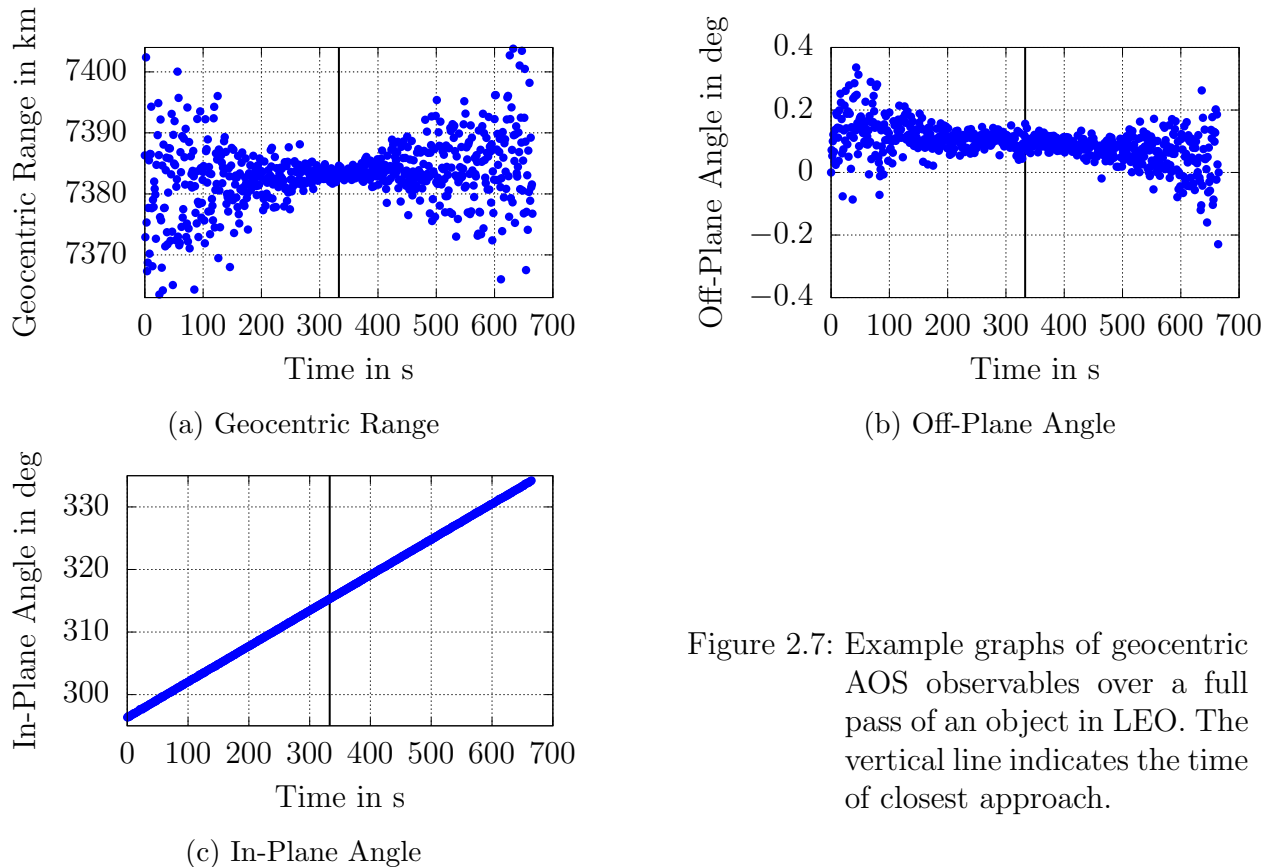
Figure 2.7: Example graphs of geocentric AOS observables over a full pass of an object in LEO. The vertical line indicates the time of closest approach.

The last alternative is the geocentric AOS. The angles are the same as explained previously, but the observer's location is replaced as a reference point by the geocentric coordinate origin in the Earth centre. This shall reduce the variation in the off-plane angle further, which can be seen in Figure 2.7. The newly defined plane is very close to the orbital plane. Thus the in-plane motion is approximately linear for nearly-circular LEO orbits and the off-plane angle should remain close to zero. In the example, due to the larger noise at larger ranges and the definition of the AOS plane at the edges of the tracklet, the off-plane angle θ_2 is tilted against the expected 0°-line, but with a clear linear trend which would be equivalent to the orbital plane. Additionally, the topocentric range is replaced by the geocentric range for consistency and to facilitate the transformation into an inertial position, which is used as a fitting output. Again, this transformation leads to a statistical correlation of the errors in the inertial positions requiring a 3x3 covariance matrix in (X, Y, Z). The resulting attributable is the same as $\mathcal{A}_{\mathrm{XYZ}}$. This geocentric AOS cannot be used with optical measurements because it requires the topocentric range information for the conversion to geocentric angles and range.

As mentioned in Section 2.2.1 all observables are fitted independently of each other because the amount of data is usually not sufficient for a fully correlated fit as presented in Equation 2.3 and it is assumed that no initial information on the measurement accuracy is provided, which would be necessary for the error transformation into the new system. This refers to both versions of the AOS and the inertial system, where the errors of the transformed observables would be coupled due to the transformation from the azimuth-elevation system. The results show that this approximation is sufficiently good for the purpose of correlation.

Finally, it should be remarked that if the errors in azimuth-elevation were very large (several degrees), the transformation to a geocentric system would lead to a breakdown of the errors' assumed normal distribution due the curvature in the topocentric spherical coordinate system. However, it can be assumed that a radar sensor's angular uncertainty is small enough that this effect is not present.

An in-depth analysis has been performed to derive a consistent set of rules for the fitting of attributables regarding the choice of the order of the polynomials. This is necessary for the processing of surveillance radar measurement which have different dwell times in the FoR.

2.2.3 Analysis and Results

Evaluation Method

In the following, the evaluation process for the attributable fitting is explained. For this analysis, only simulated radar measurements are used to have a reliable and precise ground truth. This is necessary to compare the fitting results and derive the statistical properties as described in the following.

Different experiments concerning the fitting of the attributables have been performed (Reihs et al., 2021). For these tests, a population of objects in LEO is used consisting of 1500 objects. The restrictions on the visibility are reduced to $el > 5°$ and $\rho < 2500$ km to maximise the number of obtained tracklets which usually results in 5000 - 6000 tracklets per experiment. For this analysis, the concept of absolute and relative errors is introduced regarding the observables. The absolute error ΔA_x of observable x is derived by taking the difference between the value obtained via the attributable fitting and the true, noiseless value of the observable at the same epoch. It is important that the mean of the absolute error $\mu_{A,x}$ over the entire population is close to zero, otherwise the estimation of the parameter is biased. If the absolute error is related to the estimated uncertainty σ_x, the relative error for a single value is calculated as $\Delta R_x = \frac{\Delta A_x}{\sigma_x}$ which transforms the error to the z-scale, a normalised Gaussian distribution with the idealised properties of the mean $\mu = 0$ and the standard deviation $\sigma = 1$, to make the different individual errors comparable, also see Section 3.2.1. Actually, the resulting distribution would be a Student's t-distribution, but for a sufficient number of data points, this distribution converges to a standard normal distribution which will be assumed for all following experiments. Thus the overall standard deviation σ_R of the relative error over the entire population of attributables should be close to one to confirm a realistic estimation of the error. This value is calculated in two steps. After getting the initial standard deviation $\sigma_{R,0}$, all values with $\Delta R_x > 3 \cdot \sigma_{R,0}$ are removed to avoid a biased statistic due to extreme outliers and the final result σ_R is obtained from

the new data set. The same approach is also applied to the absolute errors. The absolute and relative errors of a population are shown in Figure 2.8 with the azimuth angle as an example. The plots in the following will condense this information to an errorbar showing $\mu \pm \sigma$ for both the absolute and relative error.
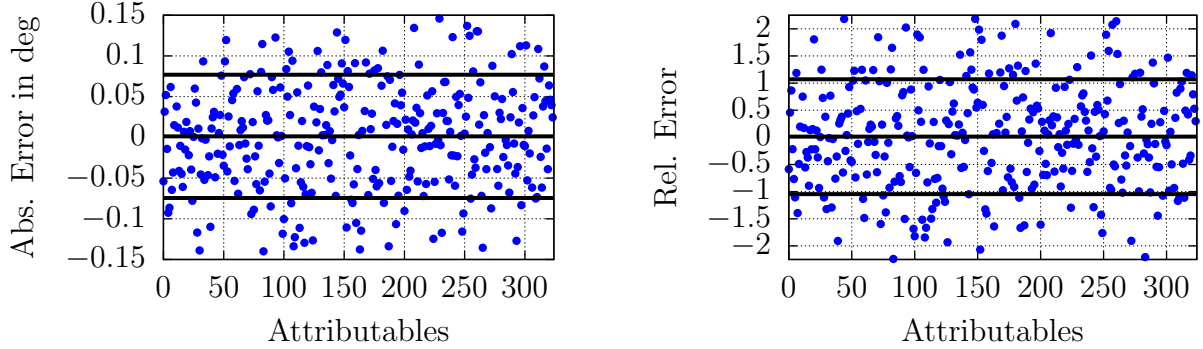
Figure 2.8: Example of absolute and relative errors: azimuth. The bold lines indicate the mean and mean $\pm$ standard deviation

For the two AOS, it has been mentioned in Section 2.2.2 that the errors between the observables are correlated in the attributable after the transformation back to azimuth-elevation or inertial coordinates, respectively. To check whether these correlations are also well-captured, the squared Mahalanobis distance, see Section 3.2.1, between the fitted attributable and the noiseless reference measurement is calculated:

$$M_d^2 = \vec{d_M}^T \cdot C_{\text{meas}}^{-1} \cdot \vec{d_M} \;, \tag{2.10}$$

where $\vec{d_M}$ is the vector containing the differences between the fitted value and the ground truth. C_{meas} is the estimated covariance matrix. Theoretically M_d^2 should be distributed according to a $\chi^2(\nu)$-distribution with ν degrees of freedom. This distribution has a mean of $\mu = \nu$ and a variance of $\sigma^2 = 2\nu$ (Abramowitz and Stegun, 1965), which can be checked against the values from the fitted population. For the cases here, the transformation from topocentric AOS to azimuth-elevation leads to a 2x2 covariance matrix for the angles and thus $\nu = 2$ and from geocentric AOS to inertial position gives $\nu = 3$. The other fits are independent and thus not checked together with the correlated errors.

Fitting Example: Length of Tracklet

As an example for the optimisation of the chosen polynomials, the influence of the tracklet length on the accuracy of the fitting process is analysed. This has been performed with different measurement frequencies, i.e. time between two consecutive detections within a tracklet, but it was found that, although it causes slight differences, this does not change the overall trend of the accuracies and thus only one selected frequency value per observable is shown as an example. These different frequencies are referred to as t_ff-data for a case with t_f seconds between two detections. The following plots compare different polynomials, up to the fourth order.

Topocentric Range and Range-Rate

The range-rate has to be fitted for all coordinate systems, because it cannot be replaced or transformed. An example of its fit results for the first four orders is shown in Figure 2.9. It can be seen that the point at which the quadratic fit becomes better than the linear one considering the absolute error is at approx. 30 s and after approx. 130 s the fourth order fit becomes the best. Also for the relative errors, the given orders of the polynomial are close to one within their respective intervals, which indicates a well-approximated uncertainty.
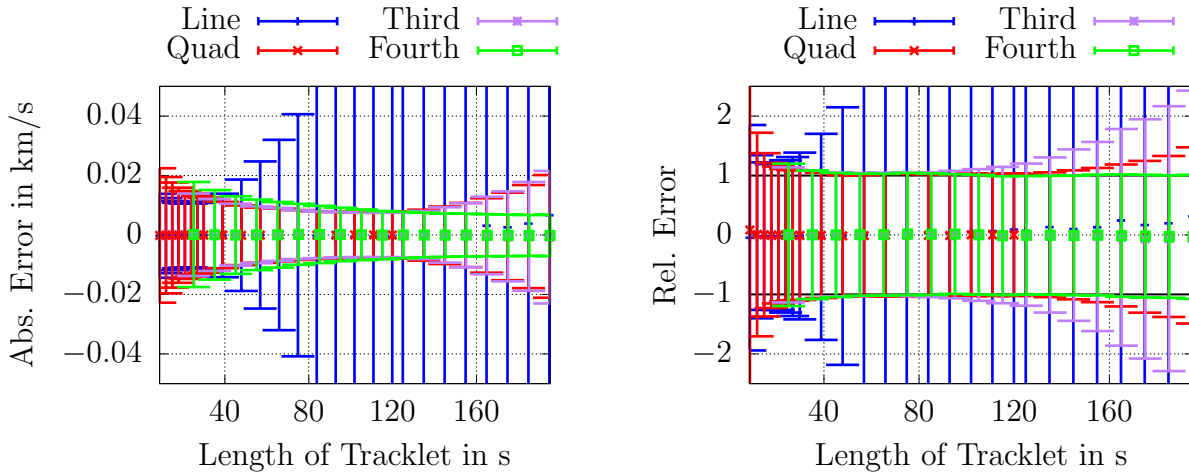
Figure 2.9: Range-rate errors for different tracklet lengths using 3f-data.

Figure 2.10 depicts the errors of the topocentric range, which is required for the two topocentric coordinate systems. Even for relatively short tracklets, the linear fit introduces a negative bias due to the curvature of the range measurements and is not even in the plotted range any longer. Independent from the measurement frequency, this bias reaches approximately -1 km at 30 s and grows exponentially to -10 km at 100 s. Thus only the quadratic fit is a reasonable choice for the range attributable from the beginning, but its absolute error is growing for tracklets longer than 60 s. Afterwards a fourth order fit is the better choice, which has increased errors from approx. 140 s onwards. The relative error for the quadratic fit is close to one for lengths smaller than 40 s. The fourth order fit shows some inconsistencies regarding the relative error, but it is a much better approximation than the quadratic one after approx. 50 s.

Azimuth-Elevation

The result of the azimuth fitting is shown in Figure 2.11. At approximately 25 s, the absolute error of the quadratic fit becomes lower than the linear one's which increases rapidly after this time. Regarding the relative error, both fits are comparable until the same 25 s mark and afterwards the linear fit has larger deviations than one which implies an underestimation of the uncertainty in the fitting process. The quadratic fit shows a good representation of the error up to approx. 80 s. Afterwards the fourth order fit has the smaller absolute error and the better error distribution.
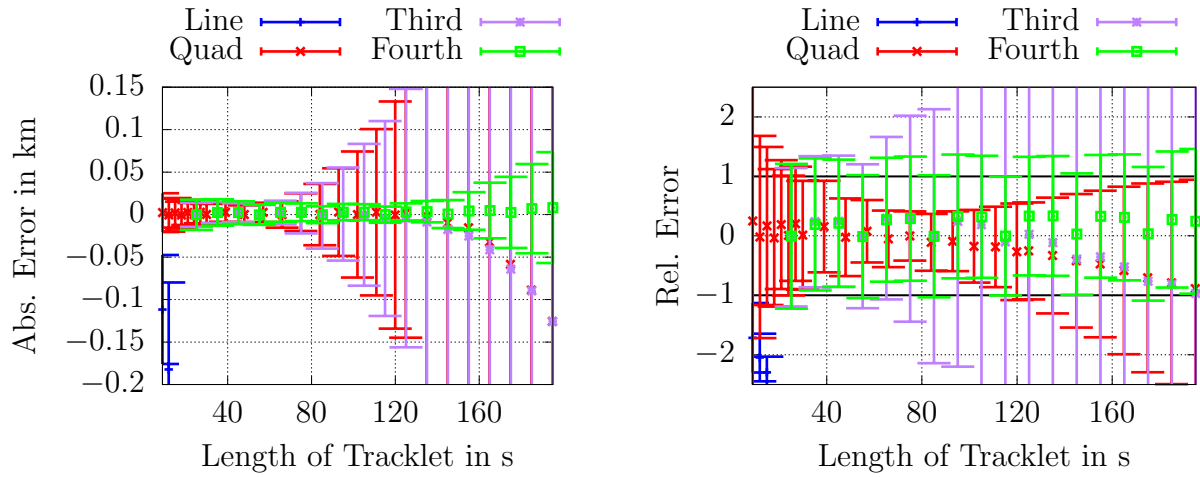
Figure 2.10: Topocentric range errors for different tracklet lengths using 3f-data.
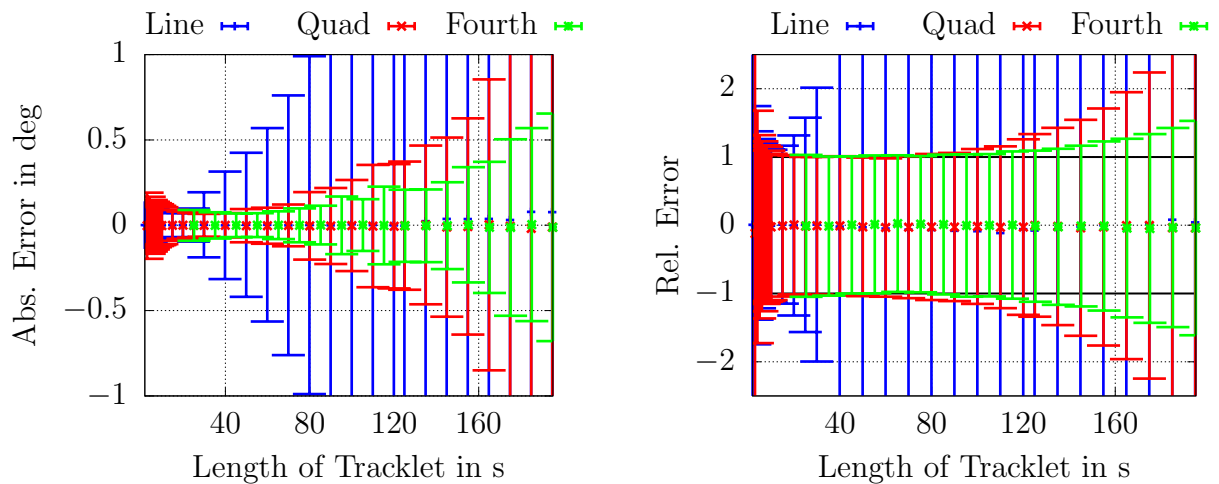
Figure 2.11: Azimuth errors for different tracklet lengths using 1f-data.

Concerning the elevation, shown in Figure 2.12, the linear fit has the lowest and nearly constant absolute error for short tracklets. The quadratic fit reaches the level of the linear fit at approx. 40 s and afterwards maintains its accuracy whereas the linear one's is degrading rapidly. The relative error is reasonable for both fits up to approx. 40 s and thereafter only the quadratic fit maintains a consistent relative error. The fourth order fit becomes better for tracklets longer than approx. 120 s.
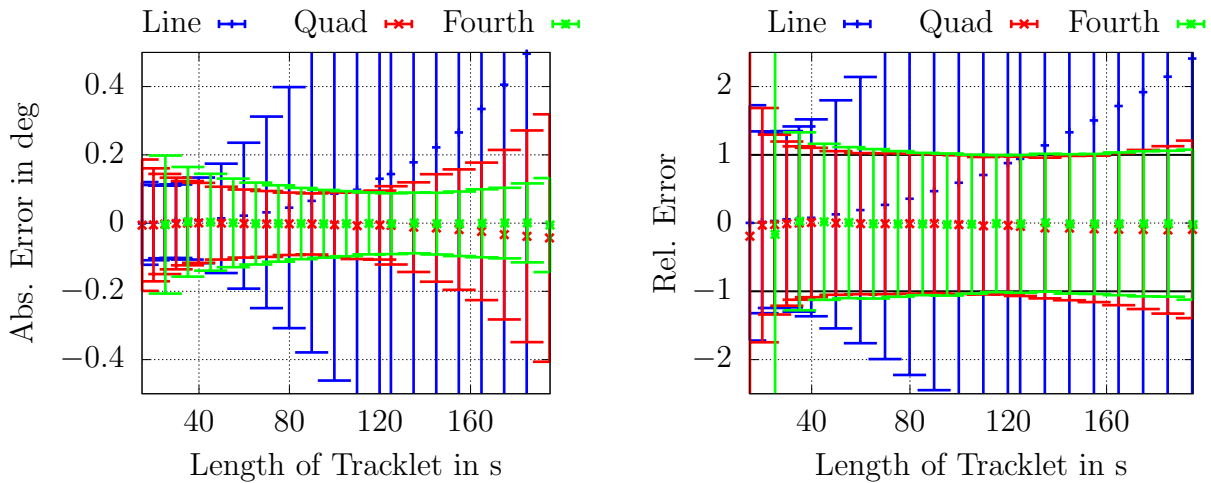
Figure 2.12: Elevation errors for different tracklet lengths using 5f-data.

Geocentric Inertial Positions

For the three geocentric inertial coordinate axes, the results are given in Figures 2.13-2.15. The X- and Y- coordinates are similar to each other and have a low error for the linear fit in the beginning, which increases with time after approx. 50 s. From there on the quadratic fit has the lowest error. Concerning the relative error, the one of the linear fit is increasing after 30 s while the quadratic one remains close to one within the checked range.
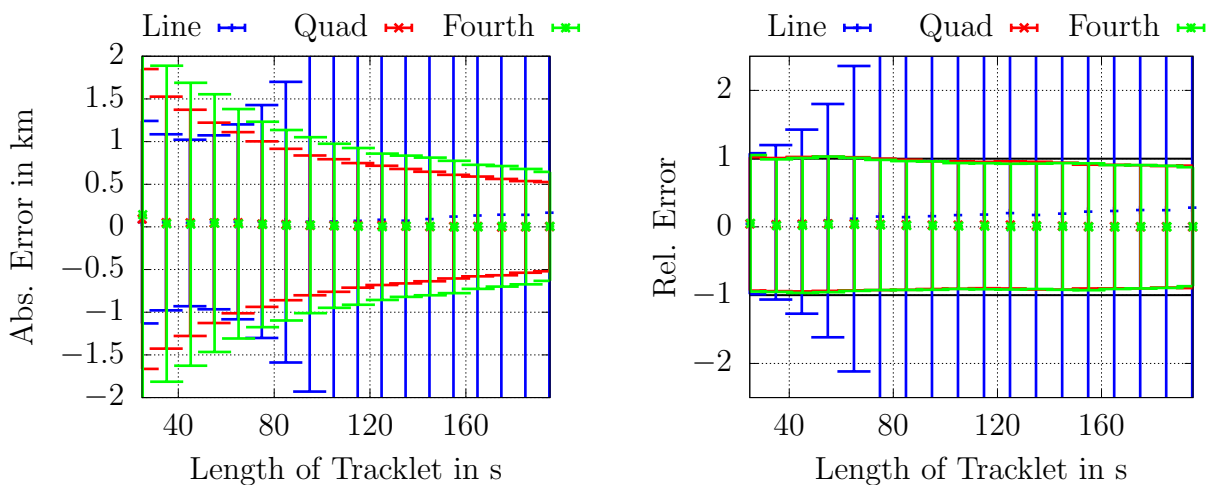
Figure 2.13: Position errors (X) for different tracklet lengths using 1f-data.
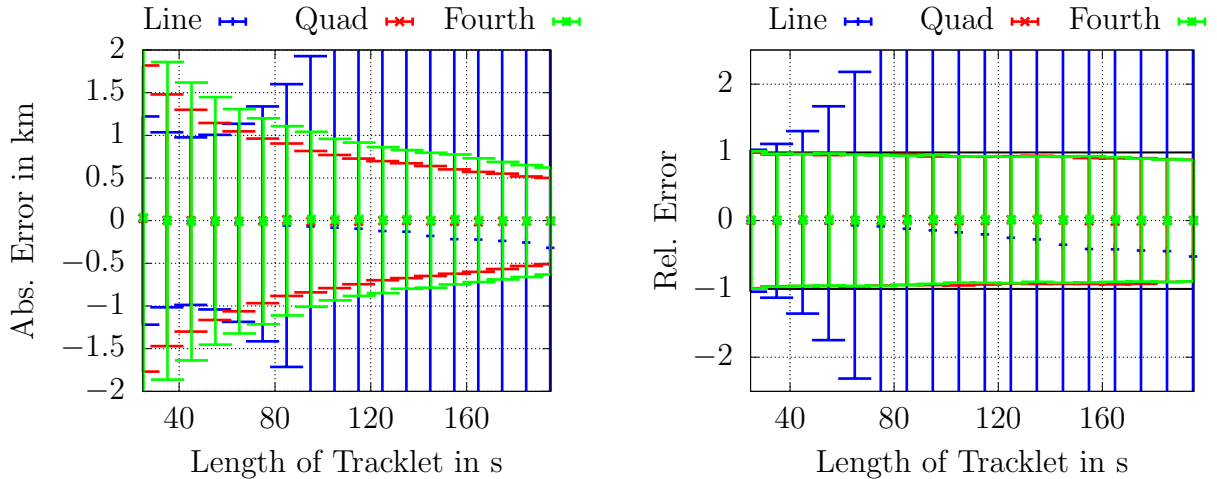
Figure 2.14: Position errors (Y) for different tracklet lengths using 1f-data.

For the Z-position, the linear fit is also acceptable for short tracklets but it starts to build up a bias for longer tracklets. The linear fit cannot model the slight curvature of the coordinate over time, which leads to a consistent positive error in the Z-component due to the station location in the northern hemisphere, whereas for the X- and Y- coordinates there are both positive and negative errors which cancel out for the population mean. The quadratic fit is the best option for longer tracklets. The main problem for this frame is the dependence on the orbit of the observed object, which makes it more difficult to have a consistent fitting approach.
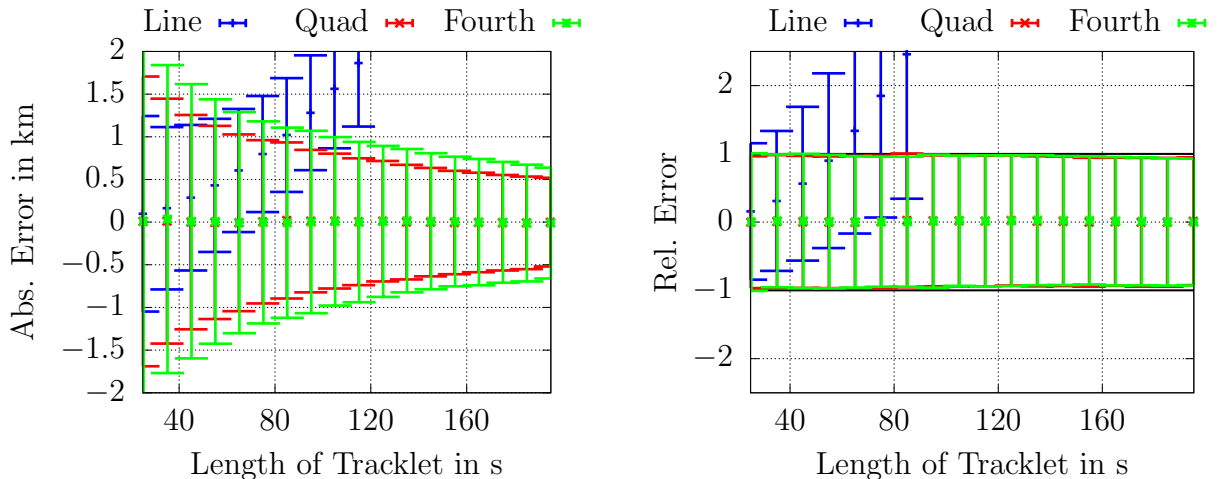
Figure 2.15: Position errors (Z) for different tracklet lengths using 1f-data.

Topocentric AOS

As described in Section 2.2.2, the fitting of the attributable is done in the topocentric AOS but these angles are then transformed back to azimuth-elevation, which are used for the correlation and thus also used as a comparison to the ground truth in this section. The results are shown in Figure 2.16 and Figure 2.17. For both observables, the linear fit is the

best choice until approx. 30 s and afterwards the quadratic fit becomes better in terms of both absolute and relative error. For very long tracklets (> 130 s), the fitting should be extended to use a fourth order polynomial. Regarding the absolute error, it should be noted that especially for long tracklets an improvement compared to the direct azimuth fitting of at least a factor of five can be observed.
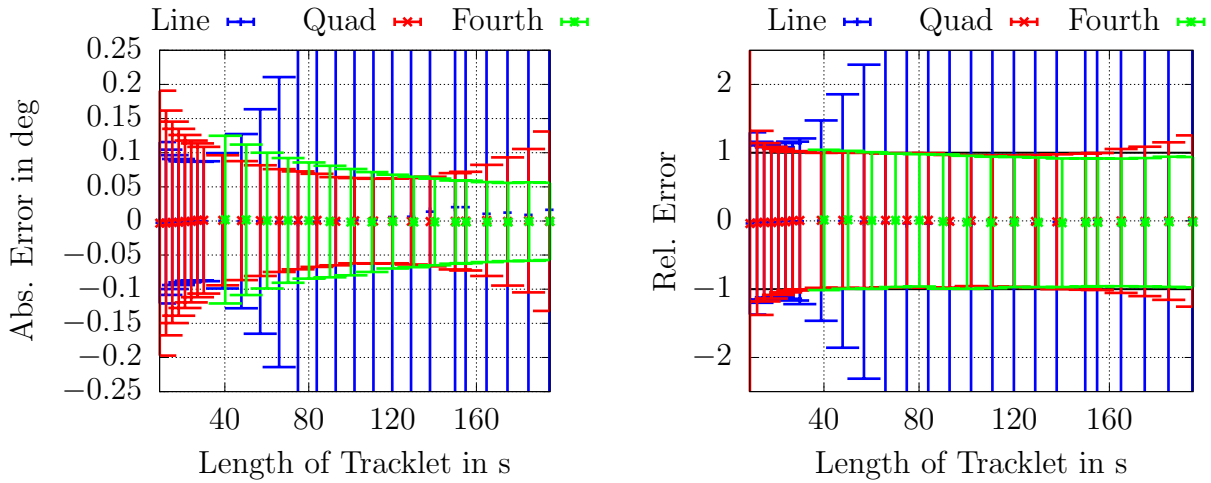
Figure 2.16: Azimuth errors (derived from topocentric AOS) for different tracklet lengths using 3f-data.
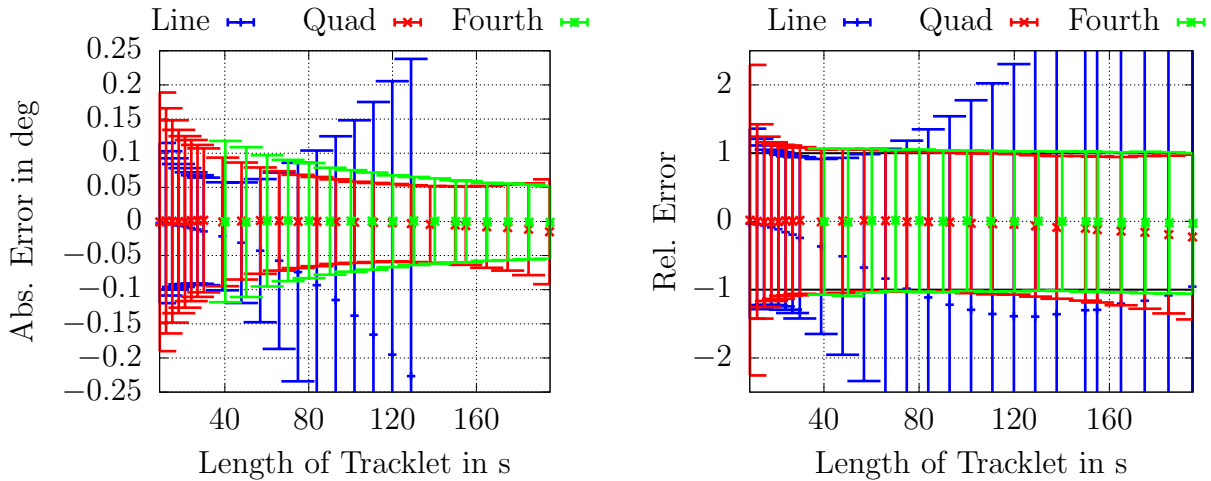
Figure 2.17: Elevation errors (derived from topocentric AOS) for different tracklet lengths using 3f-data.

Additionally, the back-transformation from AOS introduces a statistical correlation between the angular errors, which is checked via the Mahalanobis distance. The results for mean and variance are shown in Figure 2.18. It can be seen that for the quadratic and fourth order fits using tracklets longer than 30 s, the values of the fitted population are close to the expected values indicated by the bold line, whereas for shorter tracklets and the linear fit this is not the case.
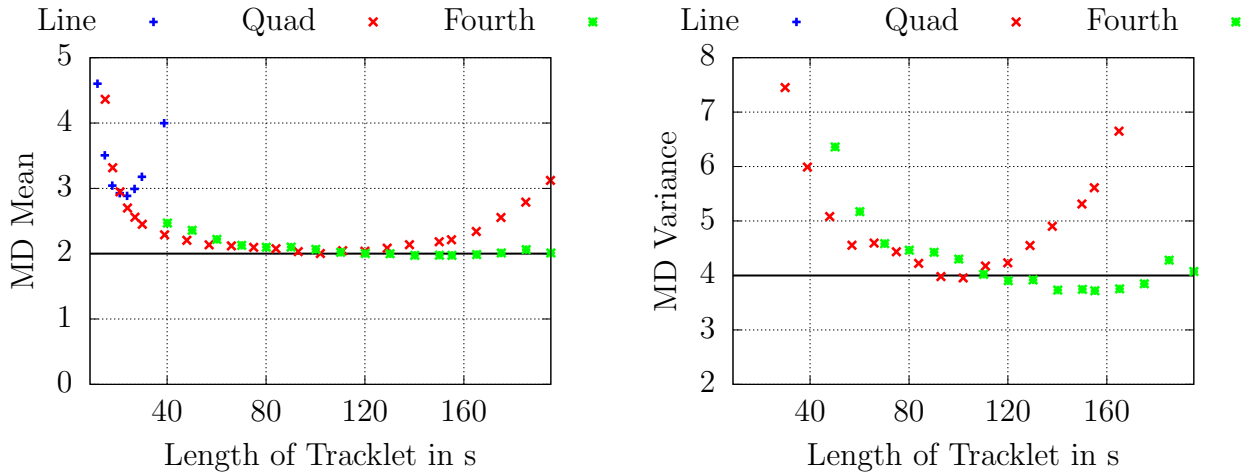
Figure 2.18: Mean and variance of Mahalanobis distances (derived from the topocentric AOS) of azimuth-elevation errors for different tracklet lengths using 3f-data. Theoretically expected values indicated by a bold line.

Geocentric AOS

The geocentric AOS is transformed to inertial positions after the fit. Because the results for the three axes are similar, only the X-axes is shown in Figure 2.19. It is visible that the linear fit is the best choice for all tracklet lengths. This suggests that the coordinates of this system are very stable over the pass. Although the absolute error is comparable to the direct fitting in (X, Y, Z), the higher consistency over the entire population is an improvement. Also here, the errors of the three positions become correlated which allows it to test the distribution of the Mahalanobis distances, see Figure 2.20. While the mean is well-approximated for the linear fit, the variance is approaching the theoretical value for longer tracklets but does not reach it. This could be due to the assumption of independent observables in the AOS during the fit. The effect of this will be discussed further in the Section 5.1.
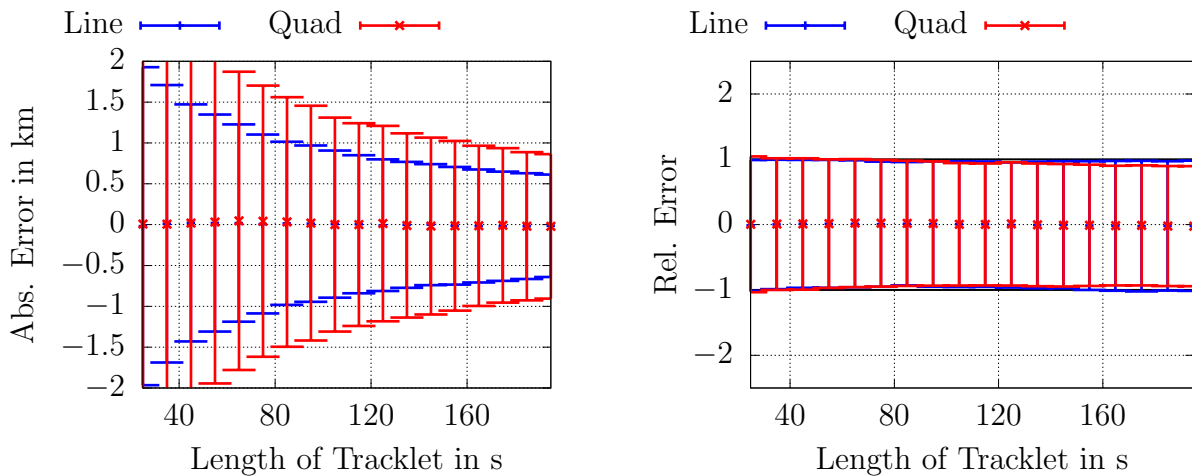
Figure 2.19: Position errors (X, derived from geocentric AOS) for different tracklet lengths using 3f-data.
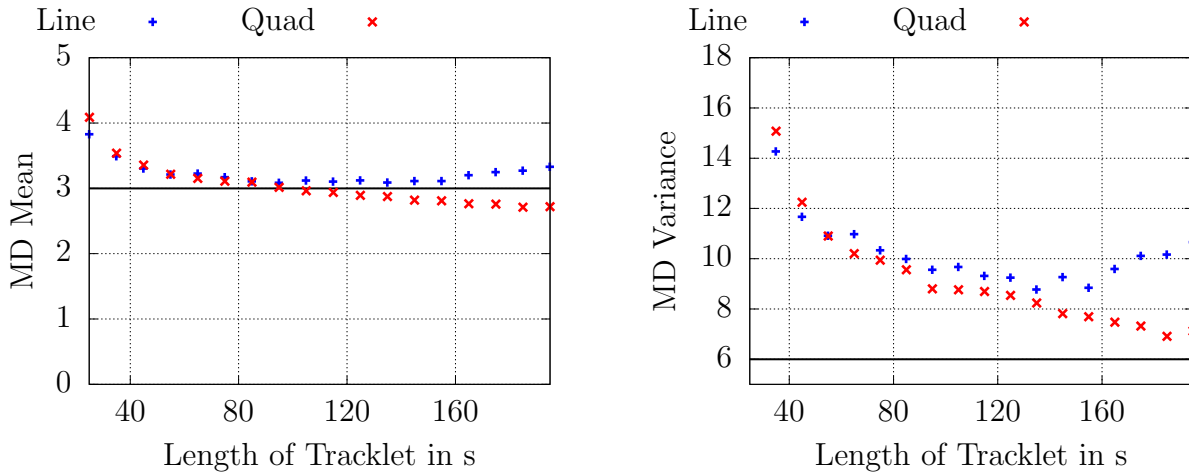
Figure 2.20: Mean and variance of Mahalanobis distances (derived from the geocentric AOS) of the (X, Y, Z) positions for different tracklet lengths using 3f-data. Theoretically expected values indicated by bold line.

Results of the Analysis

A set of fitting rules for a group of tracklets with different lengths t_T has been derived from the analysis in (Reihs et al., 2021). These rules are derived from the presented examples and are intended to keep the order of the polynomial as small as possible because especially for long tracklets with very sparse data, it may happen that there are not enough data points to use a high order polynomial. The resulting rules are presented in Table 2.1. From this summary, the geocentric AOS and the (X, Y, Z)-positions seem to contain the most stable observables as they require the least different orders of the fit.

Table 2.1: Rules of fitting depending on the tracklet length.

Range-Rate	≤ 30 s 1st order	30 s - 130 s 2nd order	≥ 130 s 4th order	
Range (topocentric)	≤ 60 s 2nd order	60 s - 150 s 4th order	≥ 150 s 6th order	
Azimuth	≤ 25 s 1st order	25 s - 80 s 2nd order	80s - 150 s 4th order	≥ 150 s 6th order
Elevation	≤ 40 s 1st order	40 s - 120 s 2nd order	≥ 120 s 4th order	
Inertial geocentric Positions (X Y,Z)	≤ 30 s 1st order		> 30 s 2nd order	
Angles AOS topocentric	≤ 30 s 1st order	30 s - 130 s 2nd order	≥ 130 s 4th order	
All observables AOS geocentric	all lengths 1st order			

The derived rules are applied in Section 5.1 to process a group of tracklets from a simulated surveillance radar campaign. In this context, the impact of the different coordinate systems is compared for different scenarios. The experiments in Section 5.2 are also based on the definition of the new coordinate systems and the related rules.

OBSERVATION ASSOCIATION

3.1 Approaches to Observation Association

When associating observations to each other or to existing orbits, two different approaches exist: single-target and multi-target tracking. Single-target tracking means that every object is treated independently from the remaining population. The most simple example is updating an existing orbit with a single new measurement, for example in a Kalman filter. This would assume that the association between object and measurement was already established, which is no trivial case in most situations. To solve this, an association test can be added before the new measurement is incorporated into the state. In case of associating a set of new measurements to a set of objects, each object-measurement combination is tested individually without consideration of the other associations. This approach has the advantage that the single association test can be relatively simple, but it has to be performed for all possible combinations of objects and measurements. It also leads to the question what happens if the single associations are contradictory when analysed over the entire population of objects, for example due the association of the same measurement to different objects. To solve these problems, multi-target tracking considers all objects and measurements together. This has the advantage that it is possible to find a combination of associations which is optimal with regard to a given cost function and is also non-contradictory in itself.

In the present work, aspects from both single- and multi-target tracking are used. A large part of the thesis focuses on the pairwise association of measurements, see Section 3.2, which can be considered to be part of the single-target theory because once an association between these two measurements has been made, it is assumed that they belong to the same object. As already mentioned, this leads to problems when multiple, contradicting associations are made. To avoid these contradictions for the creation of new objects, the graph network, see Section 3.3, is introduced as a post-processing of the pairwise associations. The graph network can be considered as a multi-target processing technique because it considers all observations and generates a set of consistent objects. Due to its computational efficiency, it does not add much processing time to the overall association process. Thus, it can serve as an extension of the pairwise association into the domain of multi-target tracking without using a full multi-target tracking approach.

3.2 Pairwise Association

3.2.1 Statistical Background

A normal distribution $\mathcal{N}$, also called Gaussian distribution, is commonly used to model statistical uncertainties. It is parametrised by the mean value μ and the standard deviation σ, which define the probability density function p_{N}. This density function is shown in Figure 3.1 for a normal distribution over the random variable x and is referred to as $\mathcal{N}(x|\mu, \sigma)$. The integral of this curve is the probability $\mathcal{P}$ of drawing a random value within the integration bounds. It can also be extended to the multidimensional case $\mathcal{N}(\vec{x}|\vec{\mu}, \Sigma)$ for a vector as a random variable $\vec{x}$ with mean $\vec{\mu}$ and covariance matrix Σ.
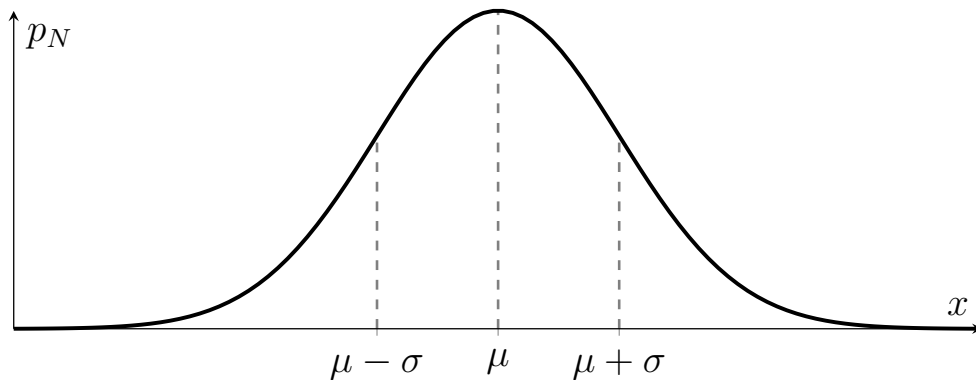
Figure 3.1: An example of a normal distribution with mean μ and standard deviation σ.

The parametrisation of the curve can be exploited for statistical gating. Independent of the specific values of μ and σ, it is always the case that $\mathcal{P}(\mu - \sigma \leq x \leq \mu + \sigma) \approx 68.3\%$ as one example. This property can be used for the so-called z-score $z = |x - \mu| \cdot \sigma^{-1} = |\Delta x| \cdot \sigma^{-1}$. Its value can be used to calculate the probability to draw a sample from the distribution below a given z-score ($|\Delta x| < z \cdot \sigma$), e.g. $\mathcal{P}(z \leq 1) \approx 68.3\%$. Thus if one wants to capture the most probable 68.3% of the events from a known normal distribution, all events with $z \leq 1$ shall be accepted. The extension of this concept to the multi-dimensional case is the

Mahalanobis distance M_d (Mahalanobis, 1936):

$$M_\mathrm{d} = \sqrt{\Delta \vec{x}^T \cdot \Sigma^{-1} \cdot \Delta \vec{x}} \; , \tag{3.1}$$

using the offset $\Delta \vec{x} = (\vec{\mu} - \vec{x})$. The Mahalanobis distance follows a probability density function $\chi(\nu)$, with ν being the degrees of freedom, i.e. usually the number of dimensions of $\vec{x}$. An example for the function $\chi(2)$ with two degrees of freedom can be seen in Figure 3.2. Also the χ-distribution can be used for statistical gating via its integral, e.g. for $\nu = 2$, $\mathcal{P}(M_\mathrm{d} < 3) \approx 99\%$. The function $\chi(1)$ is the distribution of the z-score. Coming back to the previous example, the cumulative distribution function of $\chi(1)$ at $M_\mathrm{d} = 1$ is 68.3%. Alternatively, the square root in Equation 3.1 can be removed, which results in M_d^2 following a $\chi^2(\nu)$-distribution with similar statistical properties.
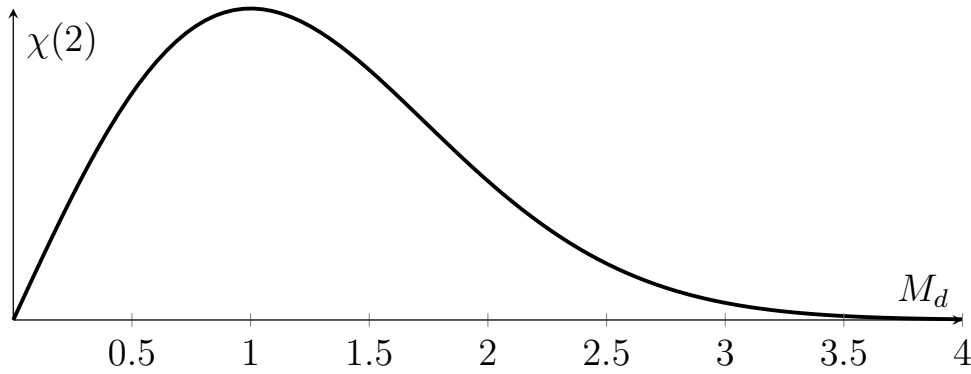
Figure 3.2: An example of the χ-distribution with two degrees of freedom.

Combination of Distributions

If two normal distributions $\mathcal{N}_1(\vec{x}_1|\vec{\mu}_1, \Sigma_1)$ and $\mathcal{N}_2(\vec{x}_2|\vec{\mu}_2, \Sigma_2)$ shall be compared, the difference $\Delta \vec{x} = \vec{x}_1 - \vec{x}_2$ is distributed according to (Johnson and Bhattacharyya, 2010):

$$\mathcal{N}(\Delta \vec{x}|\vec{\mu}_1 - \vec{\mu}_2, \Sigma_1 + \Sigma_2) \; . \tag{3.2}$$

If it shall be tested whether two distribution can give the same value $\vec{x}$, thus assuming $\Delta \vec{x} = \vec{0}$, the Mahalanobis distance for this case is:

$$M_\mathrm{d} = \sqrt{\Delta \vec{\mu}_{1,2}^T \cdot (\Sigma_1 + \Sigma_2)^{-1} \cdot \Delta \vec{\mu}_{1,2}} \; , \tag{3.3}$$

with $\Delta \vec{\mu}_{1,2} = \vec{\mu}_1 - \vec{\mu}_2$.

Transformations

If the distribution $\mathcal{N}_x(\vec{x}|\vec{\mu}_x, \Sigma_x)$ is given and a transformation function $\vec{h} : \vec{x} \to \vec{y}$ exists, it is also possible to obtain the distribution $\mathcal{N}_y(\vec{y}|\vec{\mu}_y, \Sigma_y)$ using different transformation techniques. A simple assumption is the local linearisation around μ_x using a first order Taylor series. In this case, the transformation yields:

$$\vec{\mu}_y = \vec{h}(\vec{\mu}_x) \; , \tag{3.4}$$
$$\Sigma_y = J \cdot \Sigma_x \cdot J^T \; , \tag{3.5}$$

with the Jacobian matrix $J = \frac{\partial \vec{h}}{\partial \vec{x}}$. Depending on the function $\vec{h}$, this Jacobian may have to be found by numerical differentiation.

If $\vec{h}$ is non-linear, the local linearisation may not give sufficiently accurate results. Assuming, that the distribution is still Gaussian in y, two common approaches to avoid these non-linearities during the transformation are the unscented transformation (Uhlmann, 1995), which uses a set of specific sample points, or the Monte Carlo transformation, which creates a large number of points by drawing samples from the distribution and then transforms all these points individually. The resulting distribution is calculated from these transformed points. For highly non-linear transformations, it may be the case that the distribution in y is not Gaussian, in which case the error representation in y cannot be modelled with a Gaussian curve.

3.2.2 Previous Research

The association problem for observations of orbiting objects, also referred to as correlation or linkage in the literature, has been considered in the past with various approaches. The underlying idea is that an orbit determination from a single pass or tracklet does not yield accurate orbits, which makes it more difficult to associate new observations with the newly initialised object. Combining observations from different epochs with a sufficient separation may improve the quality of the orbit due to the increased amount of information and potentially the larger coverage of the orbit.

Many association methods are based on the concept of the *admissible region* by (Milani et al., 2004). This concept is closely related to the attributable, see Section 2.2. The admissible region was originally proposed for the association of optical observations of asteroids. After the definition of the optical attributable, only two values are missing to define an orbit, i.e. the range ρ and range-rate $\dot{\rho}$. Further restrictions, e.g. limits on the orbital energy, are defined to analytically find an area in the ρ-$\dot{\rho}$-plane which shall contain the orbit of the observed object. If this admissible region is sampled and the resulting orbits are propagated to the epoch of another observation, a comparison at this second epoch can be used to check if the two observations belong to the same object. This concept has been extended to Earth-orbiting objects for both optical and radar observations (Tommei et al., 2007; Farnocchia et al., 2010). For radar measurements, the plane of the admissible region is $\dot{\alpha}$-$\dot{\delta}$. Conditions to restrict the region can include a minimum perigee altitude or a negative orbital energy to guarantee an Earth-bound orbit.

Several methods use the admissible region as a basis and extend its application. Some of these are briefly explained in the following. (DeMars and Jah, 2013) has introduced the interpretation of the admissible region as a two-dimensional statistical distribution. Initially, a uniform function over the entire region is used because no solution within the region is more probable than another. When new measurements are received, the propagated orbits from the admissible region are used to update the probability distribution. Over time, the correct orbit shall be identified as a peak of the probability distribution. This approach combines the initial orbit determination and association without requiring a specific distinction. It is rather included in the filtering process to update the orbit, which can also reject measurements that do not fit the current probability distribution. An equivalent approach has also been proposed for radar measurements (DeMars and Jah, 2014).

The admissible region can also be transformed to a boundary value problem considering a pair of tracklets instead of a single one. (Schumacher et al., 2013) proposed a set of restrictions for a pair of tracklets to eliminate pairs which cannot belong to the same object. These rules are mainly based on the expected orbit, e.g. minimum and maximum values for the semi-major axis or eccentricity, but also include a test on the initial orbit from two positions. (Siminski et al., 2014) defined the correlation as an optimisation problem in the ρ_1-ρ_2-space to find the minimum Mahalanobis distance for the differences in the four optical angle rates $(\dot{\alpha}_1, \dot{\delta}_1, \dot{\alpha}_2, \dot{\delta}_2)$. An efficient search algorithm can be applied and thus it is not necessary to sample the entire admissible region with candidate orbits. (Siminski, 2016) also tested this optimisation as an initial value problem similarly to the classical admissible region, but this was found to perform worse than the boundary value formulation. (Mann et al., 2019) proposed the integration of numerical propagation into the initial value problem to consider perturbations. A shooting method is applied to find a matching orbit between the two tracklets.

Another type of approach projects the admissible region as a two-dimensional manifold into the six-dimensional space of possible orbital elements (Maruskin et al., 2009; Fujimoto et al., 2014). If two of these manifolds are propagated to a common epoch, they can be tested for an intersection. If an intersection is found, this point represents the orbit connecting the two tracklets. This method is computationally expensive because it requires to model the manifold as a large number of sample points, which all have to be propagated.

Independent from the admissible region, (Gronchi et al., 2010) proposed a correlation method based on the conservation of the integrals of motion. This method extends an initial orbit determination by (Taff and Hall, 1977) to include a similarity measure for the correlation decision. The orbit is found as a root of a polynomial, that has at least an order of 20 (Gronchi et al., 2011).

The method by (Pirovano et al., 2020) is based on a least squares orbit determination from a short arc of optical observations which has a large uncertainty. This uncertainty, which is mainly concentrated in two dimensions along the directions of the covariance's two largest eigenvalues, is propagated and updated using differential algebra. Solutions with large residuals after the integration of additional measurements are pruned from the considered area in 2D-space until a small area with a distinct minimum can be found.

Concerning the association of radar measurements, the orbit determination from a single pass is also a common approach. In this case, both an initial orbit determination and orbit refinement calculation can be applied to each pass. The passes can be propagated to a common epoch and then compared in a selected orbit space. (Hill et al., 2012) compared a variety of coordinate systems and propagation methods. It is concluded that performing the uncertainty propagation with an unscented transform using mean equinoctial elements was the best option. A similar approach was proposed by (Vananti et al., 2017). There, the association was performed using covariances in curvilinear coordinates. This approach was also extended to combine radar and optical measurements for the correlation based on an orbit determination from the radar tracklet. This orbit is propagated to the epoch of the optical measurement and the comparison is made in observation space.

Considering that a number of N tracklets gives $\frac{1}{2} \cdot N \cdot (N-1)$ total combinations of two tracklets, testing all pairs can become time-consuming and computationally expensive. To reduce the computational demand by avoiding to test all possible combinations, (Zittersteijn et al., 2016) applied an heuristic search using a genetic algorithm. This approach also allows it to associate three or more tracklets with each other, which otherwise would increase the number of existing combinations even further.

3.2.3 Discriminator Approach

The work presented in this thesis follows the discriminator approach based on a separate initial orbit determination and correlation decision from (Siminski, 2016). In the optical case, an iteration on the two range values $\rho_{1,2}$ is necessary to obtain two positions for the IOD. The angular rates remain as a discriminator and can be compared to those which were estimated from the newly derived orbit using the Mahalanobis distance between the two distributions, see Equation 3.3. If this distance is smaller than the threshold, which depends on the degrees of freedom and chosen percentage of included points based on the cumulative distribution function, the hypothesis is accepted that the two distributions are equivalent and the two tracklets are assumed to be correlated. The case of a true correlation which is identified as such, is called *true positive* (TP). The larger the percentage of included points, the less probable it is to miss such a true association, which would be called a *false negative* (FN). However, the larger the threshold, the more likely it is to accept a wrong correlation, called *false positive* (FP), of tracklets from different objects.

Extending this correlation approach to the radar case, the iteration on the range is no longer necessary because these values are included as measurements. However, it still has to be considered that especially for LEO, there can be multiple possible solutions with different numbers of revolutions. Thus, the correlation of radar measurements can be considered as an optimisation over the number of revolutions. It may also be possible to use more information than the six input observables or consider all possible solutions, see Section 3.2.4 and Section 3.3. The eight observables of two separate radar measurements may be combined differently to derive an initial orbit, which also leads to different discriminators, see Section 4.2. Details on the implemented orbit determination and on the calculation of the Mahalanobis distance are presented in Section 4.3.1.

3.2.4 Additional Validation

The association from two radar observations is based on a relatively low amount of information. Thus, the results cannot be considered as final and definitive. Especially if the two sets of observables are attributables from a series of observations, see Section 2.2, there is still more data available. Within this work, two approaches to extract more information from the full tracklet are used. The rest of this section is taken from the publication (Reihs et al., 2021) and has been adjusted for the use in this thesis.

The first one is referred to as *Residuals Post Processing* (RPP). The attributable does not consider the direction of motion, i.e. the derivatives of the angles, because the angular measurements have large uncertainties and thus the estimation of their derivatives has a large uncertainty which may not be reflected properly in the fit. If two tracklets are correlated via their attributables, the underlying full tracklets can be used to calculate the residuals of the

single observations based on the resulting orbit of the correlation. An example is given in Figure 3.3 showing the residuals of azimuth and elevation for a false positive correlation. The linear trend in the azimuth direction is clearly visible which indicates that the orbit and the tracklet are not matching. To identify these pairs reliably, a Student's t-test (Johnson and Bhattacharyya, 2010) checks if there is a linear trend in the residuals. This approach was introduced in (Fujimoto et al., 2014). The tested hypothesis is that the slope of a straight line fitted to the residuals is equal to zero, meaning that there is no trend in the data. This hypothesis is rejected if the resulting test statistic p_t is smaller than a given threshold. The value p_t is the integral over the $\chi^2(\nu)$-function with the degrees of freedom depending on the number of data points. The integration bounds are calculated based on the estimated slope and its uncertainty. If this hypothesis is rejected, thus a linear trend in the residuals is assumed, the correlation is rejected as well. While the t-test works well for long tracklets, it may not be possible to identify linear trends from shorter tracklets reliably.
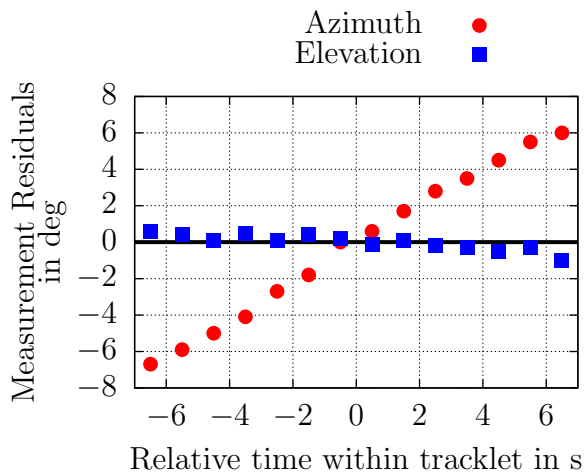
Figure 3.3: Example of the residuals in azimuth and elevation after the initial orbit determination based on attributables for a single tracklet.

A comparable test is done using the range measurements. Figure 3.4 depicts the range residuals of a tracklet against the orbit which was calculated from the attributable correlation. In this case, it is a true positive correlation but with a wrong estimation of the number of revolutions between the detections which leads especially to a wrong estimate for both the semi-major axis and the eccentricity. This causes that the range residuals over the entire tracklet become biased, but the zero residual at the reference time ($\Delta t = 0$ s) confirms that the attributable is matching the orbit. Ideally for a true correlation with a correct orbit, these residuals should be close to a random normal distribution consistent with the sensor noise. In order to extract this information and test if the residuals are biased, a second-order polynomial is fitted to the range residuals:

$$\Delta\rho = \frac{1}{2} \cdot c_2 \cdot \Delta t^2 + c_1 \cdot \Delta t + c_0 \ . \tag{3.6}$$

The absolute value of the curvature $|c_2|$, here defined as the second derivative, is used as a further parameter for the correlation decision. If this curvature is larger than the threshold value $c_{2,\text{thresh}} = 0.002$, the correlation is discarded. This is mainly useful if there are several days between the tracklets and the semi-major axes of adjacent solutions are close to each other.
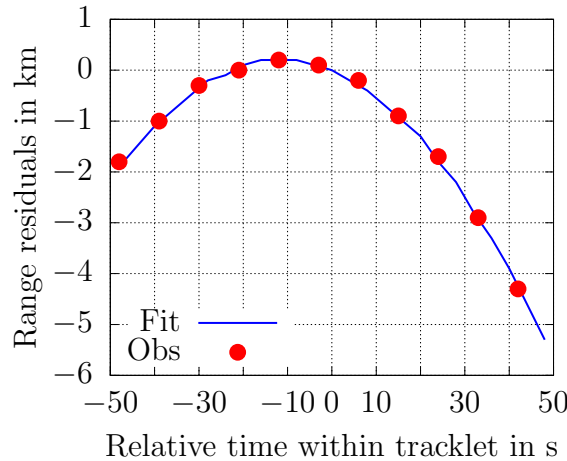
Figure 3.4: Range residuals of the initial orbit (number of measurement points reduced for better readability).

For correlations which pass both thresholds, for t-test and curvature, these information can even be combined to get an additional information. The idea is that the result p_t from the t-test should be as large as possible while the absolute value of the curvature $|c_2|$ should be as small as possible. This can be combined into a joint score S for both tracklets (T1 and T2), which becomes larger if the tracklets match the orbit better:

$$S = \frac{p_{t,\text{T1}} + p_{t,\text{T2}}}{|c_{2,\text{T1}}| + |c_{2,\text{T2}}|} \ . \tag{3.7}$$

The value of this score has no general objective meaning but it can be used to choose between solutions with different numbers of revolutions for the same pair of tracklets. Practically, this means that it is no longer only the solution with the smallest Mahalanobis distance, which is considered, but all solutions which are smaller than the threshold. Then, the score S is calculated for each solution and the one with the largest score can be chosen.

The second possible approach of using further information from the tracklet is a full least squares orbit determination. This can either follow the RPP or it can be performed directly without the RPP in between. The mean and standard deviation of the residuals after the orbit fit are compared to thresholds based on the assumed noise levels of the observables. The correlation is excluded, if this orbit calculation fails or the residuals of the measurements are larger than the selected thresholds.

3.3 Graph Network

3.3.1 Graph Theory

This section is dedicated to a short introduction to the graph theory, focused on the basic knowledge which is required to understand the following application to the correlation problem. Various textbooks about graph theory can be found for a more complete overview, e.g. (Gross and Yellen, 2004).
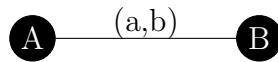
Figure 3.5: Simplified example of two nodes (A,B) and one edge (a,b).

The graph, also called network, consists of points, called *nodes* in the following, which can be connected by so-called *edges*. A simple example of two nodes A and B connected by an edge (a,b) is shown in Figure 3.5. In the application presented here, only *undirected graphs* are used, which means that there is no direction attached to the edge which would restrict the paths through the graph. An edge may also carry a *weight* to indicate a specific numerical value of the connection.

If a large set of data is received it may happen that certain parts of the resulting network are not connected, thus it may not be possible to go along the edges from Node A to D, as shown in Figure 3.6. In such a case the graph has separate *components*. Additionally in Figure 3.6 the edge (f,g) is called a *bridge*, because it is not part of a *cycle* and removing it causes the creation of two new components. A *cycle* is intuitively defined as a path through the graph which leads back to its origin without using an edge twice. It is obvious and also visible in Figure 3.6, that the smallest possible cycle consists of three nodes. In the following, this case will also be referred to as a *triangle*. Cycles (and thus also triangles) can be found efficiently in a graph by a *depth-first search*, which recursively checks all neighbouring nodes of the current node for a node which had already been visited before. More examples and details of search methods in a graph can be found in the literature.
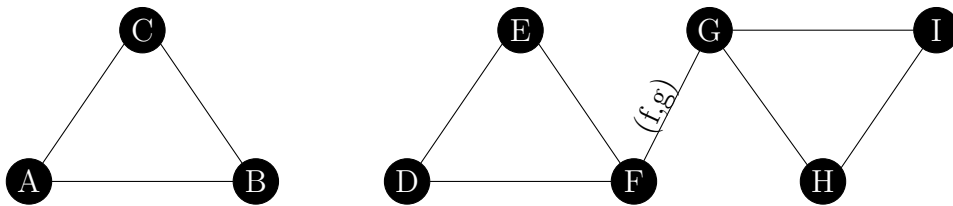
Figure 3.6: Example of two separate components and a bridge (f,g).

The formation of triangles will be important in the following and thus another observation about these structures is made. As shown in Figure 3.7, if more than three nodes are all interconnected, in this example four nodes, this structure can be broken down to a group of four triangles with the edges (a,c) and (b,d) both being shared by two triangles each.
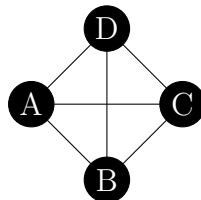
Figure 3.7: Example of four nodes with all possible interconnections.

The term *group* or *cluster* is used in the following for a collection of nodes, which are considered to be logically connected, although there do not have to be edges connecting each of them. The implementation of the graph analysis in Python uses the library *NetworkX* (Hagberg et al., 2008).

3.3.2 Application to Observation Correlation

The data to create the graph is imported from the output of the pairwise correlation routine. The tracklets are the nodes of the graph and the identified correlations are forming the edges between them. These edges have the Mahalanobis distance of the correlation assigned to them as a weight. It should also be emphasised that the following processing chain is purely within the framework of the graph theory based on the network given by the pairwise correlations and no orbital mechanics or measurements are considered at this stage. Yanez et al. (2017) proposed the application of Markov clustering to a graph to identify groups of tracklets and applied it to optical observations from telescopes in combination with the correlation method by Siminski et al. (2014).

The approach to identify the clusters in this work is described in the following. The first step is to split the graph into its components and process all components separately. For each component which contains at least one cycle, all bridges are found and removed, because a bridge cannot be part of a triangle. After removing the bridges, the number of components has increased and the next steps are again performed for all components separately.

Within each component, all triangles are identified by a simple algorithm which checks if any two neighbouring nodes A and B of the node of interest C are connected by an edge (a,b). If this is the case then (A, B, C) necessarily form a triangle. As shown in Figure 3.8 for a group of four tracklets, two triangles may share an edge, i.e. correlation, which is equivalent to sharing two nodes, i.e. tracklets. This is interpreted as an indication that these two triangles originate from the same object and thus they are merged into a common group. As a result all correlations within the group (A, B, C, D) are considered to be valid. Considering that these four tracklets originate from the same object, this approach is also robust against single missing correlations, here the correlation (b,d).
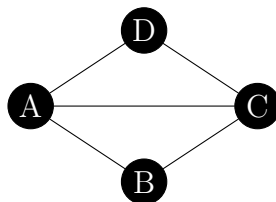
Figure 3.8: Example of a shared edge (a,c), which is results in merging the two triangles (A,B,C) and (A,C,D).

After creating a set of groups by merging triangles, it is possible that a node is part of two groups, see Figure 3.9 ignoring the dotted edges. In this case, because no correlations/edges are common to both groups, it is assumed that the node C can be part of only one group. In order to make a decision about the association of the node, the Mahalanobis distances from the pairwise correlations are considered. For the shared node, the root mean square (RMS) is calculated from all edges connecting the node to each of the two groups's nodes: here (a,c), (b,c) and (c,d) compared to (c,e) and (c,f). The node is assigned to the group which has the lower RMS. As a result, all connections from the other group to the previously shared node are removed.
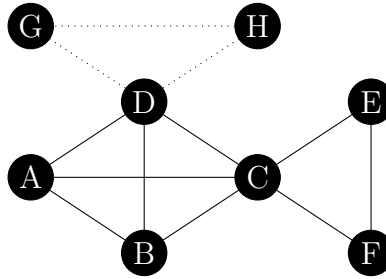
Figure 3.9: Example of cutting the connections between a shared node, here nodes C and D.

The described technique to assign nodes to a certain group can become problematic if two shared nodes are also connected. In such a case, considering the dotted edges in Figure 3.9, the order of processing the shared nodes C and D may affect the result. The edge (c,d) is part of both the comparisons to solve node D and C. If node C is processed first and is assigned to form the group (C, E, F), the processing of node D does not consider the edge (c,d), because it is already removed which may change the assignment of node D compared to the case in which D is processed including the edge (c,d).

After it was concluded from tests, that these cases are usually rare and do not influence the overall results significantly, it was decided to solve these cases with a greedy approach. All shared nodes are solved and assigned as it is optimal in that moment without considering implications on other shared nodes.

3.3.3 Considering Additional Information

To improve the results of the graph clustering even further, more information than just the Mahalanobis distance can be added to the graph's edges. As each correlation also includes an orbit, this information can also be included in the graph. Then it is possible to consider not only the consistency of the correlations but also the similarity of the orbits obtained from the correlation. It is either possible to define a threshold for a maximum difference between the same orbital elements or use the estimated covariance from the correlation. Considering that the covariance of the correlation orbit is only estimated via a simple linear mapping, the fixed threshold approach is preferred. To compare the orbital elements from different epochs without further propagation, elements should be selected which are relatively stable over at least several days. Choices could be the semi-major axis, the eccentricity or the inclination. This means that triangles are only formed or merged, if the orbits from the correlations have differences in the selected orbital elements which are smaller than a given threshold.

For the association problem in LEO, this can also be used to decide on the correct number of revolutions between the observations, see Section 4.3. To solve this, the tracklets are forming a so-called *multigraph*. This graph structure allows multiple edges with different weights (here: orbit and Mahalanobis distance) between a pair of tracklets, i.e. all correlations with a Mahalanobis distance below a given threshold and not just the minimum. This reduces the dependency on a correct selection of the number of revolutions during the pairwise correlation, because this decision can be deferred until more information is available. In combination with the conditions on orbit similarity within a triangle, the clustering process also gives a consistent solution for the resulting groups' orbit. The underlying idea is that solutions with a wrong number of revolutions are usually not consistent in their offset from

the true orbital elements, e.g. semi-major axis, as this is also dependent on the total number of revolutions. Thus it is expected that only the true correlations lead to large clusters. In case of the multigraph, there is an additional possibility of a shared node which has to be solved. A tracklet can end up in more than one group, while these groups are unconnected because they represent different sets of orbital elements. Such a case is not solved by the RMS as for a shared node, see Section 3.3.2, but a majority vote is used to decide the accepted group by selecting only the group with most tracklets.

If the resulting groups are compared to the true correlations in case of a test with knowledge of the true solution, different categories can be defined analogously to the true and false positives for pairwise correlations. A TP-group contains all tracklets from an object and no others. If there are only tracklets from the same object, but not all of them, it is called an FN-group. If tracklets from different objects are mixed within an identified cluster, it is referred to as FP-group.

3.4 Other Approaches

In addition to the pairwise correlation, the data association can also be performed as a part of a general filtering process. In this context, a filter is an estimation method to update the current state of the object based on a new measurement. They are mostly based on the Bayes rule:

$$p(x|z) = \frac{p(z|x) \cdot p(x)}{p(z)} \; , \tag{3.8}$$

with $p(a|b)$ referring to the conditional probability of a given b. The object's state is x and the measurement is z. Based on this principle, a two-step filter with a state update and a measurement update can be derived. The most famous realisation is the Kalman filter (Kalman, 1960), which is obtained by a linearisation of the involved derivatives.

Extending the Bayesian principle to the estimation of multiple objects' states in parallel leads to the domain of *multitarget tracking*. Some principles and examples from this field are given in the following, because of its common application to the tracking of space objects by radar. A more detailed overview including the founding principles and different realisations can be found in, e.g (Vo et al., 2015). Closely related to the pairwise correlation considered in this thesis is the Joint Probabilistic Data Association. It requires an assumed or known number of different objects and derives the most probable set of associations which is non-contradicting considering the principle that each observation can only be associated to one object. For example, the Mahalanobis distance for each measurement-to-state association is calculated and an overall score is defined for all accepted correlations of a consistent set of associations. The set with the lowest score can be chosen to obtain the most probable associations and to update the states with the assigned measurements according to the chosen filter.

This can be extended to the Multi Hypothesis Tracking (MHT), which does not require a hard decision on an association after each measurement step but can maintain different conflicting hypotheses of associations over a given period of time. After regular intervals, a pruning step can occur which creates consistent associations from the most probable hypotheses.

A popular framework within MHT is the use of Random Finite Sets (RFS) (Mahler, 2004). This approach models the number of objects as a probabilistic variable and maintains different probability distributions for different numbers of objects. Although this theory is very elegant and powerful, its realisation and implementation is complex. Usually, its solution can only be approximated. One example is the PHD-filter (Mahler, 2003), which propagates only the first moment of the multitarget probability distribution. In the context of space surveillance, examples for MHT algorithms using RFS include the AEGIS-FISST (DeMars et al., 2015), which uses Gaussian mixtures to propagate the multitarget density. Delande et al. (2019) applies a filter with a reduced complexity using stochastic populations. These methods do not need to perform fixed associations, but rather consider the development of the probability density function.

PERTURBED INITIAL ORBIT DETERMINATION AND ASSOCIATION

4.1 Overview

The initial orbit determination is a prerequisite for all works relying on orbital data derived from measurements and thus can be regarded as a fundamental problem of astrodynamics. To fully define an orbit, six parameters are necessary which is equivalent to the number of dimensions in the position-velocity phase space. These six parameters can either be the mentioned combination of position and velocity or a dedicated set of orbital elements, e.g. the classical Keplerian or equinoctial elements (Vallado, 2013). To compute six parameters, at least six independent information need to be provided as an input. Because the motion of the object along the orbit is a dynamic problem, orbits and observations are always valid at a given epoch which will not always be mentioned explicitly in the following.

Historically, due to the use of telescopes in the early times of astronomy, optical observations have been considered for the first IOD methods. As each optical observation gives two direction angles, a minimum of three observations is necessary. There are two famous methods based on two different approaches. Gauss' method is based on a boundary value problem to fit an orbit which is consistent with the central observation vector, while Laplace's method is an initial value problem considering the differential equations of motion. More information and discussions on these methods can be found in the literature, e.g. (Beutler, 2004a;

Taff, 1984; Vallado, 2013). A third approach which is fundamentally different is based on the conservation of the integrals of motion, i.e. the orbital energy and angular momentum (Taff and Hall, 1977). This approach was extended to include other conserved quantities and perturbations, see e.g. (Gronchi et al., 2010; Ma et al., 2018).

Another class of IOD methods uses positions in inertial space as an input. Two famous methods are based on the use of three positions. The Gibbs methods uses a geometrical approach which makes it better suited for positions with a large separation, whereas the Herrick-Gibbs method is based on a Taylor series and thus works best with closely-spaced observations (Vallado, 2013). The input of the IOD can also be reduced to two positions, which is a total of six independent information and thus the minimum to calculate an orbit. This approach is usually referred to as *Lambert's problem*. Methods to solve this problem were developed in the time of space flight, because they can be applied to radar measurements of satellites or manoeuvre planning. There are various approaches to solve this problem. A compilation and categorisation of some methods can be found in de la Torre Sangrà and Fantino (2015). Some notable methods for the unperturbed case are (Lancaster and Blanchard, 1969; Battin, 1977; Gooding, 1990; Izzo, 2015). Further examples for the inclusion of perturbations in Lambert's problem are Armellin et al. (2018) using an homotopy continuation approach and Woollands et al. (2015) using the Kustaanheimo-Stiefel transformation based on earlier work by Engels and Junkins (1981).

An overview with a large number of IOD methods for different combinations of input information can also be found in Escobal (1976).

4.2 Approaches

As described in Section 1.2, a radar can provide up to four different observables. The range, range-rate and the direction angles azimuth/elevation. Thus, the set of available observables $\mathcal{O}$ at a specific epoch t_i is:

$$\mathcal{O}_i = \{\rho_i, \dot{\rho}_i, az_i, el_i\} \ . \tag{4.1}$$

This measurement set can also be the result of an attributable fitting, see Section 2.2.

Combining two sets $\mathcal{O}_1$ and $\mathcal{O}_2$ from different epochs leads to a total of eight observables. To perform the association, it is necessary to compare the two sets based on an orbit which was derived from their combined observations. Those observables which had not been used in the orbit determination form the discriminator, see Section 3.2. Within the scope of this work, three different methods have been developed to perform the initial orbit determination and association based on different combinations of the observables. These three methods are briefly introduced in the following, before the selected method is discussed in detail in Section 4.3. All methods include a correction routine for the secular J_2-perturbations, which is required in order to have a reliable correlation for multiple days between two observations (Reihs et al., 2018). For each method, it also has to be specified whether the orbit is prograde or retrograde as both is possible and usually not known a priori.

Method 1: Lambert's Problem

$$\begin{aligned} \{\rho_1, az_1, el_1, \rho_2, az_2, el_2\} \quad &\rightarrow \quad \text{Orbit} \\ \{\dot{\rho}_1, \dot{\rho}_2\} \quad &\rightarrow \quad \text{Discriminator} \end{aligned}$$

A position in inertial space can be calculated for each detection by combining the range and angles with the known station location. Deriving an orbit from two positions is known as the classical Lambert's problem, for which various solutions have been proposed, see Section 4.1. Here, the solution is derived by an iteration over the semi-latus rectum to consider all possible solutions with different numbers of revolutions. The two range-rates remain as the discriminators.

Method 2: Initial Position and Velocity

$$\{\rho_1, \dot{\rho}_1, az_1, el_1, (\rho_2, az_2, el_2)\} \quad \rightarrow \quad \text{Orbit}$$
$$\{\rho_2, \dot{\rho}_2, az_2, el_2\} \quad \rightarrow \quad \text{Discriminator}$$

The second method is based on an initial value problem by deriving the orbit mainly from the measurements at the first epoch including the range-rate. By performing an iteration over one component of the velocity vector $\vec{v}_1$ at t_1, the complete velocity vector and thus the orbit can be derived from geometrical relations. For this, the orbital plane is required as another input and it is obtained by using the position derived from the second set of observations. The second position is only used to define the orbital plane and its exact position is not enforced in the initial orbit determination, because this would overconstrain the problem. Thus, the orbit does not necessarily include the second position and all four observables of the second measurement $\mathcal{O}_2$ can be used in the discriminator. Also for this case, there can be multiple solutions with different numbers of revolutions.

Method 3: Velocity-based Integrals of Motion

$$\{\rho_1, \dot{\rho}_1, az_1, el_1, \rho_2, \dot{\rho}_2, az_2, el_2\} \quad \rightarrow \quad \text{Orbit}$$
$$\{\Delta\omega, \Delta\varphi\} \quad \rightarrow \quad \text{Discriminator}$$

The third method also uses the range-rate $\dot{\rho}_2$ of the second measurement in the orbit determination. The iteration parameter is the L_2-norm of the velocity vector $\vec{v}_1$. Similarly to Method 2, the full velocity vector can be derived by combining the norm with the orbital plane and the range-rate $\dot{\rho}_1$. Additionally, the L_2-norm of the second velocity vector $\vec{v}_2$ is calculated via the vis-viva-equation and the vector $\vec{v}_2$ can be found by using $\dot{\rho}_2$. A valid solution is found if the combinations $(\vec{r}_1, \vec{v}_1)$ and $(\vec{r}_2, \vec{v}_2)$ have the same angular momentum and orbital energy. An orbit determination based on the conservation of these quantities had also been proposed by (Taff and Hall, 1977).

Due to the noisy measurements, the two orbits based on $(\vec{r}_1, \vec{v}_1)$ and $(\vec{r}_2, \vec{v}_2)$ are not the same, but differ by their argument of perigee and true anomaly. The other Keplerian orbital elements are the same due to the conserved quantities. Thus the differences between the orbits, namely $\Delta\omega$ and $\Delta\varphi$ can be used as a discriminator. A similar selection for the discriminator is also found in (Gronchi et al., 2010). In contrast to the other two methods, there is only one solution and not multiple solutions depending on the numbers of revolutions.

Comparison

The three developed methods have been compared in (Reihs et al., 2018). Based on these results, it was decided that Method 1 is the most promising one. Thus this method has been selected for the use in the following work. The details of the method are given in the following Section 4.3.

4.3 Method

The text and figures in this section have been taken from the publication (Reihs et al., 2020a). Partially, they have been revised and adjusted for this thesis and they are used in accordance with the copyright agreement.

4.3.1 Orbit Calculation

The approach for the calculation of the initial orbit is closely related to the classical Keplerian elements based on a variation of the iteration on the semi-latus rectum p (Escobal, 1976). This approach derives the Keplerian elements from two positions and the time between them by iterating on the value of p. The two positions $\vec{r}_1$ and $\vec{r}_2$ are in an inertial, geocentric reference frame. One common realisation of such a frame is the J2000 with the x-axis pointing towards the vernal equinox, the z-axis along the Earth rotation axis and the y-axis completes the right-handed system. First, the angle between the two observations is calculated, which represents the difference between the true anomalies $\varphi_{1,2}$:

$$\Delta\varphi = \arccos\left(\frac{\vec{r}_1 \cdot \vec{r}_2}{|\vec{r}_1||\vec{r}_2|}\right) \ . \tag{4.2}$$

Additionally, the orbital plane is set via the orbit normal vector:

$$\vec{N} = \frac{\vec{r}_1 \times \vec{r}_2}{|\vec{r}_1 \times \vec{r}_2|} \ , \tag{4.3}$$

which yields the inclination i and the RAAN Ω:

$$i = \arccos\left(N_z\right) \ , \tag{4.4}$$

$$\Omega = \arctan\left(-\frac{N_x}{N_y}\right) \ . \tag{4.5}$$

Because the two points can only define the orbital plane and not the direction of motion within this plane, the previously given solutions for the orbital elements refer to the short trajectory between the two points with $\Delta\varphi \leq 180°$ as defined by the cross product in Equation 4.3. One solution is always a prograde orbit and the other one a retrograde orbit. It is not possible to know beforehand which direction of motion is correct, thus both possibilities have to be checked for each pair. The orbital elements for the long trajectory are related to those of the short trajectory given previously by:

$$\Delta\varphi_L = 360° - \Delta\varphi \ , \tag{4.6}$$

$$i_L = 180° - i \ , \tag{4.7}$$

$$\Omega_L = 180° + \Omega \ . \tag{4.8}$$

which can also be obtained by using $-\vec{N}$ in Equations 4.4-4.5, because the orbit normal for this solution points in the opposite direction.

Concerning the remaining orbital elements, first the true anomaly at t_1 is derived by using the equations of the conic section $|\vec{r}_{1,2}| = p \cdot (1 + e\cos(\varphi_{1,2}))^{-1}$. The semi-latus rectum p and eccentricity e in this equation are the same at both points. They can be combined to eliminate the eccentricity. Additionally, $\varphi_2 = \varphi_1 + \Delta\varphi$ is used to eliminate φ_2, resulting in

φ_1 as function of p:

$$\varphi_1(p) = \arctan\left(\frac{\cos\left(\Delta\varphi\right) - \left(\frac{p}{|\vec{r}_2|} - 1\right)\left(\frac{p}{|\vec{r}_1|} - 1\right)^{-1}}{\sin\left(\Delta\varphi\right)}\right). \tag{4.9}$$

From there on, the semi-major axis a and the eccentricity e can be found easily.

To test for a valid orbit at p, it is checked whether the propagation of the orbit with the derived elements from t_1 to t_2 leads to the correct point $\vec{r}_2$. The expected true anomaly at t_2 is:

$$\varphi_2 = \varphi_1 + \Delta\varphi, \tag{4.10}$$

which is transformed to the mean anomaly M_2. The true anomaly φ_1 is also transformed to the corresponding mean anomaly M_1 and propagated to t_2 using the mean motion under the assumption of Keplerian motion. This yields M_{1,t_2}. The difference between the two mean anomalies at t_2 is the value $\Delta M = M_2 - M_{1,t_2}$, which is zero for a valid orbit connecting the two points and thus is used to identify the solutions. Figure 4.1 shows an example of the behaviour of ΔM over the semi-latus rectum p. ΔM is normalised to be in the interval $(-180°, 180°]$. The different solutions are distinguished by their number of completed revolutions N_{rev} within $\Delta t_T = t_2 - t_1$. For the practical implementation, it is helpful to define the intervals of p with the same number of revolutions such that each nearly linear graph has its own unique number of revolutions. This is achieved by setting the change of the number of revolutions at $\Delta M = \pm 180°$, as it can be seen in Figure 4.1.
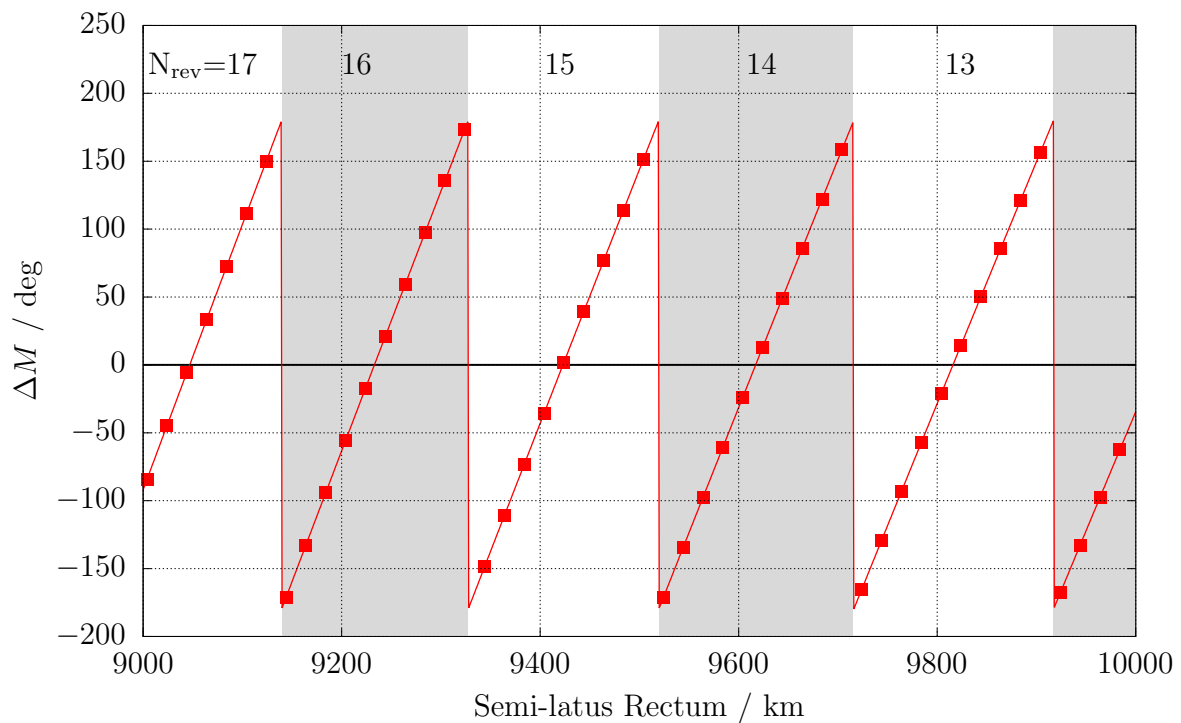
Figure 4.1: A part of the optimisation function for the semi-latus rectum with multiple possible solutions, zoomed in on the region from 17 to 12 revolutions as an example.

In practice, after an initial sampling of the ΔM-function, the root of each linear function gives a solution. For radar measurements in LEO, the interval on p with a physically possible solution is confined to the right by the growing eccentricity towards a hyperbolic orbit and to the left by a decreasing perigee altitude. Due to this decreasing perigee altitude, the second possible solution of the Lambert's problem (Gooding, 1990) can be neglected as this leads to highly eccentric orbits crossing the Earth surface. However, if this method is used to calculate an initial orbit from two observations in for example GEO, the second solution for all $N_{\text{rev}} > 0$ has to be considered as well. The slope of the ΔM-values for this set of solutions is negative (mirrored at the y-axis compared to Figure 4.1) and they can be found at values of the semi-latus rectum, which are smaller than that of the minimum eccentricity solution.

For each solution, the Mahalanobis distance is computed as a statistical distance using the combined differences of the discriminators, here $\dot{\vec{\rho}} = (\dot{\rho}_1, \dot{\rho}_2)$. As introduced in Section 3.2.1, the Mahalanobis distance is computed as (Mahalanobis, 1936):

$$M_d = \sqrt{\Delta \dot{\vec{\rho}}^T \cdot \Sigma_{M,C}^{-1} \cdot \Delta \dot{\vec{\rho}}}\,, \tag{4.11}$$

using the differences in range-rate $\Delta \dot{\vec{\rho}} = (\Delta \dot{\rho}_1, \Delta \dot{\rho}_2)$ at the epochs t_1 and t_2. This difference $\Delta \dot{\rho}_i = \dot{\rho}_{i,C} - \dot{\rho}_{i,M}$ is calculated between the measurement $\dot{\rho}_M$ and the expected value $\dot{\rho}_C$ which is computed from the newly derived orbit. The covariance matrix $\Sigma_{M,C} = \Sigma_M + \Sigma_C$ is based on the uncertainties of the observables. Σ_M contains the uncertainties of the measurements $\dot{\rho}_M$:

$$\Sigma_M = \begin{bmatrix} \sigma_{\dot{\rho}_1}^2 & 0 \\ 0 & \sigma_{\dot{\rho}_2}^2 \end{bmatrix}\,. \tag{4.12}$$

Σ_C is the uncertainty of the discriminator resulting from the calculation of the orbit. It is obtained by relating the measurement uncertainties in (ρ, az, el) to the uncertainty of the derived value $\dot{\rho}_C$. The measurement covariance Σ_S of the observables used for the orbit determination is a diagonal matrix:

$$\Sigma_S = \begin{bmatrix} \sigma_{\rho_1}^2 & & & & & \\ & \sigma_{az_1}^2 & & & \text{\Large 0} & \\ & & \sigma_{el_1}^2 & & & \\ & & & \sigma_{\rho_2}^2 & & \\ & \text{\Large 0} & & & \sigma_{az_2}^2 & \\ & & & & & \sigma_{el_2}^2 \end{bmatrix}\,. \tag{4.13}$$

By using numerical differentiation, these uncertainties can be mapped onto the resulting discriminator:

$$\Sigma_C = \left[\frac{d\dot{\rho}_{1,2}}{d(\rho_{1,2}, az_{1,2}, el_{1,2})} \right] \cdot \Sigma_S \cdot \left[\frac{d\dot{\rho}_{1,2}}{d(\rho_{1,2}, az_{1,2}, el_{1,2})} \right]^T\,. \tag{4.14}$$

As discussed in Section 3.2.1, this transformation is based on a linearisation around the given point, which is only an approximation of its true non-linear dependence. Although the general applicability of this formula is limited, this approach gives satisfying results for the work presented here. It is also assumed that the errors in the observables are not correlated and thus the matrices Σ_M and Σ_S are diagonal, but non-diagonal matrices could also be used in case of correlated errors. The matrix Σ_C is usually non-diagonal after the transformation.

Because the discriminator contains two values, the ideal distribution of Mahalanobis distances would follow a $\chi(2)$-distribution, see Section 3.2.1. With such a distribution, approximately 99% of the true correlations should fulfil $M_\mathrm{d} \leq 3$, if the errors are sufficiently normally distributed.

In the end, the solution with the lowest Mahalanobis distance is selected from all possible solutions (see Figure 4.2) for the corresponding pair of tracklets. If this distance is below a certain threshold, the pair is correlated, i.e. assumed to originate from measurements of the same object. Alternatively, the post-processing approach presented in Section 3.2.4 can be used to consider more information than the Mahalanobis distance for the selection of the most probable solution or the graph network, see Section 3.3, can consider various possible solutions.
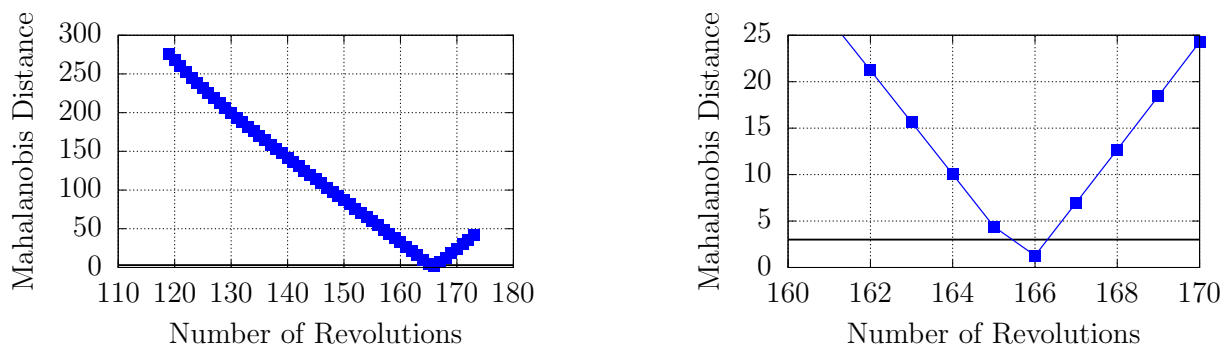
Figure 4.2: Minimum of Mahalanobis distance over the possible solutions for different numbers of revolutions with $M_d = 3$ as a reference threshold (solid line). Left: All solutions. Right: Zoom in on minimum.

4.3.2 J$_2$-Correction

The gravitational perturbation due to the Earth oblateness, referred to as J$_2$ by its term in the spherical harmonics (Pavlis et al., 2012), is the main disturbing force acting on a LEO satellite apart from drag (Beutler, 2004b). It was previously shown that the correlation without considering this J$_2$-perturbation is only possible for a very limited time between the two measurements (Reihs et al., 2018). Thus the effect of this perturbation is included in the initial orbit determination process by analytically computing and counteracting its effect as explained in the following. This affects the orbital plane, the argument of perigee and the mean motion. A comparable approach can be found in (Ma et al., 2018).

Orbital Plane

The orbital plane and thus the RAAN rotates around the Earth z-Axis due to the J$_2$-perturbation with a constant rate considering only the secular effects. This rate depends on the orbital parameters a, e, i and the mean motion n combined with the constant J$_2$ from the Earth's gravitational field and the Earth radius R_E (Vallado, 2013):

$$\dot{\Omega} = -\frac{3 \cdot J_2 \cdot R_E \cdot n \cdot \cos(i)}{2 \cdot a^2 \cdot (1 - e^2)^2} \ . \tag{4.15}$$
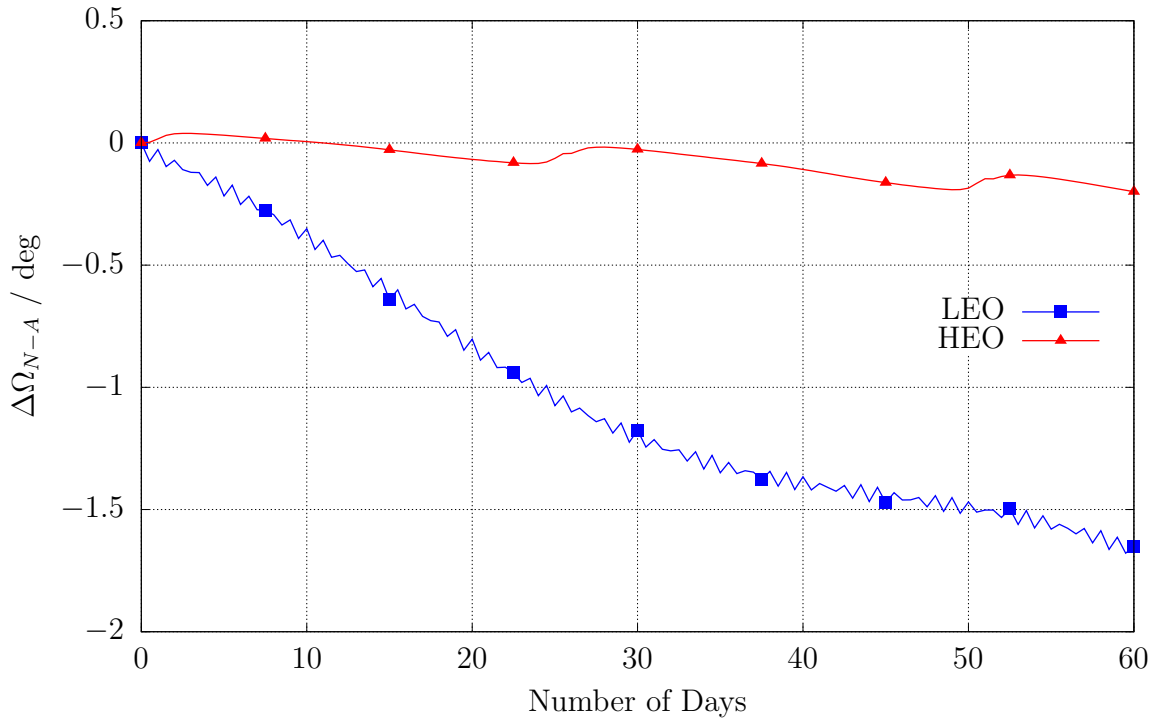
Figure 4.3: Example of the difference between the numerically propagated RAAN and the one from the analytical formula. LEO: $a = 7100$ km, $e = 10^{-5}$, $i = 30°$. HEO: $a = 27000$ km, $e = 0.7$, $i = 30°$.

Multiplying this rate with the time between the tracklets, leads to the estimated change $\Delta\Omega = \dot{\Omega} \cdot \Delta t_T$. In Figure 4.3, the result from this analytical formula is compared to a numerical propagation for the given example orbits in LEO and HEO, see Section 5.1 for details on the numerical propagation. For LEO, it can be seen that the approximation error of the analytical formula, here the difference $\Delta\Omega_{N-A}$ between the analytical and numerical result, is below 1° up to 23 days and reaches 1.5° after 50 days. For HEO, the overall changes are much lower due to the larger semi-major axis and the differences compared to the analytical model are even below 0.3° for the entire time span. Considering the other uncertainties within the orbit determination over such long periods, the analytical approach has a sufficient accuracy.

With regard to the orbit determination from two points, the rotation of the orbital plane affects both Ω and i. Even with completely noise-free measurements, the estimate of the orbital plane would be wrong due to its unconsidered rotation over time. This error increases with a decreasing spatial separation of the two measurement points. This is counteracted by rotating the second point of measurement by an angle of $(-\Delta\Omega)$ around the Earth z-Axis. An example of the effect of this rotation is displayed in Figure 4.4 for a prograde orbit together with the values of the ground truth for RAAN and inclination. It can be seen that both graphs cross their respective ground truth at $\Delta\Omega \approx 25°$ and also at $\Delta\Omega \approx 290°$. In total there are four correction angles $\Delta\Omega$ which yield a correct inclination. The other two possibilities at $\Delta\Omega \approx 150°$ and $\Delta\Omega \approx 250°$ have a RAAN of approximately 90°. These four cases with the correct inclination correspond to the four possible constellations of having

both points on the ascending or descending arc of the orbit or one on each. Although of theoretical interest, this does not cause any confusion for the actual solution of the perturbed initial orbit determination, because the correction angles $\Delta\Omega$ are converging on the correct solution, see Section 4.3.3.
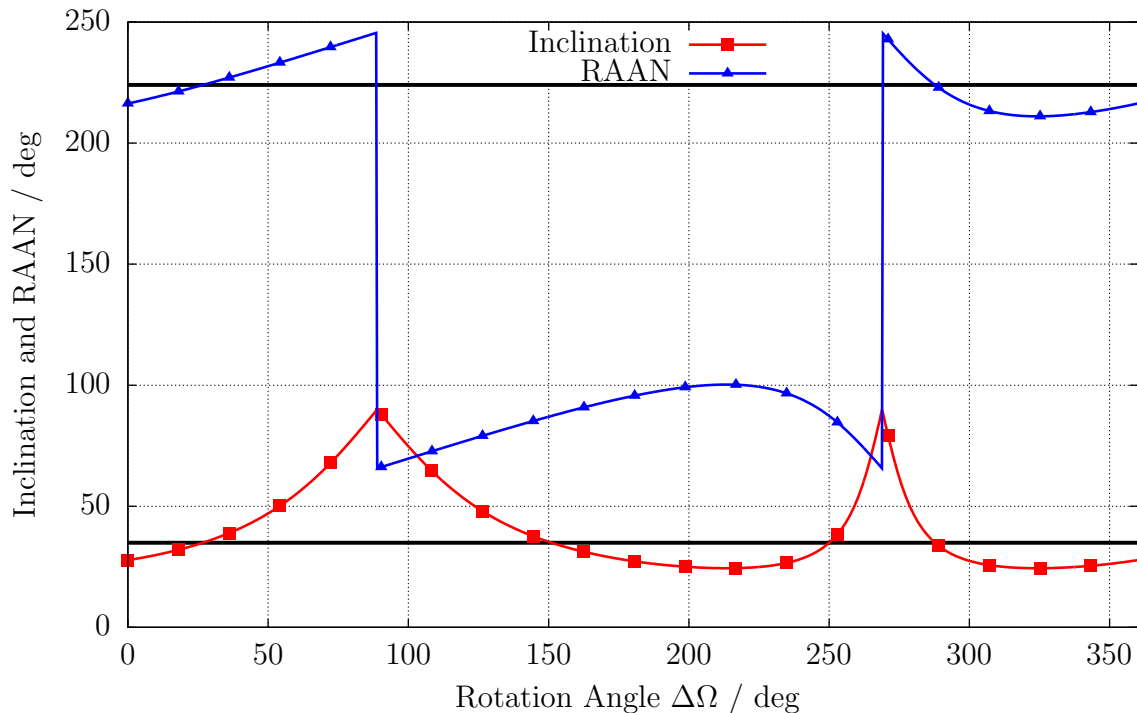
Figure 4.4: Example of the effect of the rotation of the second position on the orbital plane for a prograde orbit. Values of ground truth plotted as solid line.

This correction approach also clearly separates the treatment of prograde and retrograde orbits whose solutions both have to be checked, because the orbital plane rotates in opposite directions for these two cases as can be seen from Equation 4.15. Due to the rotation, $\vec{r}_2$ becomes $\vec{r}_{2r}$ which forces a new inclination i_r and RAAN Ω_r at t_1. It can also happen that the rotation moves the measurement to the other side of the first measurement by crossing the same geodetic longitude or the one on the opposite side of the first measurement. It was already shown in Figure 4.4 where this switch to the other side occurs at $\Delta\Omega \approx 90°$ and $\Delta\Omega \approx 270°$, that in this case there is no change from prograde to retrograde orbit because a retrograde orbit would be rotated to the opposite direction. Instead, the type of trajectory is switched between long and short leading to a 180° change of the RAAN, see Equation 4.8. This will be referred to as a *direction switch* in the following.

The described rotation gives the orbital plane at the epoch of the first measurement. To consider the rotation, the new RAAN at t_2 is calculated as $\Omega_2 = \Omega_r + \Delta\Omega$ after performing the Kepler propagation to the second point of measurement and the inclination is held constant at the corrected value i_r. The propagation is performed within the first orbital plane.
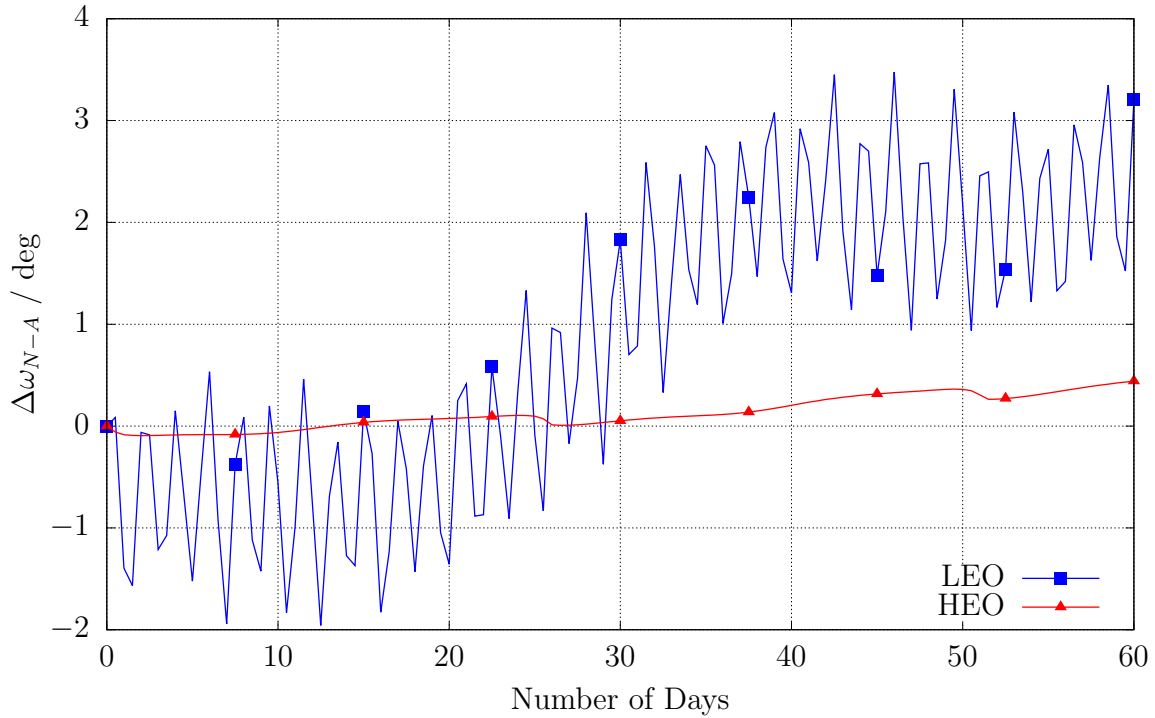
Figure 4.5: Example of the difference between the numerically propagated AoP and the one from the analytical formula. LEO: $a = 7100$ km, $e = 0.05$, $i = 30°$. HEO: $a = 27000$ km, $e = 0.7$, $i = 30°$.

Argument of Perigee

The rotation of the argument of perigee (AoP) ω changes the orientation of the elliptic orbit within the orbital plane depending on the same elements as the rotation of the plane previously (Vallado, 2013):

$$\dot{\omega} = \frac{3 \cdot J_2 \cdot R_E \cdot n \cdot (4 - 5\sin^2(i))}{4 \cdot a^2 \cdot (1 - e^2)^2} \; . \tag{4.16}$$

Again this formula is tested against the numerical propagation as shown in Figure 4.5. The difference in LEO between them is below 3° for most of the time span, which is an acceptable deviation considering the remaining uncertainties and the low eccentricities in LEO. Regarding the HEO object for which the location of the perigee is much more important, the differences are below 0.5° within the considered time span. This shows that the accuracy of the analytical formula is sufficient for the application presented here.

To counteract this rotation, the angle between the observations is reduced by this perigee rotation angle:

$$\Delta\varphi_{\mathrm{r}} = \Delta\varphi - \Delta\omega \; . \tag{4.17}$$

This is visualised in Figure 4.6. As only the radii of the two positions $\vec{r}_1$ and $\vec{r}_2$ are used in the orbit determination, the rotation by $\Delta\omega$ projects the radius of the second position as $\vec{r}_{2r}$ onto the orbit at the epoch t_1 of the first measurement and thus improves finding the shape of the orbit. After propagating to t_2, the new AoP is set to $\omega_2 = \omega_1 + \Delta\omega$ keeping the

anomaly constant and thus rotating $\vec{r}_{2r}$ back to the original point $\vec{r}_2$. In the shown example, the rotation moves the second measurement to the other side of the first measurement, which forces some additional bookkeeping within the implementation of the algorithm, but leads to no additional problems.
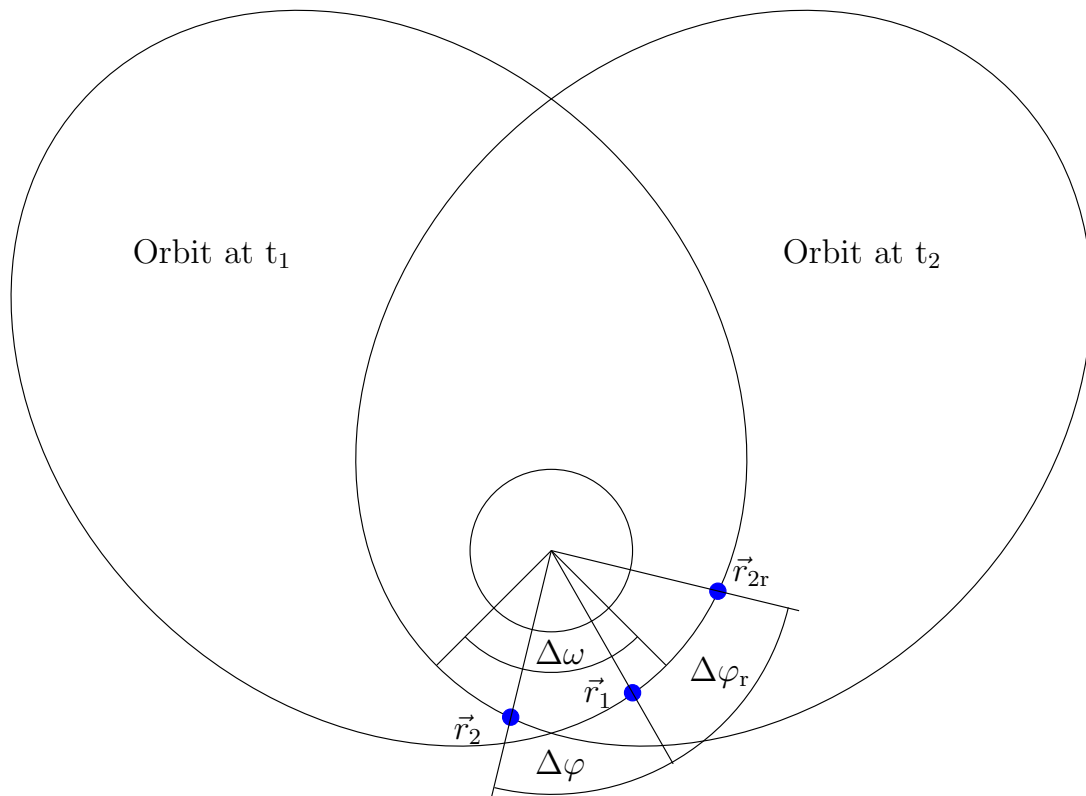
Figure 4.6: Simplified example of the perigee rotation within the J$_2$-correction.

Mean Motion

The Keplerian mean motion $n_K = \sqrt{\mu_E \cdot a^{-3}}$ is also affected by the Earth oblateness and yields a perturbed mean motion (Vallado, 2013):

$$n_{J_2} = n_K \left(1 + \frac{3 \cdot J_2 \cdot R_E^2}{4 \cdot a^2} \cdot \frac{\left(2 - 3\sin^2(i)\right)}{(1 - e^2)^{\frac{3}{2}}} \right) \ . \tag{4.18}$$

The mean anomaly can be propagated with this perturbed mean motion $M_{1,t_2} = M_1 + n_{J_2} \cdot \Delta t_T$. As can be seen from equation 4.18, the sign of the correction of the mean motion changes at $i_n = 54.74°$ from positive to negative and back to positive at $i_{n2} = 125.26°$. Thus for an object with $i < i_n$ the mean motion will appear faster than expected for the corresponding semi-major axis. Within the correlation this case would lead to a systematic underestimation of the semi-major axis. Figure 4.7 gives an example of the semi-major axis for the correlation of an object with $i = 41°$. If no J$_2$ correction is applied to the mean motion, the semi-major axis is underestimated in a consistent way, whereas the corrected

version yields estimates close to the value of the ground truth, which is the mean semi-major axis over one revolution as the Keplerian propagation does model short-periodic changes in the osculating semi-major axis during one revolution. If $i_n < i < i_{n2}$, the estimated semi-major axis would be larger than its true value.
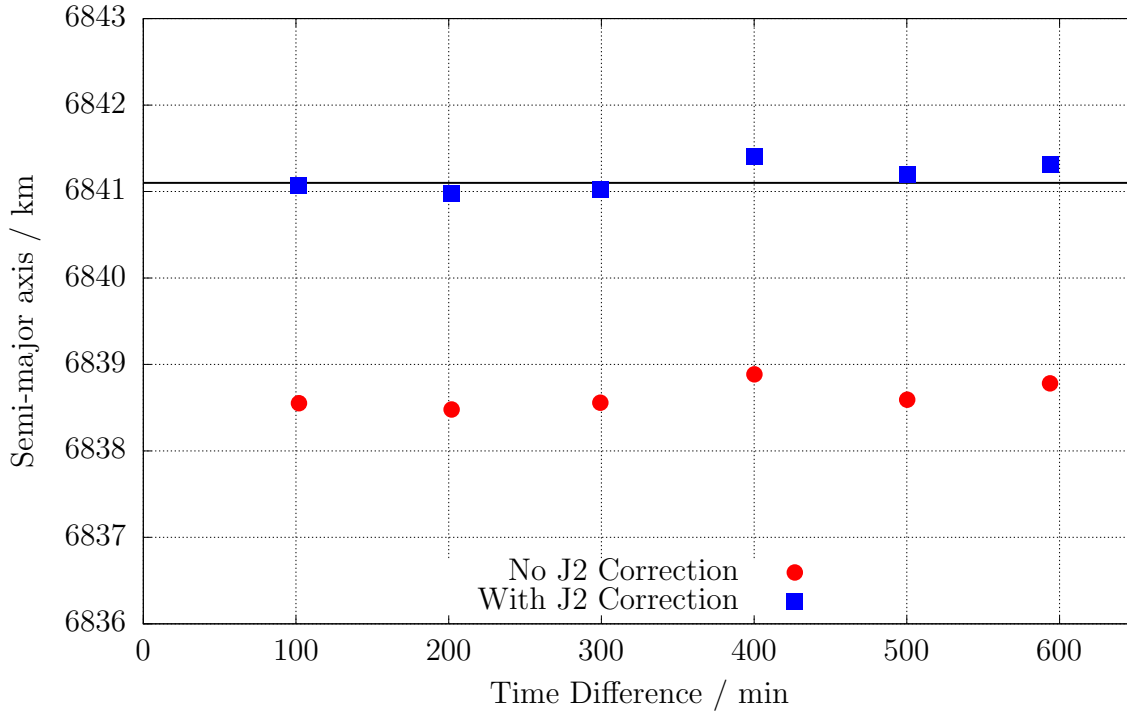
Figure 4.7: Effect of the J_2 correction on the calculated semi-major axis. Ground truth plotted as solid line.

4.3.3 Convergence Behaviour

Standard Case

For the following experiments, the parameters of the simulations are explained in Section 5.1. The standard convergence of the J$_2$-correction uses an iterative correction of the orbital plane. Each calculated orbit gives certain correction values until the changes in these corrections are less than a given threshold, which is equivalent to a convergence of the orbital plane. An example is shown in Figure 4.8 for two tracklets separated by approximately 14 days with the orbital elements $[a = 6896.7$ km, $e = 0.00185$, $i = 34.9°$, $\Omega = 284.4°]$ at t_1. The values of RAAN and inclination are plotted together with their ground truth in addition to the Mahalanobis distance. It can be seen that only a few steps are necessary to get close to the true value. To test for a successful convergence, the difference between the correction values $\Delta\Omega$ and $\Delta\omega$ for the current and previous iteration are compared. Once their difference is smaller than a given convergence threshold for both, the iteration is stopped.

This method of convergence usually applies if the $\Delta\Omega$-correction does not lead to a direction switch, defined in Section 4.3.2. This is the case when $\Delta\Omega$ is smaller than the separation in geodetic longitudes between the two points for all applied corrections during the iteration. Thus it depends on both the time between the detections and the relative geometry between them. This approach can be used to solve the majority of cases, especially for low inclinations ($i < 60°$).
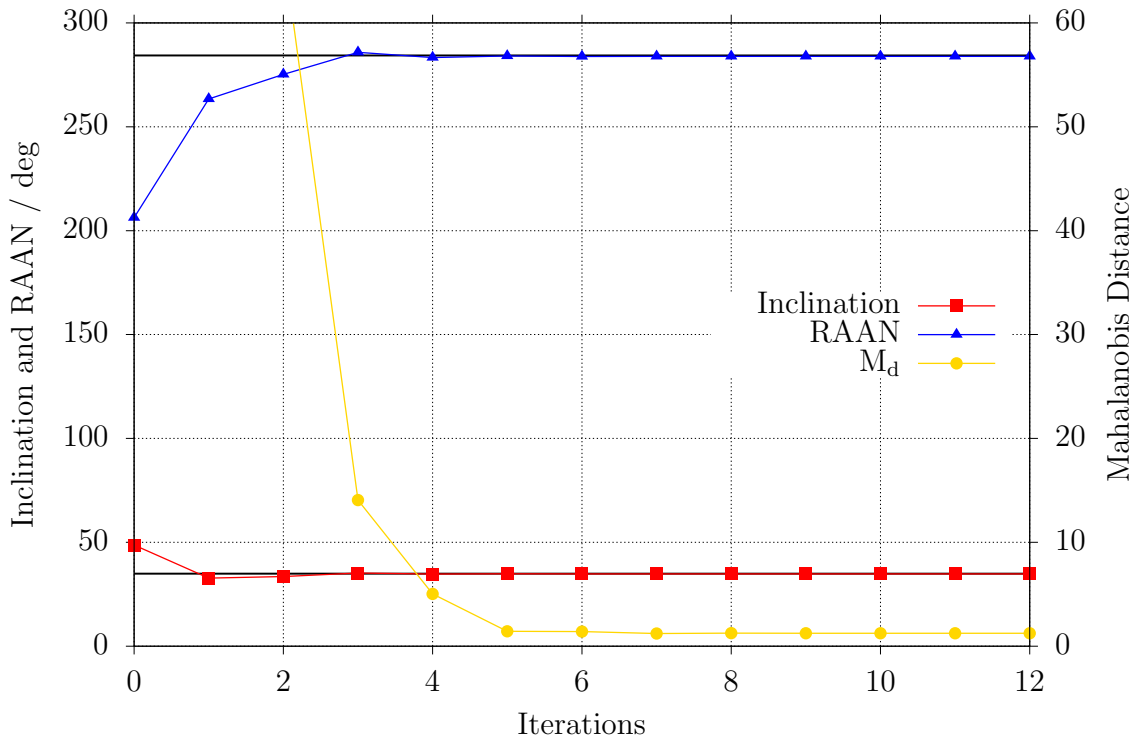
Figure 4.8: Example for the standard convergence of the orbital plane. Ground truth plotted as solid line.

Special Case

For orbits with higher inclinations, especially polar orbits, it happens frequently that the direction of motion between the two points has to be changed during the iterative correction in order to maintain a pro- or retrograde orbit, as it was shown in Figure 4.4. This behaviour can lead to convergence issues and depending on the geometry between the two points this can even happen for low inclinations. Figure 4.9 gives an example of such a failed convergence using the same object as in the previous section at a different reference time with the elements $[a = 6895.7$ km, $e = 0.00158$, $i = 35.0°$, $\Omega = 193.2°]$. The tracklets are separated by nearly six days, equivalent to 88 revolutions. As it can be seen the solution converges on a stable orbital plane but with a very large Mahalanobis distance. In this case, after the switch to the other side, the geometry of the points is such that the larger the rotation $\Delta\Omega$ the smaller the inclination, which increases the next correction as given by Equation 4.15 and thus a positive feedback loop is built until the semi-major axis increases enough to stop the divergence. This is shown in Figure 4.10 with the solution of the standard approach from

Section 4.3.3 at $\Delta\Omega \approx 41°$ close to the maximum semi-major axis and behind the switch to the other side at $\Delta\Omega \approx 35°$. In the following it is explained how to find the other two solutions at $\Delta\Omega \approx 33.5°$ and $\Delta\Omega \approx 36.5°$, of which only the second one is the true solution as can be seen from the values of the ground truth.
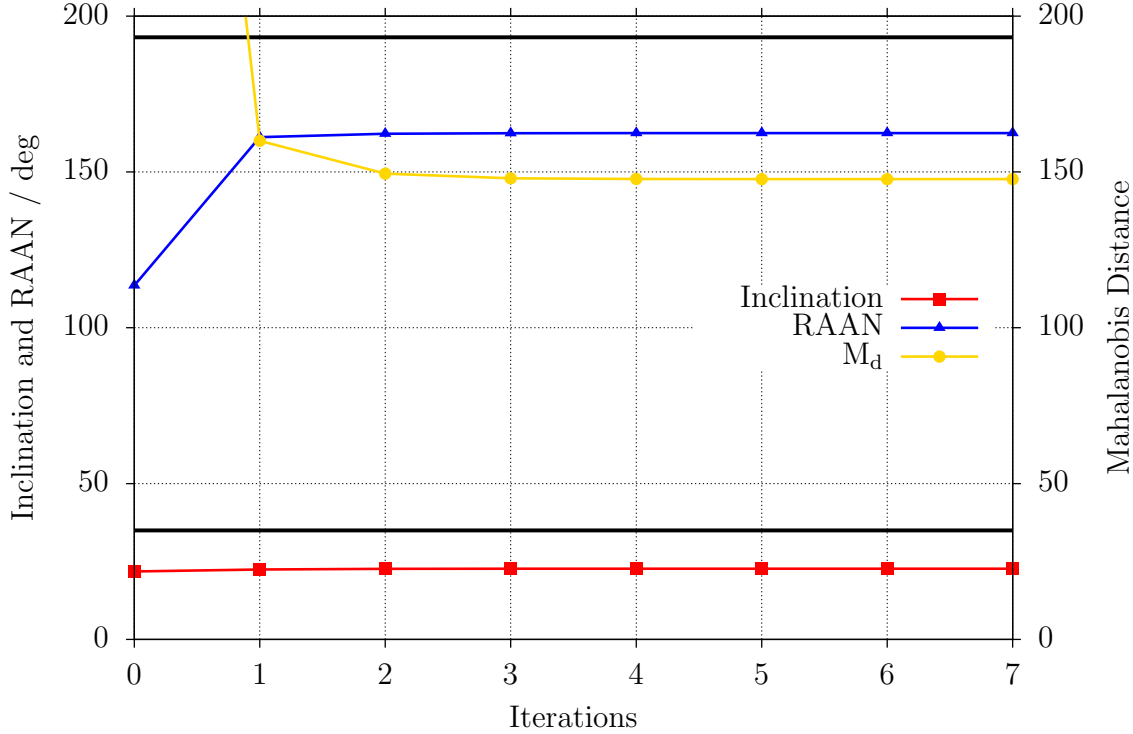
Figure 4.9: Example of a wrong convergence of the orbital plane. Ground truth plotted as solid line.

After identifying this problem, it was decided to test another approach for the convergence by applying a certain correction $\Delta\Omega_C$ to the second measurement point and comparing it to the correction, which results from the obtained orbital elements a_c, e_c and i_c:

$$\Delta C = \Delta\Omega_C - \Delta\Omega\left(a_c, e_c, i_c\right) \tag{4.19}$$

If the applied and resulting corrections are the same, thus $\Delta C = 0$, a possible solution is found. The result of this procedure, applied to the same example as the failed standard convergence shown before, is depicted in Figure 4.11 together with the Mahalanobis distance for the obtained solutions. It can be seen, that there are three possible solutions as already shown in the previous plots. One before the switch and two after it. The standard convergence usually ends up at the far right solution once it switches over. By selecting the smallest Mahalanobis distance of the three possibilities, it is clear that the central solution at $\Delta\Omega \approx 36.5°$ with $M_d \approx 2$ is the correct one compared to $M_d \approx 650$ and $M_d \approx 150$ for the other two possibilities. In this first step only the rotation of the orbital plane is used because this is the dominating perturbation. Once the root is found, also the other corrections can be applied.

The shape of the ΔC function is similar for all examples, except for retrograde orbits, where the function is basically mirrored along the $y = 0$ axis due to the opposite sign of $\Delta\Omega$.
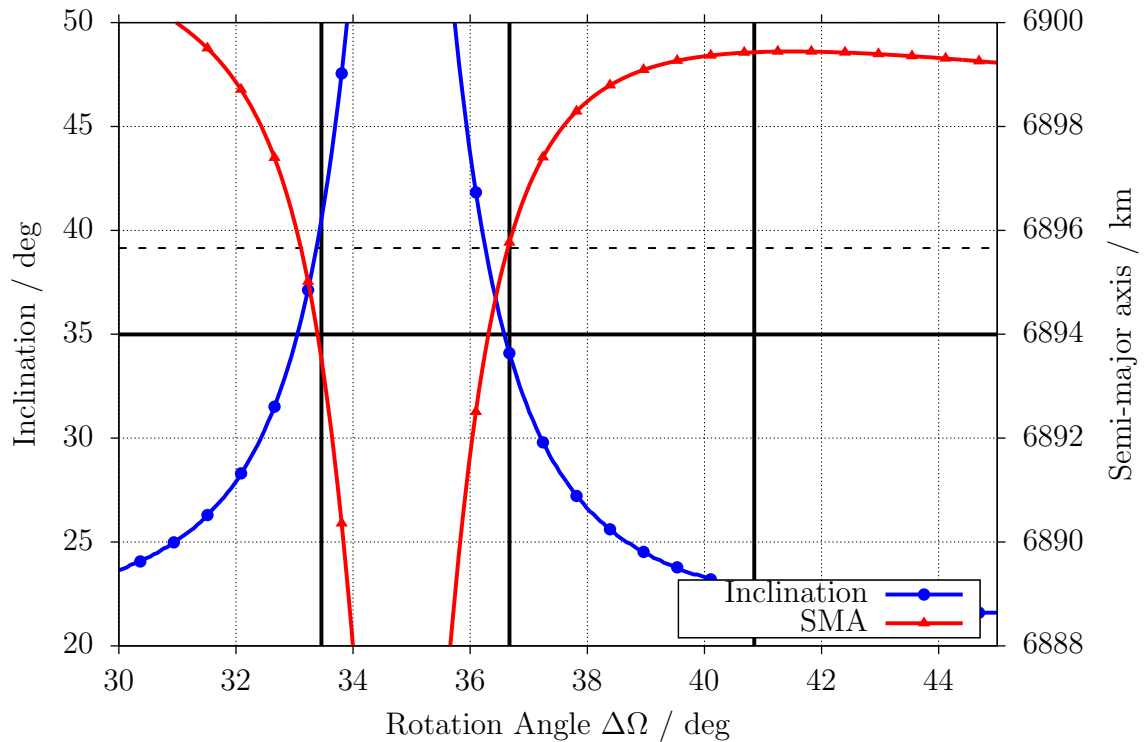
Figure 4.10: Semi-major axis and inclination for a wrong convergence of the orbital plane. Values of the ground truth plotted as solid line for inclination and dashed line for semi-major axis. The vertical lines indicate the three possible solutions with stable orbital planes.
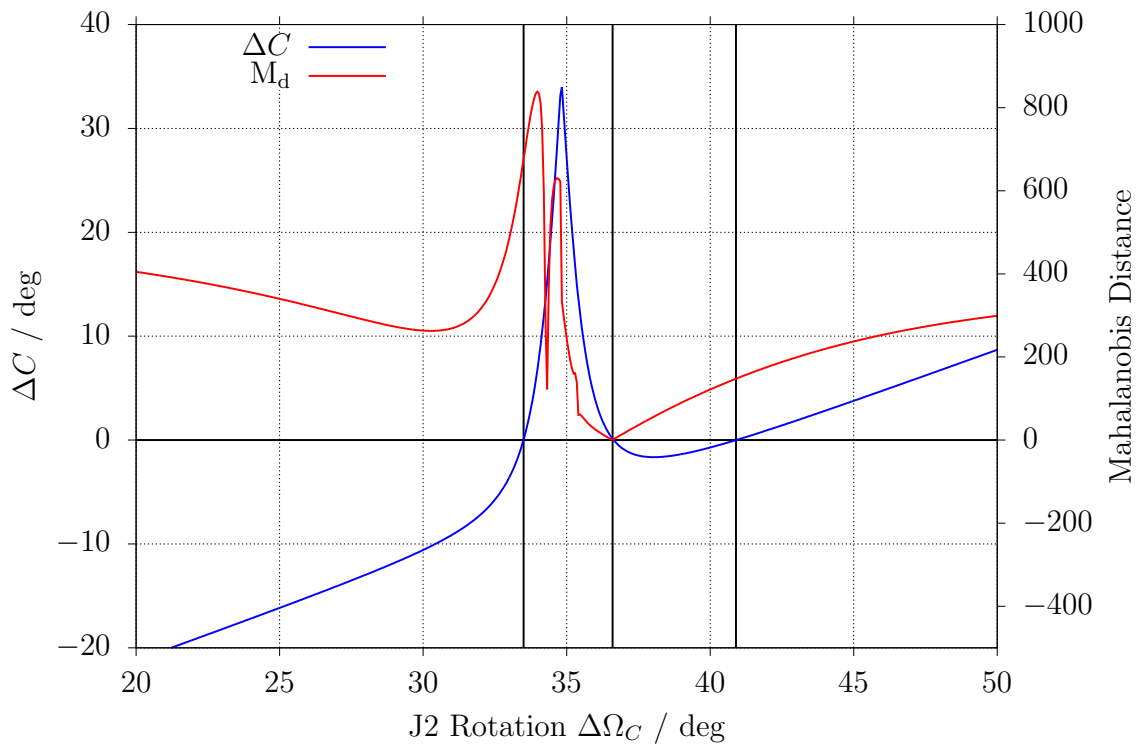
Figure 4.11: Example of the special convergence routine by checking the Mahalanobis distance at all $\Delta C = 0$.

EXPERIMENTS AND VALIDATION

5.1 Simulated Surveillance Radar Campaign

The figures and text in the following subsection have been taken from (Reihs et al., 2021) and have been adjusted for the use in this thesis.

5.1.1 Simulation Parameters

Radar observations of the objects in the LEO population have been simulated with a surveillance radar scanning an area of $60° \times 20°$. The objects are extracted as TLE from Space-Track[1] using the conditions $a < 8400$ km and $e < 0.1$, which results in more than 10 000 objects in total. The TLE are used to get a representative sample of space object orbits, while the actual propagation is performed using numerical propagation with (Orekit, 2018). The dynamics are modelled with a 16x16 geopotential model, atmospheric drag (DTM2000 atmosphere, cannonball model), solar radiation pressure and lunisolar perturbations. The location of the radar is chosen at a low latitude to increase the coverage of orbital inclinations without simulating a specific real station, but this mainly influences the coverage of the observed satellites and should be of minor importance for the correlation. The noise values given in the table increase with an increasing range due to the decrease of the signal-to-noise ratio (Skolnik, 2001). Additionally, the simulations can have four different intervals between the detections within a tracklet, denoted by 1f, 3f, 5f and 8f in the following corresponding

---

[1] `https://www.space-track.org`

to 1 s, 3 s, 5 s, and 8 s between detections respectively. This detection frequency is mostly dependent on the size of the FoR and the scanning strategy. A smaller FoR could be sampled at a higher rate but would produce shorter tracklets. This is a radar design trade-off. The details of the simulated radar are given in Table 5.1.

Table 5.1: Radar sensor characteristics: field of regard and noise.

Radar, Latitude / Longitude	25°N / 10°E
FoR, Azimuth	150° - 210°
FoR, Elevation	50° - 70°
Interval between detections	1 s, 3 s, 5 s, 8 s
Duration	24 hours
Reference range for noise	750 km
Angles, σ	0.17°
Range, σ	20 m
Rate, σ	20 $\frac{m}{s}$

The distribution of the overall dwell times in the FoR, and thus the effective tracklet lengths t_T, are shown in Figure 5.1. It can be seen that the distribution peaks at approx. 50 s which is due to objects in sun-synchronous polar orbits ($a \approx 7200$ km) crossing the FoR in meridional direction. Another smaller peak occurs at approx. 100 s which is caused by objects in higher LEO regions ($a \approx 7800$ km). Depending on the location of the station, it may happen for a south-oriented FoR that an object with an inclination slightly smaller than the station's latitude passes exactly along the east-west direction through the FoR which can lead to a tracklet of several minutes. The following experiments will consider tracklet lengths up to three minutes (180 s) to cover at least a part of these outliers. This was also the basis for the fitting analysis, see Section 2.2, which lead to the definition of the fitting rules based on the tracklet length, see Table 2.1.
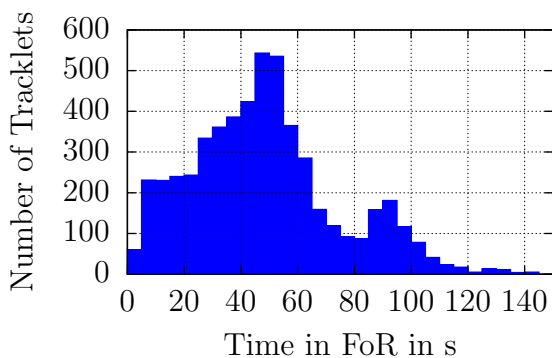
Figure 5.1: Dwell times in the field of regard for the simulated observation campaign.

Considering the results in (Reihs et al., 2021), the geocentric AOS is the most promising coordinate system for the correlation and thus the survey results mainly use these coordinates. As a comparison, the other three coordinate systems are tested with the 3f-data only. The total numbers of pairs and true correlations are given in Table 5.2 for the different detection frequencies. Tracklets which do not have enough data points to fit the polynomial of the required order are removed, e.g. for a linear fit a minimum of three detections. This explains the reduced number of tracklets for longer detection intervals. In order to reduce the

number of false negative correlations, the threshold for the following tests is set to $M_{\mathrm{d}} = 5$. This is also necessary due to the shift of Mahalanobis distances to larger values, which is caused by a specific characteristic of the J_2-perturbed orbit determination. This is discussed in Section 5.1.2. Also the already mentioned bias due to the correlation of the errors before the fit, see Figure 2.20, is introducing an offset for the geocentric AOS.

The correlations are processed with the RPP and a final least squares orbit determination, see Section 3.2.4. The thresholds for the least squares are the mean and standard deviation of the residuals. It is set for the angular observables at $\mu_{T,LS,A} = 0.11°$ (0.17°) and $\sigma_{T,LS,A} = 0.3°$ (0.4°). The values in parentheses are used for the experiments using 5f- and 8f-data to consider the increased uncertainty due to less data in the tracklet. The thresholds for the ranges are set at $\mu_{T,LS,\rho} = 10$ m and $\sigma_{T,LS,\rho} = 40$ m. These values are chosen slightly higher than the known performance of the radar, see Table 5.1, to account for the uncertainty due to the relatively small amount of information from two passes. Only pairs which also pass this final least squares test are accepted.

Table 5.2: Total combinations and true correlations for the geocentric AOS using different detection frequencies.

Scenario	Tracklets	Total Combinations	True Correlations
1f	4 772	11 383 606	717
3f	4 598	10 568 503	683
5f	4 384	9 607 536	636
8f	4 055	8 219 485	568

5.1.2 Results

Overview

The processing of the experiments takes approx. 24 - 27 hours per simulation on a computer with four Intel Core i5-3470 CPU (3.20 GHz) running three processes in parallel. Because parallelisation of the pairwise correlation problem is simple, more parallel processes on a capable computer could be used to reduce the processing time further, which should be of no concern for an operational system. The results of the survey experiments are presented in Figure 5.2. In the plot, true positive (TP) refers to the confirmed correlations after the least squares and false negative (FN) refers to the true correlations, known from the simulations, which were found but did not lead to a converged least squares with sufficiently small residuals. All results show a distinct peak of true positives, which shifts towards lower Mahalanobis distances with an increasing observation interval. This will be explained in the following subsection. All experiments have a share of false positives and non-converged least squares, which increases with more time between the detections.

Table 5.3 summarises all results for the different experiments. Two main effects are visible. The first is, that the share of detected true positives increases with the detection interval, because the tail of the distribution which is cut at the threshold becomes less due to the mentioned shift of the Mahalanobis distances. For the 1f-data, an increase in the M_{d}-threshold would also lead to more TP, but at a higher computational cost because more FP

would require a further test with the least squares orbit determination. Opposed to that, the share of converged least squares orbit determinations decreases with an increased detection interval, because less data is available in the tracklets. To counteract this, the acceptance threshold of the least squares has been increased for the 5f- and 8f-data, which also leads to a significant increase in false positives. Without the increased threshold, the FP-level for the 8f-data would also be around 2 % but with only 50 % converged TP.

(a) 1f-data

(b) 3f-data

(c) 5f-data

(d) 8f-data
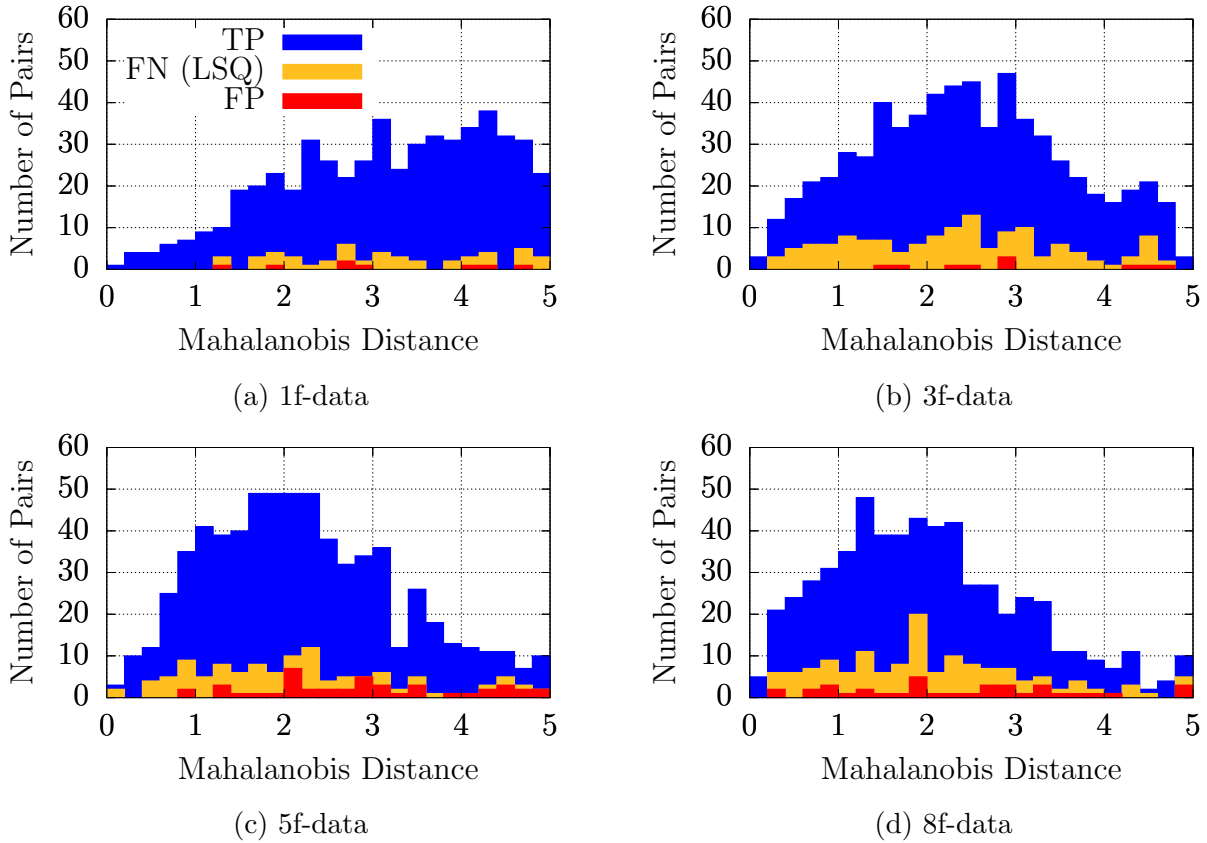
Figure 5.2: Histograms of correlation results for the surveys with different detection intervals.

As a comparison, Table 5.3 also shows the results for the other three coordinate systems using the 3f-data. Compared to the geocentric AOS, it is visible that the percentage of true positives is larger for the other systems, especially directly after the attributable correlation. This suggests that the shift in the Mahalanobis distances is only partially due to the bias explained in the next section, but also caused by the missing consideration of the error correlation as shown in Section 2.2. Increasing the correlation threshold to $M_d = 7.5$ would let the geocentric AOS also reach the 99.8% of true positive correlations like the other systems at a false positive rate of still only approx. 95 % before the least squares. The number of false negative correlations due to a non-converging least squares is similar for all coordinate systems. Thus the main difference between the coordinate systems is the efficiency with regard to the minimisation of false positives to reduce the computational effort, but the resulting number of confirmed correlations is similar for all the systems. This may also be

due to the definition of the FoR which has a maximum elevation of 70°. If a radar's FoR includes $el = 90°$, thus the singularity in the azimuth-elevation system, tracklets passing close to this singularity might lead to more differences between the results of different coordinate systems.

Table 5.3: Results of the correlation of survey campaigns. (*) indicates a higher acceptance threshold for the least squares, see text.

Coordinates	Freq.	After Attr.		After LSQ	
		TP	FP	TP	FP
geo. AOS	1f	73.9 %	81.4 %	67.8 %	1.6 %
geo. AOS	3f	95.5 %	90.6 %	76.7 %	1.9 %
geo. AOS	5f	97.0 %	93.8 %	85.2 % (*)	7.2 % (*)
geo. AOS	8f	96.0 %	96.1 %	76.9 % (*)	7.6 % (*)
top. AOS	3f	99.8 %	97.9 %	80.2 %	1.7 %
AzEl	3f	99.8 %	98.0 %	79.2 %	1.8 %
XYZ	3f	99.7 %	97.8 %	81.3 %	1.8 %

Estimation Bias

In the results shown, the distribution of the Mahalanobis distances appeared to be shifted compared to the expected distribution which is a χ-distribution with two degrees of freedom due to the two-dimensional discriminator vector under the assumption that the values of the discriminators are normally distributed. In case of this south-staring survey campaign, the normality of the discriminators breaks down because of the measurement geometry and short-periodic perturbations. Especially objects on polar orbits are detected once on their ascending and once on their descending arc within 24 hours, thus they do not exhibit an approximately integer multiple of revolutions between detections. The applied J_2-correction of the mean motion does only correct the perturbed motion for a full revolution, thus non-complete revolutions are estimated with a bias in the semi-major axis. This effect can be seen in Figure 5.3, which relates the biases in the semi-major axis to the RAAN for polar orbits. For one day of measurements from a single station, the RAAN is related to the direction of motion (ascending or descending arc at first detection), which can be seen via the range-rate $\dot{\rho}_1$ at the first pass. For a south-staring FoR, a negative range-rate (approaching) is caused by an object on the ascending part of a polar orbit. This is discussed further in Section 5.2.

Combining this bias, which influences especially the velocity, with the measurement geometry of observing either near-maximum positive or negative range-rates on the descending or ascending arc, respectively, leads to an offset of the discriminator values to opposite, positive and negative, directions. Thus, there is no normal distribution any more and the errors are larger than expected from the measurement statistics. If the discriminator $\Delta\dot{\rho}$ is split into one part for the measurement uncertainty $\Delta\dot{\rho}_M$ and one part due to the bias of the semi-major axis $\Delta\dot{\rho}_a$, the Mahalanobis distances become shifted towards larger values because the estimated uncertainty C_M only refers to the measurement:

$$\begin{aligned} M_d^2 &= (\Delta\dot{\rho}_M + \Delta\dot{\rho}_a)^T \cdot C_M^{-1} \cdot (\Delta\dot{\rho}_M + \Delta\dot{\rho}_a) && (5.1) \\ &= \Delta\dot{\rho}_M^T \cdot C_M^{-1} \cdot \Delta\dot{\rho}_M + 2 \cdot \Delta\dot{\rho}_a^T \cdot C_M^{-1} \cdot \Delta\dot{\rho}_M + \Delta\dot{\rho}_a^T \cdot C_M^{-1} \cdot \Delta\dot{\rho}_a \ . && (5.2) \end{aligned}$$
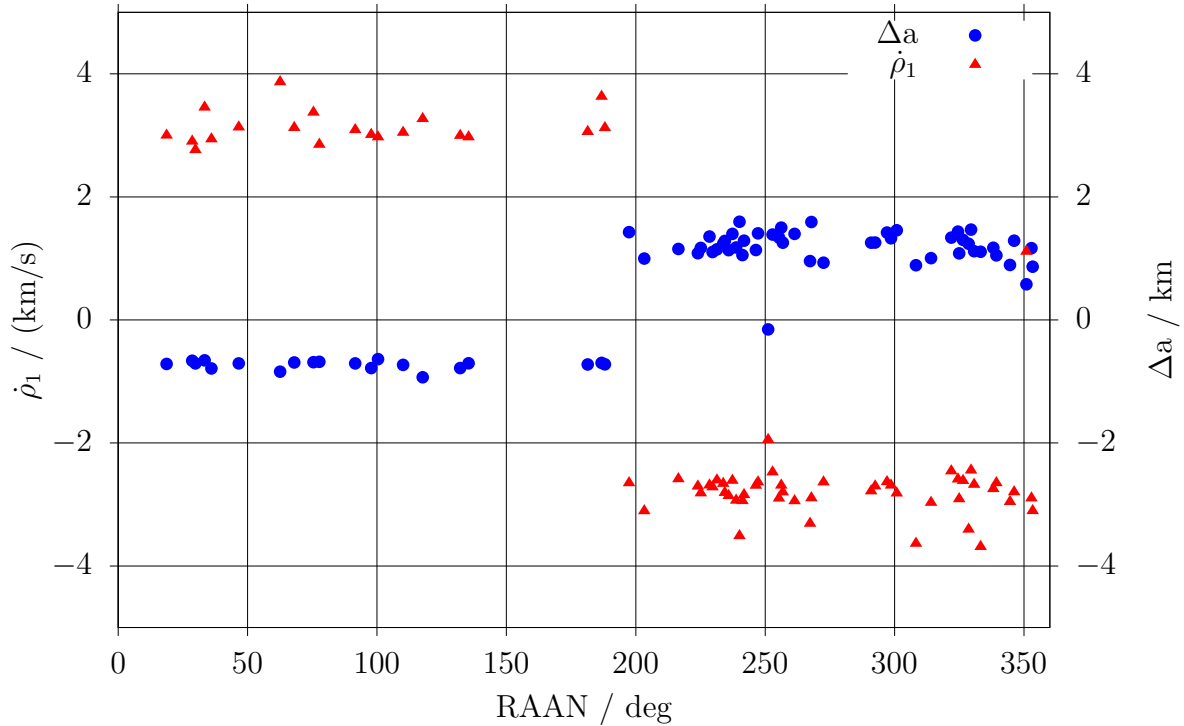
Figure 5.3: Distribution of discriminators $\dot{\rho}_1$ and Δa for the 3f-survey over the RAAN using objects on polar orbits.

In Equation 5.2, only the first term is χ^2-distributed, while the remaining terms including $\Delta\dot{\rho}_a$ are introducing the observed bias, which is independent of the measurement uncertainty. The larger the uncertainty in C_M, the smaller the effect of the bias terms because $\Delta\dot{\rho}_a$ is independent of the measurement noise. Because of that, the distribution shifts closer to expected values for the experiments with larger detection intervals, which have higher absolute uncertainties.

5.2 Real Radar Observations

After the experiments with simulated data showed promising results, this section uses real radar data. The data is provided by the commercial operator LeoLabs, Inc [2] and is introduced in more detail in the following. The results have been presented in (Reihs et al., 2020c) and parts of this publication are used in the following section.

5.2.1 Data Set

LeoLabs, Inc. currently operates three radars: the Poker Flat Incoherent Scatter Radar (PFISR) in Alaska (US), the Midland Space Radar (MSR) in Texas (US) and, the most recent addition, the Kiwi Space Radar (KSR) in New Zealand. The data set used for this work contains radar data from the PFISR and the MSR in the time period from 27 March 2019 to 22 April 2019. The detected objects are mainly in LEO. In total there are more

[2]https://www.leolabs.space

than 10 000 different objects in the data set. The number of passes is 301 287 in total, 232 111 for PFISR and 69 176 for MSR. The two radars have different numbers of passes due to their different sensitivity and design. MSR is a one-dimensional phased array radar with a fence-like FoR along one direction. This also leads to much shorter passes compared to PFISR. PFISR is a two-dimensional phased array radar with a star-shaped FoR and thus can cover a larger part of an object's pass above the horizon. For more information on the radars, see e.g. (Nicolls et al., 2017; Griffith et al., 2019). The radar data also contains an association of the detections to the object IDs, which makes it possible to check the identified correlations for their correctness by assuming these given object-tracklet associations as the ground truth.

The data consists of scheduled tracking arcs which for PIFSR may include several short measurement bursts separated by possibly tens of seconds long gaps during the pass. This leads to a distribution of measurement points as sketched in Figure 5.4 which is much different than that of a survey radar like the one considered in Section 5.1. Because the data is mainly intended for the update of already catalogued objects, the radar data focuses on the range and range-rate information, which are the two precisely measurable observables for a radar. However, as explained in the Section 4.3, the IOD requires positions and thus also the angular information is required. The data itself contains only the pointing direction of the radar beam without any further quantification of the uncertainty or beamwidth, which makes the derivation of the attributables more challenging.

The attributables are fitted according to Section 2.2 but the angular observables, i.e. azimuth and elevation, need special treatment. Artificial Gaussian white noise is added to the angular measurements to consider the uncertainties for the least squares fit through the observations. For PFISR, there may be large gaps without a measurement during one pass as explained earlier. To avoid problems with the fit due to these gaps, the measurements from a single pass are split if there is a gap of more than 15 seconds. After this split, only the subset of the measurements with most detections is used for the attributable fitting. This reduces the length of the fitted arc significantly compared to the arc length measured from first to last detection of the entire pass, but it is necessary in order to improve the fitting. The attributable is fitted and defined in the geocentric AOS.

However, this approach also makes it more difficult to estimate the uncertainties from the fit. Instead, the errors are estimated from fixed error assumptions for the observables and then transformed into the inertial frame of the positions used in the IOD. Additionally, it has to be considered that real measurement data contains outliers and mis-tagged observations, which makes it also necessary to detect fitted attributables with bad data points in order to remove them.

After the fitting, there are 207 377 attributables for PFISR and 59 924 for MSR. Those contain in total more than 3.5 million true correlations between them, which shows that the data set is well suited for the following association experiments.

For the following experiments, the RPP as described in Section 3.2.4 is only used for the PFISR data because the MSR's fence-like field of regard makes it difficult to estimate a trend in the angular motion from the pass. In case of PFISR, the entire tracklet is used for the RPP, which also includes parts that may have been ignored for the attributable fit due to gaps between the detections. Also, only full passes with a length of at least four seconds are considered for the RPP, otherwise there is not enough information in the pass to make a decision.
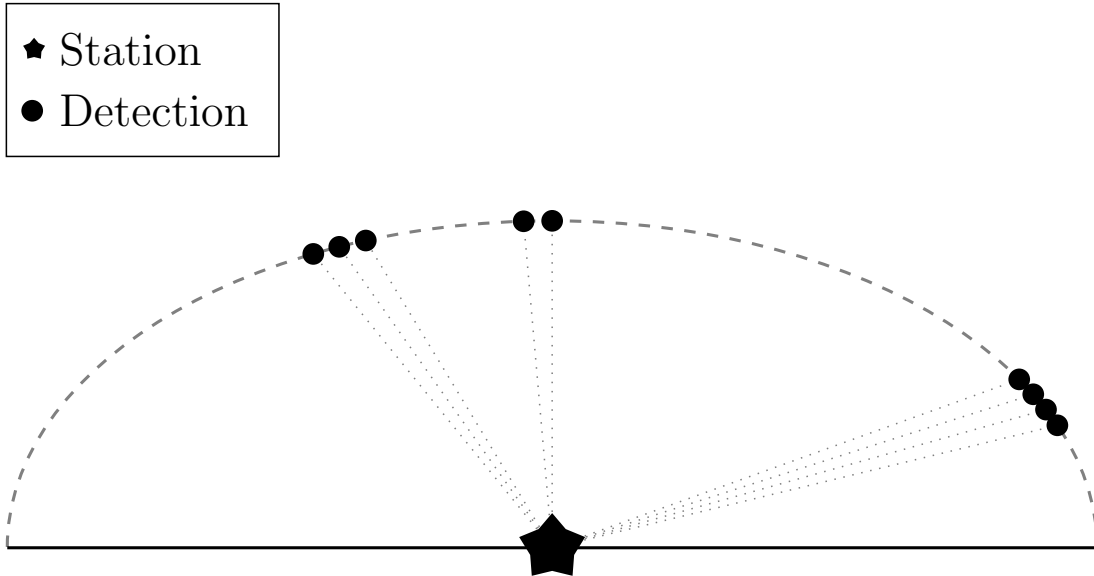
Figure 5.4: Example of distributed detections taken by PFISR over one pass.

In the following, there are further subgroups of the data set based on the orbital regime. The category *low LEO* refers to the semi-major axis $a \leq 6878$ km, *medium LEO* to 6878 km $\leq a \leq 7278$ km and *high LEO* to 7278 km $\leq a \leq 7578$ km. For all LEO objects there is the condition for the eccentricity $e \leq 0.1$.

5.2.2 True Positive Correlation Results

As a first proof-of-concept and to further investigate the attributable-based correlation, the initial experiments in this section test only known true positive correlations, i.e. between tracklets which are known to originate from the same object. This is done in order to quantify the association performance for different scenarios and confirm that the association is possible with the present data set.

Initial Orbit Determination

As explained in Section 4.3, selecting the correct number of revolutions between the two passes is a crucial step in the initial orbit determination and correlation. In order to test the robustness of the perturbed initial orbit determination, some experiments have been performed in which the known true number of revolutions has been used to get only the correct solution. This IOD mode is used to test if it is possible to derive the correct orbit with the developed method, which is a prerequisite for performing the data association and it also gives the maximum achievable correlation performance with this method.

This IOD mode has been performed for the three LEO regimes using tracklets measured with PFISR. Figure 5.5 shows the resulting percentage of false negatives, i.e. failed initial orbit determinations, over the number of revolutions between the respective tracklets for the medium LEO case, which is representative of all three LEO regimes. The total percentage of FN is 3.11%, without a visible trend for an increasing number of revolutions. The periodic peaks are mainly due to the observation geometry, because if two tracklets are separated by a multiple of a sidereal day and measured at the same station again, the two detections are

very close to each other, if they are projected on the orbit. In combination with the nodal precession of the orbital plane, the two measurements are in an inertial frame at similar latitudes but with a shift in longitude which makes it more difficult to find a first orbit to start the J_2-correction.

The closer the two measurements are to each other in inertial space, also after the J_2-rotation, the larger is the influence of errors in the attributable's position, especially for estimating the orbital plane. This also leads to the second restriction of the performance, which are bad attributable fits. As explained in Section 5.2.1, the obvious errors have been filtered but there are still some attributables left in the data set which have an error from the truth that is larger than the assumed uncertainty. However, Figure 5.5 shows that it is possible to have successful IODs for up to 350 revolutions between the detections, which is equivalent to around 24 days for this orbital regime.
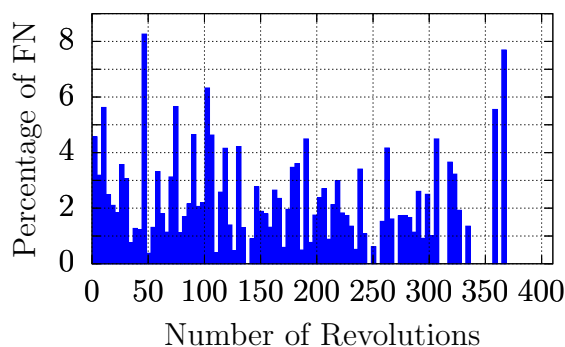
Figure 5.5: Percentage of false negatives for the initial orbit determination from PFISR measurements.

Correlation Results

The following experiments in this subsection test all true correlations for a given subset of the data, which includes both the association test as well as the selection of the number of revolutions from the acceptable solutions. As explained in Section 5.2.1, the RPP is only applied for PFISR, while for the MSR the lowest Mahalanobis distance is always chosen as a solution. For a better presentation of the results, there is a further separation of the correlations into those which have less than three days, less than 100 revolutions and more than three days between the paired tracklets. The cases with less than three days are probably most interesting for the creation of a new catalogue object, whereas the correlations over longer time spans are mainly a test of the method's robustness. Because the computational demand of the correlation increases with the time between the tracklets due to an increased number of possible orbits between them, the tests for less than three days use 10 000 tracklets and those for more than three days use 2 000 tracklets. As a correlation threshold, $M_d < 10$ is used to maximise the identifications.

<u>PFISR</u>

The results of the experiments are given in Figures 5.6-5.8 for the medium LEO case as an example, the other two cases have similar results and are discussed later. Considering the false negatives on the right hand side of the plots, the pattern of the peaks due to observations which are multiples of one day apart was already shown and explained previously. The

increased number of FN compared to the IOD mode are mainly due to the rejection of the correct solution in the RPP or the failure of an additional check regarding the range-rate differences. As explained in Section 4.3, the differences in range-rate are scaled by their uncertainty to calculate the Mahalanobis distance. Here, another filter has been added which rejects all correlations where the sum of the absolute values of the two range-rate differences is larger than 150 m/s. This is done in order to reject correlations with very large covariances due to their observation geometry. If the covariance reaches a size where a difference of more than 150 m/s is still scaled to $M_d < 10$, nearly anything could be correlated from this pair and to avoid false positives these associations are also rejected.

Considering the percentage of solutions with a wrong orbit, a steady increase with the number of revolutions reaching up to 35% at 100 revolution is observed which finally converges at a maximum of approximately 70%. Focusing on the correlations within 1-2 days, there are usually 5% to 10% of solutions with a wrong orbit (TPWO), i.e. the incorrect number of revolutions. It should also be considered that the selection of a wrong orbit does not mean that the correct orbit has not been found but just that it was not the selected solution, which will be discussed in Section 5.2.3. Over longer times, there seems to be a pattern in the peaks of the TPWO, but this will be discussed in the following using the MSR data.

Comparing the medium LEO case to the low LEO in Figures 5.9-5.11 and to the high LEO case in Figures 5.12-5.14, one can see that the differences are minimal. The main difference is that there are less false negatives for the high LEO, which may be explained by both, the missing effect of drag and the higher orbits, which gives a larger margin of error to define an orbit without intersecting the Earth surface if the eccentricity is estimated wrongly.

(a) Wrong Orbit

(b) False Negative
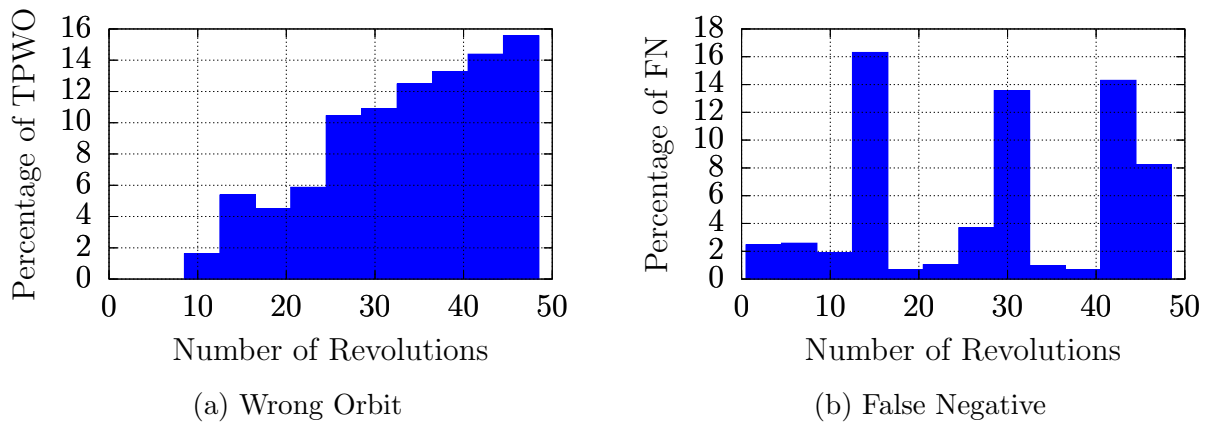
Figure 5.6: Correlation results using PFISR data (medium LEO) for less than three days between the detections.

(a) Wrong Orbit

(b) False Negative
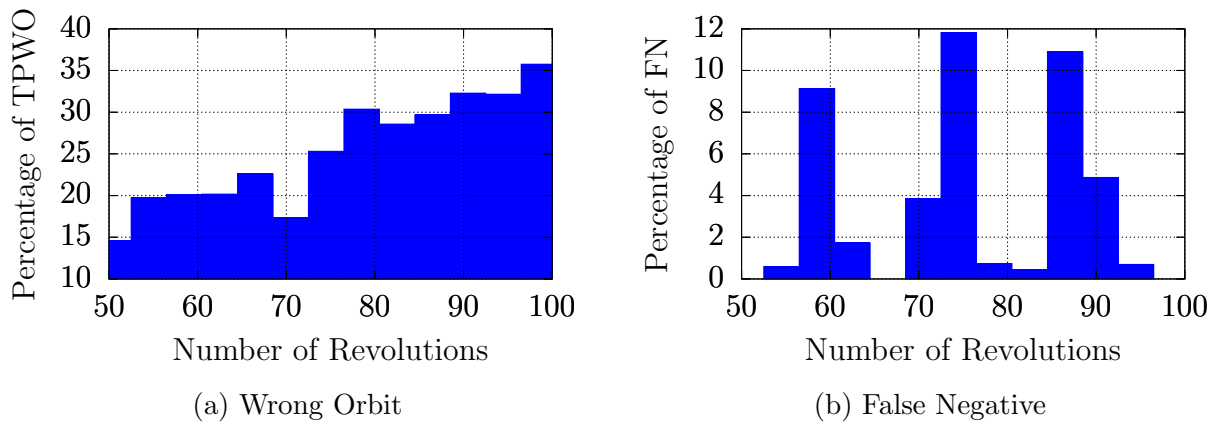
Figure 5.7: Correlation results using PFISR data (medium LEO) for up to 100 revolutions between the detections.

(a) Wrong Orbit

(b) False Negative
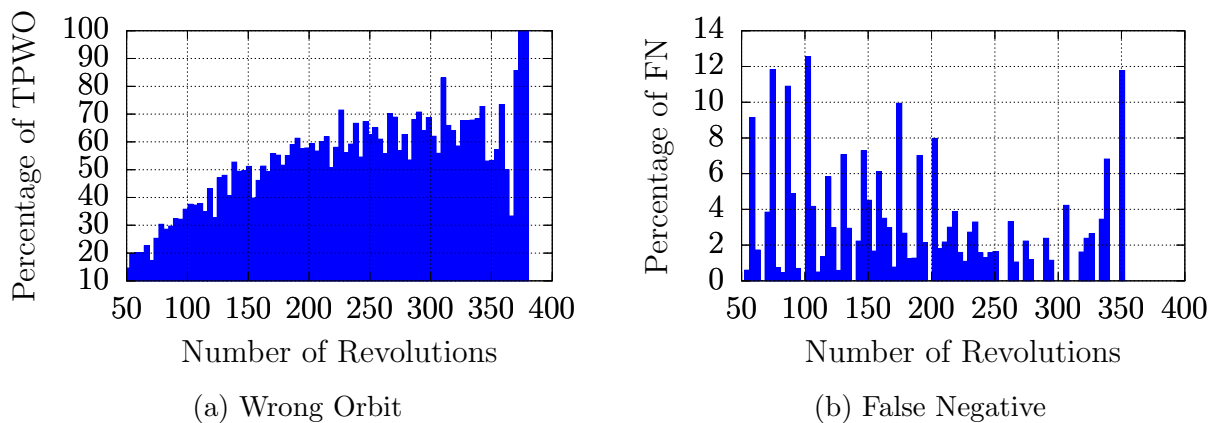
Figure 5.8: Correlation results using PFISR data (medium LEO) for more than three days between the detections.

(a) Wrong Orbit

(b) False Negative
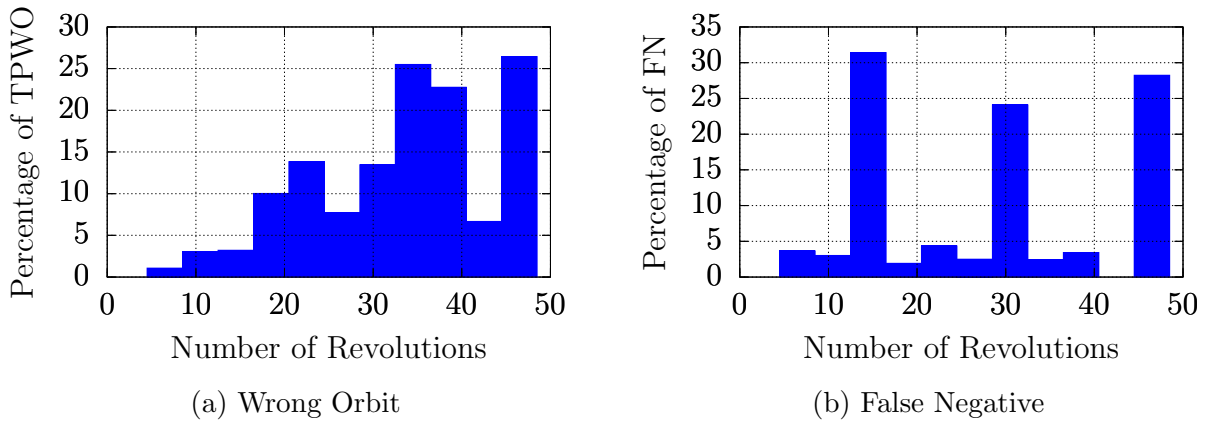
Figure 5.9: Correlation results using PFISR data (low LEO) for less than three days between the detections.

(a) Wrong Orbit

(b) False Negative
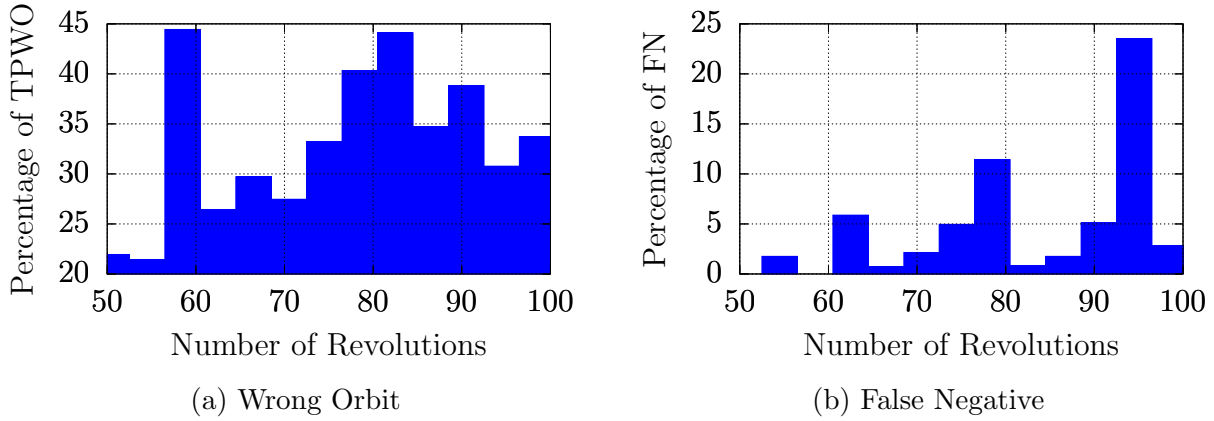
Figure 5.10: Correlation results using PFISR data (low LEO) for up to 100 revolutions between the detections.

(a) Wrong Orbit

(b) False Negative
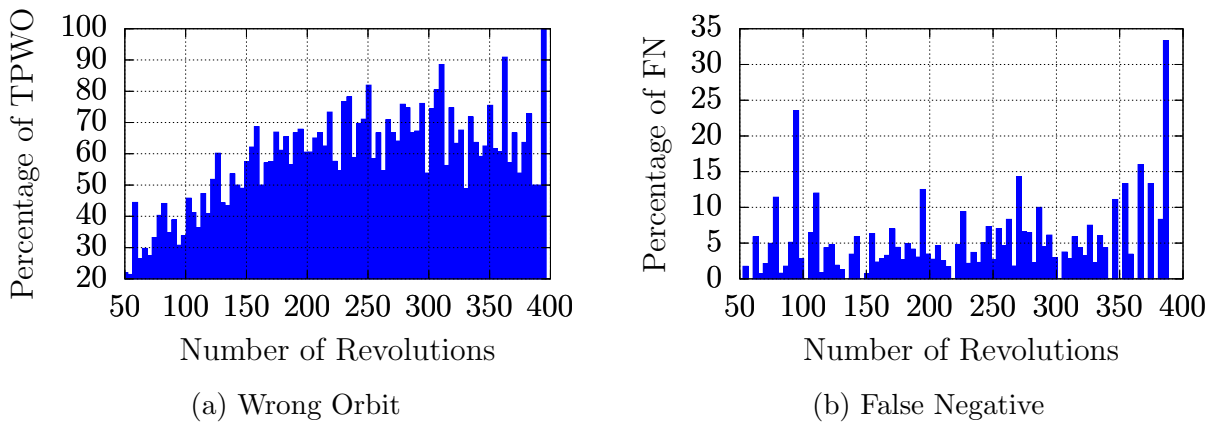
Figure 5.11: Correlation results using PFISR data (low LEO) for more than three days between the detections.

(a) Wrong Orbit

(b) False Negative
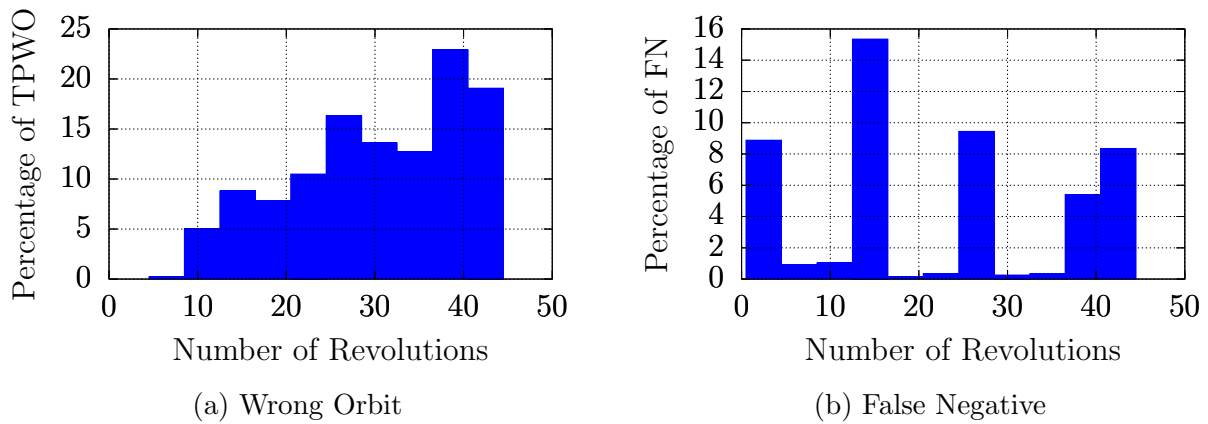
Figure 5.12: Correlation results using PFISR data (high LEO) for less than three days between the detections.

(a) Wrong Orbit

(b) False Negative
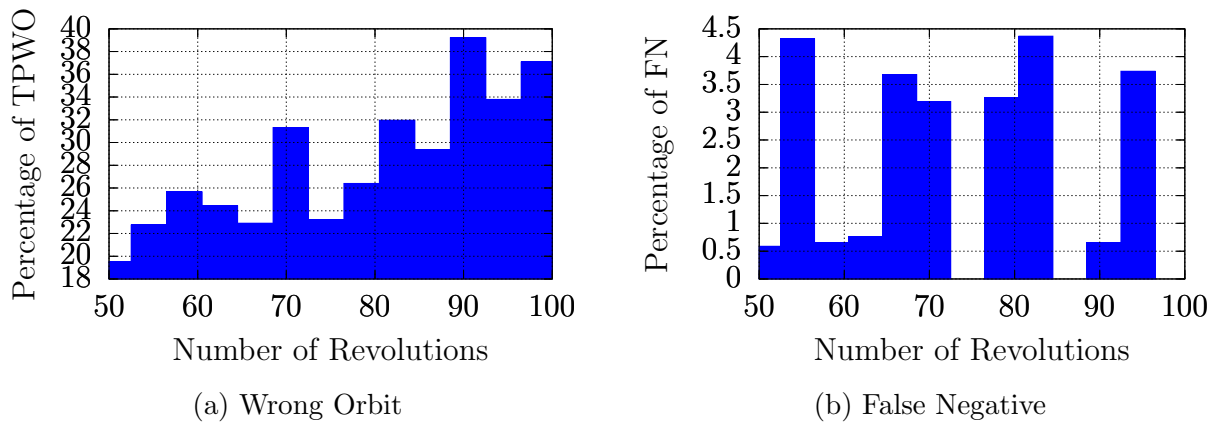
Figure 5.13: Correlation results using PFISR data (high LEO) for up to 100 revolutions between the detections.

(a) Wrong Orbit
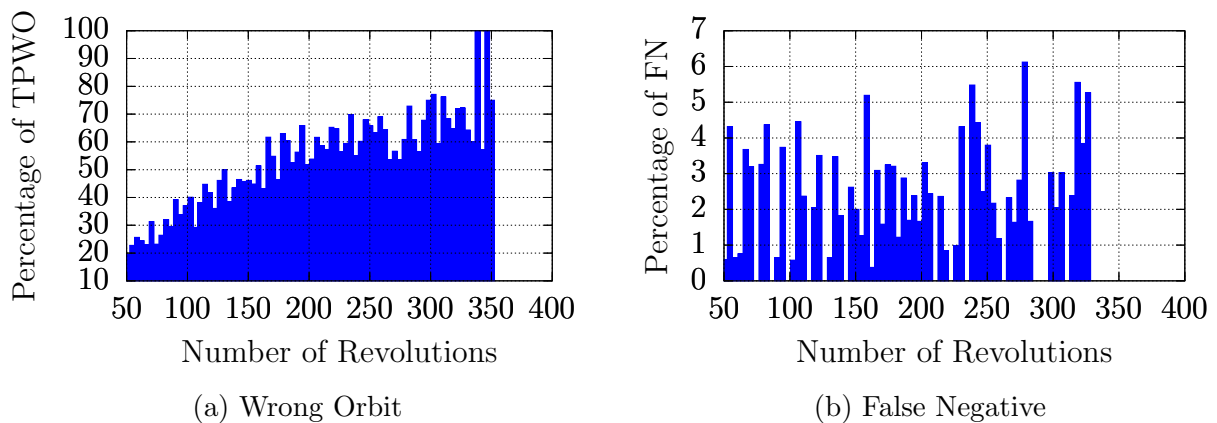
(b) False Negative

Figure 5.14: Correlation results using PFISR data (high LEO) for more than three days between the detections.

MSR

The experiments are again shown for the medium LEO as a representative example in Figures 5.15-5.17. The percentage of false negatives is slightly higher than those for the PFISR. Concerning the solutions with a wrong orbit, the dependency on the time between the detections is much stronger than for PFISR because MSR is at a lower latitude. Thus if an object is detected on different segments of its orbit, those detections can be further apart than for the PFISR station which always samples the orbit at northern polar latitudes. The larger spatial separation between the two detections improves the estimation of the orbit and reduces the sensitivity to uncertainties in the measurements. It also helps to select the correct solution concerning the number of revolutions because the range-rates at the two epochs are more representative of the entire orbit. The value of the TPWO for MSR is approximately 80% at the peaks and thus slightly higher than the one for PFISR but between the peaks it reaches much lower levels. It should also be remembered that there is no RPP for the MSR to select the correct number of revolutions. Also here the difference to the low LEO, see Figures 5.18-5.20, and the high LEO, see Figures 5.21-5.23, are small.

(a) Wrong Orbit

(b) False Negative
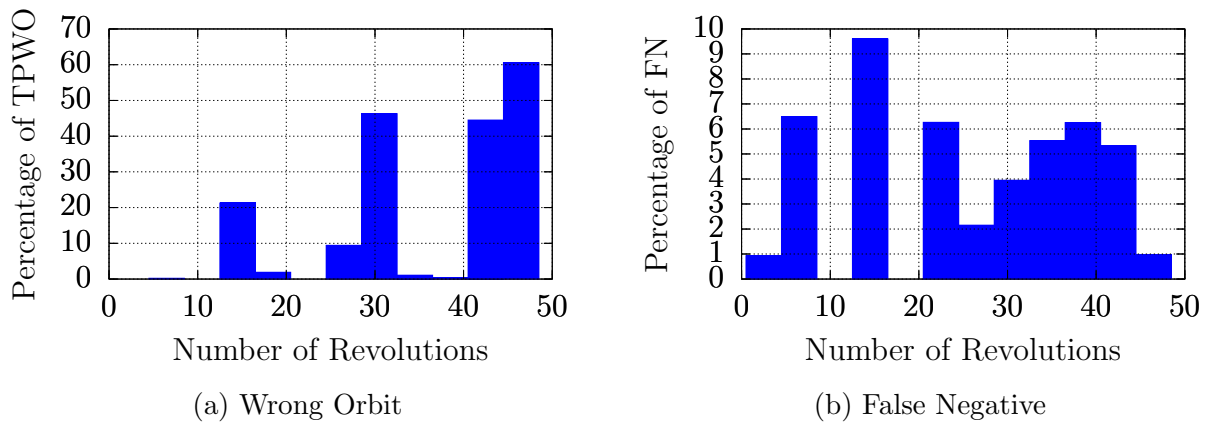
Figure 5.15: Correlation results using MSR data (medium LEO) for less than three days between the detections.

(a) Wrong Orbit

(b) False Negative
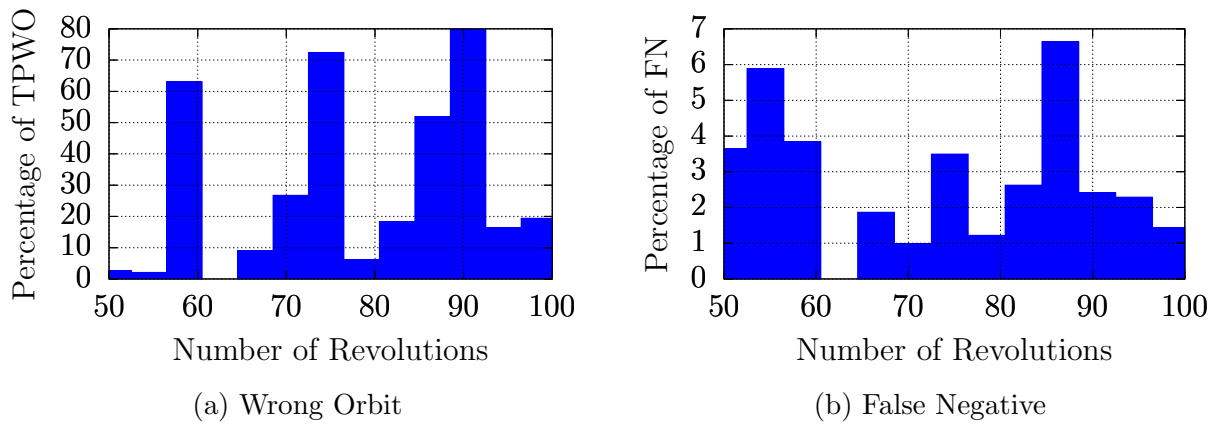
Figure 5.16: Correlation results using MSR data (medium LEO) for up to 100 revolutions between the detections.

(a) Wrong Orbit

(b) False Negative
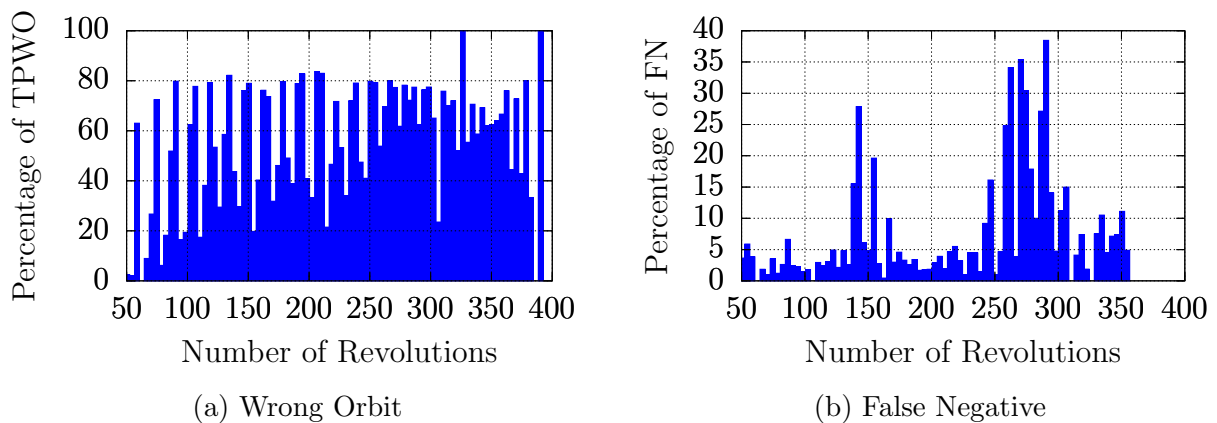
Figure 5.17: Correlation results using MSR data (medium LEO) for more than three days between the detections.

(a) Wrong Orbit

(b) False Negative
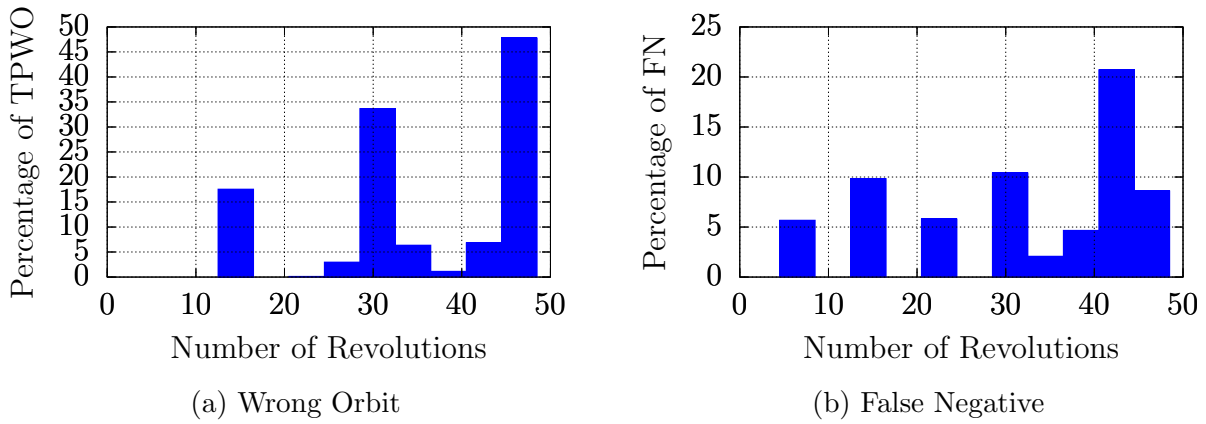
Figure 5.18: Correlation results using MSR data (low LEO) for less than three days between the detections.

(a) Wrong Orbit

(b) False Negative
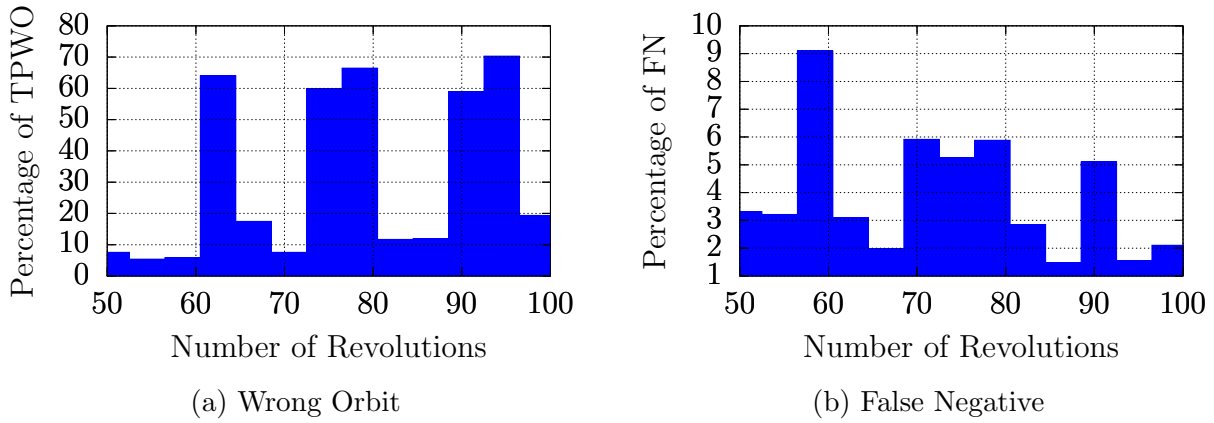
Figure 5.19: Correlation results using MSR data (low LEO) for up to 100 revolutions between the detections.

(a) Wrong Orbit

(b) False Negative
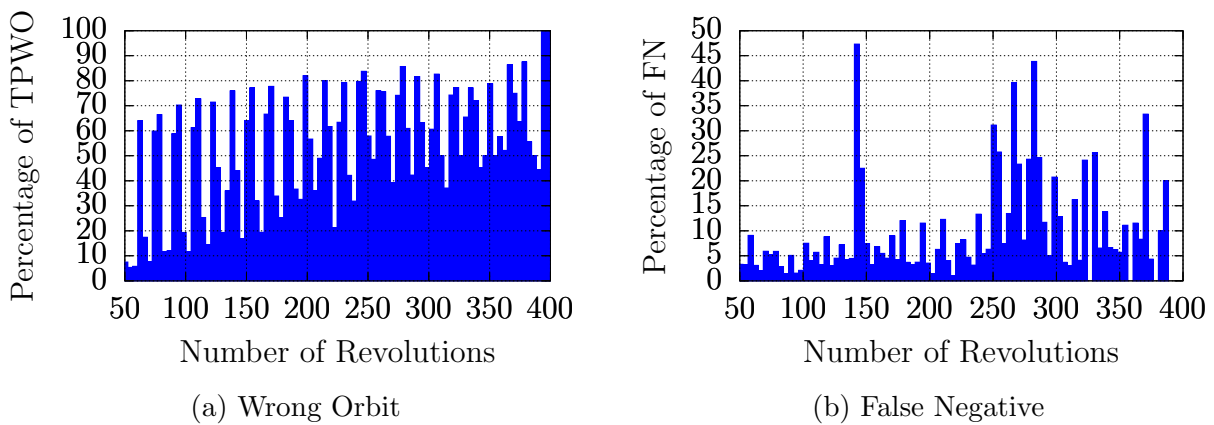
Figure 5.20: Correlation results using MSR data (low LEO) for more than three days between the detections.

(a) Wrong Orbit

(b) False Negative
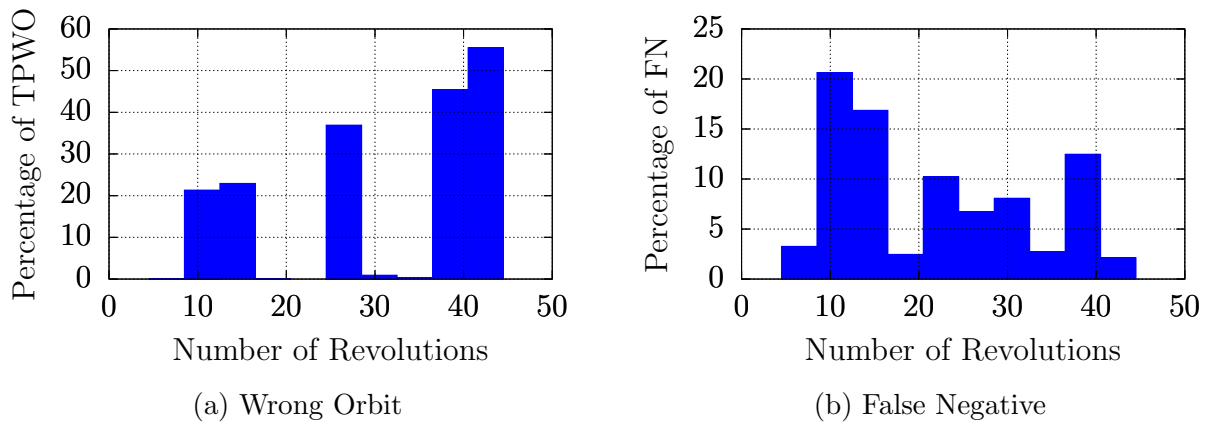
Figure 5.21: Correlation results using MSR data (high LEO) for less than three days between the detections.

(a) Wrong Orbit

(b) False Negative
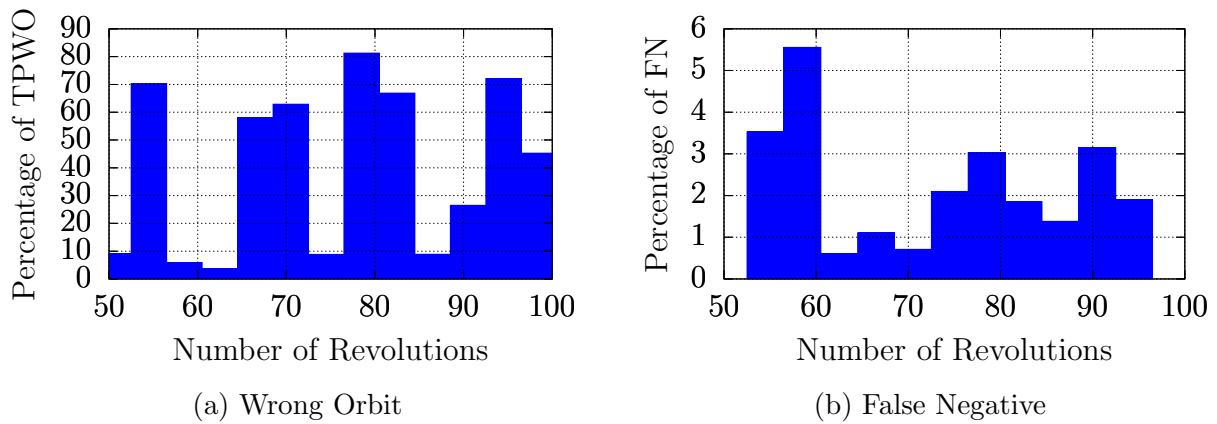
Figure 5.22: Correlation results using MSR data (high LEO) for up to 100 revolutions between the detections.

(a) Wrong Orbit

(b) False Negative
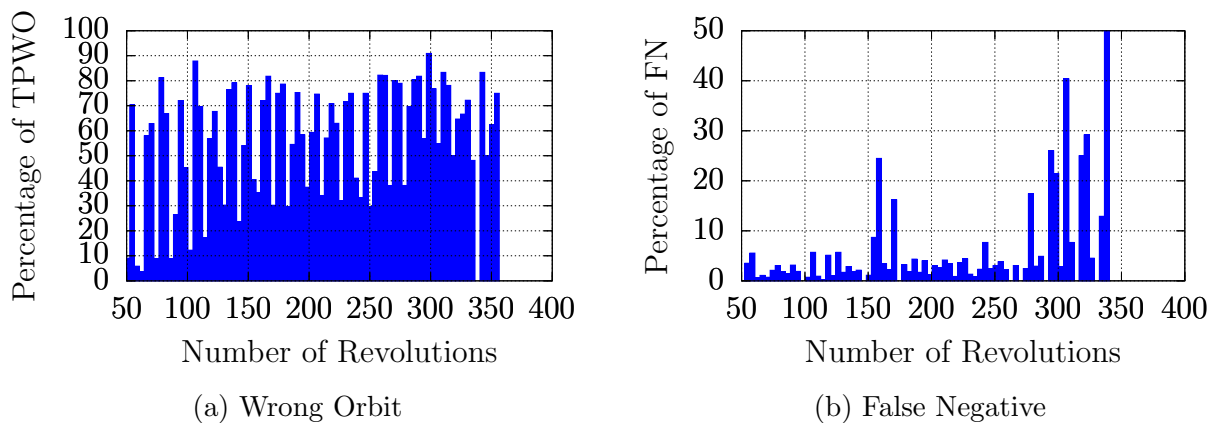
Figure 5.23: Correlation results using MSR data (high LEO) for more than three days between the detections.

M$_d$-Distribution

As mentioned in Section 4.3, the calculated Mahalanobis distances for the correlations should theoretically follow a χ-distribution with two degrees of freedom, here named $\chi(2)$. Figure 5.24 shows the relative frequency of the true positive correlations' Mahalanobis distances compared to the theoretical $\chi(2)$-distribution using the medium LEO MSR data from the previous section. It is clearly visible that the resulting distribution does not match the expected one. As discussed in Section 5.1.2, the J$_2$-perturbed propagation for the initial orbit determination is only bias-free for a complete revolution, otherwise the short-periodic perturbations lead to discrepancies between the estimated mean motion and the perturbed motion. To confirm this assumption, Figure 5.25 includes only correlations which are less than one day apart for objects on polar orbits ($80° < i < 100°$) and splits them into those with and without complete revolutions. It is visible that the one with the complete revolutions matches the theoretical distribution sufficiently considering the artificial estimation of the uncertainty, see Section 5.2.1. Additionally, the $\chi(2)$-distribution requires normally distributed errors which can probably not be guaranteed with real measurement data and the further non-linearities in the orbit determination process.
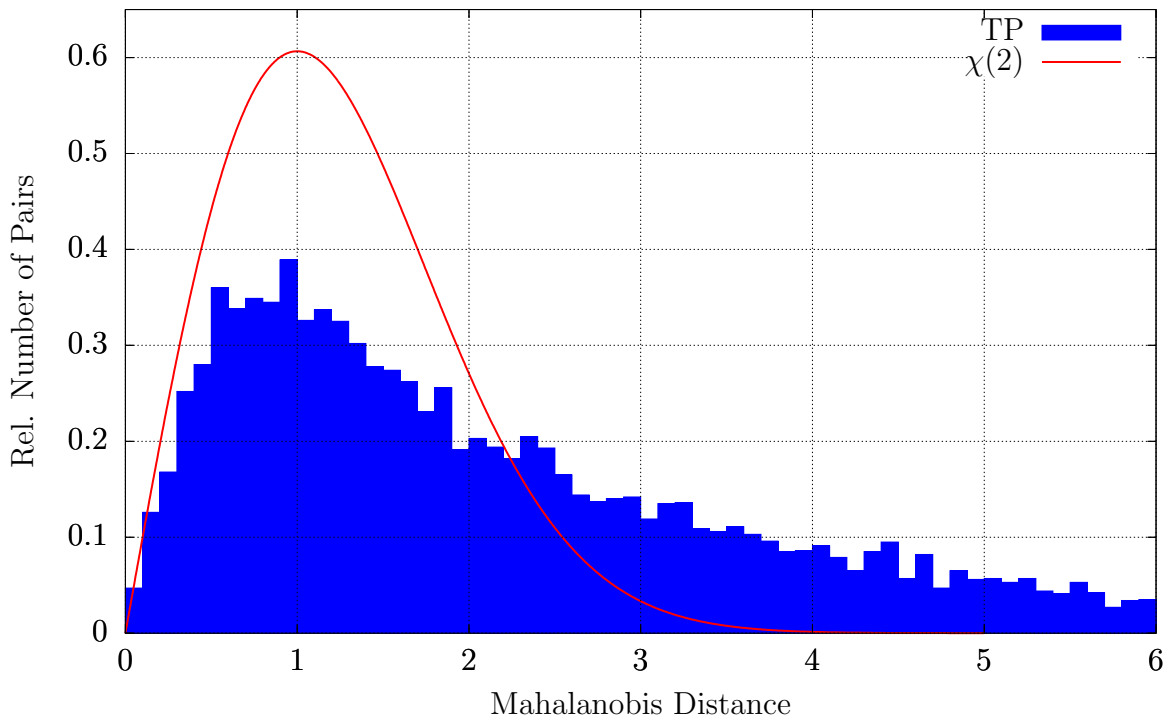
Figure 5.24: Relative frequency of Mahalanobis distances for MSR (medium LEO) compared to the theoretical $\chi(2)$-distribution.

As an additional visualisation, Figure 5.26 shows the biases in the semi-major axes which result from the bias in the perturbed mean motion over the number of revolutions. These values are derived by comparing the orbit from the correlation with a mean reference orbit from TLE. Those correlations with complete revolutions at $N_{\mathrm{rev}} = [14, 15, 29, 30, 44, 45]$ have normally distributed values around zero mean, whereas the incomplete revolutions show positive or negative biases of the mean depending on the path between the detections. One

(a) Complete revolutions   (b) Incomplete revolutions
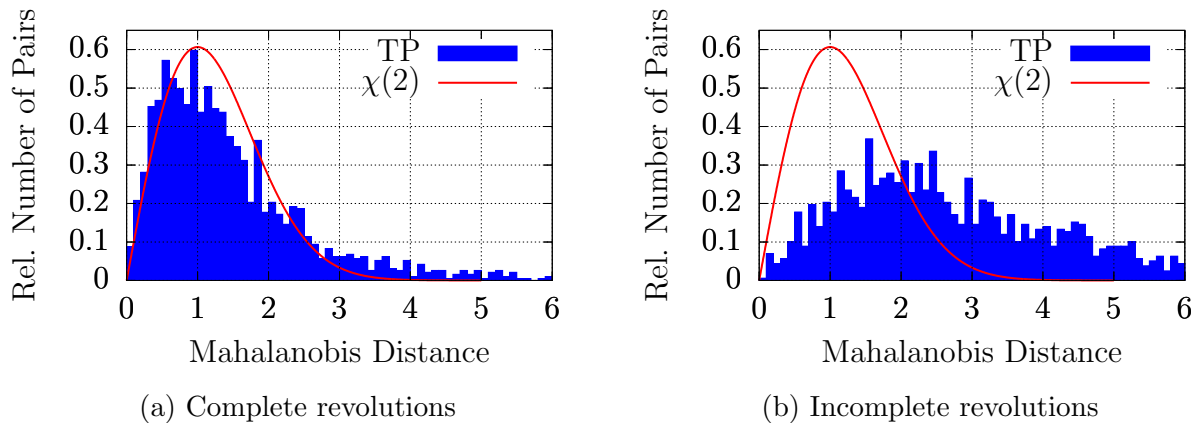
Figure 5.25: Relative frequency of Mahalanobis distances for MSR (medium LEO, polar orbits, max. one day apart) compared to the theoretical $\chi(2)$-distribution.

corresponds to the short path via the north and the other to the long path via the south. The positive and negative biases reduce for an increasing number of revolutions, because the final incomplete revolution becomes less influential. Their absolute mean values are roughly equal for a similar number of revolutions, because they should combine to zero for a complete revolution.

Mixed Stations

As a next step, the correlation is attempted with tracklets from different sensors, i.e. one from PFISR and one from MSR. Firstly, the cases for the direct short trajectory between the two stations, i.e. the ones measured at both stations within 10-15 minutes, are considered. The Mahalanobis distances for these correlations are shown in Figure 5.27a and it is visible that these distances are highly biased and shifted towards larger values. Again this is due to the short-periodic perturbations, which cannot be compensated by further revolutions. This also leads to a large uncertainty on the semi-major axis, see Figure 5.27b, if the computed semi-major axes are compared to the corresponding reference values.

For the remaining correlations, the results are shown in Figures 5.28-5.30 using the medium LEO orbits. Considering the FN correlations, the combined case is better than both the MSR and PFISR individually due to the guarantee not to have two measurements very close to each other in inertial space because of the latitudinal separation of the stations. Considering the true positives with wrong orbits, the results should be compared to those of MSR because also the mixed stations case is not using the RPP to select the number of revolutions but only the minimum Mahalanobis distance. This shows that the peaks of TPWO are smaller than those of MSR-only, although the percentages between the peaks are higher now. Because the two stations are still relatively close to each other, the periodic changes in the wrong orbits are visible although less pronounced than for MSR-only.
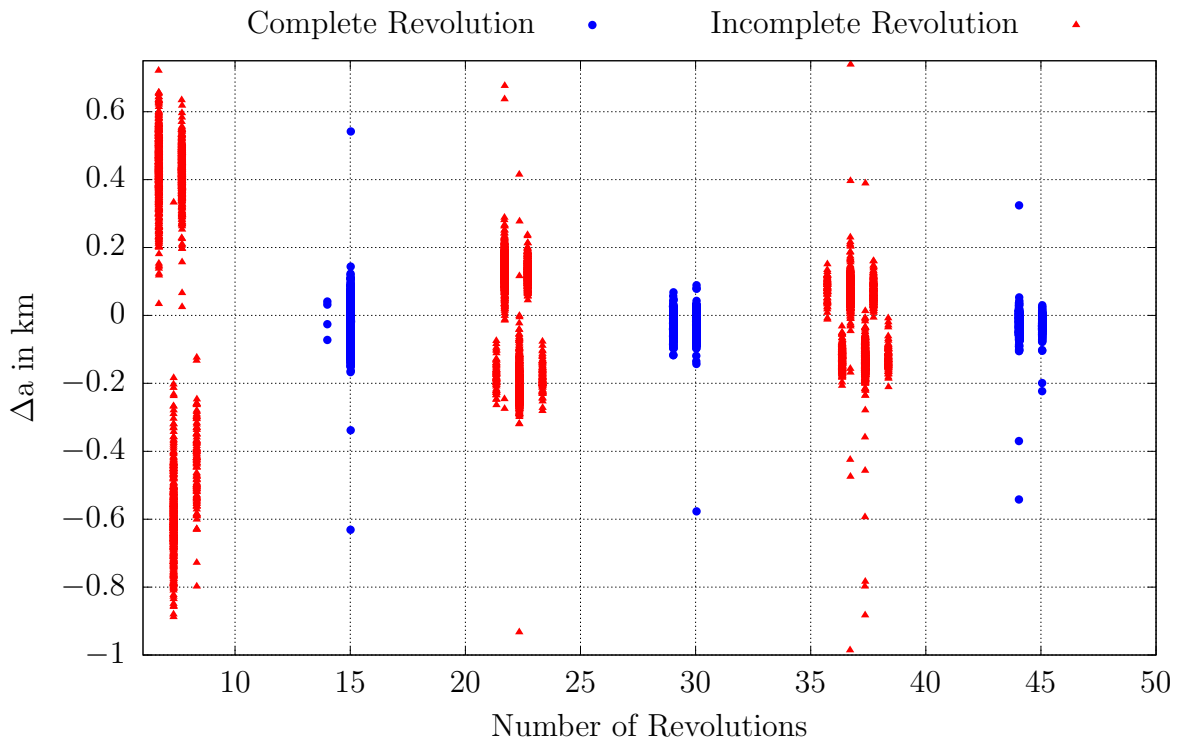
Figure 5.26: The relation between the number of revolutions (complete and incomplete) and the bias in the semi-major axis for objects on polar orbits (MSR, medium LEO).

(a) M_d-distribution

(b) Estimation error semi-major axis
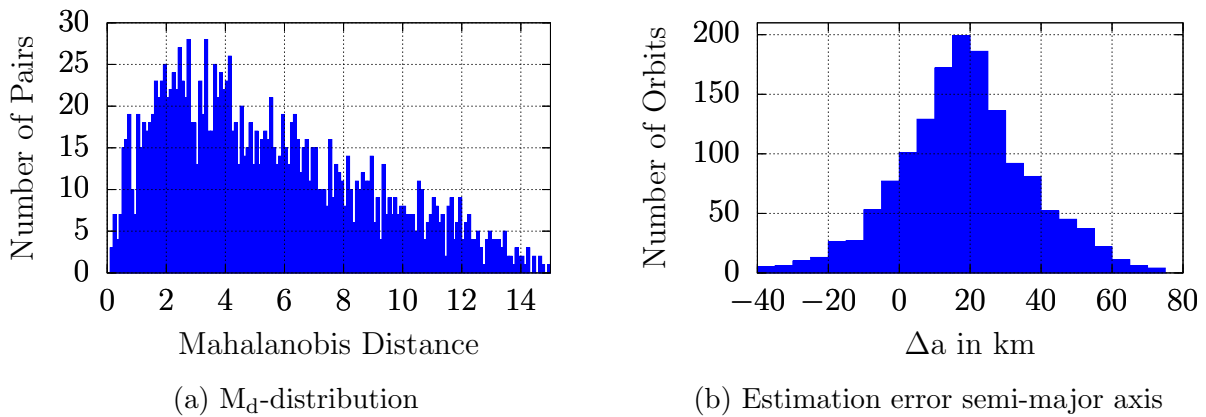
Figure 5.27: Correlation results for MSR-PFISR direct short trajectories.

(a) Wrong Orbit

(b) False Negative
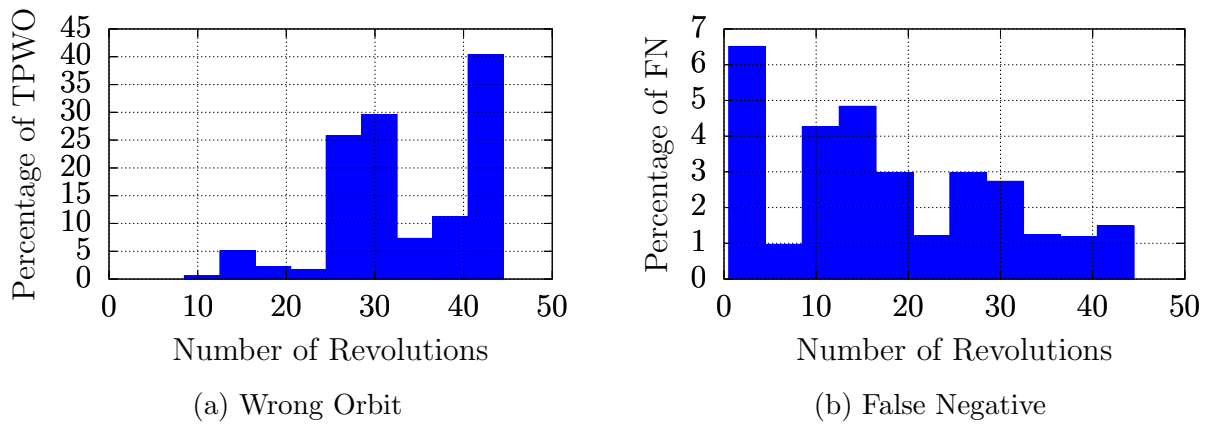
Figure 5.28: Correlation results using mixed data (medium LEO) for less than three days between the detections.

(a) Wrong Orbit

(b) False Negative
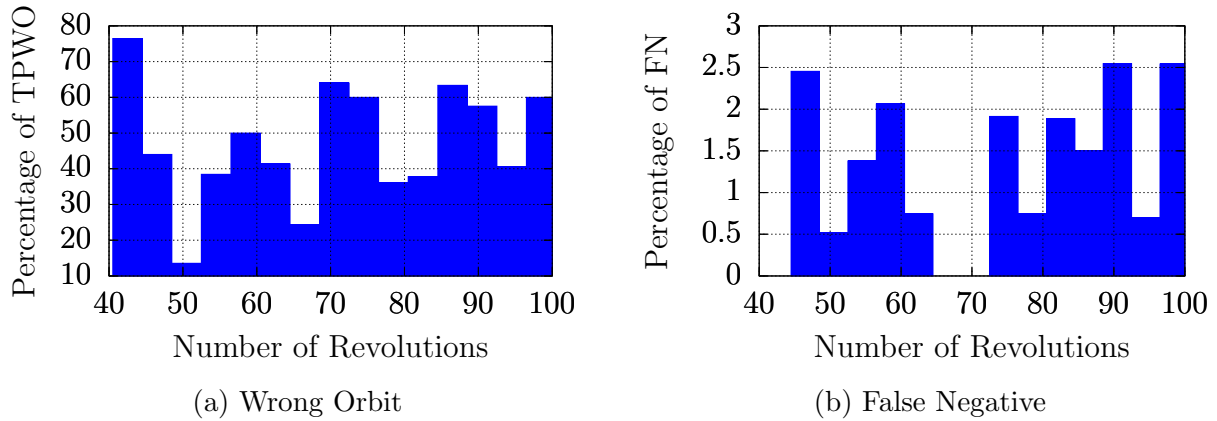
Figure 5.29: Correlation results using mixed data (medium LEO) for up to 100 revolutions between the detections.

(a) Wrong Orbit

(b) False Negative
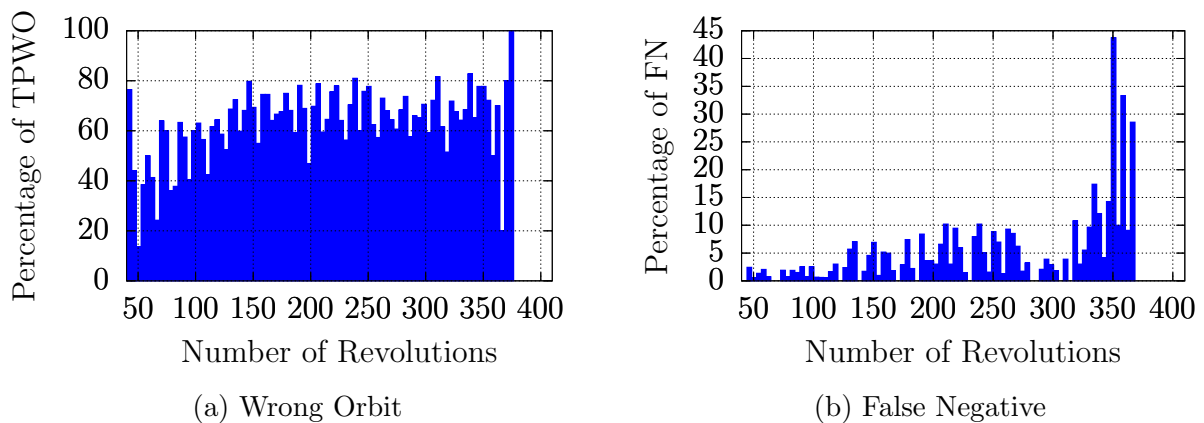
Figure 5.30: Correlation results using mixed data (medium LEO) for more than three days between the detections.

Influence of Drag

The propagation in the initial orbit determination does not consider drag, see (Reihs et al., 2020a) and Section 4.3. In order to show the effect of this limitation, six Microsat-R debris objects resulting from the Indian ASAT test with quickly decaying orbits have been selected from the PFISR data set. These objects are initially at perigee altitudes of 270 km - 340 km and their respective semi-major axes decrease by 10 km - 70 km during the observation campaign. They all re-enter in the following months and thus this is an extreme case of drag-affected orbits. Figure 5.31 depicts the percentage of false negatives for the IOD of these objects. There is once again a clear pattern showing more FN for detections which are on the same segment of the orbit. This is because an unconsidered change in the orbital altitude is especially difficult to handle for the IOD if the measurements are very close in inertial space. As the most extreme example, consider Figure 5.32 with two detections D_1 and D_2 at exactly the same location on the orbit, but the second detection is lower in altitude due to drag. This makes it impossible to derive an orbit around Earth from the two points without considering drag. Due to this effect, drag-affected orbits can be handled better if the measurements are further apart in inertial space, although their semi-major axis and eccentricity may still be estimated imprecisely. This is shown in Figure 5.32 using detection D_3 on the opposite side of the orbit, which makes it possible to derive the orbit in red, although it is more eccentric than the actual true orbit.
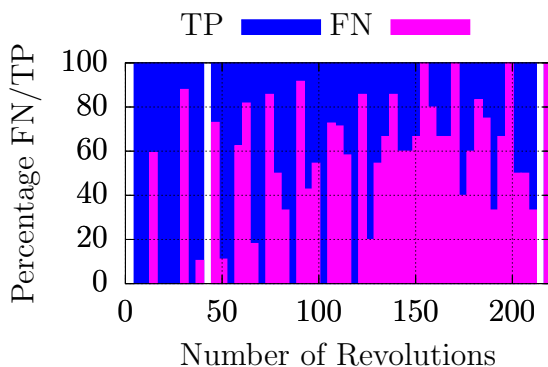
Figure 5.31: Resulting true positive and false negative IODs using PFISR data of highly drag-affected debris objects.

Influence of Manoeuvres

For the following test, it is analysed how the correlation works in the presence of manoeuvring operational satellites. The ESA missions Sentinel-1A and Aeolus are selected as both perform 5-6 manoeuvres of different types during the campaign. Aeolus performs an orbit raising manoeuvre with a velocity increase in along-track direction of $\Delta v \approx 10 \frac{cm}{s}$ every week. Sentinel-1A has one manoeuvre of that size during the considered time frame and some additional smaller manoeuvres.

The IOD mode is used to check whether it is still possible to derive the correct orbit. The results are shown in Figure 5.33. It is visible that the majority of the initial orbits can be derived. Also analysing the correlations regarding their epoch and comparing them to the manoeuvre epochs does not lead to further insights. Thus it can be concluded that the operational manoeuvres of these satellites are probably too small to have an impact on the initial orbit determination, especially with regards to the other uncertainties in the process.
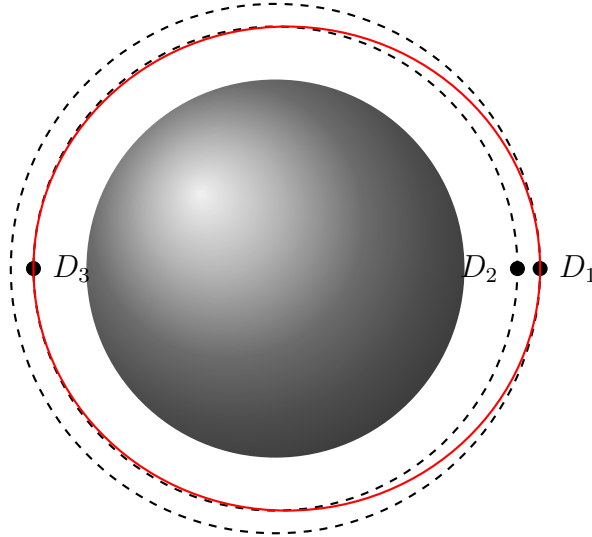
Figure 5.32: The influence of drag on the IOD process.

(a) Aeolus

(b) Sentinel-1A
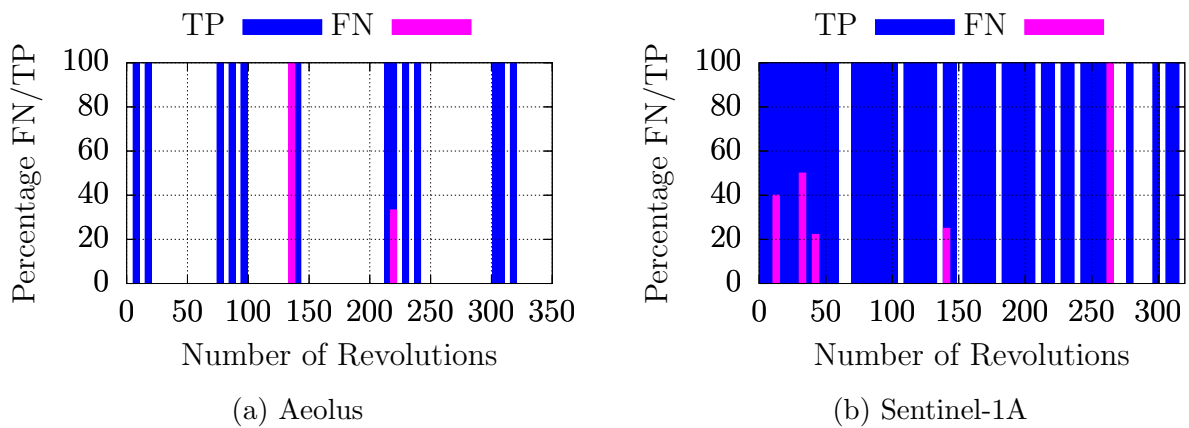
Figure 5.33: Resulting true positive and false negative IODs using PFISR data of manoeuvring operational ESA satellites.

5.2.3 Catalogue Build-up Process

The experiments up to now included only testing the known true correlations. In order to test the build-up of a catalogue, the identification of the true correlations is an important step. Two approaches are shown in the following. The first one has been described in Section 3.2.4 and uses an additional least squares orbit determination on the two complete tracklets with a threshold for the residuals, see also Section 5.1 for a similar approach using simulated measurements. The second approach creates a graph network from all the correlations including the information on the orbit. This approach is based on the internal consistency of the correlations among each other, see Section 3.3. The following experiments test all correlations from the used subset of the data, thus it is now also possible to have false positive associations.

Least Squares Orbit Determination

This processing approach adds a final least squares orbit determination using all observations from the passes and the orbit from the correlation as an initial solution. To increase the robustness of this orbit determination, it includes both the Levenberg-Marquardt algorithm as well as a line search along the current step, which is achieved by scaling the current correction term with a range of scalar values. Outlying measurements are detected and removed by comparing the individual residuals to the mean and standard deviation of the entire set of residuals. A measurement is discarded, if its residual value is more than three standard deviations away from the mean. The angular measurements are used with a low weighting to support convergence, but the orbit determination mainly relies on range and range-rate. The angles are corrupted with additional Gaussian white noise before using them for the orbit determination, because the provided tracking angles are not directly measured but derived from the pointing and thus do not contain a measurement uncertainty which was explained in the context of the data set.

If the mean μ and standard deviation σ of the residuals over both tracklets of the converged orbit are smaller than the thresholds given in Table 5.4, the orbit is accepted and the correlation is confirmed. All of the thresholds have to be met, which has proven to be a useful decision criterion. The residuals of the angles are included with a relatively large margin because it helps to remove false positives. These thresholds are certainly not universal, but depend on the radar system. The decision on the threshold values is also an optimisation procedure, because it has to be decided between the number of acceptable false positives and false negatives. In case of a cataloguing approach with additional steps after the least squares, it may be an option to allow more false positives in order to have less false negatives and assume that the cataloguing conditions afterwards filter the false positives. From the results of the previous experiments the threshold to accept a correlation after the first step and process it further is set to $M_{d,thresh} = 5$.

To simulate the regular work of such a cataloguing system, the experiments are performed for one batch of 24 hours of PFISR data, which gives enough true correlations while keeping the overall processing demand acceptable. There is no assumption of an existing background catalogue which could be used to correlate the observations directly with known objects. Thus, this experiments simulates a cold start of a catalogue.

Table 5.4: Maximum values of the residuals to accept a least squares fit.

Parameter	μ_{thresh}	σ_{thresh}
Range /m	10	20
Doppler / m/s	7.5	20
Azimuth / rad	0.015	0.025
Elevation / rad	0.01	0.02

Single Day - All Tracklets

Using all tracklets measured by PFISR between April 1, 12 UTC and April 2, 12 UTC, approximately 8.9 million correlations from 4 216 tracklets have been checked. Only 933 of these correlations are true ones. The results are summarised in Figure 5.34a. It includes the numbers of true positive, false positive and false negative correlations before and after the additional least squares as well as the number of correlations which were not tested with the least squares because one of the two tracklets was shorter than 4 s. The plot shows that there are approximately 7 500 identified correlations before the least squares with roughly 90% false positives. This does not include the correlations which are excluded from the RPP and least squares because of their length. The false negative correlations are those with $M_{\text{d}} > 5$ or a failed IOD. After the least squares the percentage of false positives has decreased to approximately 16%, while also 84 true positives do not meet the thresholds of the least squares. Subtracting the correlations which are excluded from the least squares, approximately 80% of correlations in the data set have been found.

For the interpretation of these numbers it has to be considered that the measured passes are not optimised for the initial creation of catalogue objects, thus the considered passes might be relatively short. The combination of only two passes is already relatively little information but if these passes are short, then the information content and thus the chance to distinguish confidently between true and false positives becomes less. For example, the majority of accepted false positive correlations has at least one tracklet which is shorter than 15 s. False positive correlations from longer tracklets are also due to the high latitude of PFISR which means that even a hypothetical, non-existent orbit is only sampled around the most northern parts. A better distribution of the measurements could constrain this hypothetical orbit more and possibly lead to the detection of its inconsistency with the measurements. The MSR is not used for this type of experiment because the tracklets are presumably too short to allow a confident initial orbit from two passes.

It also has to be considered that the radar is operating by creating various short tracking arcs, thus the length of the overall pass is not necessarily proportional to the overall data points acquired as it would be for a survey radar. To investigate the influence on the number of data points, Figure 5.34b depicts the percentage of true positive correlations within the accepted solutions over the number of data points in the considered passes. It is visible that the majority of false positive correlations have at least one pass with less than 20 detections. Considering the false positives with more than 20 detections in both passes, these are mainly resulting from objects in the Russian communication constellation at 74°-inclination and 1 400 - 1 500 km altitude.

(a) Distributions after different steps

(b) TP depending on number of detections
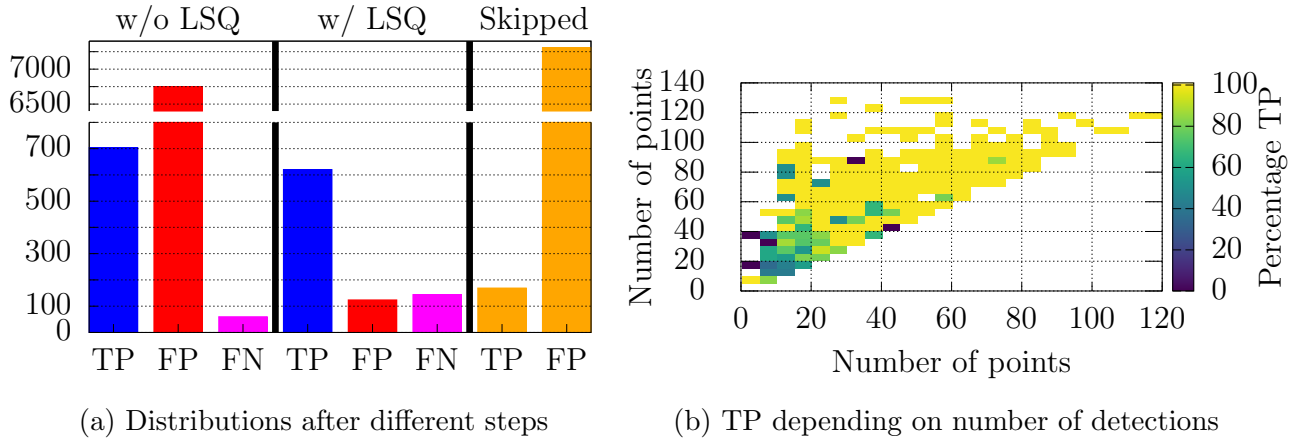
Figure 5.34: Correlation results using all PFISR detections within 24 hours.

Considering the processing time, running a least squares for each candidate solution takes a long time. In this case, the calculation was performed on three processes in parallel with a total runtime of approximately 80 hours for each on a laptop with an Intel Core i5–6200U CPU with 2.30 GHz. The processing time of a single least squares is mainly dependent on the number of measurement points and the time between the two tracklets as this influences the computation time for the propagation.

Single Days - Medium LEO

As an additional test, four other days have been selected to run the correlation over the detections from 24 hours. Here, the data set is limited to the objects in medium LEO to reduce the computation time, which is now approximately 20 hours per experiment, while still having a realistic chance for false positives due to objects in similar orbits. The results are summarised in Table 5.5. From nearly 10 million checked pairs, more than 1 000 true correlations are identified, which is approximately 80% if skipped pairs are excluded. The final correlations also contain nearly 20% false positives, but similar to the previous experiment those are mainly due to measured passes with a low number of detections.

Graph Analysis and Voting

The process of the graph analysis was introduced in Section 3.3. Here, the aspect of the correct determination of the number of revolutions is important because in the LEO case there may be multiple solutions leading to a correlation. As an example for this, Figure 5.35 shows two different true positive correlations and their Mahalanobis distances over the number of revolutions with an assumed threshold of $M_{\mathrm{d}} = 5$. For the case of two detections being 35 revolutions apart, there is just one solution below the threshold, which is the correct one, but the more revolutions between the detections the shallower this minimum becomes because also the differences in semi-major axis between two adjacent solutions become smaller. For Figure 5.35a this difference is 130 km, whereas for Figure 5.35b it is only 14 km, which also leads to smaller variations in the orbital speed and thus range-rates. In total there are five solutions below the threshold for the case in Figure 5.35b. Especially

Table 5.5: Results of single day correlation using medium LEO objects.

Start Epoch	Ground Truth				Correlation Results		
	$N_{\text{tracklets}}$	N_{pairs}	N_{TP}	$N_{\text{TP,skipped}}$	N_{FN}	N_{TP}	N_{FP}
April 2, 12 UTC	1 990	1 979 055	472	104	69	299	97
April 3, 12 UTC	2 401	2 881 200	466	116	72	278	111
April 4, 12 UTC	1 983	1 965 153	283	70	43	170	15
April 5, 12 UTC	2 498	3 118 753	492	92	73	327	14
Total		9 944 161	1 713	382	257	1 074	237

for correlations with long time spans between the detections, it may be difficult to justify rejecting solutions which are not the minimum but still at a reasonable value. The large percentage of solutions with a wrong orbit as seen in the previous sections also shows that selecting the correct number of revolutions from a single pair of tracklets is very challenging.

(a) 2.5 Days

(b) 22 Days
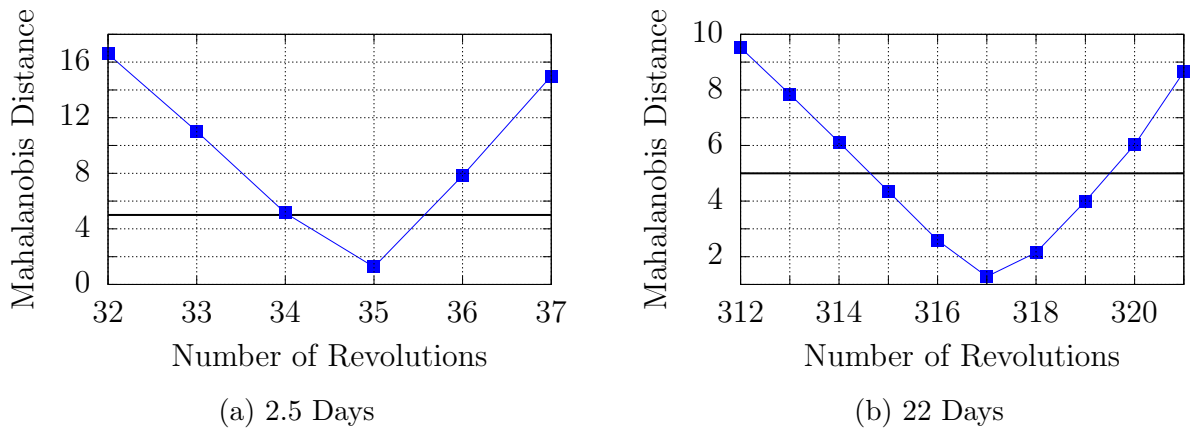
Figure 5.35: Two examples of the Mahalanobis distances over the numbers of revolutions (PFISR, medium LEO).

To improve the results, the multigraph approach is applied which means that it is possible to have multiple edges between the same pair of nodes to represent different orbits, see Section 3.3.3. The thresholds for the formation of triangles are set to $\Delta a < 2$ km for the semi-major axis and $\Delta i < 0.85°$ for the inclination. For highly perturbed orbits, e.g. due to drag, these conditions would need to be reconsidered, due to more changes in the orbit. Because the process in the graph network is computationally very efficient compared to the

least squares and increases its reliability with more available correlations, the threshold to add a correlation to the graph is set to $M_{\mathrm{d,thresh}} = 10$ to maximise the number of candidate solutions for the following experiments. This approach can be applied to both the removal of false positives as well as the selection of the correct semi-major axis for a certain group.

Semi-major Axis Selection

As a first test, it is checked whether it is possible to select the correct semi-major axis from a group of tracklets. Two objects are chosen from the PFISR detections: TLE ID 32783 (28 tracklets) with $[a = 7008.769$ km, $e = 0.002$, $i = 98.04°]$ and TLE ID 4719 (27 tracklets) with $[a = 7292.150$ km, $e = 0.013$, $i = 99.88°]$. Running the standard correlation with a hard selection of the semi-major axis leads to the percentages of wrong orbits as shown in Figure 5.36a. In total approximately 50% of the correlations have a wrong orbit. Processing now all candidate solutions, which passed both the $M_{\mathrm{d,thresh}}$ and the RPP, with the described graph approach under consideration of the orbital elements leads to two groups with the correct orbit containing all of the corresponding object's tracklets. Thus the graph can be used to derive the correct solution from all possible correlations.

To give an impression on the number of the considered solutions per correlation, Figure 5.36b depicts this number over the corresponding correlation's number of revolutions. As one would expect, the more revolutions the higher is the number of considered correlations with the majority reaching 5-15 correlations per pair for more than 100 revolutions and less than five before 50 revolutions.

(a) Wrong orbit at minimum

(b) Number of considered solutions
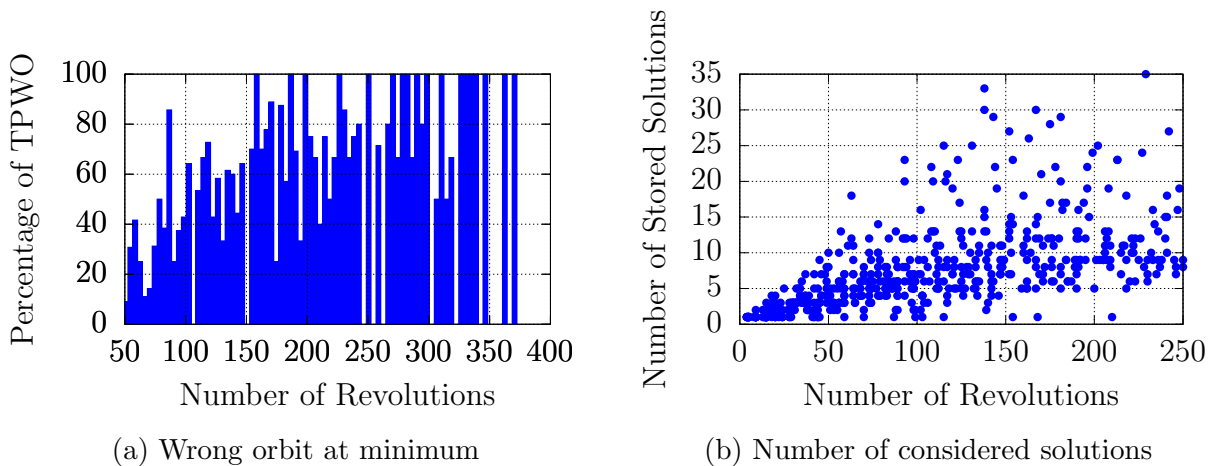
Figure 5.36: Results comparing the percentage of the wrong orbits at the minimum M_{d}. (left) to the number of solutions smaller than $M_{\mathrm{d,thresh}}$.

Single Sensor - 5 Days

As a next step, the graph approach is tested in the presence of possible false positives. In order to have sufficient tracklets per objects, this test uses 1 500 PFISR tracklets from April 1, 12 UTC to April 6, 12 UTC of medium LEO objects. This leads to approximately 1.1 million total pairs to be checked including around 2 600 true correlations. There are 277 objects with at least three tracklets, 186 with at least four tracklets, 116 with at least five tracklets and 57 with at least six tracklets.

Figure 5.37a gives an overview over the numbers of true and false positive correlations before and after the graph processing. Initially there are more than 10 000 false positives compared to approximately 2 000 true positives. After the analysis using the graph, the false positives are reduced to 21 correlations, while there is only a small reduction in true positives. To consider the number of identified objects instead of correlations, Figure 5.37b uses the following categories: TP-all designates an identified group which contains all and only tracklets from the same object, whereas a group with FN does not contain all tracklets of the object. The FP-group contains tracklets from different objects. Finally the missed groups are those objects with at least three tracklets that did not end up in an identified group. This is mainly the case when exactly three tracklets for one object are present and one of the correlations is missed, thus no triangle can be formed. In total, more than 80% of the objects are identified correctly, which also includes the selection of the correct semi-major axis and inclination. The FP-groups usually are not completely mixed with tracklets from different objects but they contain only one wrong tracklet among a group of true ones.

(a) True and wrong correlations

(b) Types of groups after clustering
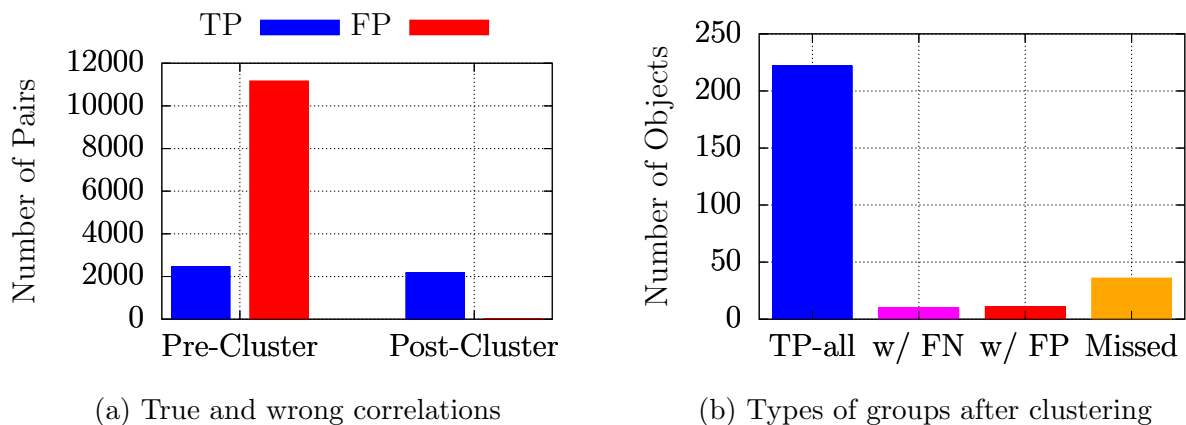
Figure 5.37: Results of the correlation experiment (PFISR - 5 days) showing the true and false positive correlation (left) and the types of the identified groups.

In this case, the runtime is approximately 20 hours on three parallel processes for the creation of the candidate correlations. The graph analysis afterwards takes less than 10 seconds. Performing a least squares orbit determination for each of the candidate correlations instead would lead to a significant increase in processing time of tens of hours.

OPERATIONAL PROCESSING APPLICATIONS

6.1 Automated Database Maintenance

The text and figures in the following section have been used from the publication (Reihs et al., 2020b).

6.1.1 Overview

The previous chapters focused on the identification of pairs of tracklets from the same object to generate candidate orbits for a space object database. The following section considers the subsequent steps for the build-up of a database. This includes the confirmation of objects with a sufficient quality after the initial correlation and the monitoring of existing catalogue objects to track their current quality. Here, the term *quality* refers to having an orbit which fulfils a performance criterion depending on the application of the catalogue, e.g. it is accurate enough to allow a confident association of subsequent measurements over a defined period of time. However, here it is not the goal to build an implementation of a cataloguing algorithm, but to find quantitative measures which can be used to support such a system.

The association of a tracklet to a catalogue orbit will be analysed first, because it is a prerequisite for the maintenance of a catalogue. Afterwards, the object confirmation and maintenance is analysed. It is the goal to define measures which can be checked with as much autonomy as possible to limit the manual interaction of an operator.

6.1.2 Tracklet-Catalogue Association

Problem Statement

For this part of the thesis, it is assumed that a database (or catalogue) of space objects already exists. This database contains orbits and their covariances. If new measurements are received, it shall be tested whether they originate from an object in the catalogue by comparing the stored orbits to the measurements. The uncertainties of the measurements are also assumed to be known. The association between a catalogue orbit and a tracklet is performed by transforming the measurement and the orbit, propagated to the measurement epoch, including their uncertainties into the same coordinate system for a comparison. The importance of the selection of this coordinate system is due to the transformation of the covariance matrices, which are assumed to be Gaussian in the original system and shall maintain their normality after the transformation. For example, the transformation between the measurement system and the orbit state is usually non-linear and thus for large uncertainties of the orbit this transformation may not lead to a good representation of the covariance in measurement space. Practically, this also depends on the observation geometry and the dynamics of the observed objects.

Because the orbit's state vector can be transformed into the standard radar and optical observables, making the association in the measurement space is always possible. The use of other systems for the comparison depends on the observables and is discussed in the following separately for optical and radar observations. In case of optical measurements, it is not possible to directly transform the observables into the position-velocity state space of the orbit, because the range to the detected object is missing to derive its position. In order to compensate this, one can assume that the range is equivalent to the expected value at the measurement epoch based on the catalogue orbit. Alternatively, the optical measurements

can be projected onto the orbital plane and the corresponding position is used to estimate the range (Frueh et al., 2009). The difference to the catalogue state is calculated in the cartesian RTN coordinate system, which originates in the object's current cartesian position. Its first axis is aligned with the radius vector and the second axis points in the direction of motion, but depending on the orbit's eccentricity it may not be aligned exactly with the velocity vector. This approach was extended by (Siminski and Flohrer, 2019) using a curvilinear coordinate system according to (Vallado and Alfano, 2014). In this case, the projection of the optical measurement into a full state is found by either finding a state which sets the radial position and velocity differences to zero or by directly minimising the Mahalanobis distance between measured and expected position. These approaches are useful if the orbit uncertainties are large and the observation geometry is such that the transformation from the orbit state to the measurement space is highly non-linear which affects the mapping of the covariance onto the measurement space. As a counterexample, the uncertainty of objects in GEO can usually be transformed into the optical measurement space with a simple linear mapping, which will be used in Section 6.4.

Considering radar observations, the range is part of the measurement and thus a position can be derived directly from the measurements. The catalogue state and the measured position can be compared directly in a cartesian or curvilinear RTN coordinate system. Another option is to derive an initial orbit from the new tracklet and, instead of using the position-velocity space, compare two Keplerian orbits in their element-space, see e.g. (Hill et al., 2012; Vananti and Schildknecht, 2019). However, if there is only a single or very few detections during the pass, there is no good chance of obtaining a reliable orbit.

The previously mentioned approaches can all use the Mahalanobis distance as a criterion for the association decision. Apart from this, (Hill et al., 2012) describes a fixed gating approach for radar measurements based on the differences between the measured and predicted positions in RTN coordinates without considering the covariances. Another approach is to calculate the divergence between two probability distributions, here measurement and state, to decide whether they belong to the same object, see e.g. (Giza et al., 2010; Hussein et al., 2015).

Association Test

The following analysis focuses on radar measurements and the association decision is taken via the Mahalanobis distance in a common coordinate frame, which can be derived directly from the detection without an orbit determination. The resulting problem is to find an appropriate frame for this comparison. The difficulty of finding a good frame for the comparison is due to the overlapping effects of the measurement and orbit errors.

As an example, consider an object in an orbit $[a = 6878$ km, $e = 0.001$, $i = 86°]$ which is detected at $\rho = 544$ km and $el = 67°$. The position uncertainty in the orbit's curvilinear RTN frame is $[0.01, 15.0, 0.01]$ km and the measurement uncertainties are $[\sigma_\rho = 0.01$ km, $\sigma_{\dot{\rho}} = 0.01$ km/s, $\sigma_{az,el} = 1.0°]$. The assumed uncertainties are mainly dominated by the along-track error of the orbit and the angular error of the radar. Figure 6.1a shows the resulting distribution of measurements from a Monte Carlo experiment using the mentioned uncertainties projected into the cartesian TR-plane and it appears to be well-shaped as no distortions are visible in this plot. To explain how this cloud of points is created, Figure 6.1b separates the effects of the orbit and the sensor noise and shows a cut through the TR-plane at N=0 km. For the orbit noise, it is visible that the large along-track error makes the

curvature of the orbit visible leading to a non-normal distribution in this frame. The second set of points shows the effect of the radar noise. This distribution is tilted and curved, thus also not normal in the given frame. The distribution of the radar noise is highly dependent on the observation geometry but this plot allows it to deduce that there is no frame which can fit both distributions to be normal.

(a) Combined
(b) Single sources
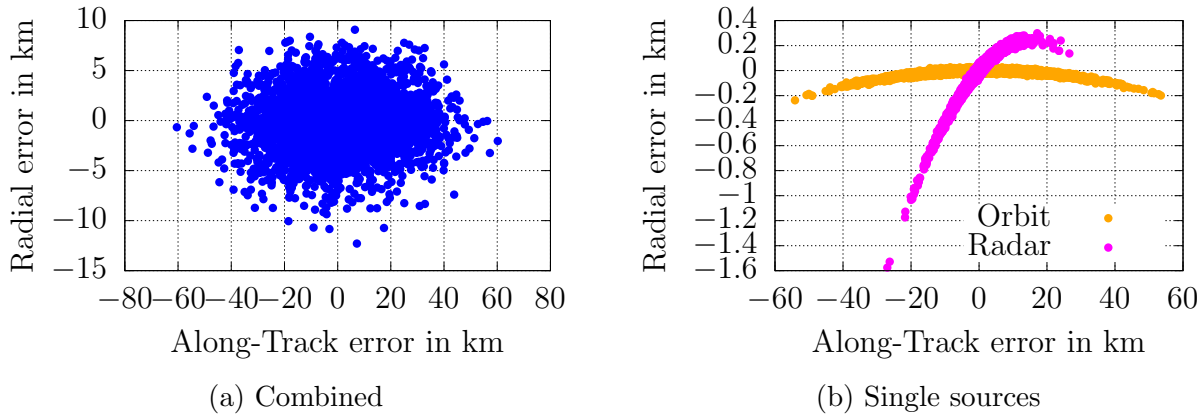
Figure 6.1: Distribution of measured positions by combining the noise of the radar and the orbit's position uncertainty. (b) is cut along RT-plane

For the following tests, a catalogue state is assumed to be known including the orbit and its covariance. Based on this state as a reference, the true and to the observer unknown position of the object is obtained by corrupting the catalogue state with different levels of orbit noise in the RTN frame according to its covariance. Thus, it is implicitly assumed that the covariance in the catalogue is realistic. Measurements with the given sensor noise are derived from the true state. The squared Mahalanobis distance M_d^2 is calculated between the measurement and the catalogue state in different coordinate systems. If this is performed for a large set of observations, the resulting distribution of M_d^2 should follow a $\chi^2(\nu)$-distribution with the degrees of freedom ν equal to the number of compared variables per observations, see Section 3.2.1. The degrees of freedom are $\nu = 4$ for the direct use of the radar observations $(\rho, \dot{\rho}, az, el)$ and $\nu = 3$ for the comparison of RTN positions. Different statistical parameters are derived from the M_d^2-distribution and compared to the theoretical values of the $\chi^2(\nu)$-distribution. Those parameters are the mean $(\mu = \nu)$, the median $m \approx \nu \cdot \left(1 - \frac{2}{9\nu}\right)^3$ and the variance $(\sigma^2 = 2\nu)$ (Abramowitz and Stegun, 1965). Additionally, the threshold values of $\chi^2(\nu)$ are checked for which there should be a cumulative value of 5% and 95% of the samples to test both ends of the distribution for a possible shift of the values. The threshold at 99.9% of the $\chi^2(\nu)$-distribution is checked to detect the frequency of outliers. These outliers are removed for the calculation of the remaining statistical properties to increase the robustness of these parameters. Thus, this outlier rate should be at 0.1% which represents the most strict condition as can be seen in the following. The resulting heatmaps depict the difference between the value obtained from the sampled distribution and the theoretically expected one.

This experiment uses a population of 1 000 different LEO objects for a simulation of observations from a single station over seven days. This leads to approximately 25 000 passes in total. To limit the computational time, 2 500 passes are randomly selected for the following tests. Each test uses the same set of passes. The noise values are set to $[0.01, \sigma_\mathrm{T}, 0.01]$ km in the orbit's curvilinear RTN frame and $[\sigma_\rho = 0.02$ km, $\sigma_{\dot\rho} = 0.01$ km/s, $\sigma_{az,el}]$ for the measurements. The dominating noise values σ_T and $\sigma_{az,el}$ are varied systematically. Only true positive correlations are tested to analyse the resulting distribution.

The following tests can be separated further into two sub-categories: single-point association and multi-point association. Single-point association refers to those methods which can be performed with a single detection, here the association in measurement space and curvilinear RTN. In contrast to that, the multi-point association requires a sequence of detections, here the time bias removal. This also adds another dimension to the analysis because the results may also be dependent on the number and spacing of the observations.

Observations

The first experiment uses the observables directly. The association is performed by comparing the measured observables $(\rho, \dot\rho, az, el)$ to those expected from the catalogue state. Combining their difference with the sum of the measurement covariance and the orbit covariance transformed into the measurement system, the Mahalanobis distances can be calculated. The distribution of the resulting distances of the entire population is compared to the expected values of the $\chi^2(4)$-distribution and the differences between them are shown in Figure 6.2. Figure 6.2a contains the percentage of outliers. This number becomes significantly larger than 0.1% for along-track errors of more than 5 km. For the remaining parameters, it might be argued that the association is acceptable for up to 7.5 km along-track (AT) uncertainty. All parameters show roughly constant results for the same AT value, whereas the differences continuously increase for increasing AT uncertainties at a constant sensor noise. This behaviour confirms that this coordinate system is not sufficient for large AT uncertainties due to the non-linearity of the transformation into the measurement system, which increases its effect with an increasing size of the orbit covariance. It should also be considered, that for a sensor with a very low sensor noise ($\sigma_{az,el} = 0.001°$), the sensitivity to the along-track noise is much higher with the degradation starting already at $\sigma_\mathrm{T} \approx 1$ km.

Curvilinear RTN

The observations (ρ, az, el) and their covariance matrix are transformed into the orbit's curvilinear RTN system to perform the association in this system. This system can, as one would expect, tolerate also large along-track uncertainties. In contrast to the cartesian RTN, it considers the curvature of the orbit for a growing along track error (Vallado and Alfano, 2014). As visible in Figure 6.3, the outlier condition is met for all along-track errors up to $\sigma_{az,el} \approx 0.25°$. For the remaining parameters, as opposed to the previous example in the measurement space, the differences are now increasing for an increasing sensor noise, but there is no clear boundary at a certain sensor noise value. The larger the AT uncertainty, the larger also the acceptable sensor noise.

Observations – Time Bias Removal

(a) Outside 99.9%

(b) Difference Mean

(c) Difference Median

(d) Difference Variance

(e) Difference 5%
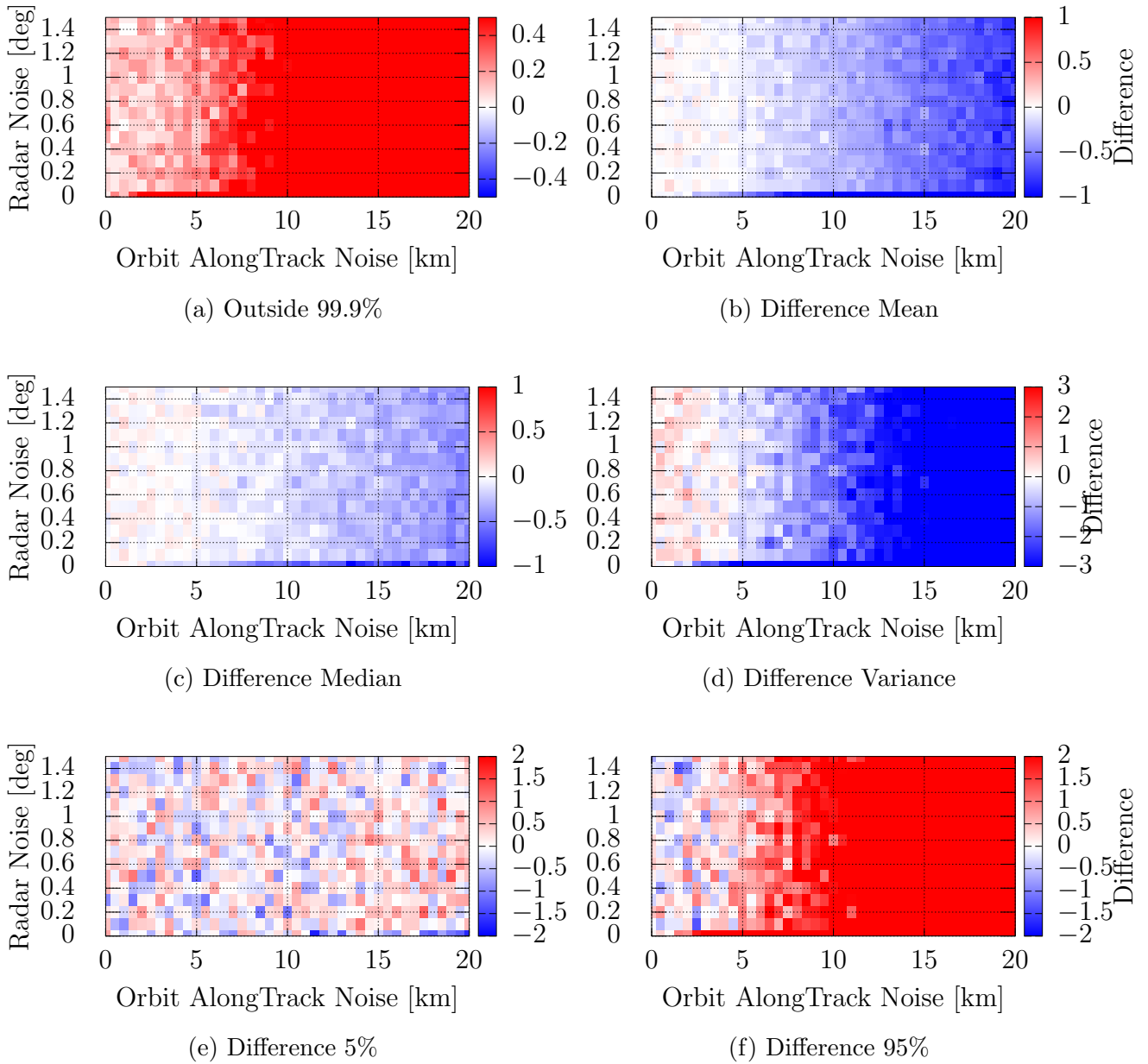
(f) Difference 95%

Figure 6.2: Difference to the theoretically expected values of the M_d^2-distribution using the observables directly.
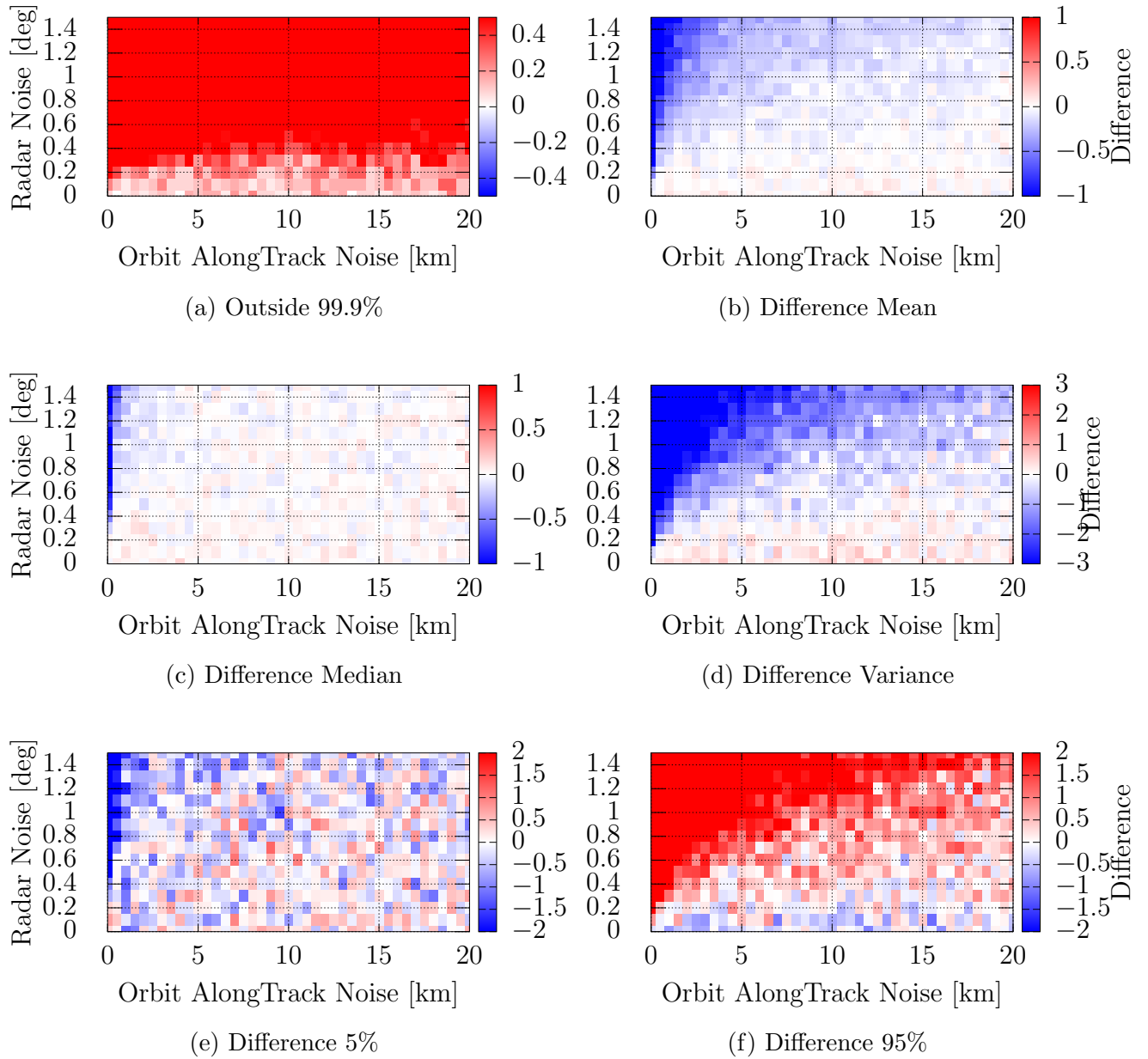
Figure 6.3: Difference to the theoretically expected values of the M_d^2-distribution using the curvilinear RTN coordinates.

As another approach to improve the association, it is attempted to use the advantages of the sensor coordinates of the measurements while mitigating the effect of the along-track error. This is done by first calculating the position differences between the catalogue and measured (ρ, az, el)-position in the curvilinear RTN for all detections in the tracklet. Because it is assumed that the along-track error is dominating and consistent between multiple detections, it is attempted to quantify the along-track error by averaging over the individual along-track errors which are affected by both the orbit and sensor noise. This mean along-track error $\overline{\Delta AT}$ is then transformed to a time bias Δt_{AT} by dividing $\overline{\Delta AT}$ by the total orbital velocity. The reference orbit from the catalogue is propagated by Δt_{AT} to correct the catalogue state before deriving the reference measurement from it for the comparison to the actual measurements. The uncertainty of the mean time bias Δt_{AT} is used as the new along-track orbit uncertainty and replaces the initial uncertainty of this component in the covariance matrix before transforming it to the measurement coordinates.

The results using this approach are shown in Figure 6.4. Concerning the general trend, it is visible that now the boundary towards a declining quality of associations is towards larger measurement noise and not towards larger along-track noise as in Figure 6.2 in the same coordinates. When comparing to the curvilinear coordinates in Figure 6.3, the results are in general worse now with the exception of the cases with large angular sensor noise and low along-track noise (top left corner). However, for this area the direct usage of the observations is better than the ones without the time bias and thus the removal of the time bias apparently does not improve the association.

<div align="center">

Least Squares-based Time Bias Removal

</div>

Concerning the removal of the time bias, it is also attempted to use the high-precision range information as a useful information. For this, a least-squares problem is set up to minimise the range residuals by varying the time bias Δt_{AT} when propagating the reference orbit. The new along-track uncertainty is again derived via the fit, but it is very small now, thus the measurement errors dominate. The association is done in the measurements' frame as before. The results for tracklets with 42s-3f (15 data points) are shown in Figure 6.5 and they are much better than the previous results even for large along-track errors. Because this fit is strongly dependent on the length of the tracklet and its density, a second experiment is shown in Figure 6.6 using 40s-10f (5 data points) tracklets. The results are now slightly worse but still in an acceptable range. For the final association decision, also the size of the time bias compared to the expected along-track error would need to be considered in order to ensure that the correction value is not larger than expected, which is not done in this simplified test.

Summary

The conclusion from this analysis is that there is no single coordinate system which gives the best results, but depending on the conditions either the observable coordinates or the curvilinear RTN is better. Thus, it should rather be considered if there is either a relatively low noise sensor or a relatively high-confidence orbit. In general, the smaller covariance is the one which should be transformed to another system, because it has the better chance of remaining sufficiently normal. Another option would be to try to reduce the effect of a non-normal distribution by using Gaussian Mixtures Model (GMM). For GMM, a probability distribution is modelled by a sum of weighted normal distributions, which can be used to

(a) Outside 99.9%

(b) Difference Mean

(c) Difference Median

(d) Difference Variance

(e) Difference 5%
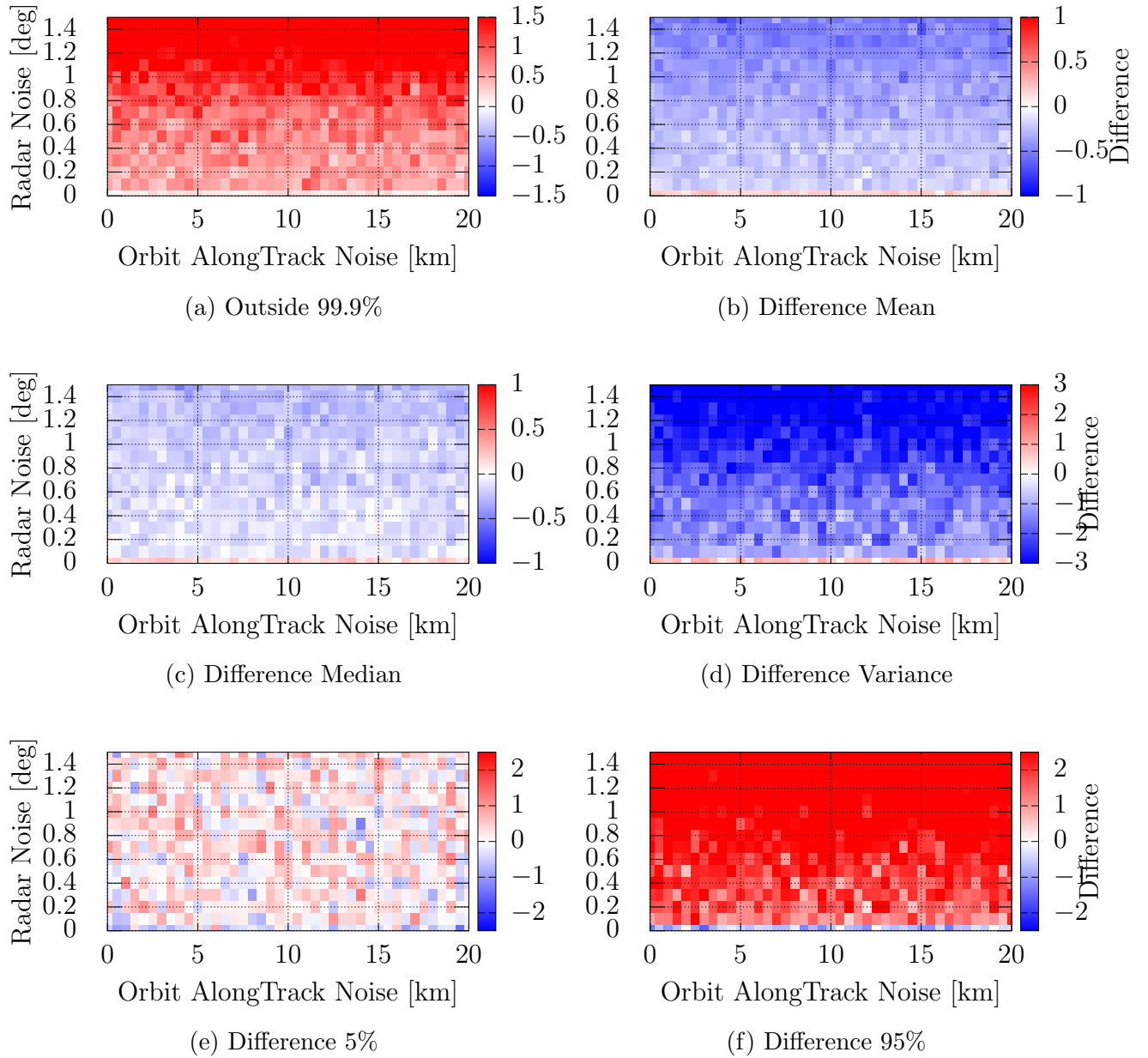
(f) Difference 95%

Figure 6.4: Difference to the theoretically expected values of the M_{d}^2-distribution using the observables with the removed time bias.

(a) Outside 99.9%

(b) Difference Mean

(c) Difference Median

(d) Difference Variance

(e) Difference 5%
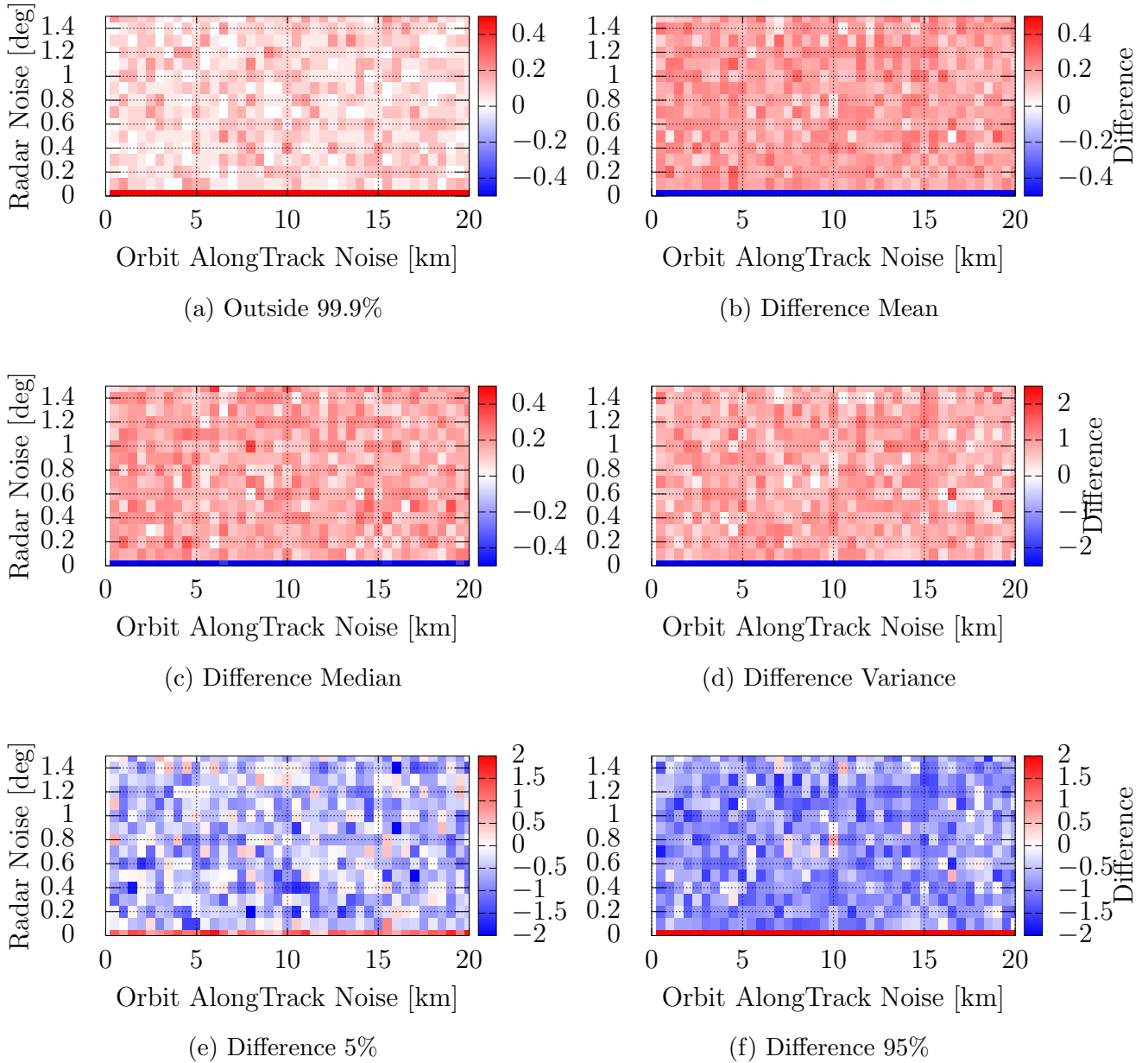
(f) Difference 95%

Figure 6.5: Difference to the theoretically expected values of the M_{d}^2-distribution using the observables with the removed time bias via the least squares of the range residuals (42s-3f).

(a) Outside 99.9%

(b) Difference Mean

(c) Difference Median

(d) Difference Variance

(e) Difference 5%
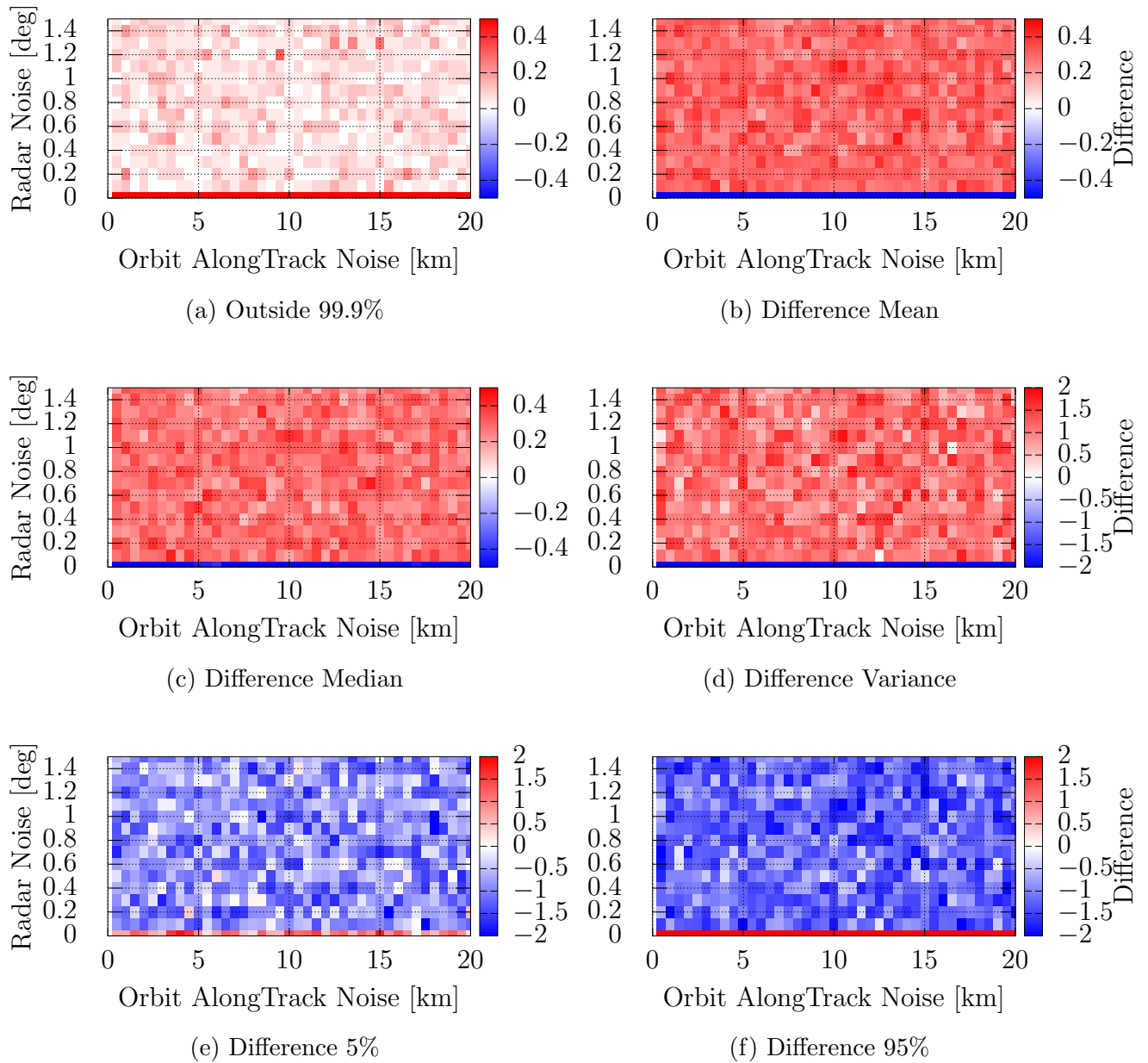
(f) Difference 95%

Figure 6.6: Difference to the theoretically expected values of the M_d^2-distribution using the observables with the removed time bias via the least squares of the range residuals (40s-10f).

model any other distribution assuming a sufficient number of components is used. However, defining an equivalent of the Mahalanobis distance for GMM which allows statistical gating seems to be not available. Alternative distance measures such as the Kullback–Leibler divergence do not have the same statistical gating behaviour as the Mahalanobis distance and thus would need some additional calibration.

6.1.3 Object Confirmation and Maintenance

Overview

Within the catalogue build-up process, a decision has to be made whether and when a new object is introduced into the catalogue. This includes switching from tracklet-tracklet association to the previously discussed orbit-tracklet association for future observations of this object. This decision can be based on different parameters, which is discussed in the following.

The first approach for this is to use known track confirmation algorithms from multi-target tracking. A relatively simple one is to define N expected passes based on the current trajectory and then accept an object if m detections are made, thus m-out-N method (Bar-Shalom et al., 1989). Another option is the use of the sequential likelihood ratio test (Blackman and Popoli, 1999), which has already been applied to orbit cataloguing (Pittelkau, 2016).

The second approach is the use of information theoretic measures. Such work is often based on (Rényi et al., 1961). Most applications in space surveillance have been performed with regard to sensor tasking, first by (Kreucher et al., 2004) and later extended by (DeMars and Jah, 2011; DeMars et al., 2012; Gualdoni and DeMars, 2017). Although sensor tasking might be considered to be related to cataloguing, this aspect rather covers the catalogue maintenance than the build-up.

In the following, information theoretic measures are used to make decisions on the confirmation of objects and their current quality. To distinguish further from the scheduling aspect, the work focuses on survey sensors without dedicated tracking like the one in Section 5.1. This is also related to the tracklet-orbit correlation, because it might include a first step of associating new tracklets with preliminary orbits before a decision concerning the status can be taken.

Object Confirmation - Theory

When a new object is created through the tracklet-tracklet correlation, an objective value based on the current information should be used to establish whether the orbital information for this object is good enough to include the object in the catalogue for regular maintenance. This means that its orbit needs to be sufficiently precise to perform the tracklet-orbit association reliably for a defined time span.

In practice, the quality of the orbit is dependent on several factors such as the number of passes, their geometry and their lengths. Due to the large variability and inter-dependence of these different parameters, it is preferred to have a characteristic value to quantify the available information and make it comparable between different cases with different conditions.

The most promising quantity from information theory is the differential entropy H of the probability density function $p(\vec{x})$ (in unit *bits*) (Cover, 2006):

$$H(p(\vec{x})) = -\int_{-\infty}^{\infty} p(\vec{x}) \log_2 \left(p(\vec{x}) \right) d\vec{x} \ . \tag{6.1}$$

The smaller the entropy, the more information is available. For an n-dimensional multivariate normal distribution $\mathcal{N}(\vec{x}|\vec{\mu}, \Sigma)$ with mean $\vec{\mu}$ and covariance Σ, this can be solved analytically to:

$$H(\mathcal{N}(\vec{x}|\vec{\mu}, \Sigma)) = \frac{1}{2} \log_2 \left((2\pi e)^n \det \left(\Sigma \right) \right) \ . \tag{6.2}$$

It should be noted, that the differential entropy does not share all properties with the classical Shannon entropy for discrete probability distributions, e.g. it can become negative. Some approaches exist to work around this, but here the differential entropy is used as presented in Equation 6.1.

Object Confirmation - Experiments

As an initial experiment, it is attempted to relate the entropy of the state at the epoch of the least squares orbit determination (LSQ-OD) to the along-track uncertainty of the propagated covariance matrix after up to three days. The entropy of the state is calculated in Keplerian elements using the mean anomaly and also the propagation of the covariance is performed in that system because the error distribution keeps its Gaussian nature for a longer period of time in an orbital-elements-based system (Hill et al., 2012). At each point of interest, this covariance can then be transformed to the curvilinear coordinates to get an along-track uncertainty.

To search for a relation between the differential entropy and the propagated size of the covariance, different conditions have been used for the tracklet length, the number of passes and the noise level of the observations based on the same group of LEO objects as in the previous section. Figure 6.7 shows the size of the covariance in along-track direction after 48 hours of propagation over the entropy at the orbit determination epoch. There are two different types of passes: those with a fixed number of observations (40 s length with an observation every 5 s and 42 s length with an observation every 3 s) and those with a random number of detections per pass (Random Length/RanLen: 3-7 seconds between observations with 3-13 observations in total). For the random length, there is also an experiment with an increased angular noise of the sensor, $\sigma_{az,el} = 0.4°$ instead of $\sigma_{az,el} = 0.25°$. Additionally, there are LSQ-ODs from two and three passes. Also considering the situation after 72 hours in Figure 6.8, it is visible that the data clearly follows an overall trend where also the different measurement conditions overlap. This also shows that depending on the observation geometry, an orbit which is calculated from three passes is not necessarily better than one using only two passes with a better observation geometry or temporal distribution. The use of the differential entropy seems to give a general measure of the available information and thus becomes independent of the specific parameters of an orbit determination.

As a second visualisation, Figure 6.9 shows the percentage of along-track uncertainties which are below 15 km as an example for the same measurement scenarios as before. Also here, it is visible that the different cases form a consistent trend, although there are some outliers. These plots show that it should be possible to give a statistical boundary of the propagated covariance based on the entropy of the covariance after the orbit determination.
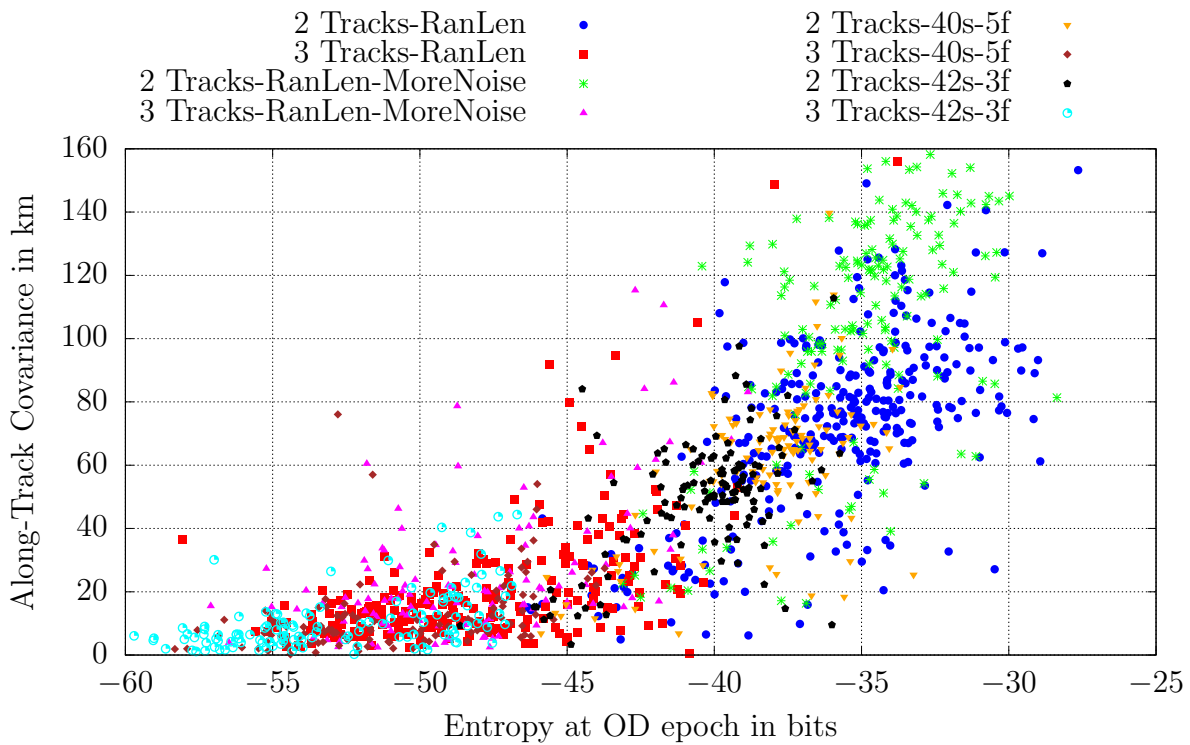
Figure 6.7: Entropy at OD epoch and the resulting along-track covariance after 48 hours for different cases.
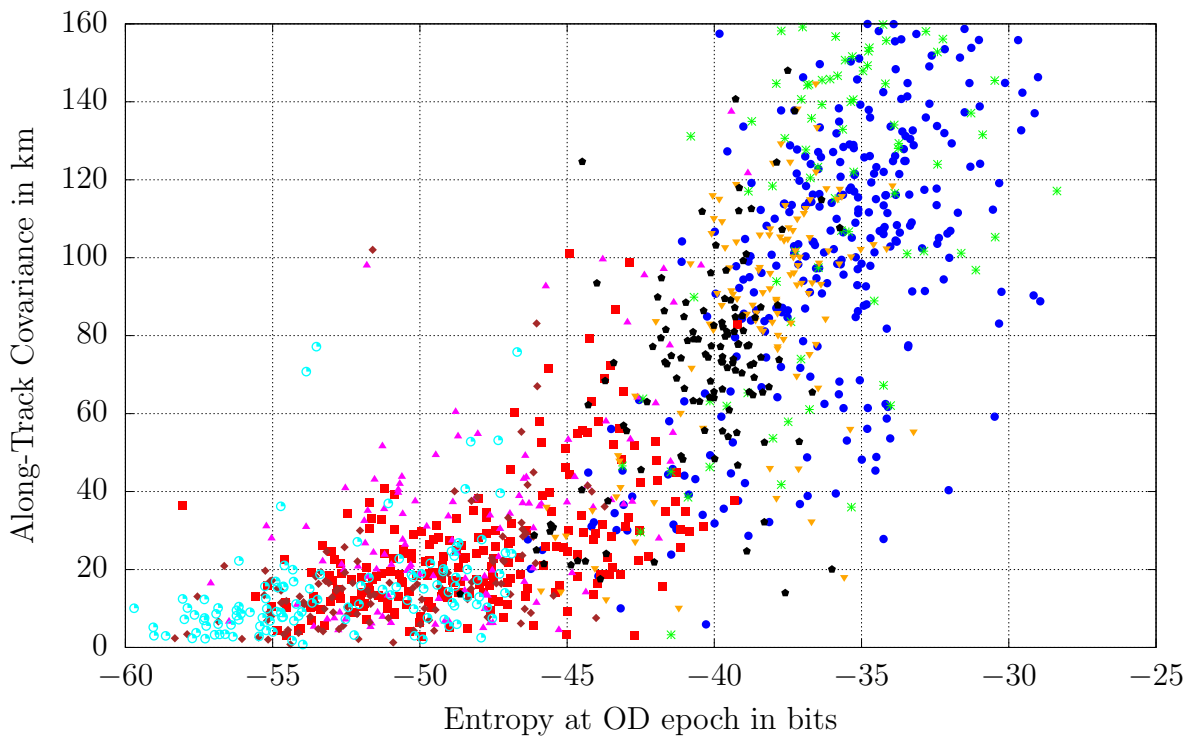
Figure 6.8: Entropy at OD epoch and the resulting along-track covariance after 72 hours for different cases.

(a) 48 hours

(b) 72 hours
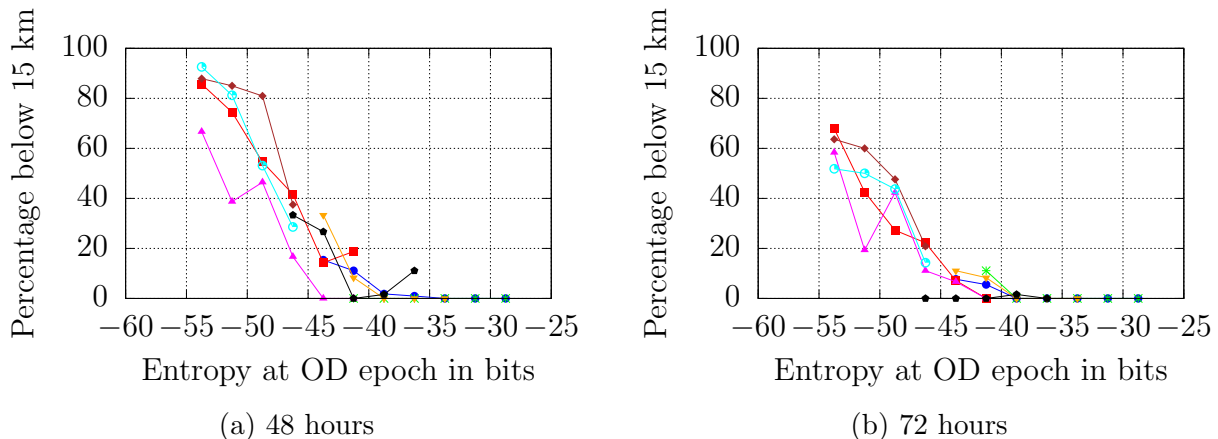
Figure 6.9: Entropy at OD epoch and the resulting percentage of along-track covariance below 15 km for different cases.

The exact performance criterion for a database accepting σ_{T} as an along-track uncertainty after t days would depend on its application. If the goal is to maintain these objects' orbits by a given sensor network, these numbers would depend on the sensor characteristics, whereas a database for conjunction assessment would probably require other specifications. Thus, there is no intention of defining a threshold here, but only to show the usability of the entropy as a concept.

To test the combination of the object confirmation and orbit-tracklet association, an experiment was performed which included both the initial creation of the object and the association of subsequent observations. For each object, an LSQ-OD is performed with the first two passes and it is checked whether the differential entropy $H < -50$ bits, which is derived from the previous experiments. If $H > -50$ bits, the next pass is added to the LSQ-OD until the condition is met. It is assumed that the tracklet-tracklet correlation correctly identifies these candidates. After the orbit uncertainty is below the threshold, the resulting orbit is propagated to all later observations and the orbit-tracklet association is attempted in different coordinate systems. The total time span of simulated observations is seven days. The subsequent measurements are only used to test the association and they are not integrated into the orbit as an update. Only orbits and tracklets from the same objects are tested for an association, thus there is no possibility of a false positive result.

The association is performed either in curvilinear RTN positions or measurement space. Four different approaches for the association are used in each coordinate system. The most simple one uses only one observation, independent of the total tracklet length, which serves mainly as a reference case. The other three are designed to use the entire information from the tracklet. The "Sum"-case uses the squared sum of the Mahalanobis distances over all m observations in the tracklet:

$$M_{d,total}^2 = \sum_{i=1}^{m} M_{d,i}^2 \; . \tag{6.3}$$

Theoretically in case of independent errors, this would lead to a $\chi^2(m \cdot \nu)$-distribution with the degrees of freedom equivalent to m times the degrees of freedom of the single observation (3 for curvilinear RTN and 4 for observations). Another approach is the "Time Bias Removal" (TBR) as explained in the previous section by minimising the range residuals. As a third approach, the association is performed for each detection within the tracklet and the entire

pass is accepted if more than a given percentage of observations in the tracklet have been positively correlated. This approach is called "Ratio" in the following. The association threshold for all tests is set at the cumulative value of 95% of the corresponding χ-distribution depending on the degrees of freedom.

Table 6.1: Success Rate of Orbit-Tracklet Association.

System		Random Length	40s-5f	42s-3f
Observations (meas. space)	Single	92.2	86.2	87.1
	Sum	94.4	89.8	93.9
	TBR	85.2	76.1	76.0
	Ratio	96.7	92.9	94.4
Curvilinear RTN	Single	92.9	87.5	89.0
	Sum	97.1	93.3	96.8
	TBR	86.3	83.1	81.6
	Ratio	98.5	96.7	97.8

Tracklets with a fixed length (40s-5f and 42s-3f) and with random lengths as explained in the previous section are used for the simulation. The results are shown in Table 6.1. If the probability distributions were matched perfectly, it would be expected to have exactly 95% of positive associations for the cases Single, Sum and TBR. The case Ratio should have 100%. It can be seen in the table that the actual association rates are slightly lower which is probably due to wrong estimates of the covariance after OD and propagation. Especially, the time bias removal is not even reaching 90% for any of the experiments.

(a) Curvilinear RTN   (b) Observation
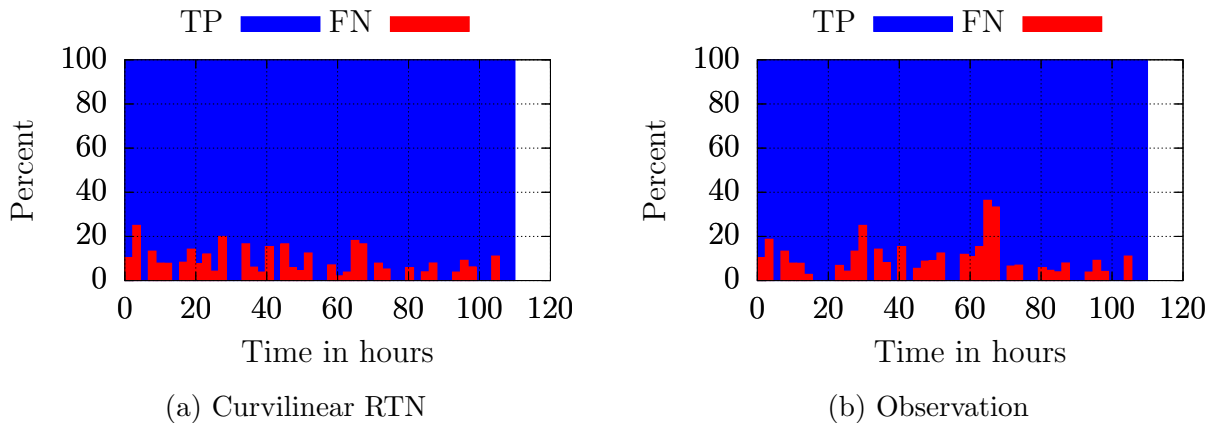
Figure 6.10: Percentage of TP and FN over the time between LSQ-OD and association.

Some additional plots are used to analyse the reasons. Figure 6.10 shows the percentage of true positive (TP) and false negative (FN) associations over the time between the LSQ-OD epoch, i.e. the orbit's reference epoch, and the epoch of the observation for the association of the single observations in both coordinate systems. It can be seen that there is no trend of an increased FN percentage with more time between the orbit's reference epoch and the

measurement. Figure 6.11 shows the same data set over the difference between the along-track error ΔAT calculated from the known true reference position of the object and the along-track component σ_{T} of the covariance matrix. From these plots, it can be seen that a FN association is more likely if ΔAT is larger than σ_{T}, which also makes sense intuitively.

(a) Curvilinear RTN

(b) Observation
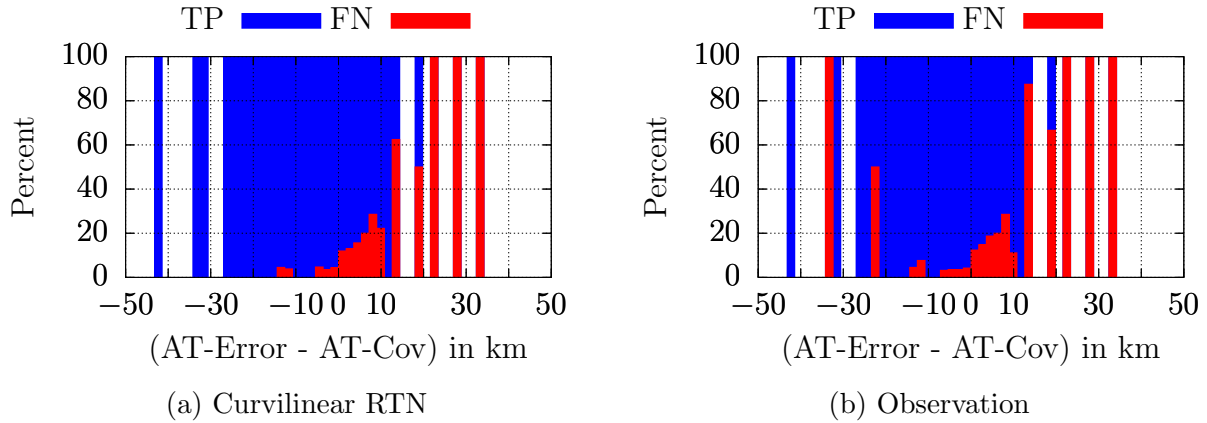
Figure 6.11: Percentage of TP and FN over the difference between the along-track component of the covariance and the present along-track error.

Additionally, the distribution of the Mahalanobis distances of the associations can be plotted to compare it to the theoretically expected χ-distribution with the corresponding degrees of freedom. Figure 6.12 depicts this comparison for the association of the single observations. In both cases, it can be seen that the theoretical distribution is roughly matched. Thus it can be suspected that the majority of the failed associations is due to outliers and not due to a general shift of the statistical distribution.

(a) Curvilinear RTN
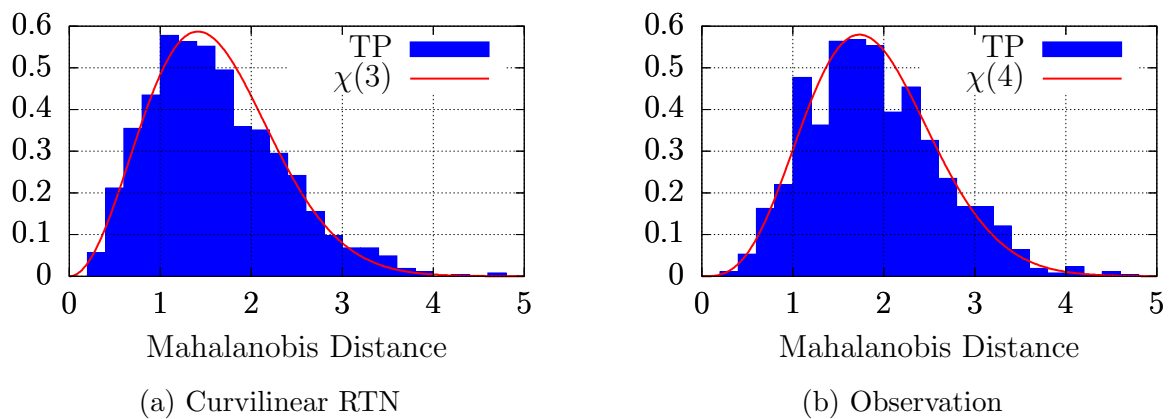
(b) Observation

Figure 6.12: Mahalanobis distance compared to reference χ-distribution for single observations (Random Length).

Using the "Sum"-approach, it had been mentioned that the degrees of freedom are equivalent to the product between the degrees of freedom of the single observation and the number of observations in the tracklet under the assumption of uncorrelated errors. However in the orbit-tracklet-association both the errors within one detection and the errors of the dif-

ferent observations within one pass are not statistically independent. Thus it can be seen from Figure 6.13, that the distribution is shifted to lower values as it effectively has less degrees of freedom, which also explains why the Sum-approach had the largest percentage of TP-associations.

(a) Curvilinear RTN
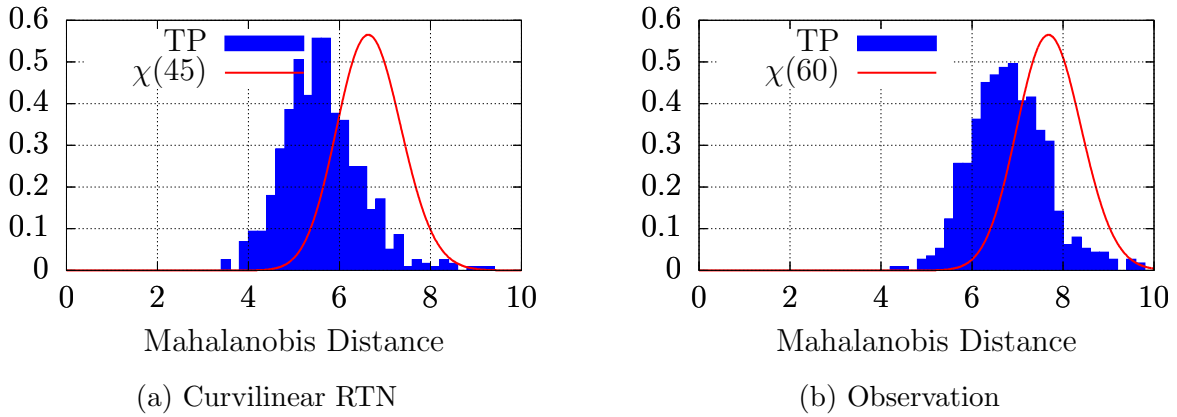
(b) Observation

Figure 6.13: Mahalanobis distance compared to reference χ-distribution for the "Sum"-approach of single observations (42s-3f).

Object Quality - Theory

To extend the work on the orbit-tracklet association, the measurements should also be used to give an impression on the current quality of the catalogue object. This parameter should reflect both the current uncertainty of the orbit and the newly received measurements as a feedback by comparing them to the expected ones based on the current orbit.

From the framework of the information theory, a property of an uncertain event from a probability distribution is the *surprisal* (or *information content*). This is used to emphasise that events with a lower probability contain more information if they occur, because they might lead to changes in the current models or assumptions. The surprisal of an event x_k with a probability $\mathcal{P}(x_k)$ is defined as (in bits):

$$I(x_k) = -\log_2\left(\mathcal{P}(x_k)\right) \ . \tag{6.4}$$

The entropy H, which was used in the previous sections, is the expectation value of the surprisal:

$$\mathrm{E}\left[I(x)\right] = H(p(x)) \ . \tag{6.5}$$

From these definitions it can be seen that an event with $\mathcal{P}(x_k) = 0$ has infinite surprisal, whereas an event with $\mathcal{P}(x_k) = 1$ has no surprisal and thus also contains no information. Classically, this concept is used for discrete probability distributions.

To transfer this to the continuous probability density functions used in the present problem, a definition of p_z has to be found as the *pseudo-probability* of the new measurement z_m, which fulfils the conditions above, while considering the uncertainty of both, the measurement and the state. This leads to the following equation:

$$p_z = \int_{-\infty}^{\infty} \sqrt{\mathcal{N}(\vec{z}|\vec{z}_e, \Sigma_{x,M} + \Sigma_M) \cdot \mathcal{N}(\vec{z}|\vec{z}_m, \Sigma_M)} \ d\vec{z} \ , \tag{6.6}$$

where $\mathcal{N}(\vec{z}|\vec{z}_e, \Sigma_{x,M} + \Sigma_M)$ is the assumed normal distribution of the expected measurement $\vec{z}_e$ based on the current state. The uncertainty of this distribution is taken from the sum of the measurement uncertainty Σ_M and $\Sigma_{x,M}$, which is the state's uncertainty Σ_x projected into the measurement space. The distribution $\mathcal{N}(\vec{z}|\vec{z}_m, \Sigma_M)$ is the one around the newly received measurement $\vec{z}_m$ with the measurement uncertainty Σ_M. This definition fulfils the criterion to be equal to 1 only if the two distributions are exactly the same, meaning that there is no uncertainty on the state and the expected measurement is matched exactly. If there is no overlap between the distributions, the probability is 0. Although, Equation 6.6 uses the normal distribution as an example, any probability distribution can be used. The value p_z is mathematically not a probability because its integral over all possible realisations of the measurement $\vec{z}_m$ is larger than one. However, it is also possible to use this integration over all $\vec{z}_m$ to find a normalisation constant which can be used to give p_z the properties of a probability distribution. Due to the log-operation of the surprisal, this normalisation would only lead to a constant offset, which will not be considered in the following. The surprisal is then calculated as:

$$I(z) = -\log_2 (p_z) \ . \tag{6.7}$$

This leads to measurements with a low surprisal if there is a small state uncertainty and the measurements are close to the expected ones. The integral for p_z can either be multidimensional and consider all observables or use only the most precise measurement as this provides the most information. In case of the radar, this is the range.

The idea behind this selection is that it considers both the difference between the expected and received measurement (Δz) and indirectly also the size of the state uncertainty. The larger the state uncertainty, the larger also the minimum achievable surprisal, which makes sense considering that an object with a large uncertainty should not be a high-quality object with a low surprisal. At the same time, the surprisal also becomes sensor-dependent if there are different noise levels between sensors. For most cases, a more precise sensor can produce measurements with a higher level of surprisal because it can sample the uncertainty area at a finer resolution. In principle it could be possible to compare different sensors' minimum surprisal values based on the same orbit and observation geometry.

The behaviour of the surprisal is visualised in Figure 6.14 for an example with an along-track error of a few kilometres which dominates the range uncertainty compared to the sensor's measurement uncertainty. The sensor's noise and the difference compared to the expected measurement Δz (called error in the plot) is varied systematically. It is visible that for a given measurement error Δz the surprisal reduces with an increased sensor noise, because the reliability and thus the information content of the measurement reduces. If the sensor noise is fixed, the surprisal is the least for $\Delta z = 0$, because this confirms the current estimate of the orbit and thus has the smallest possible information gain. As can be seen in the plot, the difference Δz is much larger than the sensor noise, thus the variance due to the sensor noise is only leading to minor variations of the surprisal.

One possibility to remove the sensor-dependency would be to normalise the surprisal by the minimum surprisal of the sensor, which is calculated as $I_{Sensor,0} = I(z_m = z_e)$.

To further analyse the variability of the surprisal, a Monte Carlo experiment was conducted for a single state with a covariance matrix in RTN coordinates. The measurements were generated after the actual state error was randomly sampled from the state covariance. For each range measurement, the surprisal is calculated. The results are given by the plot "Ref" in Figure 6.15, which shows the variation of the surprisal due to different realisations of
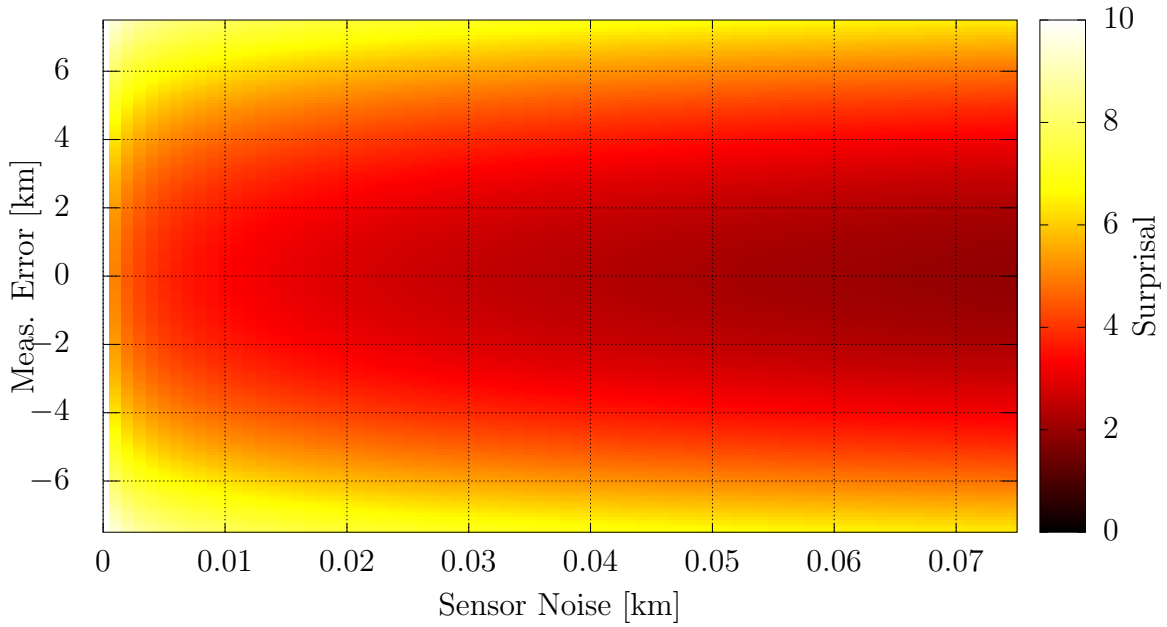
Figure 6.14: Surprisal over different sensor noise level and the offset (error) compared to the expected measurement.

(a) Histogram

(b) Cumulative
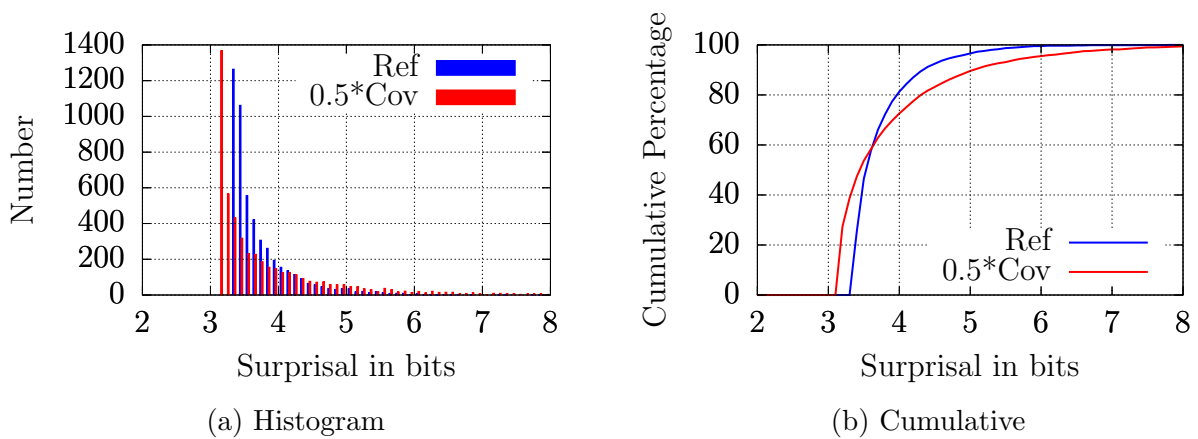
Figure 6.15: Experiment comparing the reference results to those obtained with a covariance of half the actual size.

the along-track error. As a comparison, the same calculation has been performed under the assumption that the current estimate of the covariance is only half of the sampled one, thus overly optimistic. This leads to two opposing effects. In cases where the actual along-track error is small enough to be consistent even with the smaller covariance, it leads to smaller values of the surprisal because the uncertainty is less. At the same time, the tail of the surprisal values in the histogram becomes more pronounced because the measurements with larger offsets are unexpected and thus contain more information. This second case, when the error is larger than what would be consistent with the covariance matrix, is the one which should be detected and as it can be seen the surprisal is a possible tool for that.

Object Quality - Experiment

To test the proposed parameter, the same experiment setup as in the previous section has been used. The orbit determination is performed on subsequent tracklets until $H < -50$ bits and the resulting orbit is then propagated to all following measurements. Here, also the surprisal is calculated as described for each new measurement.

The results are shown in Figure 6.16 with the along-track error calculated from the (in the real case unknown) true position on the x-axis and the size of the along-track covariance as a colour code. The surprisal is again calculated by using only the range measurement. It can be seen that very low values of the surprisal are reached for small along-track errors and covariances as expected. The zoomed version in Figure 6.17 also shows that objects with a low along-track error but a large covariance lead to a larger surprisal, because they contain more information.
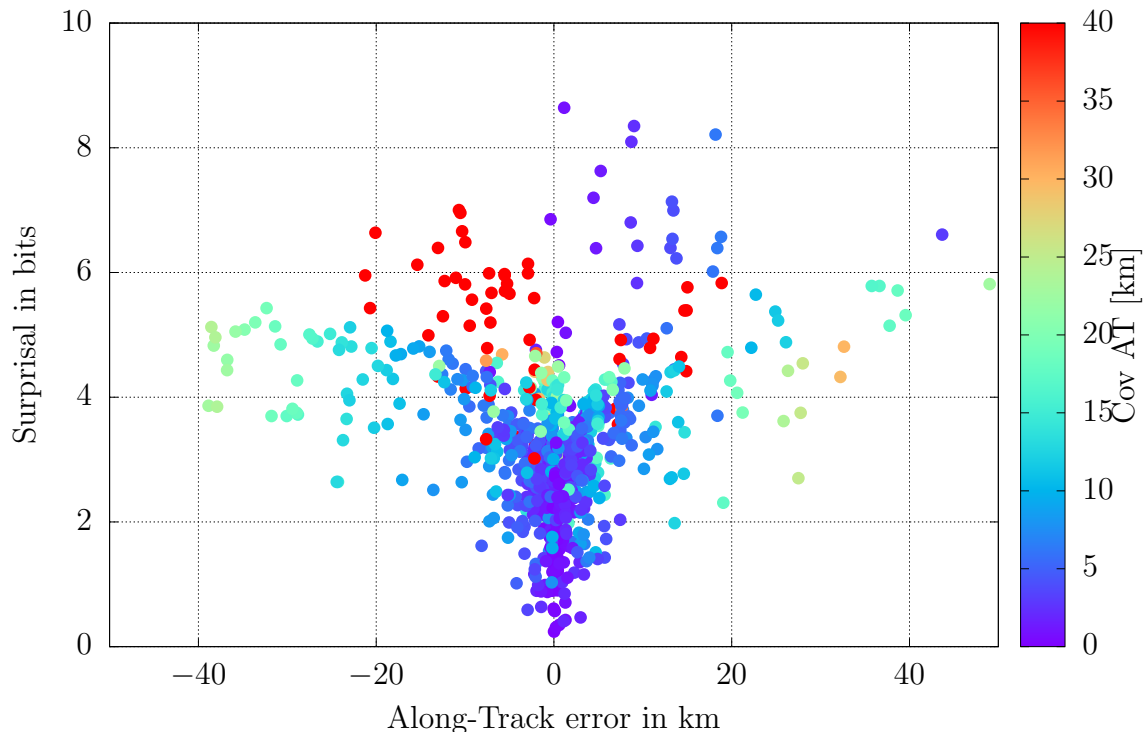
Figure 6.16: Surprisal over along-track error and covariance using propagated orbits from the orbit determination.
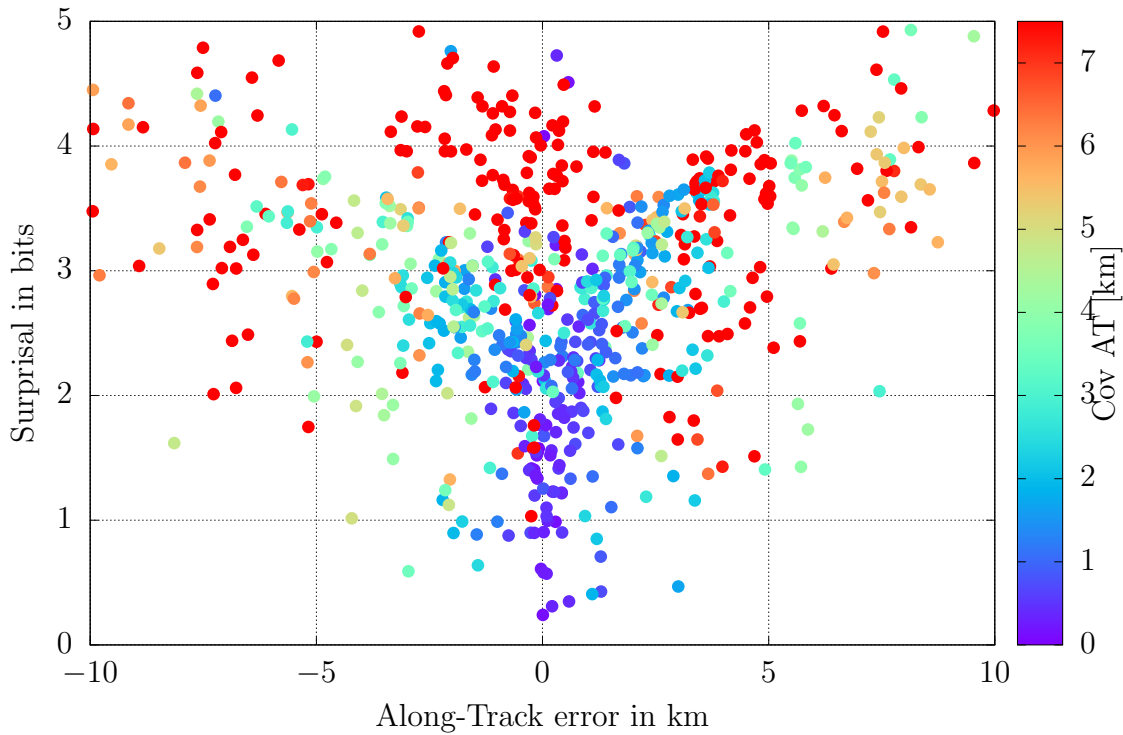
Figure 6.17: Surprisal over along-track error and covariance using propagated orbits from the orbit determination (zoom).

6.2 Radar-Optical Association

The text and figures in this section have been taken from the publication (Reihs et al., 2019a). Partially, they have been revised and adjusted for this thesis and used in accordance with the copyright agreement.

6.2.1 Overview

The region of the Highly Eccentric Orbit, e.g. the Geostationary Transfer Orbit (GTO), also shows increasing space debris populations, mainly due to breakup events (Braun et al., 2019). As the HEO objects pass through LEO and potentially also close to GEO, they pose a potential collision risk for objects in both these important regions and may even couple the overall collision risk for objects in these distant orbits by connecting them (McKnight et al., 2018). In order to mitigate this risk at least for conjunctions involving active satellites which can perform collision avoidance manoeuvres, the orbits of HEO objects have to be maintained with the help of regular observations. Using radar and optical measurements in their traditional, standard approach, a radar only observes objects in the LEO region and a telescope focuses on objects in high altitudes close to GEO. If HEO objects are only observed in this way, the detections are all around its perigee or apogee, respectively depending on the type of sensor. Such an observation pattern would severely limit the information available and increase the uncertainties of the calculated orbits. Thus it is expected that a combined

processing of radar and optical measurements improves the quality of the orbits. While the routine update of an orbit stored in a database can be done involving different measurement types, the treatment of detections which cannot be assigned to a known object is more challenging and is considered in the following for the correlation problem.

6.2.2 Correlation Method

By combining one optical and one radar tracklet the available attributable vectors are:

$$\mathcal{A}_{AE} = \{t_r, \rho_r, \dot{\rho}_r, az, el\} , \tag{6.8}$$

$$\mathcal{A}_{Opt} = \left\{t_o, \alpha, \delta, \dot{\alpha}, \dot{\delta}\right\} , \tag{6.9}$$

containing the radar measurements: range ρ_r, range-rate $\dot{\rho}_r$, azimuth az, elevation el, and the optical measurements: right ascension α, declination δ and their time-derivatives $(\dot{\alpha}, \dot{\delta})$ as described in Section 2.2.1. Both are given at their respective epoch, t_r and t_o.

In order to apply the IOD method from Section 4.3, it is necessary to add a hypothesis on the range ρ_o at the epoch of the optical measurement t_o. This is also a simplification compared to the correlation of two optical tracklets, which requires two hypotheses for the IOD (Siminski et al., 2014). This range hypothesis is combined with the radar range and angular measurements to compute the orbit between the two positions.

$$
\begin{array}{rcl}
\{\rho_o\} & \rightarrow & \text{Hypothesis} \\
\{\rho_r, az, el, \rho_o, \alpha, \delta\} & \rightarrow & \text{Orbit} \\
\left\{\dot{\rho}_r, \dot{\alpha}, \dot{\delta}\right\} & \rightarrow & \text{Discriminator}
\end{array}
$$

Similarly as in Section 4.3 for the radar case, also here the Mahalanobis distance is calculated from the elements in the discriminator by comparing their measured value x_{M} to the value x_{C} which is computed from the newly derived orbit.

In practice, this approach leads to an optimisation problem of finding the best hypothesis on the optical range, i.e. the one which results in the lowest Mahalanobis distance. Once a value for the range ρ_o is set, two positions are available and thus the perturbed initial orbit determination can be performed. A line search along ρ_o with a numerical gradient approximation is performed to find the minimum of M_{d}.

As a first step, the topography of the loss function M_{d} shall be analysed to test if it can be optimised easily. One example of a loss function is given in Figure 6.18. Depending on the time between the two tracklets, the connection of the two points may be possible with different numbers of completed revolutions which was also the case for the radar measurements in LEO. In the plot, it can be seen that there is a distinct minimum for each number of revolutions with different minimum values. The absolute minimum and true solution can be found at ten revolutions in this example.

To analyse this further, Figure 6.19 depicts the Mahalanobis distance over the hypothetical range for the absolute minimum from the previous plot which represents one single optimisation problem of the correlation. A distinct minimum encompassed by two nearly linear slopes is visible, which should be found in an optimisation process using numerically calculated gradients. Practically, the minimum for each feasible number of revolutions has to be calculated and then the one with the lowest Mahalanobis distance is chosen as the final solution.
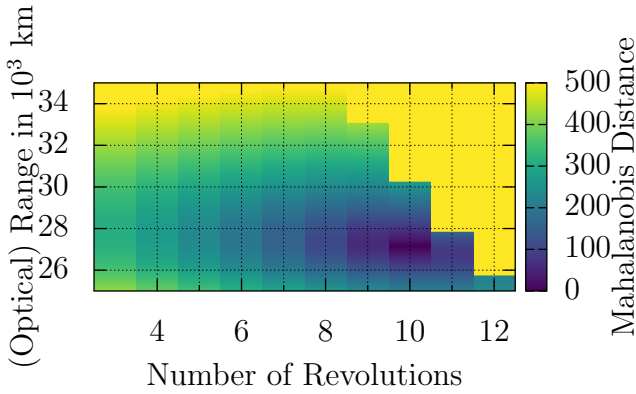
Figure 6.18: Example of the loss function M_d for a specific pair of radar-optical tracklets.
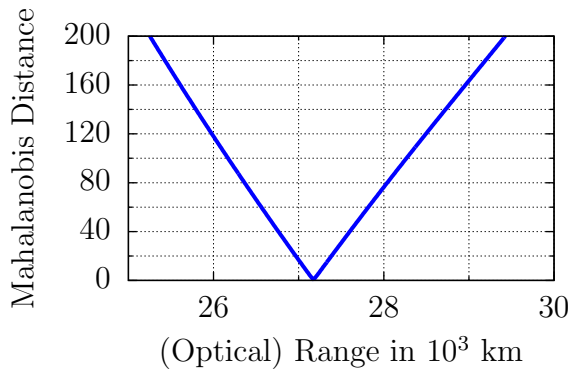
Figure 6.19: Example of the one-dimensional optimisation problem for one specific number of revolutions.

6.2.3 Simulations

The simulated measurements use an object population extracted from Space-Track which is propagated numerically using (Orekit, 2018) with the same propagation settings as in Section 5.1. Different measurement stations and object populations in HEO are simulated with the parameters given in Table 6.2. Depending on the scenario, the simulations have different durations ranging from three days for a multi-station setup to eleven days for a single station in central Europe. Different scenarios are necessary because the sub-population which can be observed at perigee by a radar and close to apogee by a telescope at night-time is limited. In order to obtain a larger sample, the results from the different radar-optical surveys are merged to create the following plots.

Table 6.2: Definition of the FoR and the measurement standard deviations σ (Radar: values at $\rho_r = 750$ km).

Size FoR, Radar	$60° \times 20°$
Angles (Radar), σ	$0.17°$
Range, σ	20 m
Rate, σ	$20 \frac{m}{s}$
Angles (Optical), σ	1"

For the optical measurements, the tracklet length is 90 s with a measurement each 15 s which is consistent with real measurements of HEO objects at the AIUB observatory in Zimmerwald. In case of the radar tracklets, their length depends on the dwell time in the Field of Regard, which can be up to two minutes and is approx. 40 s on average. These tracklets are used for the radar-optical case whereas the radar-only case employs 40 s tracklets without FoR to increase the number of detections and true correlations. The RPP is also used for these experiments.

(a) Radar-only   (b) Radar-Optical
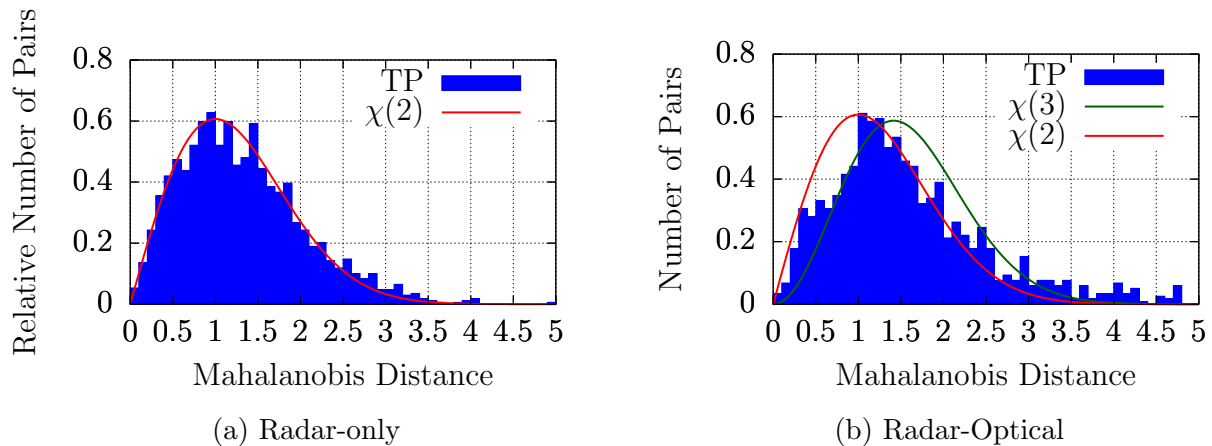
Figure 6.20: Distribution of the true positives' Mahalanobis distances.

The following analysis focuses on the results of the true positives. For all experiments, there are less than 5%-10% false positives after the RPP, which are not considered in the following. The distributions of the radar-only case in Figure 6.20a and of the radar-optical case in Figure 6.20b are shown as relative numbers to compare them to the theoretically expected χ-distribution of the Mahalanobis distances depending on the degrees of freedom which usually is equal to the number of elements in the discriminator. Thus, the radar-only case has two degrees of freedom and the radar-optical case has three. As one can see, the radar-only case matches the expected χ-distribution very well, whereas the radar-optical one is slightly shifted to lower Mahalanobis distances but still exhibits a clear peak in the expected region. The plot with the radar-optical case also includes the comparison to the $\chi(2)$-distribution, because the degrees of freedom are not necessarily equivalent to the dimension of the discriminator. The reason is that the iteration on the optical range during the optimisation removes one degree of freedom. Here, the use of different measurement types at different locations on the orbit probably leads to a good approximation of the orbit, while using the true (but here unknown) range should lead to a matching $\chi(3)$-distribution. In Section 6.3, this is discussed further for the space-based optical-only case.

The remaining analysis covers the influences of the different elements in the radar-optical discriminator to test whether the different physical measurement types have any specific or dominating influence on the correlation. Firstly, the range-rate discriminators are compared between the cases for radar-only and the radar-optical in Figure 6.21. Although the plot is two-dimensional, the range-rate discriminator for the radar-optical case is only one-dimensional and thus plotted along the x-axis. It is clear that the range-rate discriminators are similar in magnitude for both cases, which is also consistent with the assumed measurement noise. It shall also be noted that the two-dimensional distribution of discriminators for the radar-only case is consistent with a normal distribution, showing no biases or preferences

Radar-only • Radar-optical▲
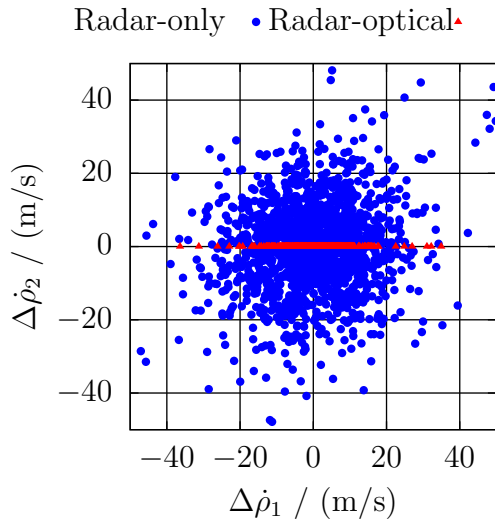
Figure 6.21: Distribution of the differences of the range-rate discriminators comparing the radar-only and radar-optical case.

to any direction, which implies that both range-rates have similar distributions of their differences in the discriminator. This is consistent with the orbit determination method, because it does not prefer one of the two positions and thus the discriminators should be distributed evenly. The same is true for the radar-optical case as the majority of the points are close to zero. Additionally, for the radar-optical case the discriminators in the optical part are compared in Figure 6.22. Also here, the discriminators are evenly distributed between the two angular rates within the same order of magnitude.
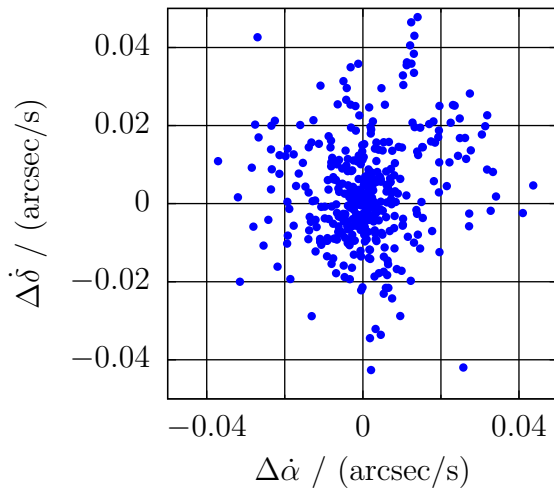
Figure 6.22: Distribution of the differences of the angular rates discriminators for the radar-optical case.

In order to analyse the influence of the discriminator in the radar-optical case in more detail, the covariance matrix $\Sigma_{M,C}$, and thus also the Mahalanobis distance, is separated into the different elements of the discriminator and the uncertainties are split into their two contributing parts, i.e. the measurements and the computed values from the orbit. This is achieved by assuming a diagonal correlation matrix without cross-correlations between the different discriminators, which can be used as an approximation although this would usually not be the case. The overall covariance matrix $\Sigma_{M,C}$ of the discriminators is the sum of the measurement and computed orbit covariance as explained in Section 4.3:

$$\Sigma_{M,C} = \begin{bmatrix} \sigma^2_{\dot{\rho}_r,M} + \sigma^2_{\dot{\rho}_r,C} & 0 & 0 \\ 0 & \sigma^2_{\dot{\alpha},M} + \sigma^2_{\dot{\alpha},C} & 0 \\ 0 & 0 & \sigma^2_{\dot{\delta},M} + \sigma^2_{\dot{\delta},C} \end{bmatrix} \quad (6.10)$$

In combination with Equation 3.1 this leads to the following simplification for the calculation of the Mahalanobis distance:

$$M_{\mathrm{d,total}} = \sqrt{M^2_{\mathrm{d},\dot{\rho}_r} + M^2_{\mathrm{d},\dot{\alpha}} + M^2_{\mathrm{d},\dot{\delta}}} \ . \quad (6.11)$$

The Mahalanobis distance for one discriminator x is calculated as:

$$M^2_{\mathrm{d},x} = \frac{\Delta x^2}{\sigma^2_{x,M} + \sigma^2_{x,C}} \quad (6.12)$$

With some algebraic transformations, this can be generalised to:

$$\frac{1}{M^2_{\mathrm{d},x}} = \frac{1}{M^2_{\mathrm{d},x,M}} + \frac{1}{M^2_{\mathrm{d},x,C}} \ , \quad (6.13)$$

with $M_{\mathrm{d},x,M}$ and $M_{\mathrm{d},x,C}$ as the Mahalanobis distances only due the measurement or orbit computation:

$$M^2_{\mathrm{d},x,M/C} = \frac{\Delta x^2}{\sigma^2_{x,M/C}} \ . \quad (6.14)$$

These relations are used in the following for further analyses.
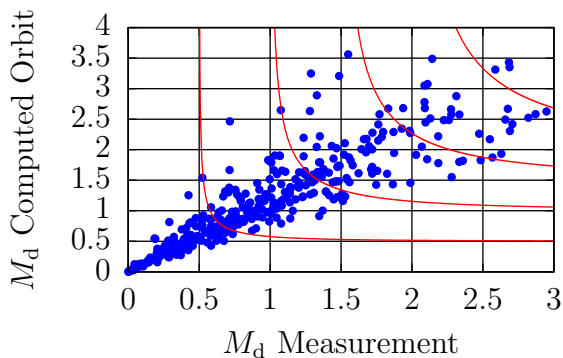
Figure 6.23: Contributions of the measurement and orbit uncertainties to the Mahalanobis distance at the radar measurement in the radar-optical case. Lines of constant combined Mahalanobis distance are added for $M_{\mathrm{d}} = \{0.5, 1.0, 1.5, 2.0\}$.

Figure 6.23 depicts the range-rate discriminator split in its components, i.e. the measurement and orbit uncertainty. Lines of constant combined Mahalanobis distance are added to the plot according to Equation 6.13. It is visible that both components contribute approximately equally to the total Mahalanobis distance of the radar measurement. In contrast to that, Figure 6.24 compares the same values for the angular rates. In this case, the Mahalanobis distance due to the orbit is larger than the one due to the measurement. The lines of constant total Mahalanobis distance are predominantly acting as vertical straight lines, thus the total Mahalanobis distance is dominated by the measurement, see Equation 6.13. Effectively this means that $\sigma^2_C \ll \sigma^2_M$, yielding $M^2_{\mathrm{d},C} \gg M^2_{\mathrm{d},M}$. The uncertainty due to the orbit computation is smaller than the one due to the measurement and contributes less to the total uncertainty when they are added.
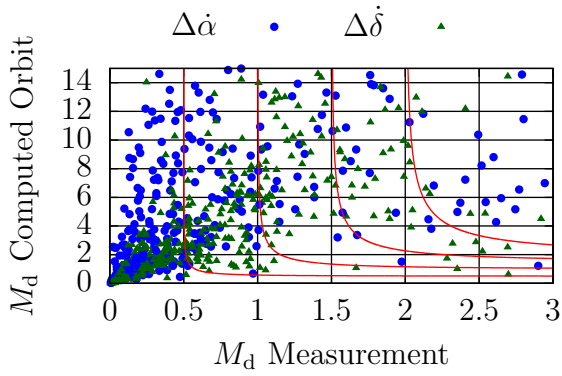
Figure 6.24: Contributions of the measurement and orbit uncertainties to the Mahalanobis distance at the optical measurement in the radar-optical case. Lines of constant combined Mahalanobis distance are added for $M_d = \{0.5, 1.0, 1.5, 2.0\}$.
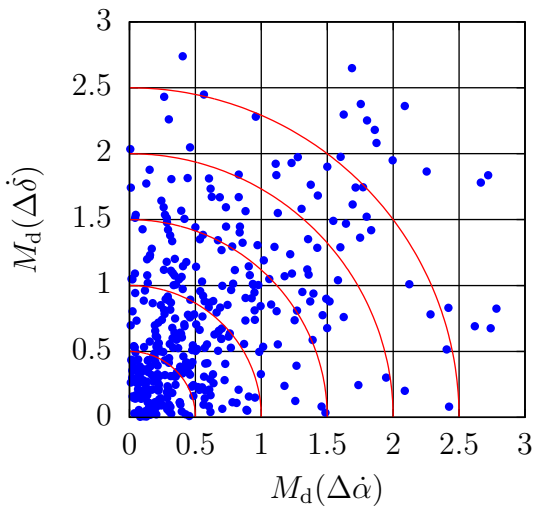
Figure 6.25: Contributions of the optical measurements to the total Mahalanobis distance in the radar-optical case. Lines of constant combined Mahalanobis distance are added for $M_d = \{0.5, 1.0, 1.5, 2.0, 2.5\}$.

Finally the influence of the different discriminators is compared according to Equation 6.11. Also here the lines of constant Mahalanobis distance are added which form an arc of a circle. Figure 6.25 compares the two optical discriminators, i.e. the angular rates. It is visible that considering the entire population both parts contribute equally to the total optical Mahalanobis distance.

The comparison between the radar-discriminator and the two optical discriminators is shown in Figure 6.26. Also here, it is visible that both measurement types contribute equally to the total Mahalanobis distance. Combining this information with the one derived from Figure 6.25, it is concluded that all three discriminators contribute equally to the total Mahalanobis distance.
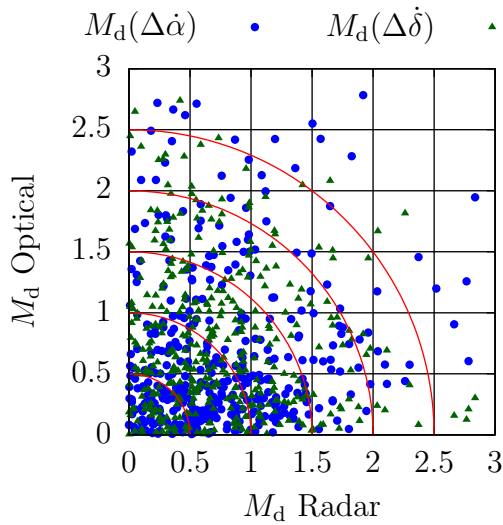
Figure 6.26: Contributions of the radar and optical measurements to the total Mahalanobis distance in the radar-optical case. Lines of constant combined Mahalanobis distance are added for $M_{\mathrm{d}} = \{0.5, 1.0, 1.5, 2.0, 2.5\}$.

In Figure 6.27, the correlation results are compared with regard to the standard deviations for the estimation of the orbital elements semi-major axis a, eccentricity e, inclination i, right ascension of the ascending node Ω and argument of perigee ω, which are derived by comparing them to their respective ground truth of the simulation. It can be seen that the radar-optical measurements have better results than radar-only in all cases. Especially the location of the perigee and the estimation of the orbital plane is significantly better.
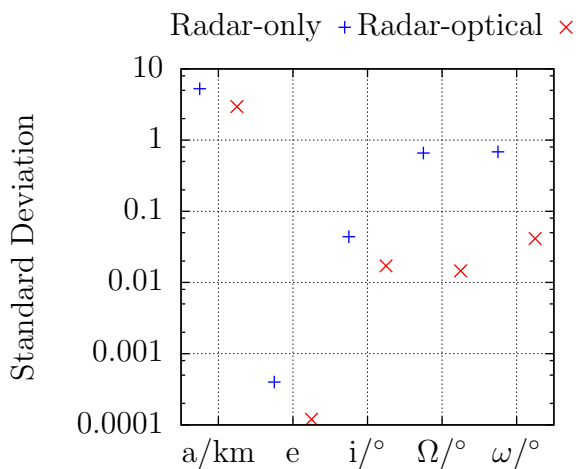
Figure 6.27: Comparison between the radar-only and radar-optical case for the standard deviations of the estimation errors of the orbital elements when compared to the ground truth.

6.2.4 Discussion

Concerning the details of the radar-optical correlation, one could see that the discriminators are all evenly distributed and their separated Mahalanobis distances are of similar magnitude. Thus, it can be concluded that neither of the discriminators is dominating the uncertainties and the method considers all in a similar way. It was also shown that the Mahalanobis distance of the angular rates is mainly dominated by the measurement uncertainty compared to the uncertainty of the computed orbit. This implies that the angular rates are rather robust against the noise in the parameters used for the orbit estimation, at least when compared to the measurement noise. It is concluded that neither of the uncertainties can be ignored to reduce the computational burden of the correlation process, because all contribute equally to the result even with different physical measurement types.

Considering the orbits, the main improvement of the radar-optical case is due to the better coverage of the orbit. The radar measurements are always close to the perigee, while the optical telescopes can add measurements close to the apogee. This improves especially the estimation of the orbital plane and the shape of the ellipse as the angle between the two radius vectors used in the orbit determination increases. Concerning the semi-major axis, it was also estimated more precisely in the radar-optical case for a large data sample, but if the radar and optical measurements are close together, i.e. during the same revolution within a few hours, the estimation of the semi-major axis becomes significantly worse.

Finally, this approach also suffers from a degradation if the measurements are close to being on exactly opposite sides of the orbit, thus roughly 180° apart. In this case, problems may arise due to the rotations during the J_2-correction because the definition of the orbital plane is very sensitive to small changes in this region.

One challenge of applying this combination of measurements to practical space surveillance is that the population of objects which can be observed at the perigee by a radar and at night-time at apogee by a telescope is very limited for single stations. Thus, this observation fusion method is probably most effective in multi-station networks which can reliably observe a majority of the relevant near-Earth regions.

6.3 Space-based Optical Sensor

Preliminary results of this analysis have been published in (Reihs et al., 2019b) and are partially used in the following section.

6.3.1 Introduction

The increase of the space debris population is also affecting the region of the Geosynchronous Orbit (GSO), see Section 1.1, which includes the Geostationary Orbit (GEO). The term GEO is used here to refer to the specific subset of objects which have a low inclination, a low eccentricity and an orbital period of one sidereal day within the GSO region. The GSO region is defined here to encompass the orbits with: 38 000 km $< a <$ 46 000, $e < 0.25$ and $i < 25°$. Objects in these high-altitude orbits are usually observed with telescopes from ground. These ground-based telescopes have the disadvantages that their observations can be restrained by bad weather or atmospheric seeing for example and that due to the co-rotation of objects in GEO not all objects are visible from one site. One possibility to mitigate these disadvantages

is to place a telescope on a satellite and take the observations from space. Some operational space-based sensors already exist, e.g. the SBV/MSX (Sharma et al., 2002), Sapphire (Scott et al., 2013) and NEOSSat (Abbasi et al., 2019). The European Space Agency (ESA) is currently developing technologies and components for a proposed mission as well. The basic mission idea is to observe objects in GSO from an observer satellite in a sun-synchronous, polar orbit in LEO (Flohrer et al., 2011). With such a design, the objects in GSO would pass through the region illuminated by the sun on average once per day giving the chance to observe each object in GSO daily with a single sensor. Studies funded by ESA have already investigated different aspects of such a mission, e.g. the camera design (Utzmann et al., 2014), the mission design and operations (Utzmann, 2013), and also the development of an in-situ simulator to model optical measurements using a real camera system (Utzmann et al., 2017).

The choice of the observer orbit and the targeted orbital regime for the observations, taken from (Flohrer et al., 2011) for the present analysis, is the main influence on the characteristics of the entire mission. Other proposed mission designs include equipping commercial GEO satellites with a camera (Lowe et al., 2010), the use of constellations for LEO-to-LEO monitoring (Felicetti and Emami, 2016; Du et al., 2019) or the observation of non-GSO objects from LEO (Hu et al., 2017).

Considering the orbit determination from a single tracklet, several analyses of its feasibility and quality can be found in the literature for different mission designs and observation strategies, see e.g. (Vallado, 2010; Ansalone and Curti, 2013; Sciré et al., 2015; Li et al., 2018) for a non-exhaustive list.

Also for the space-based optical observations, the tracklet correlation can be used to generate candidate orbits with more confidence and more initial data than those from a single tracklet. Of the already discussed correlation methods for ground-based optical observations, see Section 3.2.2, only the method by (Fujimoto and Scheeres, 2013) has been explicitly tested for space-based observations. Another example of a method for space-based optical observation correlation can be found in (Lei et al., 2018) using a LEO-to-LEO mission design.

This overview already shows a large variety of possible scenarios for a space-based space debris monitoring mission and the processing of the observations. The introduced current mission design by ESA is used and the correlation method is chosen as the one by (Siminski et al., 2014). It should also be noted that a space-based sensor is just one part of an overall monitoring system (Donath et al., 2010) and the aspect of the fusion between ground- and space-based measurements will also be considered.

6.3.2 Mission Design

The basic mission design of observing from a polar LEO to GSO was introduced in (Flohrer et al., 2011) for a sun-synchronous orbit close to the terminator plane. The observation geometry based on recent ESA studies (Utzmann, 2013) is shown in Figure 6.28. Two fences to observe the objects are created at a fixed angle $\Delta\alpha_F$ relative to the anti-solar (AS) direction, here $\Delta\alpha_F = (9°, 31.5°)$ locating both fences on the same side next to the Earth shadow. The separation of the fences is chosen such that an object with an orbital period of one sidereal day requires 1.5 hours to reach the second fence for a follow-up observation. The definition of the fences in that way also gives relatively stable illumination conditions for the observations over the year (Flohrer et al., 2011). To increase the visibility in these

fences, the observer orbit is rotated further away from the terminator plane compared to (Flohrer et al., 2011). The orbital elements are provided in Table 6.3. Figure 6.29 depicts the percentage of the time over one revolution of the observer during which an object with $[a = 42164$ km, $e = 0]$ would be visible at different positions relative to the AS direction and the equatorial plane. Being visible is defined here as not being in the Earth shadow and the line-of-sight has to be unobstructed by the Earth including its atmosphere (assumed $h_a = 150$ km). The most striking features in the plot are the Earth shadow, which is above the equatorial plane in February, and the region with constant visibility, which is shifted from the AS direction by the same angle as the RAAN from the terminator plane and above the equatorial plane due to the observer orbit's inclination. An observer on an orbit with $i = 90°$ would have an even distribution above and below the equatorial plane, but the lack of the sun-synchronous motion would not allow constant observation conditions.

Considering the observations, it is assumed that the sensor is able to detect all objects crossing a fence without further consideration of the satellite's pointing strategy or the technical details of the detector. Studies about the detectability are beyond the scope of this work, but this is also discussed in (Flohrer et al., 2011). The length of the measured tracklets and the intervals between the detections within a tracklet also depend on the specific design of the payload and the on-board processing. The current assumptions are given in Table 6.4. Additionally, it is assumed that by using GPS it is possible to have a high-precision orbit for the observer satellite which means that errors or uncertainties of its positions are negligible compared to the other measurement uncertainties.
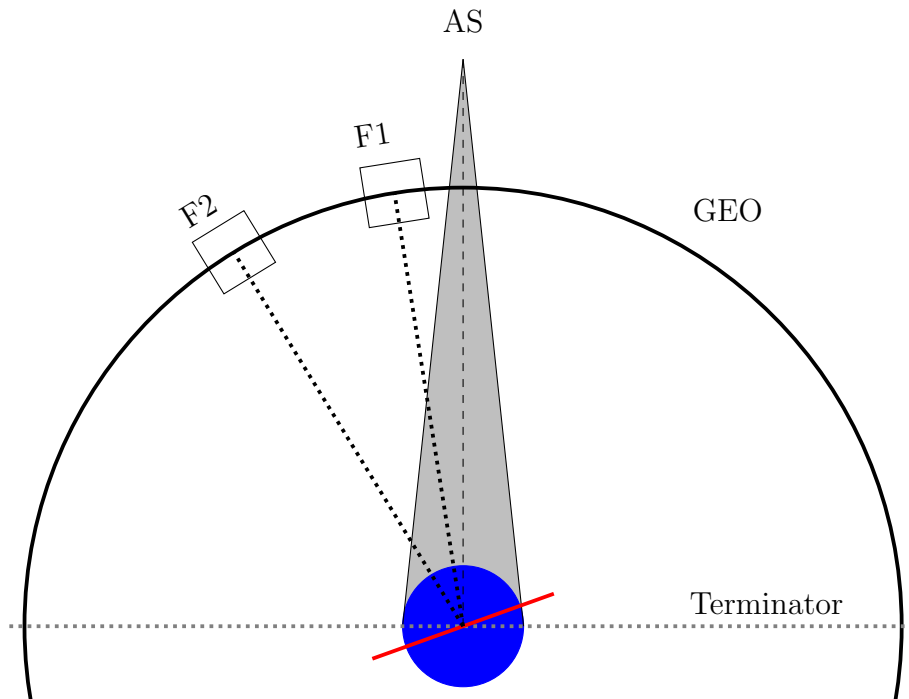
Figure 6.28: Sketch of the observer's orbit (red) and the two fences (F1, F2) which are defined relative to the anti-solar direction (AS).

Table 6.3: Orbital elements of the observer platform at Feb 11, 2019, 18:00 UTC.

Semi-major Axis, a	7128.0 km
Eccentricity, e	0.00001
Inclination, i	98.39°
Right Ascension of the Ascending Node (RAAN), Ω	74.04°
Argument of Perigee (AoP), ω	0.0°
True Anomaly, φ	0.0°
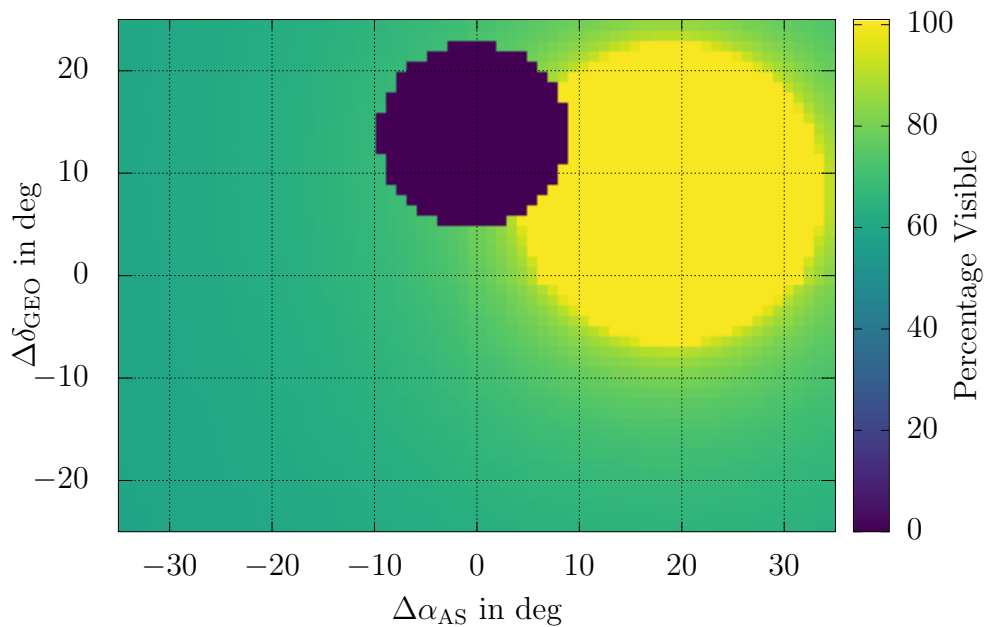
Figure 6.29: Visibility of objects in GSO relative to the anti-solar direction and the equatorial plane as a percentage of time during one revolution of the observer in February.

6.3.3 Correlation Method

Attributables

Due to the dynamics of the space-based observer, a third order polynomial was chosen for the attributables in this work:

$$\theta_{\alpha,\delta} = \bar{\theta}_{\alpha,\delta} + \dot{\bar{\theta}}_{\alpha,\delta} \cdot \Delta t + \frac{\ddot{\bar{\theta}}_{\alpha,\delta}}{2} \cdot \Delta t^2 + \frac{\dddot{\bar{\theta}}_{\alpha,\delta}}{6} \cdot \Delta t^3 \ . \tag{6.15}$$

This was decided after an analysis based on the accuracy of the fitted values and their uncertainties, see Section 2.2.1 for further information on the process of fitting and testing. The resulting attributable including the angular acceleration and the reference time t is:

$$\mathcal{A}_{SBO} = \left\{ t, \bar{\alpha}, \bar{\delta}, \dot{\bar{\alpha}}, \dot{\bar{\delta}}, \ddot{\bar{\alpha}}, \ddot{\bar{\delta}} \right\} \ . \tag{6.16}$$

(a) Angles

(b) Rate

(c) Acceleration
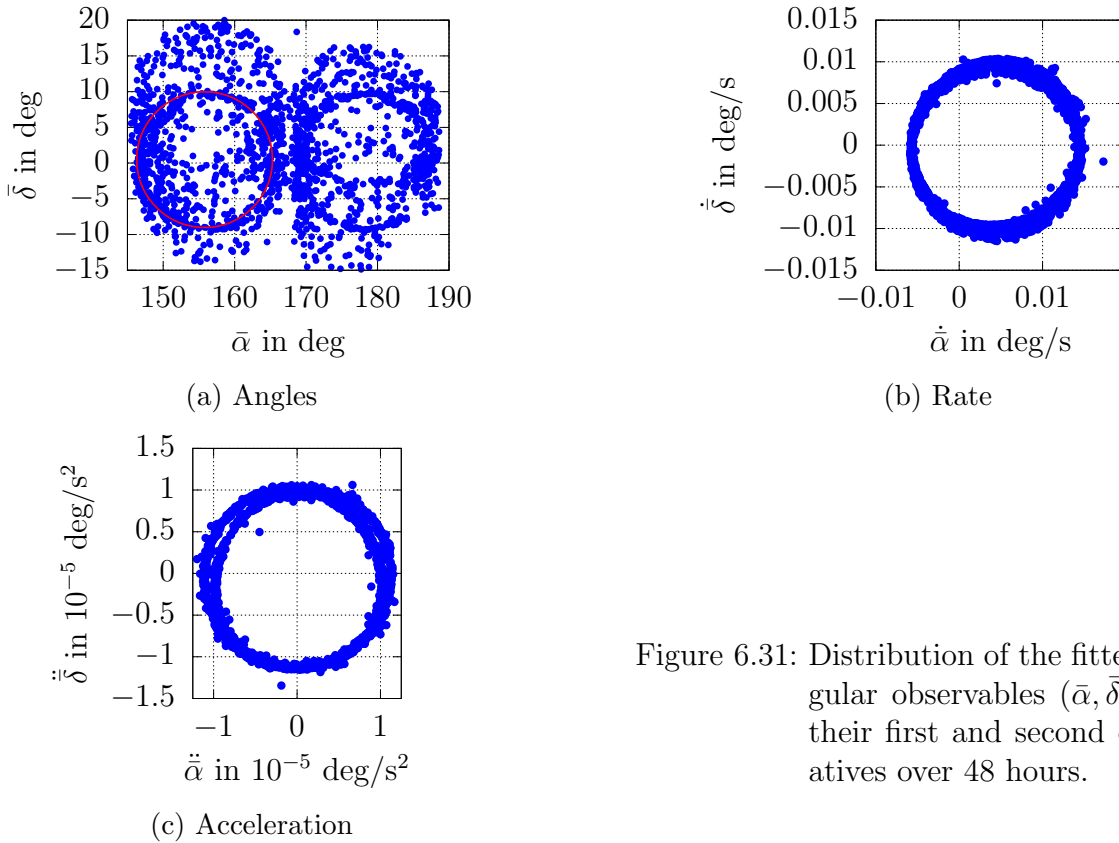
Figure 6.31: Distribution of the fitted angular observables $(\bar{\alpha}, \bar{\delta})$ and their first and second derivatives over 48 hours.

The distribution of the resulting values of the attributable can be seen in Figure 6.31 for an example of approx. 1700 attributables detected in the two fences. All observables show distinct features due to the observation geometry and observer motion. The angles show a separation of the two fences and have a distinct circular structure in each of them, which is due to detected GEO objects. The angular rates and accelerations are distributed in the shape of a circle which mirrors the observer motion and these values are similar for the two fences. In the acceleration, a slight difference between the two fences can be seen by the two overlapping circles, which is less obvious for the rates.

Association

The association of the tracklets $(\mathcal{A}_{SBO,1}, \mathcal{A}_{SBO,2})$ is performed using the method described in (Siminski et al., 2014), which is based on a two-dimensional search on the two unknown range values (ρ_1, ρ_2) from the observer to the observed object. Combining these ranges with the angles $(\alpha, \delta)_{1,2}$ gives two positions from which an initial orbit can be derived, see Section 4.1. For the resulting orbit, the angular rates (and also accelerations) can be calculated and compared to the ones from the attributable. The differences between these values are scaled by their uncertainties and summed up using the Mahalanobis distance M_d. Figure 6.32 gives an example of a correlation of two tracklets from an object in the GSO region roughly 24 hours apart and detected twice in the same fence. The minimum is well visible and can be found by using a BFGS-search (Press, 2007). The uncoloured regions in the plot are those where the initial orbit determination fails to yield a feasible, Earth-bound orbit. In order to initialise the search, a good starting point can be found by tracing the line in (ρ_1, ρ_2)-space that gives the same angular momentum at the two points (Siminski, 2016). As can be seen from the plot, this line is passing closely to the minimum, but also passes through a large part of the undefined area. To improve this initialisation, a new condition has been developed which is also plotted. This condition assumes that the L_2-norms $|\cdot|$ of the observed satellite's position vectors $\vec{r}_{S1}$ and $\vec{r}_{S2}$ are equal for both detections, which is a good approximation for detections in the same fence and low eccentricity objects. Combined with the observer positions $\vec{r}_{O1}$ and $\vec{r}_{O2}$ and the line-of-sight vectors $\vec{L}_1$ and $\vec{L}_2$, this yields:

$$|\vec{r}_{S1}| = |\vec{r}_{S2}|, \tag{6.17}$$

$$|\vec{r}_{O1} + \rho_1 \cdot \vec{L}_1| = |\vec{r}_{O2} + \rho_2 \cdot \vec{L}_2|. \tag{6.18}$$

This relation leads to a rectangular hyperbola in the (ρ_1, ρ_2)-space as can be derived via the conic sections of which only the branch in the first quadrant is of interest:

$$\rho_2(\rho_1) = \sqrt{\rho_1^2 + 2 \cdot \rho_1 \cdot \langle \vec{L}_1, \vec{r}_{O1} \rangle + \langle \vec{L}_2, \vec{r}_{O2} \rangle^2 + |\vec{r}_{O1}|^2 - |\vec{r}_{O2}|^2} - \langle \vec{L}_2, \vec{r}_{O2} \rangle , \tag{6.19}$$

using $\langle \vec{x}, \vec{y} \rangle$ to denote the inner product. As visible in the plot, this line is constantly within the area with a defined solution and also passes closely to the minimum. In practice, this line is sampled and the Mahalanobis distances at all the points are calculated. The search is started from the minimum along that line. If an object is observed in two different fences (or for a ground-based system at different times during the night), this initialisation should still be valid for objects with a moderately eccentric orbit.

As the pairwise correlation can be considered as an initial step in the cataloguing process, another layer of clustering the tracklets based on the correlations between them is applied using the graph network, see Section 3.3.

6.3.4 Experiments

Simulation

For the experiments, more than 1 300 objects have been extracted as TLE from Space-Track using the conditions: 38 000 km $< a <$ 46 000, $e < 0.25$ and $i < 25°$, which has already been referred to as GSO previously. The measurements are simulated by numerically propagating both the observer's and the objects' orbits using (Orekit, 2018). The numerical
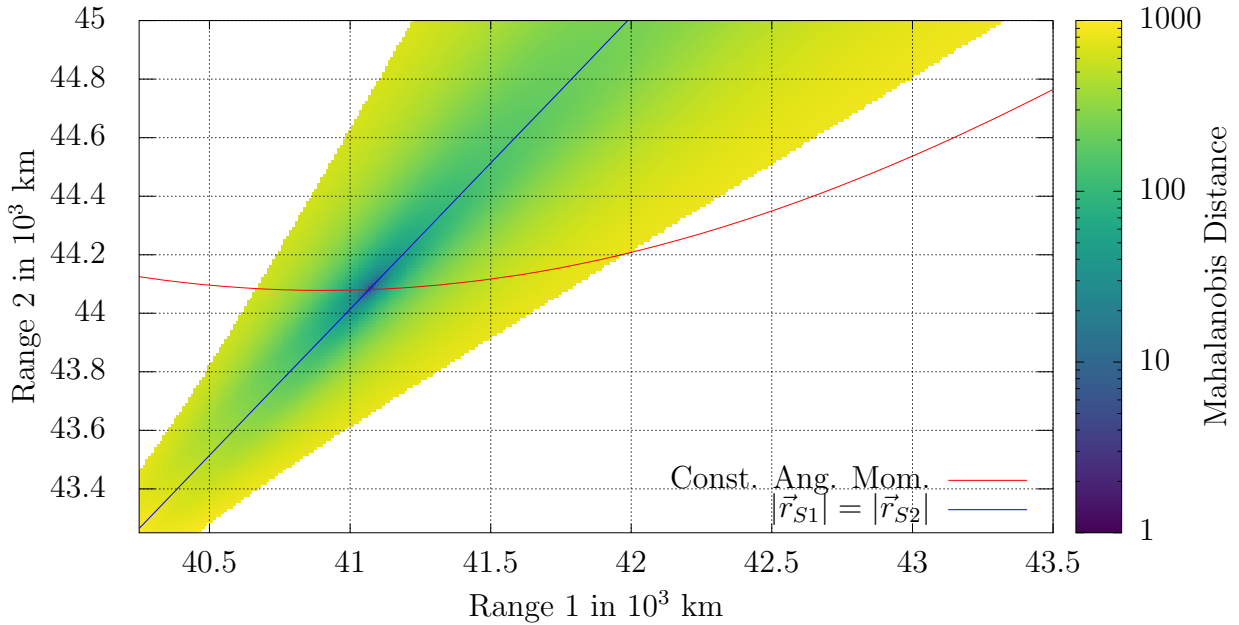
Figure 6.32: Example of the M_d loss function for a pair of tracklets detected in the same fence after 24 hours.

propagation uses a 16x16 gravitational field, luni-solar perturbations and solar radiation pressure. Gaussian white noise with $\sigma = 1''$ is added to the angular observables (α, δ). An object is observed if it crosses the fence within $[\Delta\alpha_F, \Delta\alpha_F + \Delta\alpha_w]$ while not being in the Earth shadow and having an unobstructed line-of-sight above the Earth atmosphere. The location of the detection within the fence is obtained by selecting a random start point within the fence, because no scanning strategy is simulated in this work. The further settings of the simulation are given in Table 6.4. All parameters depending on the technical design of the sensor, e.g. the time between detections, are preliminary assumptions based on the recent ESA studies, which may still change.

For the processing of the baseline scenario in the following, a pre-filter during the correlation rejects pairs of tracklets which cannot originate from the same object based on the time between them, the distances between the fences and the constraints on the extracted objects' semi-major axes. For example, if two tracklets measured in the same fence are separated by less than 18 hours, their correlation is immediately rejected. To reduce the computational burden further, those true correlations with the largest separation in time, i.e. the first detection in the first fence and the second detection in the second fence, are also filtered out. Thus, if an object has the expected average number of four tracklets, it can lead to a maximum of five correlations. For the pairwise correlation this is no problem if the reference number of expected true correlations is correctly adjusted for it, but considering the clustering algorithm this is an additional challenge.

Table 6.4: Parameters of simulation.

Start time	Feb 11, 2019, 18:00 UTC
Duration	48 hours
Objects	1 377
Fence position, $\Delta\alpha_F$ (rel. to AS)	9°, 31.5°
Fence width, $\Delta\alpha_w$	3°
Tracklet length	120 s
Detection interval	5 s
Noise	1″

Baseline Scenario

The 48-hour baseline scenario using two fences leads to more than 5000 tracklets which agrees with the expectation of detecting each GSO object four times within this period. The distribution of the resulting correlations' Mahalanobis distances is shown in Figure 6.33a. Although a visible and dominant peak of true positives is present, the amount of false positives is clearly disturbing as it makes up more than half of the correlations for a threshold of $M_d = 4$. Applying the graph clustering algorithm (see Section 3.3) to the correlations leads to the remaining correlations as shown in Figure 6.33b. A clear reduction of false positives to approx. 20% is visible. From the plot, it can also be suspected that a smaller correlation threshold could improve the results further. The effect of different thresholds is shown in Figure 6.34 concerning the percentage of false positives and true positives. As one would expect, the reduction of the threshold leads to less false positives. The difference between before and after the clustering in percentage points is nearly constant for the range shown here. Compared to that the percentage of true positives increases slightly up to $M_d = 4$ and remains on a nearly constant level after that. Also the number of true correlations which are removed during the clustering reduces slightly with larger thresholds.

(a) Before Clustering
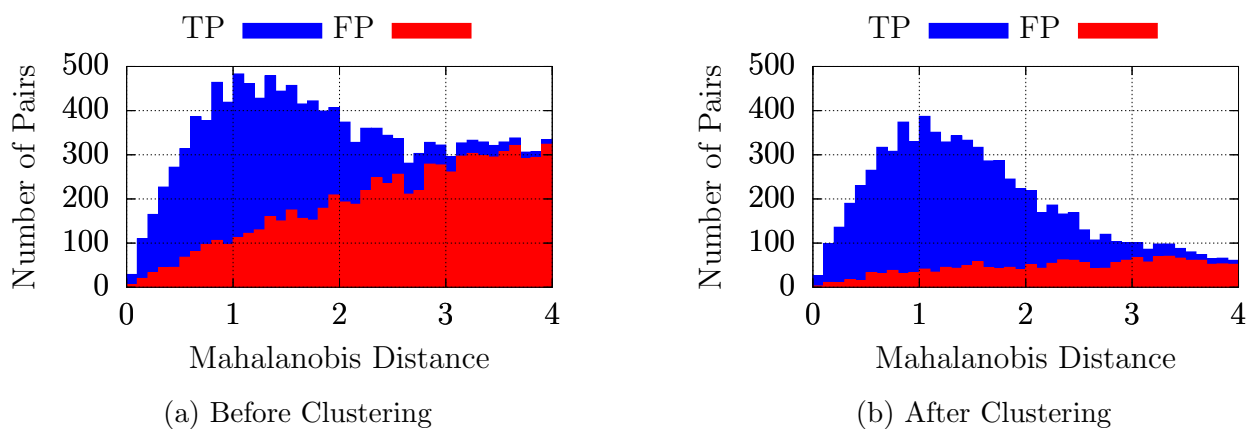
(b) After Clustering

Figure 6.33: The distribution of Mahalanobis distances for the threshold $M_d = 4$ after the pairwise correlation (left) and after the clustering (right).

(a) False Positives
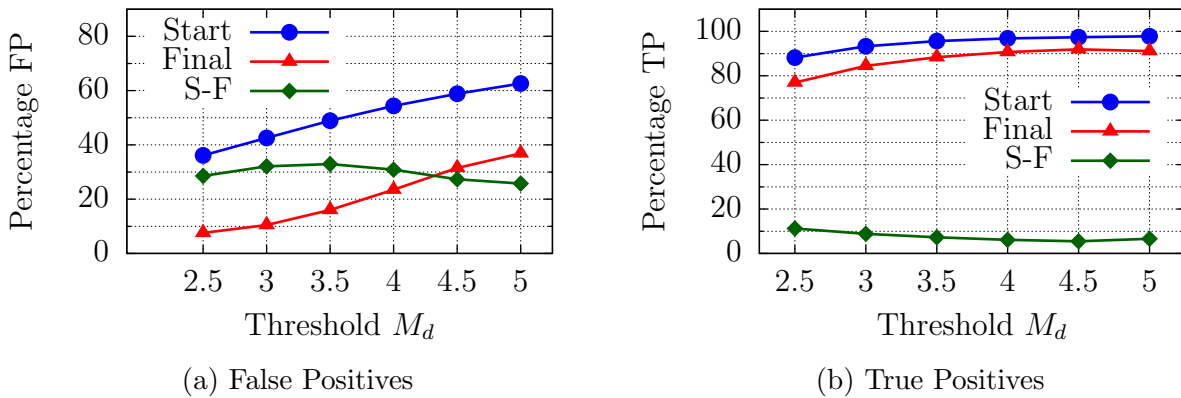
(b) True Positives

Figure 6.34: The percentage of false and true positives after the graph analysis depending on the M_d-threshold after the pairwise correlation. S-F indicates the difference between the start and final value.

To analyse the effect of the clustering algorithm further, Figure 6.35 shows the development of the number of true and false positive correlations over the different processing steps in the graph network. These steps, see Section 3.3, are the initial network, the creation of triangles, the merging of the triangles and the separation of connected groups (cutting). One can see, that the creation of triangles is the most effective step to reduce false positives. Also the final step of assigning shared tracklets between multiple clusters to only one of them has a visible effect and compensates the slight increase after merging the triangles. The number of true positives is only slightly affected by the reductions. As mentioned in Section 3.3.2, the final step of cutting the overlapping clusters is non-deterministic which gives some variability to the results. However, as shown in Table 6.5 the variation of the resulting correlations is rather low compared to the absolute numbers, less than 1%.
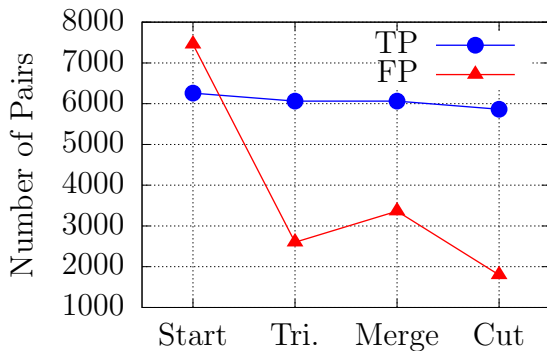
Figure 6.35: Number of true and false positives over the different filter steps.

Table 6.5: Statistics of the graph analysis filter for 20 individual runs.

	Mean	Standard Deviation
True Positive	5843.10	8.29
False Positive	1794.60	14.82

Analysing only the numbers of true and false correlations is not a very intuitive quantity concerning the quality of the results and might be misleading. As a better measure, the number of identified objects is taken. This is derived by analysing the final clusters with at least three tracklets and checking whether they contain only tracklets from one object, similarly to the analysis in Section 5.2.3. The result of this analysis shown in Figure 6.36 reveals that nearly 70% of all objects in the simulation are identified as a separated cluster. If the FN-groups are added, which contain only three out of four tracklets but no tracklets from other objects, this percentage rises to 78%. For a threshold of $M_d = 3$, the number of objects in TP-groups decreases to 63%, because some true positive correlations are removed, but if the FN-groups are included the overall percentage is at 82%.
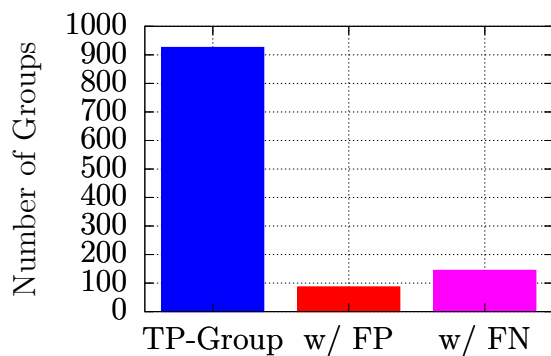
Figure 6.36: Comparison of the identified groups after the clustering analysis for a threshold of $M_d = 4$.

False Positive Analysis

Further analysis has been performed on the false positive correlations to better understand their origins and help design possible improvements in the mission. Figure 6.37 displays the semi-major axis and inclination of all objects which are involved in false positive correlations before the clustering. This shows that the vast majority of these objects are longitude/latitude controlled GEO objects with low inclination, low eccentricity and semi-major axis of one sidereal day. Considering that GEO objects are often co-located in similar areas, it is not surprising that it is difficult to distinguish such closely-spaced satellites. In order to check the possible resolution of co-located GEO objects, Figure 6.38 shows the difference in geocentric longitude along GEO between the objects of the wrongly associated tracklets for both before and after the clustering algorithm. The main peak in both plots is close to zero with a width of a few degrees, which seems to indicate the resolution of GEO objects. Before the clustering, there are two additional peaks at approx. 13° and 38°. They originate from an effect in the measurement geometry which makes it more likely to have false positive associations between two GEO objects, if the observer satellite is at the same position during the measurement of each of the two tracklets, especially if the two tracklets are measured in the same fence. Due to the observer satellite's period of approx. 99 minutes, 15 complete revolutions of the observer lead to an equivalent motion in GEO of approx. 373°, thus detecting objects which have an offset of 13° compared to the satellite in the first detection. Another revolution of the observer adds 25° and leads to the second peak at 38°. The orbit which connects these two tracklets is usually an eccentric orbit ($e \approx 0.15$) with a semi-major axis matching the elapsed time.

(a) Semi-major Axis
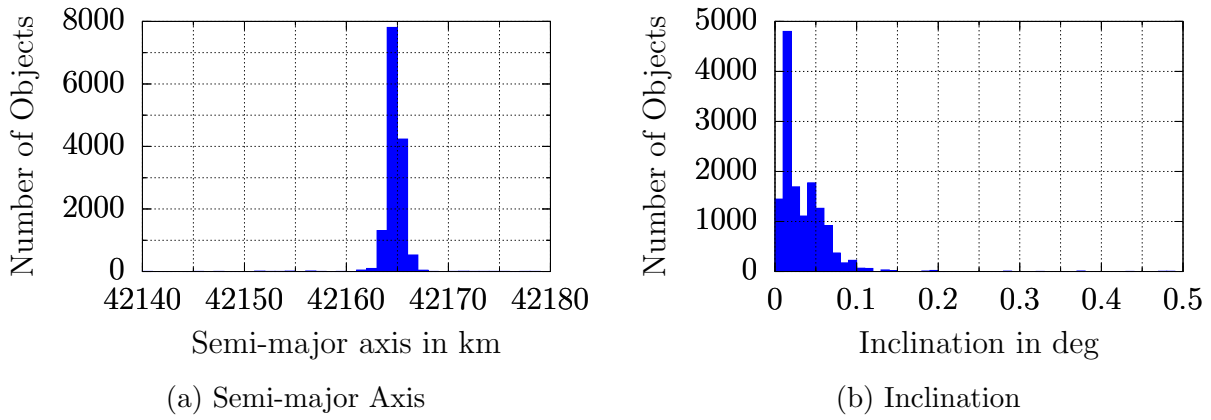
(b) Inclination

Figure 6.37: Distribution of semi-major axis and inclination of FP objects before the cluster.

(a) Before Clustering

(b) After Clustering
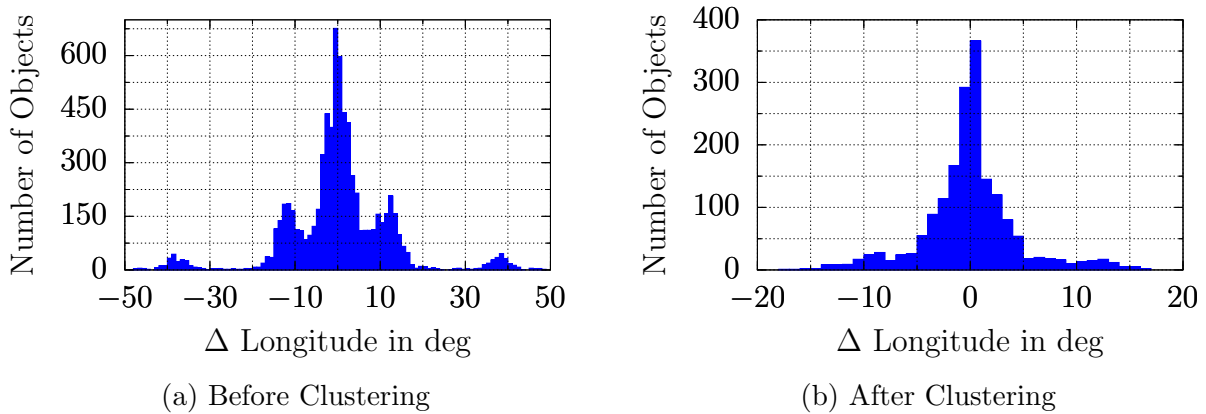
Figure 6.38: Difference in longitude of GEO objects for false positives.

The explanation for this effect can be found in the specific observation geometry combined with the dominance of the observer motion. Figure 6.39 shows a sketch of the measured angular rates of a GEO object (bold line) and of an eccentric orbit of a false positive correlation (dashed line) when being present in the same fence over one revolution of the observer. The black dot marks the spot at which the repeated observations from the same observer position are made. It can be seen that the angular rates of the eccentric solution overlaps with the one of the GEO object at that place, but not in the remaining part of the orbit. Thus the two measurements at the same spot lead to a lack of a constraint for the connecting orbit, because the GEO measurements have to be matched only at one spot and because two different GEO objects have the same angular rates when they are detected in the same fence from the same observer position. If measurements from two different fences are used the effect is less pronounced and less common, but a similar mechanism also works in that case. The majority of these false positives are removed in the clustering step. Otherwise an additional filter could reject correlations based on the observer location or the calculated orbit, which would also increase the risk of more false negatives.
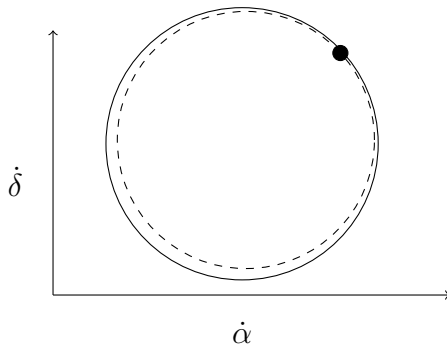
Figure 6.39: Exaggerated effect of different orbits on the angular rates.

Fence Combinations

In the context of false positives it is also important to consider the percentages of false positives depending on the combinations of fences used. The results show that for the direct correlation from fence 1 to fence 2 (difference approximately 1.5 hours for GEO) there are only 12% of false positives which is significantly less than for detections in same fences or in different fences one revolution apart as can be seen in Table 6.6. However, in order to create confidence in a new object and its orbit, detections from multiple days should be combined, which makes it necessary to also consider the correlations over one revolution which are more prone to false positives.

Revisit χ-Distribution

Another interesting aspect of the correlation is the normalised distribution of the Mahalanobis distances which should theoretically follow a χ-distribution with four degrees of freedom (Siminski, 2016). This comparison is shown in Figure 6.40a for all true correlations between detections in different fences and it can be seen that the calculated distances are slightly shifted towards smaller values, which was already mentioned in Section 6.2. Only the correlations from different fences are chosen, because the numerical estimation of the uncertainty is more unstable for detections from the same fence. The distribution is much closer to

Table 6.6: True and False Positives for different fence combinations ($M_{\mathrm{d}} \leq 4$) before the clustering (baseline scenario).

Fences	Total Correlations	False Positives
Fence 1 - Fence 2 ($\Delta t_T < 3$ h)	2 862	352 (12%)
Fence 1 - Fence 1 ($\Delta t_T \approx 24$ h)	2 847	1 579 (55%)
Fence 2 - Fence 2 ($\Delta t_T \approx 24$ h)	2 529	1 399 (55%)
Fence 2 - Fence 1 ($\Delta t_T > 20$ h)	5 393	4 046 (75%)
Total	13 631	7 376 (54%)

(a) Optimisation
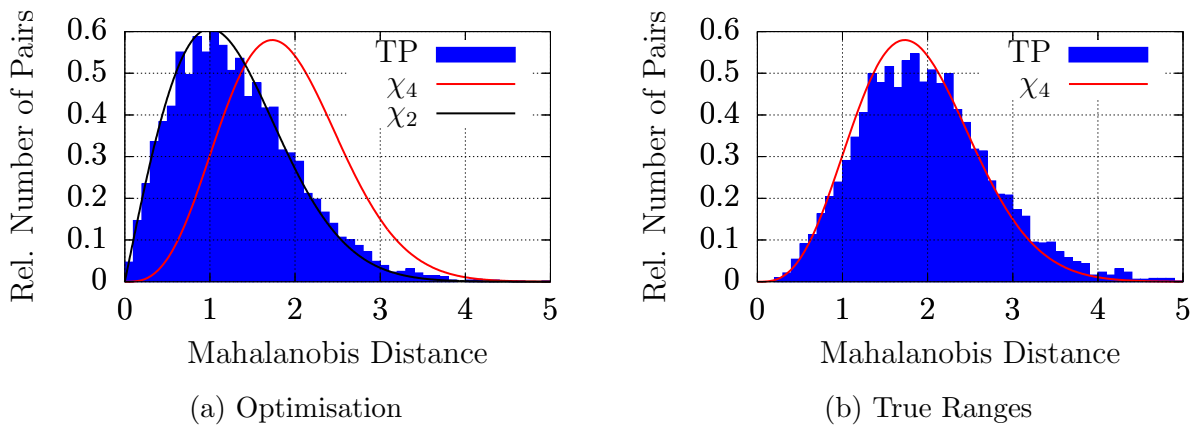
(b) True Ranges

Figure 6.40: Comparison of relative distribution of Mahalanobis distances for optimisation and forced true ranges. Only correlations in different fences are used.

the theoretical one with two degrees of freedom. The most probable explanation for this is that the two degrees of freedom during the search in (ρ_1, ρ_2)-space allow it to reduce the differences between the angular rates to a level which is even smaller than the one due to the noise of a single measurement. If these two dimensions are considered to be lost due to the optimisation, only two degrees of freedom remain, which would explain the result. This is also commonly used in the so-called reduced χ^2-test, in which the χ^2-value is divided by the remaining degrees of freedom after the fit. These degrees of freedom are usually approximated by $N - m$ using N measurements and m fitted parameters, here $N = 4$ and $m = 2$. However, estimating the degrees of freedom for a non-linear system is a problem without a general solution (Andrae et al., 2010). It is not possible to give a proof concerning the number of effective degrees of freedom. Only the evidence presented in this section indicates that for the given problem there are two degrees of freedom left, because this fits the experimental results very well. It is possible that the different dynamics of the ground-based observations lead to a different loss of degrees of freedom.

Another way to explain this effect of these lost dimensions is that if only the angular rates of one tracklet are used for the correlation decision, the Mahalanobis distances are all very close to zero for the majority of the correlations, because the two range values can be used to set the two discriminators to zero as long as they are sufficiently uncorrelated. Thus there are effectively zero degrees of freedom. Adding two components to the discriminator would be equivalent to adding two degrees of freedom to the overall system.

As a comparison, Figure 6.40b shows the distribution of the Mahalanobis distances if the true ranges from the observer to the observed object are used instead of the optimisation to search for the minimum. This leads to a well-matched 4-dimensional distribution and confirms that the estimates of the errors from the attributable fit are indeed realistic. The use of the true ranges should result in an orbit which is much closer to the true one than the one using the optimisation. If the exact true orbit was used for the calculation of the discriminator, the distribution would become perfectly 4-dimensional because now only the four measurement errors are considered independently.

A similar observation can be made by an analysis of the resulting discriminator, i.e. the differences between the angular rates in the attributable and the one computed from the orbit. In theory, those values should follow a normal distribution which is consistent with the estimated total uncertainty. Because the measurement uncertainty is much larger than the one from the orbit determination (Siminski, 2016), only the measurement uncertainty is used. In Figure 6.41, the distribution of the derived discriminator for the rate of the right ascension in the first tracklet as an example is compared to the expected normal distribution based on the average measurement uncertainty, for both the optimisation case and the case using the true ranges. The results for the other three components of the discriminator vector are similar. The distribution from the optimisation is narrower than the expected one and the central peak is much larger, which suggests an overfitting-like effect. The two-dimensional optimisation is fitted to the noisy values and reaches values which are lower than the expected values due to only noise. Compared to that, the distribution using the true ranges again fits the expected probability distribution very well.

These observations do not restrict the use of the correlation method but considering the choice of the correlation threshold a shift towards smaller values may always be expected and a lower threshold may be chosen, e.g. $M_\mathrm{d} = 3$ instead of four.

(a) Optimisation

(b) True Ranges
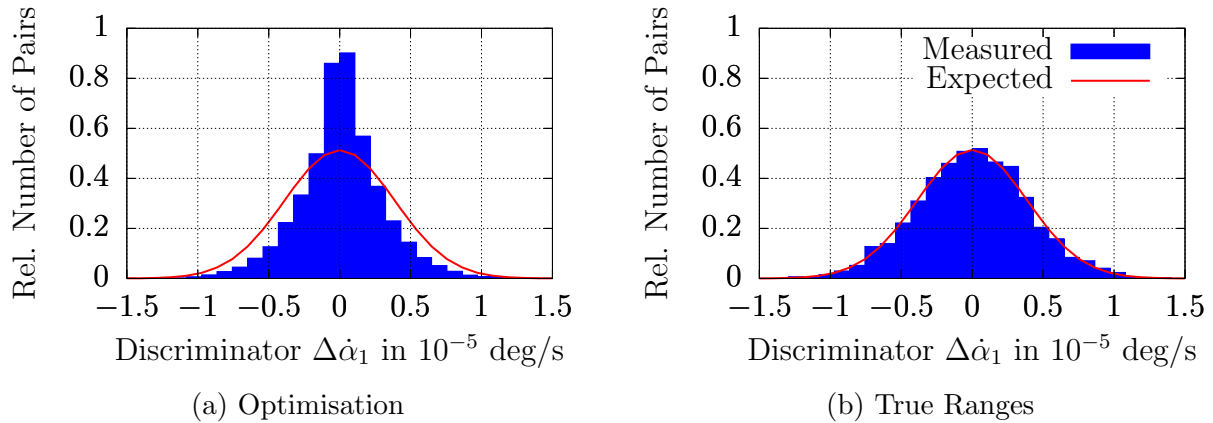
Figure 6.41: Distribution of the discriminator $\ddot{\alpha}_1$ compared to the expected normal distribution based on the measurement noise.

Angular Acceleration

Due to the third order fit of the attributable, it is possible to use also higher-order derivatives in the discriminator such as the acceleration $\ddot{\alpha}$ and $\ddot{\delta}$, which was already shown in Figure 6.31. Together with the angular accelerations, the discriminator becomes 8-dimensional, which shifts the Mahalanobis distances and thus the correlation threshold to larger values due to the increase of the degrees of freedom. Concerning the results, there is no clear improvement compared to the case of angular rates only, which is possibly due to the same dependency on the observer motion. It can be concluded that the angular accelerations are not adding independent information which improve the correlation results.

Variation of Daily Fences

In order to reduce the effect of the detections in the same fence, an additional experiment is run which introduces two new fences for the second half of the 48-hour campaign. These fences are located at $\Delta\alpha_F = [15.5°, 28.0°]$ between the first two fences close to the area of maximum visibility, see Figure 6.29. During the first day the same fences as before are used and for the second day the new fences are used. Concerning the number of false correlations and identified objects after the clustering also this experiment does not contain a major improvement leading to 72 % of identified objects including FN-groups.

As a comparison to Figure 6.38, the distribution of the GEO objects' separation in longitude of the false positives after the clustering is shown in Figure 6.42. Before the clustering there were still some higher values. This is due the same effect as explained before, which also works for two different fences. The majority of false associations is still for closely-spaced objects. The edge of the maximum is around 5° which appears to be slightly wider than before. The larger absolute number of correlations is due to the fact that for the four fences, all possible correlations are checked and for the previous one the longest correlation from fence one to fence two after one revolution was not attempted which also leads to less false positives due to the pre-selection of pairs.
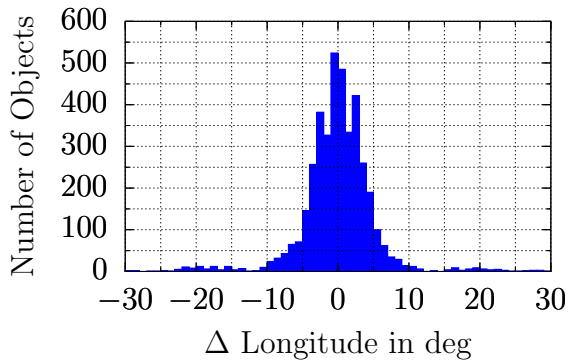
Figure 6.42: Difference in longitude of GEO objects for false positives in case of 4 fences.

Reconsidering that the correlation between tracklets which are detected on the same revolution in the two fences are less prone to false positives, this can also be observed in this case and the closer-spaced fences 3 and 4 have only 3% false positives for correlations between them, see Table 6.7. Although placing the fences closer to each other understandably improves the correlation, it also reduces the amount of information on the orbit due to the closer-spaced sampling of the orbit. In practice, the angular separation of the two fences has to be chosen as a trade-off between correlation performance and accuracy of the orbit determination.

Table 6.7: True and False Positives for different fence combinations ($M_\mathrm{d} \leq 4$) before the clustering (4-fence scenario).

Fences	Total Correlations	False Positives
Fence 1 - Fence 2 ($\Delta t_T < 3$ h)	1 398	176 (13%)
Fence 1 - Fence 3 ($\Delta t_T > 20$ h)	3 980	2 666 (67%)
Fence 1 - Fence 4 ($\Delta t_T > 20$ h)	4 087	2 809 (69%)
Fence 2 - Fence 3 ($\Delta t_T > 20$ h)	3 798	2 551 (67%)
Fence 2 - Fence 4 ($\Delta t_T > 20$ h)	3 616	2 336 (65%)
Fence 3 - Fence 4 ($\Delta t_T < 3$ h)	1 348	38 (3%)
Total	18 227	10 576 (58%)

Fusion with A Priori Knowledge - Minimum Eccentricity

Considering that the majority of false positive correlations is due to objects within GEO with low eccentricities and that the orbits of those false positives usually lead to larger eccentricities, it is attempted to use this knowledge to have a clustering approach based on these orbital properties. The basic idea is that for each correlation between two fences, a

tracklet can only be involved in one true correlation. To use this information, all correlations of each tracklet for a specific combination of two fences are checked and the correlation yielding the orbit with the smallest eccentricity is chosen. It is also checked whether the other tracklet for that combination also has the minimum eccentricity for this correlation. If this is the case, the two tracklets are considered to be confirmed and the other correlations involving any of the two tracklets are rejected. After this has been performed for all combinations of fences, another simplified clustering algorithm can be applied to find groups of tracklets. If the groups with only three tracklets are included, this leads to 83 % ($M_\mathrm{d} \leq 4$) of identified objects. For the standard clustering approach only 78 % had been reached. For the lower threshold of $M_\mathrm{d} \leq 3$, this approach leads to 81 % of identified objects, compared to 82 % using standard clustering. For the scenario with four different fences as presented in the previous section, the percentage of identified objects rises to 86 %, which is a large improvement, but this may also be due to the fact that this scenario checks all possible six correlations and does not neglect the one with the largest time in between detections.

These results suggest that the approach using the minimum eccentricity as an a priori information, outperforms the standard clustering only marginally except for the approach using four fences. Considering that this approach may lead to problems to detect new objects on unusual, i.e. more eccentric, orbits, the standard clustering may still be preferred.

Enrichment with ground-based data

In order to test whether additional ground-based data could be used to separate unresolved GEO objects, a specific group of 12 GEO satellites has been chosen such that it is visible from Europe. Observations from the Zimmerwald Observatory in Bern (Switzerland) have been simulated for these objects in two consecutive nights at different right ascensions to increase the combined information content. As a simplification, it is assumed that these tracklets have the same length and detection intervals as the ones from the space-based sensor. In total, now there are six tracklets per object in 48 hours. The correlation itself and the standard clustering algorithm yield no major improvement as the objects could still not be resolved.

As a further test for this dense cluster, another algorithm, the Kernel K-means (Zhang and Rudnicky, 2002), was applied to the data. The disadvantage of this method is that the number of groups to be found has to be given in advance. As the number of objects cannot be known beforehand, the Kernel K-means is applied iteratively by forcing a split into two groups until all groups show a sufficient consistency. Consistency means here, that the number of correlations between the objects in the group should be close to the theoretically expected number of correlations if all tracklets were connected. If a group fulfils this condition, it is not split again. The distance measure, which is used for the K-means is the Mahalanobis distance between the tracklets. If two tracklets are not correlated, the distance is set to $M_\mathrm{d} = 50$. Applying this to the dense GEO group, leads to 8 out of the 12 objects in FN-groups, most of them are split in two groups of three tracklets. If a cataloguing algorithm identifies these groups as being the same objects, the clustering could still be successful.

The same experiment was done with four days of space-based data, which results in eight tracklets per object on average, in order to see if the positive effect of the ground-based data is only due to the increased amount of measurements. This experiment leads to worse results than the 48 hours with ground-based data as only one object ends up in two three-tracklet

clusters after the Kernel K-means compared to the eight before. This suggests that the mixture of the data can indeed lead to a positive effect for the tracklet correlation. This is mainly due to the additional measurements at different times and locations on the orbit of the GEO object, because the space-based sensor can only observe it at the same locations again.

Noise Level

One of the uncertainties of a possible mission is the performance of the camera regarding the achievable noise level. In order to quantify the impact of a lower instrument performance, the same two-fence 48-hour experiments as the baseline has been performed with a higher standard deviation of the angular noise. The main results are summarised in Figure 6.43. Firstly, the percentage of false correlations after the clustering is shown on the left. There is a nearly linear increase of the FP percentage with an increasing noise level. The increase up to 75 % for $\sigma = 3''$ seems dramatic but again the number of identified objects by the clustering is the more expressive number. This shows that it is still possible to identify more than 60% of the objects, which increases to 66% if the FN-groups are included.

(a) Percentage FP   (b) Percentage Identified Objects
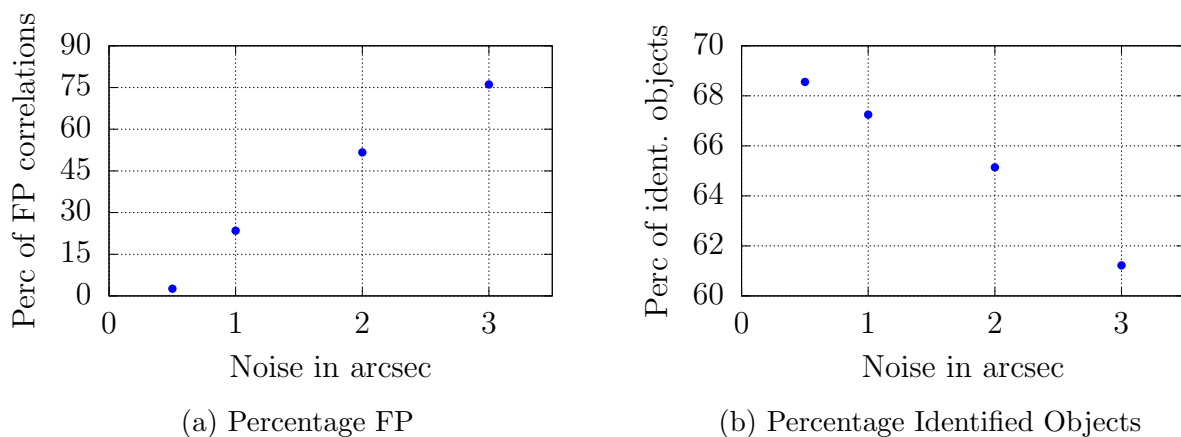
Figure 6.43: Percentage of false positives and identified objects over different noise values for $M_\mathrm{d} \leq 4$ after the clustering.

When estimating the resolution of objects in GEO, Figure 6.44 shows that the main peak at the centre now reaches until approx. $\pm 15°$, which is also a factor of three compared to the $1''$-case. Also the side peak at $38°$ cannot be reduced to a very small number any longer. This would complicate the initial catalogue build-up from scratch even more, although it might be possible to add further dedicated processing approaches to large unresolved clusters.

Seasonal Variation

Due to the characteristic long-term effects of the luni-solar and geopotential perturbations in GEO, the relationship between the RAAN and inclination leads to areas with more or less separation in latitude between the objects. The most dense regions occur where the ascending or descending nodes of the orbits are close to each other (Sharma et al., 2002). This effect leads to an increased number of false positives and a significant reduction of correctly
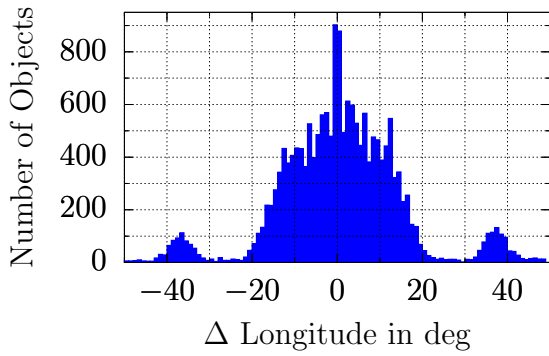
Figure 6.44: Difference in longitude of GEO objects for false positives in case of a measurement noise of $3''$ after the clustering.

identified objects as can be seen from Figure 6.45, in which the February observations are compared to those from May when the fences are located in more dense regions. The decrease is even larger than the one with the largest noise considered before, reaching only approx. 52% (63% incl. FN-groups).

One of the main reasons for this is the already discussed issue of a dominance of low-inclination GEOs ($i < 0.5°$) among the false positives. In May, the fences are pointing close to their ascending and descending nodes, which makes it difficult to separate these objects. In February, these objects show more differences in latitude due to the different inclinations and RAANs. Due to the repeated measurements in the same fence, if two measurements have a separation in latitude, the possible orbits between these measurements would have high inclinations, which are not matching the observed rates and thus are not correlated. For the detections in May, they are closer to the equatorial plane and thus it is easier to match the angular rates with a low inclination orbit.

(a) Percentage FP

(b) Percentage Identified Objects
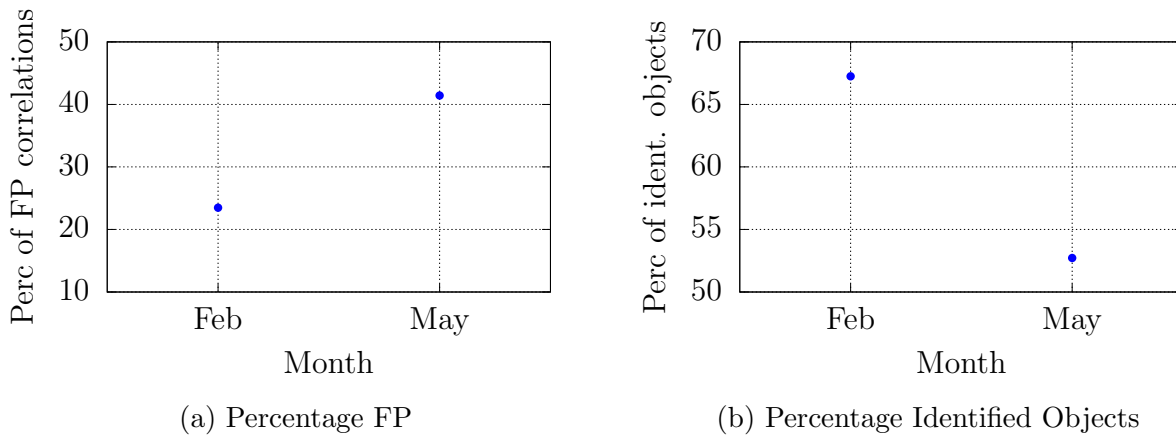
Figure 6.45: Percentage of false positives and identified objects for two different times during the year using $M_d \leq 4$ and the clustering.

6.3.5 Conclusion

The results of the experiments show that in general, the correlation of the space-based observations with the given mission design and correlation method is possible. Using 48 hours of observations and a clustering of the correlations, it is possible to identify up to 70 % of the objects in the GEO region. Depending on the exact scenario and conditions, even

values of more than 80 % have been achieved for specific cases. Considering that this is achieved by a single sensor in a short time span, this result is rather good. However, the experiments also showed that other influences like the time of the year or the noise level of the observations can lead to a degradation of the correlation performance. Bearing this in mind, an initial catalogue build-up from scratch may not be computationally efficient with the given mission. In general, the contribution of the sensor to the overall maintenance of a catalogue has to be considered as well. In the context of a complete monitoring system, it was also shown that adding ground-based observations can be helpful to split dense clusters in the GEO region using an additional Kernel K-means clustering.

6.4 Zimmerwald - Automated Processing Pipeline

6.4.1 Overview

In order to apply many of the previously discussed topics to a real-world application, an experimental automated processing pipeline has been set up for the optical observations at the Zimmerwald observatory in Bern, Switzerland, officially named Swiss Optical Ground Station and Geodynamics Observatory. The station consists of several telescopes and a laser for satellite ranging. In the following, the focus is on optical surveys executed by the telescopes ZimSMART (ZSM) and ZimTWIN (ZTW). ZimSMART has a 20 cm aperture and a field of view of approximately $3.6° \times 3.6°$. ZimTWIN consists of two similar telescopes mounted next to each other with each having a 40 cm aperture. Thus it should be more sensitive at lower magnitudes compared to ZimSMART, although the combined field of view is slightly smaller at $2.14° \times 4.28°$. For the surveys, only one of the two ZimTWIN telescopes is used and thus the available field of view is $2.14° \times 2.14°$.

The goal is to create and maintain a catalogue of space object orbits in an automated way based on survey measurements. The surveys are performed such that two fences are scanned which are roughly 75° apart in right ascension and one of these fences potentially consists of another two separate fences at a separation of approximately 25°. For objects in GEO, these distances translate to a satellite's travel times of roughly 5 hours and 1.7 hours between them, respectively. With this approach of using two pairs of fences, it is possible to have up to four measurements of a single object in one night, see (Herzog, 2013) for more details on the planning. The optimisation of the scheduling is a possible item of future work. For each night, the observations of the two telescopes are processed separately according to the flowchart in Figure 6.46. A comparable approach can be found in (Herzog, 2013). To remove tracklets belonging to publicly known objects, the measurements are compared against TLE as a first step. Those which can be associated to a TLE object are removed from further processing and the associations are stored. The same is done with the Russian Vimpel catalogue. The remaining observations are then correlated with the internal AIUB catalogue, if it already contains objects. Also here, associations are stored and also used to update the orbits in the catalogue. The details of the catalogue correlation are discussed in Section 6.4.2.

Those tracklets which remain after the two catalogue correlation steps are assumed to originate from uncatalogued objects and they are called uncorrelated tracklets (UCTs). Using them, it is attempted to identify new objects via the pairwise correlation. The entire process is described in Section 6.4.3, which also includes re-processing tracklets from the previous days if a new object has been created.

6.4.2 Catalogue Correlation

The theory of the tracklet-catalogue association is discussed in Section 6.1. For the pipeline, the association is performed in the measurement system of right ascension and declination, because even for large uncertainties the mapping of the orbit uncertainty into this system can be performed with a first-order transformation. The measurement uncertainty is assumed to be $1''$ for both, right ascension and declination.

To compare the tracklets against a given catalogue, all objects in the catalogue are tested against all tracklets without any pre-filtering. For a single comparison of one catalogue orbit against one tracklet, the orbit is propagated to the epoch of the first, middle and last observation in the tracklet to test three associations using the two observed angles. The threshold for a confirmed association is set to theoretically include 95% of the probability distribution, which is equivalent to a threshold of $M_d \approx 2.44$ in case of $\chi(2)$. If at least two of the three checked observations are below this threshold, the orbit-tracklet correlation is accepted. This considers possible outliers in the tracklet and is a variation of the "Ratio"-approach presented in Section 6.1.2. It is also possible to derive attribtutables from the tracklet and compare the derived angles and angular rates to the catalogue state. This is advantageous when cases are considered where two objects in different orbits have very similar line of sights and they can only be correctly identified by considering their angular rates.

These orbit-tracklet correlations can be performed in parallel for separate parts of either the catalogue or the tracklets and afterwards all accepted correlations are collected. Especially for closely-spaced objects in GEO, it may happen that a tracklet is associated to multiple objects or vice versa. To solve these ambiguities, the Hungarian algorithm is used (Kuhn, 1955). This algorithm minimises the total cost of an assignment problem, which is equivalent to the identification of unique associations. Here, the cost of an assignment is the average Mahalanobis distance of the three correlations and a cost matrix is built containing these average distances as costs for each orbit-tracklet correlation. The output of the algorithm is an unambiguous set of associations with the smallest sum of single costs, i.e. Mahalanobis distances.

This correlation process is performed for both the TLE catalogue and the internal AIUB catalogue. In case of the internal AIUB catalogue, the orbit covariance is the result of the least squares orbit determination, which is propagated to the epoch of the measurement. Concerning the TLE associations, these orbits do not contain an information on its uncertainty, which means that a vital information for the correlation process is missing. To overcome this, a default covariance matrix has been selected with the position uncertainty in curvilinear RTN as $[2, 25, 1.5]$ km. Using the same covariance matrix for all objects is a major simplification, but the underlying true or estimated uncertainty of the objects is dependent on various influences, e.g. the number of observations, the time since the last observation or the orbital regime. Most of these information are not available and even a
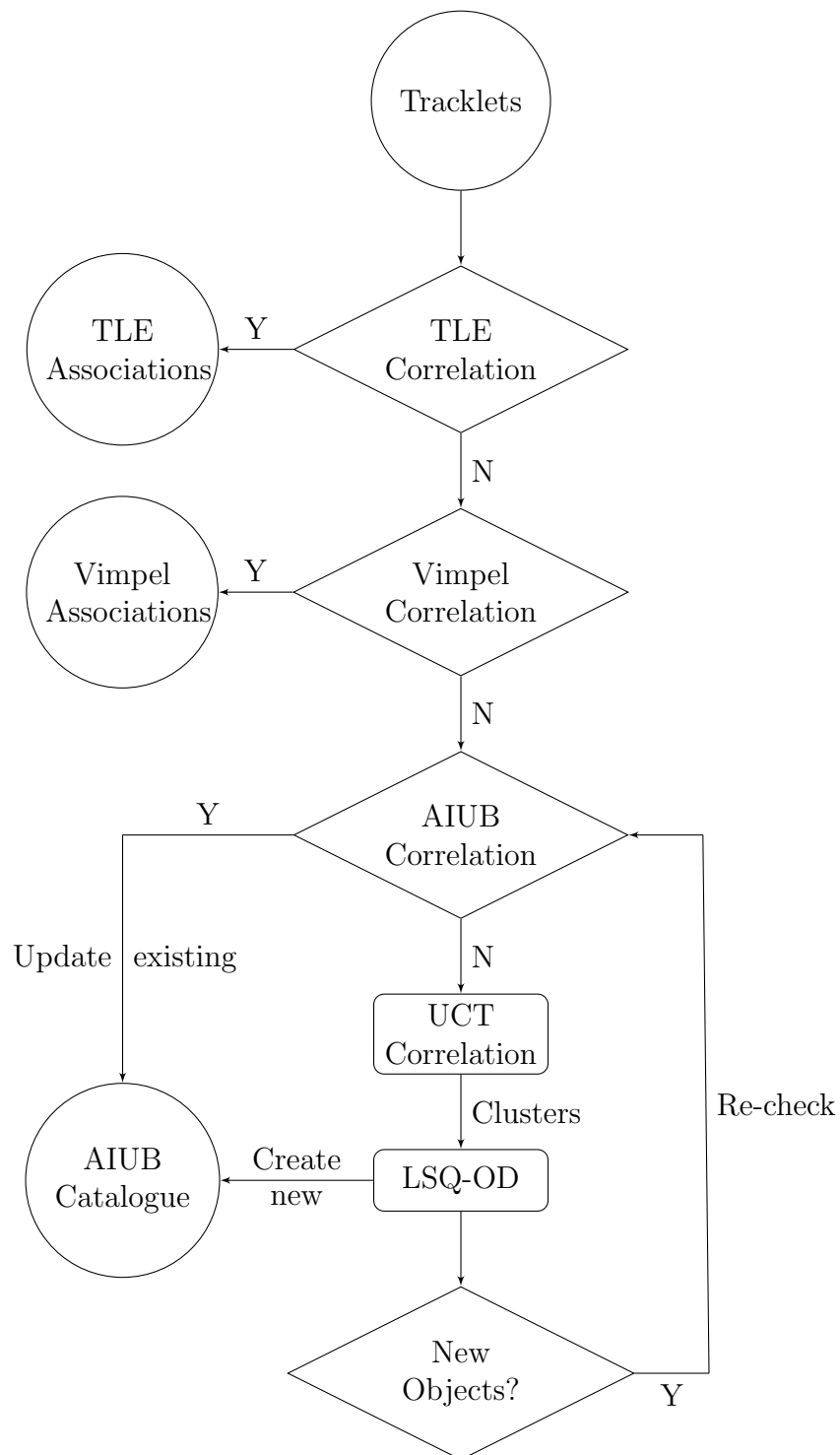
Figure 6.46: Workflow of the experimental pipeline.

rough estimate of the uncertainty for specific objects would be difficult. Thus, the simplification to use the same constant covariance for all objects is not fully realistic but considering the use-case here, it should be sufficient. To find this artificial covariance, it was decided that it is better if it is too large than too small. If the covariance is too small, a correlation may be missed which cannot be recovered later in the process, whereas a large covariance may generate multiple false positive correlations for a specific tracklet but the mentioned Hungarian algorithm can find the most probable combination of them.

Further analysis of the TLE correlation after the first weeks suggested that there are still TLE objects which are not correlated. It was identified that the error in the normal direction was often exceeded, even for operational, bright GEO satellites, which led to Mahalanobis distances above the threshold. Based on this analysis, it was decided to increase the size of the covariance's normal component to $\sigma_N = 10$ km. This relatively large offset is also in agreement with the analysis by (Frueh et al., 2009). Even with this increased covariance, there are still some outliers which are not detected. An additional post-filter has been applied to accept correlations with $M_d < 10$ under the condition that both the tracklet and the satellite had not been correlated previously. If a satellite had already been correlated to a tracklet using that night's TLE, it is rather unlikely to have a large outlier at a different epoch during the same night. Like all correlations processes, also here a balance between false positives and false negatives has to be considered. In principle, it could be possible to accept all correlations of tracklets, for which an uncorrelated TLE object is in the vicinity without checking the exact thresholds. Especially for HEO objects, the errors in the TLE can be large and then it may be reasonable to accept the closest object as an association based on the fact that there are no better candidates. This approach can also lead to false associations, for example if there are uncatalogued fragments in the vicinity of a TLE object. For completeness, those correlations with $M_d > 10$ for otherwise uncorrelated TLE objects are stored in a separate list, but the tracklets are still considered to be UCTs for the following steps to avoid missing new objects.

As introduced in Section 2.1, the Russian Vimpel catalogue focuses on objects in high-altitude orbits. It is an interesting source for another catalogue comparison, but there are some limitations to its operational use. The main problem is that some orbital elements in the catalogue only have a precision of one decimal place, which is not sufficient for a precise orbit. If the included ephemerides, which are inertial positions, are used to determine an orbit with a least squares optimisation, this self-derived orbit can be used for the correlation and the association is possible. However, considering the large number of objects in the Vimpel catalogue, it is infeasible to do this for all of them. Additionally, this catalogue is always released with a delay of two weeks and thus no up-to-date orbits can be used on the day of the measurement.

Nevertheless, a prototype of a catalogue correlation algorithm has been implemented for the Vimpel catalogue. Because of the aforementioned characteristics of the catalogue, the uncertainties should be expected to be larger than those for the TLE. To avoid false positive correlations, the Vimpel correlation is done after the TLE correlation with the remaining tracklets. Because this catalogue contains also many objects which have not been observed for a long time and the days since the last observation are given for each object, only those objects are considered which have been observed within the last ten days before the release date of the catalogue. For the objects fulfilling this criterion, the correlation process depends on its orbital regime. First, the controlled GEO objects are considered by choosing all objects

with 42 160 km $< a <$ 42 170 km and $e < 0.05$. Additionally, only tracklets are selected with an angular rate close to 15 $\frac{\text{deg}}{\text{s}}$ to remove observations which cannot originate from a GEO object. For the observations passing this filter, their line-of-sight is projected onto a sphere at GEO altitude to calculate the geocentric, Earth-fixed longitude of the observation. This longitude is compared to those of the GEO objects and for those pairs with a small separation, the full LSQ-OD is performed with the ephemerides. This newly derived orbit can then be compared to the observations with the same procedure as for the TLE, except for a slightly larger covariance with $[10, 50, 15]$ km in RTN-coordinates accepting all $M_\text{d} < 5$. In the next step, objects in HEO are considered. They are selected by having an apogee above 30 000 km and $e > 0.25$. For these objects, their given Keplerian elements are numerically propagated and compared to the observations with a threshold of $M_\text{d} < 50$. If an object-tracklet pair passes this initial threshold, the full comparison using the same LSQ-OD as in GEO is performed. Finally, all remaining Vimpel objects with an apogee above 30 000 km are collected under the term GSO. These objects are not drag-affected, thus the processing starts with a Keplerian propagation of the given state as a first filter, followed by the same steps as for the HEO.

6.4.3 Object Generation

After the catalogue correlation, the remaining tracklets are used to search for new objects. There are two different ways to create new objects for the internal AIUB catalogue. The first one is based on the pairwise correlation as already introduced in Section 6.3 using the method by (Siminski et al., 2014). The correlation is performed by collecting the UCTs of three consecutive nights to increase the chances of multiple observations of the same object. For tracklets from the same night, a correlation is tested if the two tracklets are at least 15 minutes apart to have a sufficient separation. Based on the pairwise correlations, a graph network is build as described in Section 3.3. The clustering also uses further restrictions on the orbits from the correlations by using a maximum difference between the semi-major axes $\Delta a < 25$ km and between the inclinations $\Delta i < 0.85°$ within a cluster. For each cluster of at least four tracklets, a least squares orbit determination is attempted and if the standard deviation of the residuals of the angular observables are below $1.5''$, the orbit is accepted.

One potential problem with the described approach occurs if an object is observed multiple times in a relatively short time span, e.g. less than one hour. The correlations from such closely-spaced observations have large variations in the semi-major axis because of the short time difference and thus are not detected by the clustering algorithm. A different procedure is used to detect these cases. Based on the angular rates in the attributable, it is possible to select tracklets which possibly originate from an object in GEO. The angular observations from these tracklets are projected onto the sphere at GEO distance ($r = 42\,164$ km) to derive their geocentric longitude/latitude in the Earth-fixed system. Based on the distribution of these points, the *dbscan* clustering algorithm is used to find closely-spaced tracklets (Ester et al., 1996). An example of this is shown in Figure 6.47, where four clusters can be seen as a collection of closely-spaced points. The remaining black points are not part of a cluster. The algorithm requires as an input the maximum distance between two points (here: $0.1°$) and the minimum number of points in a cluster (here: 3). For the identified clusters, a least squares orbit determination is performed with the same conditions as for the clusters from the pairwise correlation.
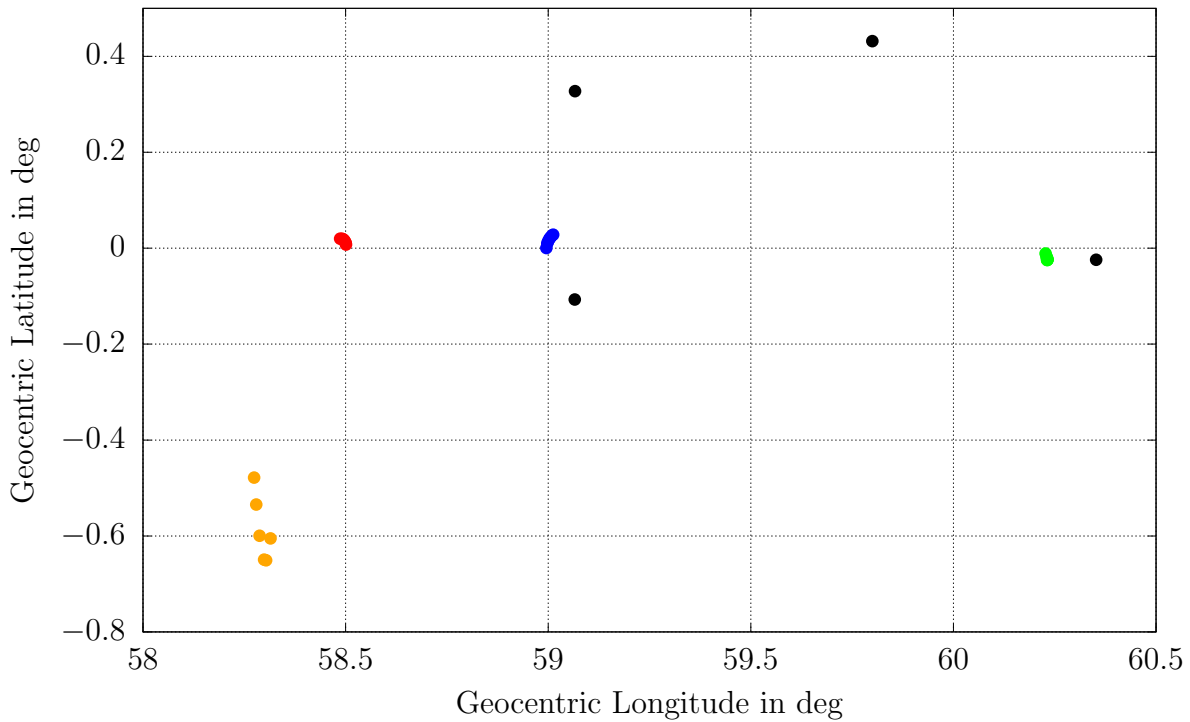
Figure 6.47: Result of the dbscan GEO clustering. Coloured points are clusters and the black ones are non-clusters.

If a new object has been identified from any of the two processes, the UCTs from the past three days are checked again to find any additional tracklets which may have been overlooked during the object generation.

While the GEO clustering process is only used for GEO objects by definition, the pairwise correlation can also be applied to HEO objects. From an analysis of the TLE correlation, it was found that HEO objects are mostly not leading to repeated observations over several nights to enable the creation of a new object. Thus the correlation is set to generate only objects with a semi-major axis fulfilling $35\,000\text{km} < a < 50\,000\text{km}$.

6.4.4 Results

In the following, some selected results of the automated processing pipeline are presented. These results are still preliminary and serve as a proof-of-concept of the automation, but in order to create a stable catalogue it would be necessary to invest more work in the planning of the surveys and potential follow-up observations of catalogue objects.

In Figure 6.48 (ZSM) and Figure 6.49 (ZTW), the daily overview of tracklets and their status is given. It can be seen that the majority of the tracklets is associated to TLE objects, up to 70%. The increase in TLE associations over time is due to the extension of the considered TLE objects. Initially, only objects on near-circular orbits in more than 30 000 km altitude were used for the association when it was still in its testing phase. After it was established that the TLE correlation using the artificial covariance works sufficiently well, the considered objects were set to include all objects with an apogee of more than 10 000 km altitude without any further restrictions on the eccentricity or inclination. This usually

leads to nearly 4 000 objects which are checked. After the increase of the covariance's normal component and the acceptance of objects above the threshold, the share of TLE associations increased to more than 90%. For nights with many observations, i.e. more than 500 tracklets from a single telescope, this TLE association can take more than one hour of processing time using three processes in parallel. Considering the processing time, it may be beneficial to perform a pre-filtering, but this is not considered at this stage. The remaining identified tracklets are either associated to an object in the internal AIUB catalogue or they have been used for the creation of a new catalogue object. In the beginning of September 2020, the Vimpel catalogue was added to the correlation process. First, only the GEO objects were checked and later also HEO and GSO as described in the previous section. With the most recent settings, usually less than 1% of the tracklets remain uncorrelated and thus of unknown origin.
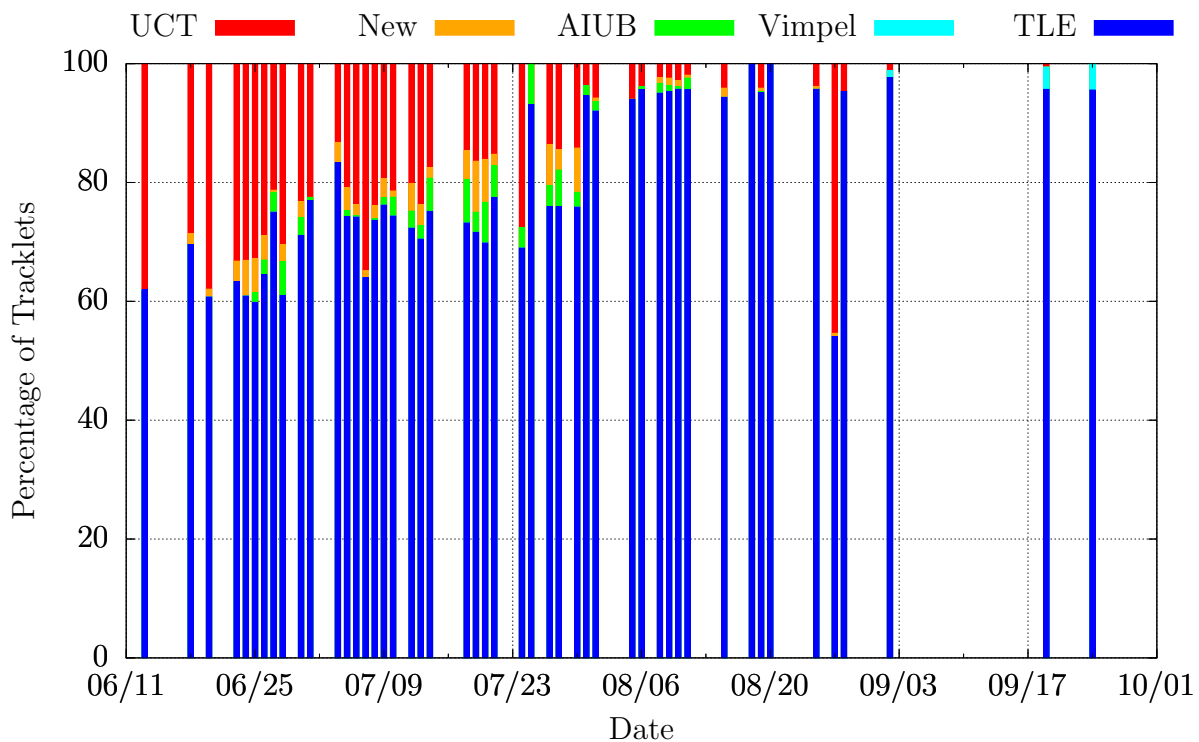
Figure 6.48: Statistics of the pipeline results for ZimSMART showing the numbers of tracklets associated with AIUB objects, TLE objects, Vimpel objects and UCTs.

Analysing the TLE correlations further, it can be distinguished which types of objects are observed. For simplicity, five different types are defined to separate the objects into groups. To classify nearly all objects, the boundaries have been set rather generously after they were already pre-filtered by apogee altitudes larger than 10 000 km as mentioned previously. The class HEO contains all objects with an eccentricity $e > 0.3$. The objects with $e < 0.1$ are sorted according to their semi-major axis. Those with 42 155 km $< a <$ 42 175 km are classified as GEO, while those with a smaller semi-major axis are belowGEO (bGEO) and those with a larger one are aboveGEO (aGEO). Additionally, the telescopes frequently observe navigation satellites as reference objects which are filtered based on their semi-major axis and inclination. The resulting classifications for the two telescopes are shown in Figure 6.50 (ZSM) and Figure 6.51 (ZTW). One can see that the objects above GEO are the largest
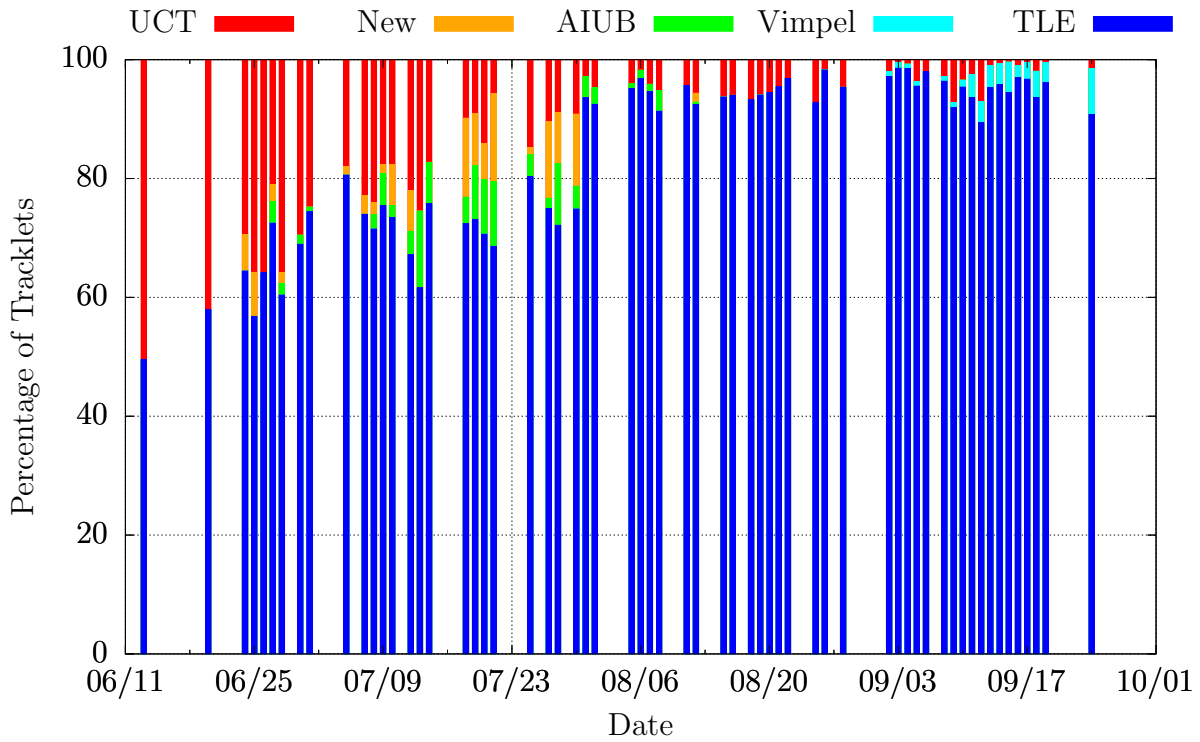
Figure 6.49: Statistics of the pipeline results for ZimTwin showing the numbers of tracklets associated with AIUB objects, TLE objects, Vimpel objects and UCTs.

group, which makes sense because these orbits are used as graveyard orbits to place retired GEO satellites and they are drifting relative to the Earth surface which makes it theoretically possible to observe all of them over a longer time span, while the objects in GEO remain above the same area. Considering the number of tracklets, the largest group is the GEO because it can be observed every night and includes many bright, well-visible objects. The other groups have comparably low numbers of tracklets, especially in relation to the number of objects, which also shows that it is less likely to observe the same object many times for these groups.

(a) Objects
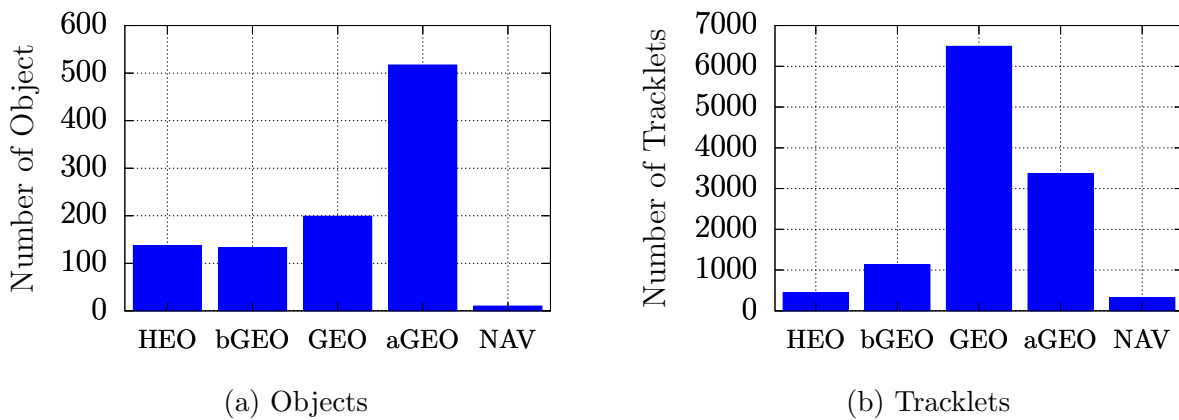
(b) Tracklets

Figure 6.50: Total number of observed TLE objects and tracklets for ZimSMART.

(a) Objects
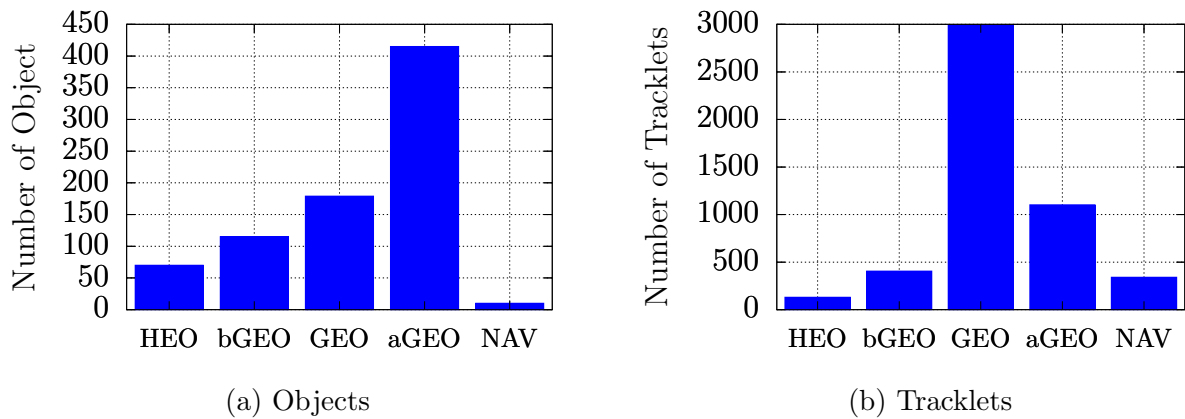
(b) Tracklets

Figure 6.51: Total number of observed TLE objects and tracklets for ZimTwin.

As a next step, the newly generated objects from the internal catalogue are analysed from the time before the Vimpel catalogue was considered in the catalogue correlation. For objects in GEO, Figure 6.52 shows the AIUB objects and those Vimpel objects which should be visible from Zimmerwald and have a magnitude of less than 14. Several overlaps between the catalogue orbits can be seen, which confirms that the automated process generates real objects and not just false alarms. Additionally, a similar plot can be generated for non-GEO objects, see Figure 6.53, and there are also two clear overlaps.
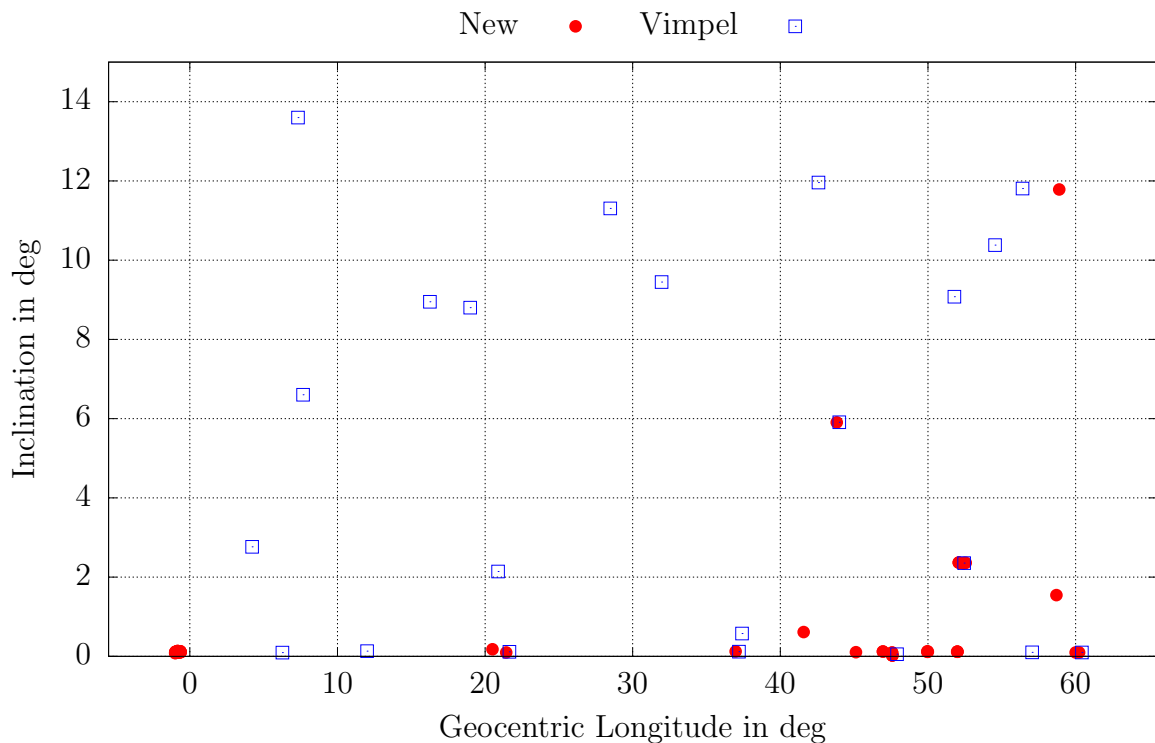
Figure 6.52: Example comparison of bright GEO objects from Vimpel and newly generated objects by the pipeline.
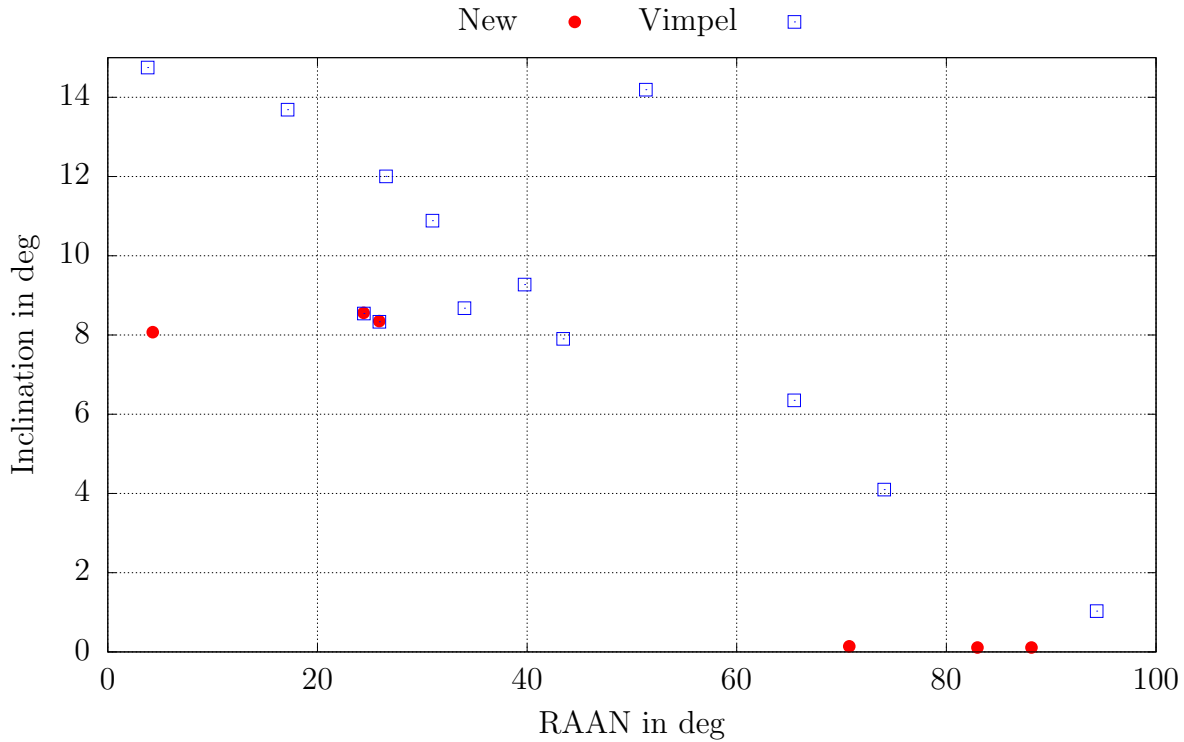
Figure 6.53: Example comparison of bright non-GEO objects from Vimpel and newly generated objects by the pipeline.

Finally, coming back to the derived measures for catalogue maintenance in Section 6.1, the following example is taken from (Reihs et al., 2020b). Figure 6.54 depicts the development of the Mahalanobis distance for the association and the surprisal over three nights. In this case, the pipeline had generated a new GEO object from one night using the clustering algorithm. For the next three nights, this orbit is propagated to the new measurement epochs and the Mahalanobis distance for the association can be calculated together with the surprisal. After each night, the orbit is updated using the newly associated measurements, see Figure 6.46. The Mahalanobis distance in the plot is relatively stable between one and two, because the differences between the expected and received measurement are scaled by the covariance. If both are decreasing, the Mahalanobis distance remains at similar values. In contrast to that, the surprisal considers the size of the covariance, which is shrinking after each night due to the incorporation of new measurements. For the second and third night there are clear decreases in the surprisal compared to the previous night, which indicates that the confidence in the object and its position has in fact increased.
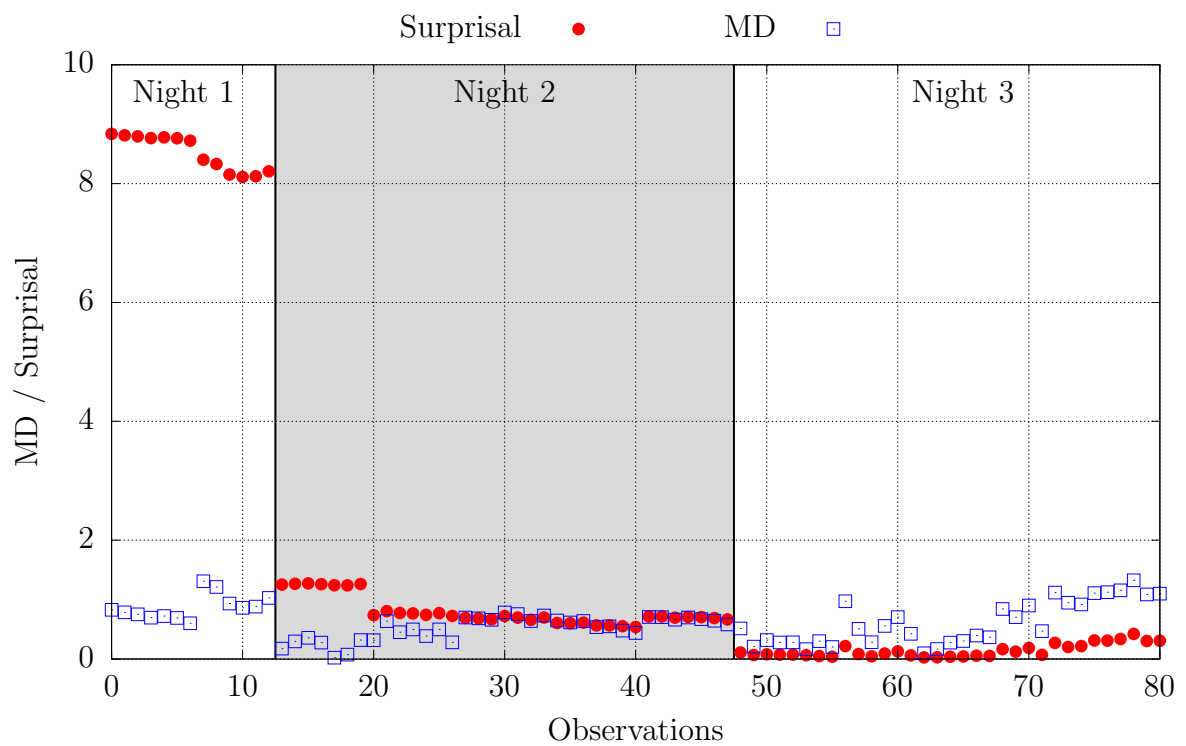
Figure 6.54: Development of Mahalanobis distance and surprisal over three nights.

CONCLUSION

7.1 Summary

The main contribution of this thesis is the introduction of a method for perturbed initial orbit determination and observation correlation from two radar tracklets. This method provides the solutions for all possible numbers of revolutions between two tracklets. It is based on the so-called Lambert's problem using two positions in inertial space, which are derived from the radar's range and angle measurements. The remaining observation of the range-rate can be used to check whether the derived orbit is consistent with the two measurements by calculating the Mahalanobis distance as a statistical distance measure. The initial orbit determination considers the secular effect of the J_2-perturbation by rotating the orbital plane iteratively and adjusting the Keplerian propagation. The most probable solution of all different numbers of revolutions can either be selected via the minimum Mahalanobis distance or after an additional post-processing. The robustness and applicability of the method was shown using real radar measurements, which included a large percentage of successful initial orbit determinations for tracklets which were more than 20 days apart. It was also shown how the distribution of different measurement stations affects the correlation process by improving the correlation performance in case of stations with a larger separation and thus a better coverage of the orbit. Concerning the cold-start of a catalogue, two different processing strategies were introduced. One is adding a least squares orbit determination using a pair of possibly correlated tracklets, while the other approach collects data over a longer time span and generates a graph network from which clusters of tracklets are derived as new candidate objects. Both approaches lead to good results, but they have different implications on the required computational resources. While the least squares needs many resources for the iterative orbit improvement of each candidate pair, the graph network is computationally very efficient but it is necessary to collect the input data for the correlation over a longer time span, which also leads to increased processing times during the correlation.

Apart from the processing of radar observations, also experiments using space-based optical measurements or mixed radar-optical measurements were performed successfully. Especially the space-based optical experiments considered the observation geometry of a realistic mission scenario which is under consideration by the European Space Agency. This analysis allowed it to understand the limitations of such a mission if it enters an implementation/design phase. Especially, the large number of false positive correlations was an important result which showed that the space-based sensor can contribute to an overall space surveillance system but not as an isolated single sensor. These results are important to understand the requirements and capabilities of such a sensor based on the extensive analysis performed within this work.

Further analysis focused on the aspects of operational processing of space surveillance measurements. This included the automated decision making process for the monitoring of the quality of existing catalogue objects. Based on the concepts of information theory, a consistent surprisal measure was introduced to derive a parameter which can be used to judge the orbit quality of an object in the catalogue. This parameter is based on newly acquired measurements and thus provides a feedback function between the stored state and the true state. The design of an autonomous processing pipeline for optical measurements at the Zimmerwald observatory combined many of the developed approaches in an operational environment of a daily update routine. It was possible to routinely process all new measurements from different telescopes to identify known objects and create new ones for a local catalogue. It was shown that the automated processing is capable of identifying TLE objects as well as creating new objects, which could be confirmed via a cross-check with the Vimpel catalogue.

Overall, the work presented in this thesis focused on the operational applicability of the developed and extended methods. Operational space surveillance has to process large amounts of data, which makes it necessary that the processing algorithms are also tested on large and realistic data sets. With this approach, it was possible to show that the developed methods in this work can contribute to an operational system. This also included showing operational limitations as in case of the space-based sensor which is rather due to the data than due to the methods themselves. These limitations are often only visible when processing large amounts of data. Several times within this work, additional processing steps had to be added in order to improve the results for large data sets, which are important implications for building operational processing chains.

7.2 Future Work

Based on the work in this thesis, possible extensions of the research are discussed in the following. For the correlation itself, the perturbed initial orbit determination can be extended to consider more effects, preferably in an analytical way to avoid increasing the computational complexity. Especially atmospheric drag for LEO or solar radiation pressure in GSO may be interesting options. However, these forces depend heavily on the modelling of multiple aspects of the environment interaction with the space object, e.g. the atmospheric density or the object's shape and attitude. If a number of simplifying assumptions is made on these aspects, it may be possible to consider these additional forces. With regard to atmospheric

drag, it was shown in this work that the negative effect on the correlation performance is mainly visible for highly drag-affected objects in combination with measurements at similar locations on the orbit. For the majority of the applications of the correlation algorithm, the dynamics as used in this work are sufficient.

In order to increase the reliability of the initial correlation with regard to avoiding false positives and selecting the correct number of revolutions, it may be possible to increase the number of used tracklets from two to three. With three observations, the correct orbit can be found more easily which was seen in the context of the multi-graph network. If the third tracklet is already integrated in the initial orbit determination, this could improve the reliability of this orbit and reduce the workload of the post-processing. One of the problems of combining three tracklets is that with an increasing total population of tracklets the resulting number of possible combinations grows even faster than for two tracklets, which also increases the overall computational demand.

Apart from the correlation itself, also the application of the algorithm can be extended. Integrating the radar correlation into an automated operational process of real radar measurements would allow it to characterise the method's performance with a large amount of data. Under such conditions it would be possible to identify important improvements of the method and the general processing approach.

As mentioned in Section 3.4, multitarget tracking is a popular approach for regularly updating a population of space objects. In combination with the correlation algorithm, it is possible to create a group of hypothetical objects from the multiple solutions of the initial orbit determination. When new measurements are received in the following, the hypothesis belonging to the correct orbit would be confirmed and could converge on a valid solution.

Using only the initial orbit determination, the method can also be applied to the estimation of transfer orbits using the first position as the current state and the second position as the desired state at a later epoch. With the multi-revolution solution, it is possible to find candidates for transfer orbits over potentially multiple days which make use of the J_2-perturbation within their manoeuvre.

With regard to the experiments of the space-based optical simulator, future work could extend the simulation of the measurements to consider more realistic pointing and detection conditions or use ESA's in-situ simulator to obtain the measurements through the complete camera pipeline. Also the role of space-based measurements in the context of a complete monitoring system with ground-based stations can be extended further to optimise the cumulative information from both systems.

BIBLIOGRAPHY

Abbasi, V., Thorsteinson, S., Balam, D. et al. (2019). 'The NEOSSat Experience: 5 years in the life of Canada's space surveillance telescope'. In: *1st ESA NEO and Debris Detection Conference*. Presented paper. Darmstadt, Germany, Jan. 2019.

Abramowitz, M. and Stegun, I. A. (1965). *Handbook of mathematical functions: with formulas, graphs, and mathematical tables*. Vol. 55. Courier Corporation, 1965.

Allan, R. and Cook, G. (1964). 'The long-period motion of the plane of a distant circular orbit'. In: *Proceedings of the Royal Society of London. Series A. Mathematical and Physical Sciences* 280.1380 (1964), pp. 97–109. DOI: 10.1098/rspa.1964.0133.

Andrae, R., Schulze-Hartung, T. and Melchior, P. (2010). *Dos and don'ts of reduced chi-squared*. 2010. arXiv: 1012.3754 [astro-ph.IM].

Ansalone, L. and Curti, F. (2013). 'A genetic algorithm for Initial Orbit Determination from a too short arc optical observation'. In: *Advances in Space Research* 52.3 (2013), pp. 477–489. DOI: 10.1016/j.asr.2013.04.004.

Armellin, R., Gondelach, D. and San Juan, J. F. (2018). 'Multiple revolution perturbed Lambert problem solvers'. In: *Journal of Guidance, Control, and Dynamics* 41.9 (2018), pp. 2019–2032. DOI: 10.2514/1.G003531.

Bar-Shalom, Y., Chang, K.-C. and Shertukde, H. M. (1989). 'Performance evaluation of a cascaded logic for track formation in clutter'. In: *Conference Proceedings., IEEE International Conference on Systems, Man and Cybernetics*. IEEE. Cambridge (MA), USA, Nov. 1989, pp. 13–17.

Battin, R. H. (1977). 'Lambert's problem revisited'. In: *AIAA Journal* 15.5 (1977), pp. 707–713.

Beutler, G. (2004a). *Methods of Celestial Mechanics: Volume I: Physical, Mathematical, and Numerical Principles*. Berlin/Heidelberg, Germany: Springer Science & Business Media, 2004. ISBN: 978-3-642-14857-6. DOI: 10.1007/b138225.

Beutler, G. (2004b). *Methods of Celestial Mechanics: Volume II: Application to Planetary System, Geodynamics and Satellite Geodesy*. Berlin/Heidelberg, Germany: Springer Science & Business Media, 2004. ISBN: 978-3-540-40750-8. DOI: 10.1007/b137725.

Blackman, S. and Popoli, R. (1999). *Design and analysis of modern tracking systems*. Norwood (MA), USA: Artech House, 1999. ISBN: 978-1580530064.

Braun, V., Lemmens, S., Reihs, B., Krag, H. and Horstmann, A. (2017). 'Analysis of Breakup Events'. In: *Proceedings of the 7th European Conference on Space Debris*. Presented paper. Darmstadt, Germany, Apr. 2017.

Braun, V., Horstmann, A., Reihs, B., Lemmens, S., Merz, K. and Krag, H. (2019). 'Exploiting orbital data and observation campaigns to improve space debris models'. In: *The Journal of the Astronautical Sciences* 66.2 (2019), pp. 192–209. DOI: 10.1007/s40295-019-00155-6.

Cover, T. M. (2006). *Elements of information theory.* Hoboken, N.J: Wiley-Interscience, 2006. ISBN: 9780471241959.

de la Torre Sangrà, D. and Fantino, E. (2015). 'Review of Lambert's problem'. In: *ISSFD 2015: 25th International Symposium on Space Flight Dynamics, 19-23 October, Munich, Germany.* 2015, pp. 1–15.

Delande, E., Houssineau, J., Franco, J., Frueh, C., Clark, D. and Jah, M. (2019). 'A new multi-target tracking algorithm for a large number of orbiting objects'. In: *Advances in Space Research* 64.3 (2019), pp. 645–667. DOI: 10.1016/j.asr.2019.04.012.

DeMars, K. J. and Jah, M. K. (2011). 'Evaluation of the information content of observations with application to sensor management for orbit determination'. In: *AAS/AIAA Astrodynamics Specialist Conference.* Girdwood (AK), USA, Aug. 2011.

DeMars, K. J., Hussein, I. I., Jah, M. K. and Erwin, R. S. (2012). 'The Cauchy-Schwarz divergence for assessing situational information gain'. In: *15th International Conference on Information Fusion.* IEEE. 2012, pp. 1126–1133.

DeMars, K. J. and Jah, M. K. (2013). 'Probabilistic initial orbit determination using gaussian mixture models'. In: *Journal of Guidance, Control, and Dynamics* 36.5 (2013), pp. 1324–1335. DOI: 10.2514/1.59844.

DeMars, K. J. and Jah, M. K. (2014). 'Probabilistic initial orbit determination using radar returns'. In: *Proceedings of the AAS/AIAA Astrodynamics Specialist Conference (2013, Hilton Head, SC)* 150 (2014), pp. 35–54.

DeMars, K. J., Hussein, I. I., Frueh, C., Jah, M. K. and Scott Erwin, R. (2015). 'Multiple-object space surveillance tracking using finite-set statistics'. In: *Journal of Guidance, Control, and Dynamics* 38.9 (2015), pp. 1741–1756. DOI: 10.2514/1.G000987.

Donath, T., Schildknecht, T., Martinot, V. and Del Monte, L. (2010). 'Possible European systems for space situational awareness'. In: *Acta astronautica* 66.9-10 (2010), pp. 1378–1387. DOI: 10.1016/j.actaastro.2009.10.036.

Du, J., Chen, J., Li, B. and Sang, J. (2019). 'Tentative design of SBSS constellations for LEO debris catalog maintenance'. In: *Acta Astronautica* 155 (2019), pp. 379–388. DOI: 10.1016/j.actaastro.2018.06.054.

Engels, R. and Junkins, J. (1981). 'The gravity-perturbed Lambert problem: A KS variation of parameters approach'. In: *Celestial mechanics* 24.1 (1981), pp. 3–21. DOI: 10.1007/BF01228790.

European Space Agency (2019). *Annual Space Environment Report.* 2019.

Escobal, P. (1976). *Methods of orbit determination.* Huntington (N.Y) USA: R.E. Krieger Pub. Co, 1976. ISBN: 978-0882753195.

Ester, M., Kriegel, H.-P., Sander, J., Xu, X. et al. (1996). 'A density-based algorithm for discovering clusters in large spatial databases with noise.' In: *Kdd.* Vol. 96. 34. 1996, pp. 226–231.

Farnocchia, D., Tommei, G., Milani, A. and Rossi, A. (2010). 'Innovative methods of correlation and orbit determination for space debris'. In: *Celestial Mechanics and Dynamical Astronomy* 107.1-2 (2010), pp. 169–185. DOI: 10.1007/s10569-010-9274-6.

Felicetti, L. and Emami, M. R. (2016). 'A multi-spacecraft formation approach to space debris surveillance'. In: *Acta Astronautica* 127 (2016), pp. 491–504. DOI: 10.1016/j.actaastro.2016.05.040.

Flohrer, T., Krag, H., Klinkrad, H. and Schildknecht, T. (2011). 'Feasibility of performing space surveillance tasks with a proposed space-based optical architecture'. In: *Advances in space research* 47.6 (2011), pp. 1029–1042. DOI: 10.1016/j.asr.2010.11.021.

Fonder, G. P., Hack, P. J. and Hughes, M. R. (2017). 'AN/FSY-3 Space Fence System– Sensor Site One/Operations Center Integration Status and Sensor Site Two Planned Capability'. In: *Advanced Maui Optical and Space Surveillance Technologies (AMOS) Conference.* Presented paper. Maui (HI), USA, Sept. 2017.

Frueh, C., Schildknecht, T., Musci, R. and Ploner, M. (2009). 'Catalogue correlation of space debris objects'. In: *Proceedings of the 5th European Conference on Space Debris.* Presented paper. Darmstadt, Germany, Apr. 2009.

Fujimoto, K. and Scheeres, D. J. (2013). 'Applications of the admissible region to space-based observations'. In: *Advances in Space Research* 52.4 (2013), pp. 696–704. DOI: 10.1016/j.asr.2013.04.020.

Fujimoto, K., Scheeres, D. J., Herzog, J. and Schildknecht, T. (2014). 'Association of optical tracklets from a geosynchronous belt survey via the direct Bayesian admissible region approach'. In: *Advances in space research* 53.2 (2014), pp. 295–308. DOI: 10.1016/j.asr.2013.11.021.

Giza, D., Singla, P., Crassidis, J., Linares, R., Cefola, P. and Hill, K. (2010). 'Entropy-based space object data association using an adaptive Gaussian sum filter'. In: *AIAA/AAS Astrodynamics Specialist Conference.* 2010.

Gomez, R., Martinez-Villa Salmeron, J., Besso, P. et al. (2019). 'Initial Operations of the Breakthrough Spanish Space Surveillance and Tracking Radar (S3TSR) in the European Context'. In: *1st ESA NEO and Debris Detection Conference.* Presented paper. Darmstadt, Germany, Jan. 2019.

Gooding, R. (1990). 'A procedure for the solution of Lambert's orbital boundary-value problem'. In: *Celestial Mechanics and Dynamical Astronomy* 48.2 (1990), pp. 145–165. DOI: 10.1007/BF00049511.

Griffith, N., Lu, E., Nicolls, M., Park, I. and Rosner, C. (2019). 'Commercial Space Tracking Services for Small Satellites'. In: *Small Satellite Conference.* 2019.

Gross, J. and Yellen, J. (2004). *Handbook of graph theory.* Boca Raton (FL), USA: CRC Press, 2004. ISBN: 1-58488-090-2.

Gronchi, G. F., Dimare, L. and Milani, A. (2010). 'Orbit determination with the two-body integrals'. In: *Celestial Mechanics and Dynamical Astronomy* 107.3 (2010), pp. 299–318. DOI: 10.1007/s10569-010-9271-9.

Gronchi, G. F., Farnocchia, D. and Dimare, L. (2011). 'Orbit determination with the two-body integrals. II'. In: *Celestial Mechanics and Dynamical Astronomy* 110.3 (2011), pp. 257–270. DOI: 10.1007/s10569-011-9357-z.

Gualdoni, M. J. and DeMars, K. J. (2017). 'An Improved Representation of Measurement Information Content via the Distribution of the Kullback-Leibler Divergence'. In: *AAS/AIAA Astrodynamics Specialist Conference.* Stevenson (WA), USA: Univelt Inc., Aug. 2017.

Hagberg, A., Swart, P. and S Chult, D. (2008). *Exploring network structure, dynamics, and function using NetworkX*. Tech. rep. Los Alamos National Lab.(LANL), Los Alamos, NM (United States), 2008.

Herzog, J., Frueh, C. and Schildknecht, T. (2010). 'Build-up and maintanance of a catalogue of GEO obejcts with ZimSMART'. In: *61th International Astronautical Congress*. Presented paper. Prague, Czech Republic, Sept. 2010.

Herzog, J. (2013). 'Cataloguing of Objects on High and Intermediate Altitude Orbits'. PhD thesis. Universität Bern, 2013.

Hill, K., Sabol, C. and Alfriend, K. T. (2012). 'Comparison of covariance based track association approaches using simulated radar data'. In: *The Journal of the Astronautical Sciences* 59.1-2 (2012), pp. 281–300. DOI: 10.1007/s40295-013-0018-1.

Hu, Y.-p., Huang, J.-y. and Chen, L. (2017). 'Space-based visible observation strategy for beyond-LEO objects based on an equatorial LEO satellite with multi-sensors'. In: *Advances in Space Research* 59.7 (2017), pp. 1751–1762. DOI: 10.1016/j.asr.2017.01.018.

Hussein, I. I., Roscoe, C. W., Wilkins, M. P. and Schumacher, P. W. (2015). 'On mutual information for observation-to-observation association'. In: *2015 18th International Conference on Information Fusion*. IEEE. 2015, pp. 1293–1298.

Inter-Agency Space Debris Coordination Committee (2007). *IADC Space Debris Mitigation Guidelines*. 2007.

Izzo, D. (2015). 'Revisiting Lambert's problem'. In: *Celestial Mechanics and Dynamical Astronomy* 121.1 (2015), pp. 1–15. DOI: 10.1007/s10569-014-9587-y.

Johnson, R. A. and Bhattacharyya, G. K. (2010). *Statistics: principles and methods*. Hoboken (NJ), USA: John Wiley & Sons, 2010. ISBN: 978-0-470-40927-5.

Kalman, R. E. (1960). 'A New Approach to Linear Filtering and Prediction Problems'. In: *Transactions of the ASME–Journal of Basic Engineering* 82.Series D (1960), pp. 35–45. DOI: 10.1115/1.3662552.

Kessler, D. J. and Cour-Palais, B. G. (1978). 'Collision frequency of artificial satellites: The creation of a debris belt'. In: *Journal of Geophysical Research: Space Physics* 83.A6 (1978), pp. 2637–2646. DOI: 10.1029/JA083iA06p02637.

Klinkrad, H. (2006). *Space Debris - Models and Risk Analysis*. Berlin/Heidelberg, Germany: Springer Science & Business Media, 2006. ISBN: 978-3-540-25448-5. DOI: 10.1007/3-540-37674-7.

Kreucher, C. M., Kastella, K. D. and Hero III, A. O. (2004). 'Information-based sensor management for multitarget tracking'. In: *Signal and Data Processing of Small Targets*. Vol. 5204. International Society for Optics and Photonics. 2004, pp. 480–489.

Kuhn, H. W. (1955). 'The Hungarian method for the assignment problem'. In: *Naval research logistics quarterly* 2.1-2 (1955), pp. 83–97. DOI: 10.1002/nav.3800020109.

Lancaster, E. and Blanchard, R. (1969). 'A unified form of Lambert's theorem'. In: *NASA Technical Note D-5368* (1969).

Lei, X., Wang, K., Zhang, P., Pan, T., Li, H., Sang, J. et al. (2018). 'A geometrical approach to association of space-based very short-arc LEO tracks'. In: *Advances in Space Research* 62.3 (2018), pp. 542–553. DOI: 10.1016/j.asr.2018.04.044.

Letizia, F., Lemmens, S. and Krag, H. (2020). 'Environment capacity as an early mission design driver'. In: *Acta Astronautica* (2020). DOI: 10.1016/j.actaastro.2020.04.041.

Lewis, H., Radtke, J., Rossi, A., Beck, J., Oswald, M., Anderson, P. et al. (2017). 'Sensitivity of the space debris environment to large constellations and small satellites'. In: *Journal of the British Interplanetary Society* 70 (2017), pp. 105–117.

Li, B., Sang, J. and Chen, J. (2018). 'Achievable orbit determination and prediction accuracy using short-arc space-based observations of space debris'. In: *Advances in Space Research* 62.11 (2018), pp. 3065–3077. DOI: `10.1016/j.asr.2018.08.038`.

Lowe, J., Vallado, D. and Hall, B. (2010). 'Technical analysis of commercially hosted optical payloads for enhanced SSA'. In: *Advanced Maui Optical and Space Surveillance Technologies (AMOS) Conference*. Presented paper. Maui (HI), USA, 2010.

Ma, H., Baù, G., Cioci, D. B. and Gronchi, G. F. (2018). 'Preliminary orbits with line-of-sight correction for LEO satellites observed with radar'. In: *Celestial Mechanics and Dynamical Astronomy* 130.10 (2018), p. 70. DOI: `10.1007/s10569-018-9867-z`.

Mahler, R. P. (2003). 'Multitarget Bayes filtering via first-order multitarget moments'. In: *IEEE Transactions on Aerospace and Electronic systems* 39.4 (2003), pp. 1152–1178. DOI: `10.1109/TAES.2003.1261119`.

Mahler, R. P. (2004). 'Statistics 101 for multisensor, multitarget data fusion'. In: *IEEE Aerospace and Electronic Systems Magazine* 19.1 (2004), pp. 53–64. DOI: `10.1109/MAES.2004.1263231`.

Mahalanobis, P. (1936). 'On the generalised distance in statistics'. In: *Proceedings of the National Institute of Science of India* 2.1 (1936), pp. 49–55.

Mailloux, R. J. (2017). *Phased array antenna handbook*. Norwood (MA), USA: Artech house, 2017. ISBN: 978-1-63081-029-0.

Mann, H. K., Vananti, A. and Schildknecht, T. (2019). 'Perturbations in the optimized boundary value initial orbit determination approach'. In: *1st ESA NEO and Debris Detection Conference*. Presented paper. Darmstadt, Germany, Jan. 2019.

Maruskin, J. M., Scheeres, D. J. and Alfriend, K. T. (2009). 'Correlation of optical observations of objects in earth orbit'. In: *Journal of Guidance, Control, and Dynamics* 32.1 (2009), pp. 194–209. DOI: `10.2514/1.36398`.

McCrea, I., Aikio, A., Alfonsi, L., Belova, E., Buchert, S., Clilverd, M. et al. (2015). 'The science case for the EISCAT_3D radar'. In: *Progress in Earth and Planetary Science* 2.1 (2015), p. 21. DOI: `10.1186/s40645-015-0051-8`.

McKnight, D., Speaks, S., Macdonald, J. and Ebright, K. (2018). 'Assessing Potential for Cross-Contaminating Breakup Events from LEO to MEO'. In: *69th International Astronautical Congress*. Presented paper. Bremen, Germany, Oct. 2018.

McLean, F., Lemmens, S., Funke, Q. and Braun, V. (2017). 'DISCOS 3: An improved data model for ESA's database and information system characterising objects in space'. In: *Proceedings of the 7th European Conference on Space Debris*. Presented paper. Darmstadt, Germany, Apr. 2017.

Merz, K., Bastida Virgili, B., Braun, V., Flohrer, T., Funke, Q., Krag, H. et al. (2017). 'Current collision avoidance service by ESA's Space Debris Office'. In: *Proceedings of the 7th European Conference on Space Debris*. Presented paper. Darmstadt, Germany, Apr. 2017.

Milani, A., Gronchi, G. F., Vitturi, M. d. and Knežević, Z. (2004). 'Orbit determination with very short arcs. I admissible regions'. In: *Celestial Mechanics and Dynamical Astronomy* 90.1-2 (2004), pp. 57–85. DOI: `10.1007/s10569-004-6593-5`.

Nicolls, M., Vittaldev, V., Ceperley, D., Creus-Costa, J., Foster, C., Griffith, N. et al. (2017). 'Conjunction Assessment for Commercial Satellite Constellations Using Commercial Radar Data Sources'. In: *Advanced Maui Optical and Space Surveillance Technologies (AMOS) Conference*. Presented paper. Maui (HI), USA, Sept. 2017.

Orekit (2018). *A space dynamics library*. 2018. URL: https://www.orekit.org/.

Pantalone, B. and Kudenov, M. W. (2018). 'Initial orbit determination using Doppler shift of Fraunhofer lines'. In: *Celestial Mechanics and Dynamical Astronomy* 130.12 (2018), p. 80. DOI: 10.1007/s10569-018-9878-9.

Pavlis, N. K., Holmes, S. A., Kenyon, S. C. and Factor, J. K. (2012). 'The development and evaluation of the Earth Gravitational Model 2008 (EGM2008)'. In: *Journal of Geophysical Research: Solid Earth (1978–2012)* 117.B4 (Apr. 2012). DOI: 10.1029/2011JB008916.

Pirovano, L., Principe, G. and Armellin, R. (2020). 'Data association and uncertainty pruning for tracks determined on short arcs'. In: *Celestial Mechanics and Dynamical Astronomy* 132.1 (2020), pp. 1–23. DOI: 10.1007/s10569-019-9947-8.

Pittelkau, M. (2016). 'False-Object Identification for Space Surveillance Catalog Maintenance'. In: *Advanced Maui Optical and Space Surveillance Technologies (AMOS) Conference*. Presented Paper. Maui (HI), USA, Sept. 2016.

Press, W. (2007). *Numerical recipes : the art of scientific computing*. Cambridge, UK: Cambridge University Press, 2007. ISBN: 0521880688.

Rachman, A., Vananti, A. and Schildknecht, T. (2018). 'Analysis of Temporal Evolution of Debris Objects' Rotation Rates inside AIUB Light Curve Database'. In: *69th International Astronautical Congress*. Presented paper. Bremen, Germany, Oct. 2018.

Reihs, B., Vananti, A. and Schildknecht, T. (2018). 'Comparison of new methods for the correlation of short radar tracklets'. In: *69th International Astronautical Congress*. Presented paper. Bremen, Germany, Oct. 2018.

Reihs, B., Vananti, A. and Schildknecht, T. (2019a). 'Tracklet-based correlation of combined radar and optical measurements'. In: *1st ESA NEO and Debris Detection Conference*. Presented paper. Darmstadt, Germany, Jan. 2019.

Reihs, B., Vananti, A., Siminski, J., Flohrer, T. and Schildknecht, T. (2019b). 'Analysing the Correlation Performance of ESA's Planned Space-based GEO Surveillance Mission'. In: *70th International Astronautical Congress*. Presented paper. Washington D.C., USA, Oct. 2019.

Reihs, B., Vananti, A. and Schildknecht, T. (2020a). 'A Method for Perturbed Initial Orbit Determination and Correlation of Radar Measurements'. In: *Advances in Space Research* 66.2 (2020), pp. 426–443. DOI: 10.1016/j.asr.2020.04.006.

Reihs, B., Vananti, A., Schildknecht, T., Siminski, J. and Flohrer, T. (2020b). 'Automated Operations for the Maintenance of a Space Object Database'. In: *71st International Astronautical Congress*. Presented paper. The CyberSpace Edition, Oct. 2020.

Reihs, B., Vananti, A., Schildknecht, T., Siminski, J. and Flohrer, T. (2020c). 'Data Association Experiments Using Real Radar Data'. In: *AAS/AIAA Astrodynamics Specialist Conference*. Presented paper. Virtual, Aug. 2020.

Reihs, B., Vananti, A., Schildknecht, T., Siminski, J. A. and Flohrer, T. (2021). 'Application of attributables to the correlation of surveillance radar measurements'. In: *Acta Astronautica* 182 (2021), pp. 399–415. DOI: 10.1016/j.actaastro.2021.01.059.

Rényi, A. et al. (1961). 'On measures of entropy and information'. In: *Proceedings of the Fourth Berkeley Symposium on Mathematical Statistics and Probability, Volume 1: Contributions to the Theory of Statistics.* The Regents of the University of California. 1961.

Schumacher, P. W., Wilkins, M. P. and Roscoe, C. W. (2013). 'Parallel algorithm for track initiation for optical space surveillance'. In: *Proceedings of the 6th European Conference on Space Debris, Darmstadt, Germany.* Presented paper. Apr. 2013.

Schildknecht, T. (2007). 'Optical surveys for space debris'. In: *The Astronomy and Astrophysics Review* 14.1 (2007), pp. 41–111. DOI: 10.1007/s00159-006-0003-9.

Sciré, G., Santoni, F. and Piergentili, F. (2015). 'Analysis of orbit determination for space based optical space surveillance system'. In: *Advances in Space Research* 56.3 (2015), pp. 421–428. DOI: 10.1016/j.asr.2015.02.031.

Scott, A., Hackett, J. and Man, K. (2013). 'On-orbit results for canada's sapphire optical payload'. In: *Advanced Maui Optical and Space Surveillance Technologies (AMOS) Conference.* Presented paper. Maui (HI), USA, 2013.

Sharma, J., Stokes, G. H., Braun, C. von, Zollinger, G. and Wiseman, A. J. (2002). 'Toward operational space-based space surveillance'. In: *Lincoln Laboratory Journal* 13.2 (2002), pp. 309–334.

Siminski, J. A., Montenbruck, O., Fiedler, H. and Schildknecht, T. (2014). 'Short-arc tracklet association for geostationary objects'. In: *Advances in space research* 53.8 (2014), pp. 1184–1194. DOI: 10.1016/j.asr.2014.01.017.

Siminski, J. A. and Flohrer, T. (2019). 'Comparison-space selection to achieve efficient tracklet-to-object association'. In: *Advances in Space Research* 64.7 (2019), pp. 1423–1431. DOI: 10.1016/j.asr.2019.07.002.

Siminski, J. A. (2016). 'Object Correlation and Orbit Determination for Geostationary Satellites Using Optical Measurements'. PhD thesis. Universitätsbibliothek der Universität der Bundeswehr München, 2016.

Skolnik, M. (2001). *Introduction to radar systems.* Boston (MA), USA: McGraw Hill, 2001. ISBN: 978-0-07-288138-7.

Taff, L. and Hall, D. (1977). 'The use of angles and angular rates'. In: *Celestial mechanics* 16.4 (1977), pp. 481–488. DOI: 10.1007/BF01229289.

Taff, L. (1984). 'On initial orbit determination'. In: *The Astronomical Journal* 89 (1984), pp. 1426–1428. DOI: 10.1086/113644.

Tommei, G., Milani, A. and Rossi, A. (2007). 'Orbit determination of space debris: admissible regions'. In: *Celestial Mechanics and Dynamical Astronomy* 97.4 (2007), pp. 289–304. DOI: 10.1007/s10569-007-9065-x.

Uhlmann, J. K. (1995). 'Dynamic map building and localization: New theoretical foundations'. PhD thesis. University of Oxford Oxford, 1995.

Utzmann, J., Wagner, A., Silha, J., Schildknecht, T., Willemsen, P., Teston, F. et al. (2014). 'A system design for space-based space surveillance'. In: *Proceedings of Small Satellites Systems and Services Symposium.* 2014.

Utzmann, J., Ferreira, L., Vives, G., Métrailler, L., Lièvre, N. and Flohrer, T. (2017). 'Optical In-Situ Monitor–A Step towards European Space-Based Debris Observations'. In: *Advanced Maui Optical and Space Surveillance Technologies (AMOS) Conference.* Presented paper. Maui (HI), USA, 2017.

Utzmann, J. (2013). *System Concept Report for SBSS Demonstrator System*. ESA Study. ESA, 2013.

Vallado, D. A. and Alfano, S. (2014). 'Curvilinear coordinate transformations for relative motion'. In: *Celestial Mechanics and Dynamical Astronomy* 118.3 (2014), pp. 253–271. DOI: 10.1007/s10569-014-9531-1.

Vallado, D. A. (2010). 'Evaluating Gooding angles-only orbit determination of space based space surveillance measurements'. In: *US Russian Space Surveillance Workshop* 10 (2010).

Vallado, D. A. (2013). *Fundamentals of astrodynamics and applications*. Hawthorne (CA) USA: Microcosm Press, 2013. ISBN: 978-1881883180.

Vananti, A., Schildknecht, T., Siminski, J., Jilete, B. and Flohrer, T. (2017). 'Tracklet-tracklet correlation method for radar and angle observations'. In: *Proceedings of the 7th European Conference on Space Debris*. Presented paper. Darmstadt, Germany, Apr. 2017.

Vananti, A. and Schildknecht, T. (2019). 'Distance between Keplerian orbits in the correlation of short arc radar tracks'. In: *KePASSA Workshop*. Logroño, Spain, Apr. 2019.

Vierinen, J., Kastinen, D., Markkanen, J., Grydeland, T., Kero, J., Horstmann, A. et al. (2019). '2018 Beam-park observations of space debris with the EISCAT radars'. In: *1st ESA NEO and Debris Detection Conference*. Presented paper. Darmstadt, Germany, Jan. 2019.

Vo, B.-n., Mallick, M., Bar-shalom, Y., Coraluppi, S., Osborne III, R., Mahler, R. et al. (2015). 'Multitarget Tracking'. In: *Wiley Encyclopedia of Electrical and Electronics Engineering*. American Cancer Society, 2015, pp. 1–15. ISBN: 9780471346081. DOI: 10.1002/047134608X.W8275.

Wilden, H., Kirchner, C., Peters, O., Ben Bekhti, N., Kohlleppel, R., Brenner, A. et al. (2017). 'GESTRA-technology aspects and mode design for space surveillance and tracking'. In: *Proceedings of the 7th European Conference on Space Debris, Darmstadt, Germany*. Presented paper. Darmstadt, Germany, Apr. 2017.

Woollands, R. M., Bani Younes, A. and Junkins, J. L. (2015). 'New solutions for the perturbed lambert problem using regularization and picard iteration'. In: *Journal of Guidance, Control, and Dynamics* 38.9 (2015), pp. 1548–1562. DOI: 10.2514/1.G001028.

Yanez, C., Dolado Pérez, J. C., Richard, P., Llamas, I. and Lapasset, L. (2017). 'Optical measurements association using optimized boundary value initial orbit determination coupled with Markov clustering algorithm'. In: *Proceedings of the 7th European Conference on Space Debris*. Presented paper. Darmstadt, Germany, Apr. 2017.

Zhang, R. and Rudnicky, A. I. (2002). 'A large scale clustering scheme for kernel k-means'. In: *Object recognition supported by user interaction for service robots*. Vol. 4. IEEE. 2002, pp. 289–292.

Zittersteijn, M., Vananti, A., Schildknecht, T., Perez, J. D. and Martinot, V. (2016). 'Associating optical measurements of MEO and GEO objects using Population-Based Meta-Heuristic methods'. In: *Advances in space research* 58.9 (2016), pp. 1778–1792. DOI: 10.1016/j.asr.2016.06.026.

Erklärung

gemäss Art. 18 PromR Phil.-nat. 2019

Name/Vorname: Reihs, Benedikt

Matrikelnummer: 17 - 127- 820

Studiengang: PhD in Physics with special qualification in Astronomy

Bachelor ☐ Master ☐ Dissertation ☑

Titel der Arbeit: Processing of Space Surveillance Observations

LeiterIn der Arbeit: Prof. Thomas Schildknecht

Ich erkläre hiermit, dass ich diese Arbeit selbständig verfasst und keine anderen als die angegebenen Quel-len benutzt habe. Alle Stellen, die wörtlich oder sinn-gemäss aus Quellen entnommen wurden, habe ich als solche gekennzeichnet. Mir ist bekannt, dass andern-falls der Senat gemäss Artikel 36 Absatz 1 Buchstabe r des Gesetzes über die Universität vom 5. September 1996 und Artikel 69 des Universitätssta-tuts vom 7. Juni 2011 zum Entzug des Doktortitels be-rechtigt ist.
Für die Zwecke der Begutachtung und der Überprüfung der Einhaltung der Selbständigkeitserklärung bzw. der Reglemente betreffend Plagiate erteile ich der Univer-sität Bern das Recht, die dazu erforderlichen Perso-nendaten zu bearbeiten und Nutzungshandlungen vor-zunehmen, insbesondere die Doktorarbeit zu vervielfäl-tigen und dauerhaft in einer Datenbank zu speichern sowie diese zur Überprüfung von Arbeiten Dritter zu verwenden oder hierzu zur Verfügung zu stellen.

Hannover, 19.04.2021

Ort/Datum

Unterschrift

Curriculum Vitae

Name   Benedikt Reihs

Date of Birth   03.09.1990

Place of Birth   Hannover, Germany

Education

2016   Master of Science in Space Technology,
Atmospheric and Space Science, research oriented,
Joint European Master in Space Science and Technology,
Luleå Technical University, Kiruna, Sweden

2016   Master
Science, Technology and Health: Physics and Astrophysics,
Joint European Master in Space Science and Technology,
University of Toulouse III - Paul Sabatier, Toulouse, France

2013   Bachelor of Science in Mechanical Engineering
(Specialization: Aerospace Engineering),
Technical University of Braunschweig, Germany

2010   Abitur
Wilhelm-Raabe Schule, Hannover, Germany